Dissertations, Master's Theses and Master's Reports

2017

Influence of Magnetic Nanoparticles and Magnetic Stress on an Ionic Liquid Electrospray Source

Kurt Joseph Terhune
Michigan Technological University, kjterhun@mtu.edu

INFLUENCE OF MAGNETIC NANOPARTICLES AND MAGNETIC STRESS ON
AN IONIC LIQUID ELECTROSPRAY SOURCE

By

Kurt Joseph Terhune

A DISSERTATION

Submitted in partial fulfillment of the requirements for the degree of

DOCTOR OF PHILOSOPHY

In Mechanical Engineering - Engineering Mechanics

MICHIGAN TECHNOLOGICAL UNIVERSITY

2017

This dissertation has been approved in partial fulfillment of the requirements for the Degree of DOCTOR OF PHILOSOPHY in Mechanical Engineering – Engineering Mechanics.

Department of Mechanical Engineering - Engineering Mechanics

Dissertation Advisor: *Dr. Lyon B. King*

Committee Member: *Dr. Jeffrey S. Allen*

Committee Member: *Dr. Chang K. Choi*

Committee Member: *Dr. Benjamin D. Prince*

Department Chair: *Dr. William W. Predebon*

The most beautiful thing we can experience is the mysterious. It is the source of all true art and science. He to whom this emotion is a stranger, who can no longer pause to wonder and stand rapt in awe, is as good as dead: his eyes are closed.

-Albert Einstein

Contents

List of Figures

xvi

xx

List of Tables

Preface

The work presented in Appendix H was completed by Benjamin D. Prince and was previously including in conference proceedings at the 50th AIAA/ASME/SAE/ASEE Joint Propulsion Conference & Exhibit. He has given me authorization to reprint here via the email provided in Figure H.1.

Acknowledgements

"You're going to work very long hours on very little pay, and you'll hate the project you choose by the time you defend…" Normally when starting a pitch to a potential PhD student, advisors chose better words than those that make most turn and make a bee line to the nearest exit; but Dr. Brad King was not a typical advisor. Maybe it was his bluntness that stayed my legs, or perhaps I subconsciously wanted a challenge. But I remained in his office and heard his concluding thoughts, *"…but being a part of this lab – the thrill of accomplishing high-risk, high-payoff projects, the ability to ignore the meaning of the word impossible, and the friendships you'll build through trial and triumph – will be incomparable to anything else you've seen thus far in life."*

Those choice words only begin to describe the experiences of my PhD career. A career that at times saw me perform with gusto and vigor, while other times I was dragged through the mud, pulling for roots, just so I could complete that one last test. But I finished! However, it is only because those that guided and supported me through the endeavor that I made it to the end. Below I have tried to acknowledge as many as I can, apologies if I have missed you.

First off, I would like to thank my primary advisor, Brad King. From the moment I stepped into your office to discuss my PhD endeavor you have been an amazing mentor in all aspects of my research, and a great chaperon into the wonders of electric propulsion. It has been an honor and privilege to work with you these many years.

To the other members of my committee, Dr. Jeff Allen, Dr. CK Choi and Dr. Ben Prince, my sincerest thanks to each of you for your willingness to pass your knowledge

Now onto the people I spent most days and nights with over the years, the Ispers past and present. First to those that had graduated but couldn't move away or couldn't stay away long, Jason and Jason. Jason S., thank you for inviting me into the world of LabVIEW. Data acquisition can be complicated but you sent me down the right path. Jason M., thank you for all your help learning the about the ins and outs of FEEPs and electron microscopy, (remember when we did those things!). Though both of us have moved on to different areas your can-do attitude never left and we're still accelerating (←get it). Next, to those that were in the lab when I began – Rob, Aaron, EJ and Mark – thank you for all your assistance and training within the Isp Lab (and of course the continuous banter). Rob, thank you for your bluntness. Sometimes when you design something that destined to fail, it's better to know prior to all the blood, sweat and tears. Aaron, thank you for helping with electronics and test setups, and remaining a constant source of crazy ideas that just might work! Mark and EJ, my time at Michigan Tech came with a tales of excitement and success, and/or utter failure and blunder, all of which would not have existed had we not begun at the same time. But, nonetheless we all made it out the better (and hopefully the wiser). To Mark, congrats we are now G2, PhD! To EJ, congrats on fatherhood, may that little bucket of joy become the next expert rocket scientist (or at least robotics master)! To the others that have come through the lab during my tenure: Amanda, I'm glad you were able to come from the far Pacific shores of California and enjoy the (as you would say) Glorious Superior shores of the UP with me and the rest of the lab. I'm glad you were able take away both a degree and a person back west! To Stephan, the Dutchman Isper: I'm glad you could come and enjoy playing around with ferrofluid. I am sorry that the potential for amazing and beautiful winters wasn't enough to entice you to stay longer, but good luck in your PhD endeavors!

To Michaël, the Swiss Maestro Isper: thank you for helping me complete the final tests of my doctoral work and putting up with our harsh winter and beautifully tepid summer! For those still working diligently in the lab, Brandon, Nathan and Liz, I'm happy that I can hand over the reins to such a wonder group of people. To Brandon: all my best wishes to you in finishing your PhD. I know the frustration that comes with the final months of testing and writing, so I'm glad to see that you're getting great results. Keep it up and you'll get there! To Liz: it's somwhat regrettable that you discovered how messy ferrofluids can be, but then again getting messy is often the only way to complete the job. I wish you all the best in finishing your degree and moving onward to Texas! To Nathan: I have been overly impressed at your willingness and ability to learn all you can about the ins and outs of the Isp lab. I'm thrilled that you can continue working on electrosprays and excited that you'll be mess around with ferrofluids for years to come!

Next, I would like to thank the numerous friends that I have made during my time in Houghton. Having each of you in my life made it easier to get through the hard days in the lab. Plus, it is through you all that I learned how to enjoy life in the UP! Special shout out to Nathan and Liz. You two have been a constant throughout my many years in Houghton. I'm glad that we could have many UP adventures all because you both found out how great it is to call the Keweenaw your home! Also, special thanks to Ben and Lianna who provided me a room to stay in when I had nowhere else to turn, and for all the fish ball soup! Finally, I would like to acknowledge that Norway is a spectacular place and has very wonderful people. You know who you are. Thanks for the memories!

Lastly, I would be remiss if I did not acknowledge all the advice, support and love from my family that got me through all my years of schooling. To my grandparents: thank you

xxx

for always being there to love and support me, and to recount for me all your wise tales about life. To my brother who never questioned why I kept going to school, but always found a way to have a great time when we were together, thanks Andy! To my sister who was a preschooler when I started college, and is now a high schooler as I graduate, there are many avenues in life, choose the one that makes you feel alive and run with it. Sometimes you become a rocket scientist at the end! And at last my parents: Mom and Dad, you've been there for me through thick and thin, always providing support (monetary and the like, *i.e.* venison and fish) and advice whenever I came to you. I cannot express how much gratitude I have for what you gave me. You raised me to seek out that which interests me and pursue it to the fullest. I finished one of my interests, now onto the next! Thank you and I love you both!

<div align="right">

Kurt J. Terhune

December 2017

</div>

Definitions

a	=	Helmholtz coil radius
α_T	=	Taylor cone angle (49.3°)
b	=	distance between Helmholtz coils
B	=	magnetic field strength (scalar)
$\mathbf{B}$	=	magnetic field strength (vector)
d_c	=	capillary diameter
d_{ext}	=	extraction distance
dt	=	time delta
δ	=	inverse of dimensionless flowrate
δ_μ	=	viscous dimensionless parameter
e	=	elementary charge
$\hat{e}_r$	=	radial component
E	=	electric field (scalar)
$\mathbf{E}$	=	electric field (vector)
$E_{a,\zeta}$	=	electric field determined by Krpoun-Shea model
E_i	=	ion kinetic energy
$\langle \epsilon_{ion} \rangle$	=	most probable ion energy
ε_0	=	permittivity of free space
ε_r	=	relative permittivity
η_{fluid}	=	fluid viscosity
η_Q	=	dimensionless flowrate parameter
η_V	=	voltage utilization efficiency
$f(\varepsilon_r)$	=	Fernandez de la Mora constant
$\mathbf{F}_{Lorentz}$	=	Lorentz force
$g(\varepsilon_r)$	=	permittivity constant for F. de la Mora scaling law
γ	=	surface tension
H	=	magnetic field (scalar)
$\mathbf{H}$	=	magnetic field (vector)
I	=	emission current
I_H	=	Helmholtz coil wire current
I_T	=	total Helmholtz coil current
$\mathbf{I}$	=	identity matrix
K	=	electrical conductivity
κ	=	ratio of FEM electric field and potential in Krpoun-Shea model
L_c	=	capillary length
L_{TOF}	=	length of time-of-flight tube
m	=	mass

m/q	=	mass-to-charge ratio
m_i/q_i	=	mass-to-charge ratio of specific ion species
M	=	magnetization of the fluid
μ_0	=	magnetic permeability of free space
n	=	number of wraps in a Helmholtz coil
ξ	=	dimensionless current
p	=	pressure of atmosphere/vacuum
$\hat{p}$	=	pressure within electrospray fluid
p_c	=	capillary pressure
p_m	=	fluid-magnetic pressure
p_n	=	magnetic normal traction
p_s	=	magnetostrictic pressure
P	=	supply pressure
q	=	particle charge
q_R	=	droplet charge
q_R^{max}	=	Rayleigh limit of droplet charge
Q	=	volumetric flowrate
r	=	radius from the center of electrospray beam-axis
r_a	=	cone apex radius
r_c	=	capillary radius
r_{Larmor}	=	Larmor radius
R_D	=	droplet diameter
R_1, R_2	=	radii of curvature of liquid meniscus
ρ	=	density
θ_B	=	beam half-angle
σ_E	=	electric stress
σ_{ST}	=	surface tension stress
t_{flight}	=	time of flight
T	=	temperature
T_r	=	radial component of thrust
$\mathbf{T_m}$	=	magnetic stress tensor
v	=	particle velocity (scalar)
$\mathbf{v}$	=	particle velocity (vector)
$v_\perp$	=	perpendicular component of particle velocity
V_{ext}	=	extraction potential
V_i	=	ion acceleration potential
V_{onset}	=	onset potential
V_ζ	=	potential used in Krpoun-Shea model
z	=	center axis of Taylor cone and/or electrospray

Abstract

Two electrospray sources were developed to operate on an ionic liquid ferrofluid; one source was a pressure-fed capillary electrospray source and the other was a novel electrospray source which used a magnetically-induced instability to produce a peak from which an electric field could extract electrospray. Multiple characteristics of electrospray operation were examined for both sources using Faraday plates/cups, a quartz crystal microbalance, a retarding potential analyzer, and a time-of-flight mass spectrometer. The ILFF electrosprays for a capillary source were shown to operate in a mixed ion/droplet regime. The mass flow of the electrospray beam was primarily transported by larger particles (potential droplets) within it. The magnetic nanoparticles increased the required flowrate and extraction potential of the source, as well as the emission current at a given flowrate. The nanoparticles also influenced the beam divergence and energy of an electrospray, increasing and decreasing each respectively with higher concentrations of NPs. The magnetic field had significant influence on the flowrate of the electrospray, as it reduced the minimum stable flowrate by upwards of 16 percent. It also was shown to decreased the emission current of ILFF electrosprays for a given flowrate, while concurrently increasing the beam energy of particles in the electrospray. Other effects of magnetic field on electrospray characteristics were either inconclusive or insignificant.

Chapter 1

Introduction

1.1. Motivation

Ionic liquid electrospray sources are a unique type of spacecraft micro-propulsion which have performance versatility linked to directly to the tailorable liquid and electrical characteristics of the ionic liquid (IL) propellant. Inherent to their operation, these propulsion devices need a backbone structure (capillary needles, solid needles and porous emitters) both to enhance the electric field, and to deliver the IL to the location with an enhanced electric field. Sources using each type of emission structure have been extensively characterized based on the propellant fluid properties and composition.[1-5] However, the preparation of these structures is often time-consuming and costly,[4, 6, 7] and the lifetime of a source is limited to how well the structures maintain their geometrically sharp features; *e.g.* just the act of operating a source causes irreparable damage to the emission site. [8-10]

A solution to the challenges associated with background structures is to eliminate them. This is possible if a liquid can act as both the backbone structure and the propellant; a ferrofluid placed into a strong magnetic field does just that. The field excites an instability in the fluid called the Rosensweig instability. The result is an array of small peaks that are remarkably similar to the structures traditionally used for electrosprays.[11] An ionic liquid ferrofluid (ILFF) developed in 2011 achieves the same 'spikey' phenomenon and has near-

zero volatility thus making it suitable for in-space electrospray applications.[12] This structure-free ILFF electrospray source was first demonstrated by King *et al.* in 2013,[13] and validated the dual-purpose use of ferrofluids in propulsion; specifically, as an electrospray emitter site and as an electrospray propellant. The demonstration provides motivation to continue to study the individual effects of the nanoparticles and the magnetic field on traditional electrospray using the novel ILFF propellant.

1.2. Aim and Scope

The main difference between work reported here and work that has been reported in hundreds of prior publications on electrospray is primarily that the fluid contains nanoparticles and a magnetic field is used to impart stress to the fluid via these nanoparticles—thus the spray behaves differently than 'classical' electrospray. The goal of this research was to (1) separate the effects of magnetic nanoparticles from the effects of magnetic stress on the stable operation of an ILFF capillary source, (2) separate the effects of magnetic nanoparticles from the effects of magnetic stress on the electrospray beam structure of an ILFF capillary source, (3) separate the effects of magnetic nanoparticles from the effects of magnetic stress on the mass-to-charge of masses emitted from an ILFF capillary source, (4) characterize the emission current from a structure-free electrospray source, (5) measure the mass-to-charge ratio of charged species emitted from a structure-free electrospray source.

The scope of this work was to measure several performance characteristics of the ILFF capillary electrospray source (CES) with and without a magnetic field applied to the source.

Specifically, the onset potential, emission current, extraction potential and flowrate (in this work, I will use flowrate to mean volumetric flow rate) that define the stability island of the CES, and the divergence, energy, and the specific mass composition of the emitted electrospray beam were all measured with and without a 200-Gauss magnetic field applied to the source. Other characteristics typically associated with performance of a thruster, including the measurement of its thrust, specific impulse, and efficiency, would help define the potential of the CES in the propulsion arena but were not in the scope of this work.

Also in the scope of this study was defining the liquid and electrical properties of the propellants. The surface tension, viscosity, and electrical conductivity of a propellant each influence different parameters of the electrospray emission, such as onset/extraction potential and emission current. Each of propellant properties were measured and/or interpolated for all propellants used in the study. The relative permittivity of each of the ILFF-based propellants was not measured. Relative permittivity of an electrospray propellant can affect the emission properties, including emission current and onset potential. However, the device required to measure permittivity was not available for this work and therefore out of the scope of this study.

The in-scope characteristics that were measured differed between each of the propellants used in the study. The lower flowrate and extraction potential boundaries of the stability island for a magnetic-field-free electrospray were only measured using the neat IL (pure ionic liquid that is free of nanoparticles) and ILFF-based propellants. The upper boundaries of flowrate and extraction potential of magnetic-field-free electrosprays using the neat IL or ILFF-based propellants was out of the scope of this study, as were the

measurement of any of the flowrate or extraction potential boundaries of the magnetic-field-free ILFF electrospray.

Onset potential as a function of magnetic field strength was only measured for the parent ILFF propellant, and the lower flowrate boundary of the stability island during magnetic field application were only defined for the ILFF-based propellants. Onset potential and upper limit of flowrate of for stable electrospray during the application of a magnetic field application for each of the different ILFF propellants were not measured, nor were any stability island boundaries of the parent magnetically-stressed ILFF. These measurements are necessary to assess how the magnetic stress affects the electrospray's full stability envelope, a useful metric in electrospray performance, however they were out of the scope of this work.

The measurement of the beam divergence, the center-axis beam energy, and the specific mass-to-charge of the emitted particles in the center of the electrospray beam of magnetic-field-free and magnetically-stressed electrosprays using neat IL and ILFF propellants were all in the scope of this study. They provided an estimate of the efficiency lost due to the off-axis trajectories, the partial-acceleration and/or the polydispersity of the emitted particles, and an assessment of the effect magnetic stress had on the beam structure. However, the measurement of these three characteristics using the parent ILFF was out of the scope of this study, as was angular-resolved beam energy and angularly-resolved specific mass-to-charge of the electrospray beam. The latter two are items of interest for this research, as the magnetic stress could affect the energy and mass distributions at higher angles from the center beam axis. However, this

required some means to rotate the electrospray source and source magnetic field in tandem relative to the diagnostics bench. The construction of which was out of the scope of this work and consequently angularly-resolved beam diagnostics.

Also, varying magnetic field strength while measuring emission current, stability island, beam divergence and energy and specific mass-to-charge of particles in the beam would be of interest to this research as it may reveal trends in each of these measurements with respect to the magnitude of magnetic field. However, this too was out of the scope of this study.

The last items in the scope of this research involve a separate electrospray source that intended to expand on the structure-free ILFF electrospray research. This included the construction of a source capable of creating a single ILFF peak of the Rosensweig instability (RP-ES) and measurement several performance characteristics of the source, specifically the emission current, and the mass flowrate and mass-to-charge of the emitted particles in the electrospray. However, as with the CES, the measurement of many other characteristics of performance, including (but not limited to) thrust, specific impulse, and efficiency were not in the scope of this work and thus not measured. Also, the measurement of particles with specific mass-to-charge greater than 5,000 amu/e would be of interest to this research as it would help determine the emission mode (pure ion, ion/droplet) of the RP-ES. However, the measurement was not viable using the mass spectrometer available during RP-ES development, and therefore not in the scope of this study. Lastly, angularly-resolved beam diagnostics of the electrospray from a Rosensweig peak is necessary to fully understand and characterize the new source; this includes beam divergence, beam energy, and beam composition. However, this was outside of the scope of this work.

1.3. Structure of Document

The structure of the rest of this dissertation follows the process I took to first learn and understand the potential of backbone-free ferrofluid peak emitters within the current electrospray propulsion field, all the way to the final realization of a measuring the specific m/q of the electrospray beam emitted from one of these peaks. As such, Chapter 2 begins the dissertation with a literature review of the necessary pieces of this research, including electrospray and electrospray propulsion, ferrofluids, and the physics within each.

With grounding in the current state of the art in electrospray measurement and the new ferrofluid propellant used in this work, Chapter 3 continues the dissertation by describing the equipment and facilities used in this research, including a single-emitter capillary electrospray source designed to exploit the magnetically-susceptible propellant, the vacuum and time-of-flights facilities at Michigan Technological University and the Air Force Research Laboratory at Kirtland AFB. It concludes with the properties of all the propellants that were used in this research.

Chapters 4 begins the first of four chapters which examine the high-conductivity ILFF propellants. Since no prior research exists in which they were used for magnetic-field-free or magnetically-stressed capillary electrospray, the goal of the chapter was to determine the stability island of the electrospray source running on all the ILFF propellants. This included adding the external magnetic stress to the source during operation. Chapter 5 presents the setup and results from two diagnostic experiments – beam divergence and stopping potential – which used the newly defined stability island of the capillary source. This goal of the diagnostics was to understand how the electrospray beam changed when

using propellants with different concentrations of nanoparticles, or when adding a magnetic stress to the operating source. Chapter 6 presents the experiments used to examine the emission products from the magnetic-field-free and magnetically-stressed electrosprays using a time-of-flight (TOF) mass spectrometer. The goal of which was to determine the mass and charge emitted particles in the electrospray and understand how nanoparticles and magnetic stress influenced their emission.

The material of Chapter 7 is presented as the final research chapter as it includes the experiments done using the backbone-free ILFF electrospray source. The results from which include the basic operation of the source, and a study of the emission products completed using the TOF mass spectrometer. It concludes by comparing the backbone-free ILFF peak electrospray source and the two traditional electrospray sources also tested in this research: solid needle and capillary.

Chapter 8 completes the dissertation with a conclusion of all the work presented, and includes potential improvements to the experimental approach and possible avenues for future research.

Chapter 2

Literature Search and Motivation

This chapter provides a summary of relevant literature including the challenges of ionic liquid (IL) electrospray in spacecraft propulsion, along with the potential for new propellants, both of which motivate my dissertation research. The chapter begins with a literature review of ionic liquid electrospray propulsion operating parameters for the devices used in electrospray propulsion. It continues with an overview of R. E. Rosensweig's ferrohydrodynamics which motivated the use of magnetic fluids in electrospray and concludes with the potential for ILFFs in the propulsion field.

2.1. Electrospray

Zeleny first showed that an electrostatic field could produce a fine spray of liquid droplets, molecules, and/or atoms from liquid meniscus.[14] The process was termed Electrospray by researchers and became the approach for multiple arenas of research including deposition, mass spectrometry, and spacecraft propulsion. The latter of these research arenas came into focus in the 1960s when Krohn developed experiments using liquid metals and viscous liquids, like glycerol.[15, 16] A pitfall of glycerol was its low conductivity, a characteristic that was poor for creating a high-impulse thruster inherent to low-thrust and low-power space propulsion. Soon after Perel *et al*.[17] developed a thruster using high-conductivity fluids H_2SO_4 and cesium which created high-specific impulse (I_{sp}) electrosprays comprised solely of ions; however, the liquids posed a health-hazard to the

researchers. The idea to use ILs as propellants that came in the early 2000s and solved some of the challenges and hazards of their predecessors.[1, 18, 19] Ionic liquids can be tailored to fit a variety of applications, including those requiring high-conductivity and low-volatility, and health hazards of the liquids are easily subdued in a laboratory environment.[20] As such a review of ILs with respect to spacecraft electrospray propulsion is the perfect avenue to determine where new propellants fit into the arena, *e.g.* the ferrofluids used in this research. However, first an overview of the underlying physics of electrosprays is necessary to properly understand the benefits of ILs and alternative propellants.

The electrospray phenomenon occurs through the imbalance of surface tension, σ_{ST}, and electrostatic stress, σ_E, on a liquid's surface. Figure 2.1. a) illustrates the force balance on the liquid surface which produces the electrospray. Electrostatic stress comes from an electric field being applied to the liquid's surface, (2.1). The surface tension stress is inherent to the internal energy of the liquid meniscus, and can be related to the geometry of the liquid meniscus, (2.2).

$$\sigma_E = \frac{1}{2}\varepsilon_0 E^2 \tag{2.1}$$

$$\sigma_{ST} = \gamma\left(\frac{1}{R_1} + \frac{1}{R_2}\right) \tag{2.2}$$
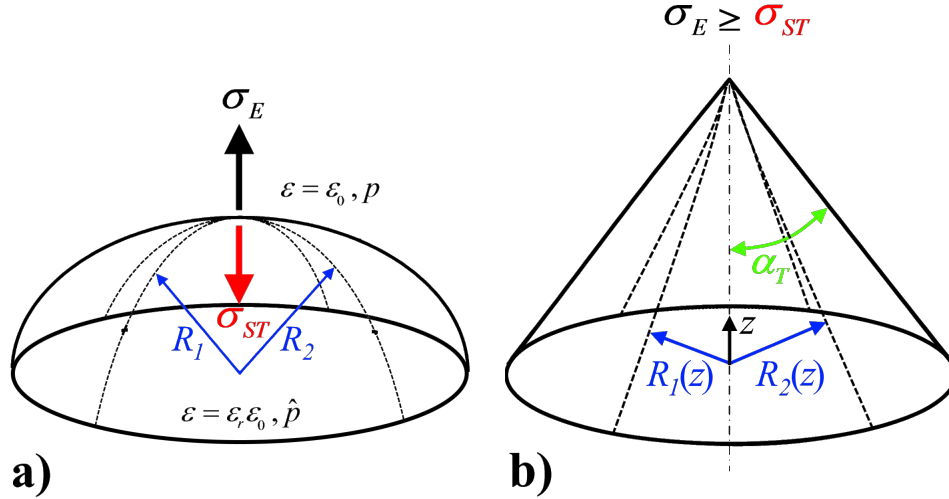
Figure 2.1. a) Force balance on the meniscus of a fluid-vacuum interface in an electric field. b) Geometry of a Taylor cone formed at the critical point when electric stress overcomes surface tension (onset) denoting the Taylor cone half-angle.

G.I. Taylor determined in his classical papers that upon the application of electric field the meniscus will deform along the direction of the field.[21-23] When a sufficient field is applied to the meniscus, the radii of curvature for the meniscus become infinitesimally small, $R_1(z)$ and $R_2(z)$ for z equal to apex height, and the meniscus deforms into a conical in shape with a half-angle $\alpha_T \equiv 49.3°$, Figure 2.1. b). Realistically, the meniscus radius cannot decrease below the nanoscale range. Instead, the increase in electric field elicits an emission of charge from the cone apex via a jet of charged particles, *i.e.* electrospray ionization onset.

Prewett and Mair and have shown that an estimate of the potential to induce onset, V_{onset}, for electrospray emitters is a function of the extraction distance, d_{ext}, the capillary diameter, d_c, and γ of the propellant, (2.3).[24]

$$V_{onset} = \ln\left(\frac{4d_{ext}}{d_c}\right)\sqrt{\frac{\gamma d_c}{2\varepsilon_0}} .$$

(2.3)

(2.3) has an inherent problem in that it assumes the radius of the liquid emitter is constant. However, the application and increase of an electric stress to the liquid meniscus and the opposing surface tension stress reduces the radius of the emitter apex. Therefore, a better model of V_{onset} requires a continuous change in radius caused by these competing stresses. Krpoun and Shea attempted to reconcile this continuously shrinking apex radius by solving the apex electric field over a series of liquid menisci, varying in apex radius, r_a.[25] The resulting model of V_{onset} in of an electrospray in ionic mode as a function of the ratio between electric field, $E_{a,\xi}$, and potential, V_ξ, used in the their FEM solution, $\kappa = E_{a,\xi}/V_\xi$, γ, and r_a:

$$V_{onset} = \frac{1}{\kappa}\sqrt{\frac{4\gamma}{\varepsilon_0 r_a}} \qquad (2.4)$$

Also in their study, Krpoun and Shea also found that V_{onset} was lower for emission cones that had half-angles larger than the Taylor cone angle (49.3°). V_{onset} will be useful in assessing the benefits using the alternative propellants presented in this dissertation.

For potentials greater than the onset potential the meniscus will emit a continuous jet of particles and charge. The mass flow and current of the resulting jet and its dependence upon fluid and electrical parameters has been studied extensively; three groups that have studied the scaling laws of electrosprays extensively are Fernández de la Mora and Loscertales in 1994,[26] Gañán-Calvo *et al.* in 1997,[27] and Chen and Pui also in 1997.[28] The former group analyzed the emission of various polar fluids to empirically determine that the droplet radius scales as,

$$R_D = 0.5(Q\varepsilon_r\varepsilon_0/K)^{1/3},$$ (2.5)

and the current emitted from an electrospray source scales as,

$$I = f(\varepsilon_r)\left(\frac{\gamma K Q}{\varepsilon_r}\right)^{1/2},$$ (2.6)

where

$$f(\varepsilon_r) = \frac{\xi}{\eta_Q},$$ (2.7)

$$\xi = I/\left(\gamma\sqrt{\varepsilon_0\rho}\right),$$ (2.8)

and

$$\eta_Q = \left[(\rho K Q)/(\gamma\varepsilon_r\varepsilon_0)\right]^{1/2}.$$ (2.9)

$f(\varepsilon_r)$ is known as the Fernández de la Mora constant, η_Q, is the dimensionless flowrate parameter, and ξ is dimensionless current. Both Gañán-Calvo *et al.* and Chen and Pui expanded on Fernández de la Mora and Loscertales' model, with the former defining $f(\varepsilon_r) = 6.46\varepsilon_r$ for electrosprays with jets having lengths much less than other geometric length of the Taylor cone, and the latter defining $f(\varepsilon_r) = 336\varepsilon_r^{-1/6} + 157\varepsilon_r^{1/6} - 0.21\varepsilon_r - 449$ for electrosprays with jets on the order of the capillary diameter. Furthermore, in the study by Gañán-Calvo *et al.* they determined that the dimensionless parameter that governed liquid acceleration process, $\delta_\mu\delta^{1/3}$, was ultimately responsible for spray current and droplet size. In the parameter,

49

$$\delta_\mu = \left[\frac{\rho \varepsilon_0 \gamma^2}{K \eta_{fluid}^3} \right]^{1/3}, \tag{2.10}$$

and

$$\delta = \frac{\gamma \varepsilon_0}{\rho K Q}. \tag{2.11}$$

Gañán-Calvo *et al.* found that for $\delta_\mu \delta^{1/3} \ll 1$ or $\delta_\mu \delta^{1/3} \leq O(1)$, the droplet size and spray current scale as $R_D \sim Q^{1/3}$ and $I \sim Q^{1/2}$, respectively, whereas if $\delta_\mu \delta^{1/3} \gg 1$ the droplet size and spray current scale as $R_D \sim Q^{1/2}$ and $I \sim Q^{1/4}$, respectively. The overall conclusion of the studies is that both viscosity and conductivity are highly influential on the scaling of current and droplet size of the electrospray. This will be examined further during the discussion on emission current using the new ILFFs used in the research presented in this dissertation (Section 4.3.3.b.).

Beyond the Taylor cone-jet region of the electrospray exist the emission products which take the form of ions and/or droplets. Lord Rayleigh found that the size of the droplets emitted from the jet can also be determined through an examination of the coulombic stability of the droplets, *i.e.* the balance of electric stress, caused by charge density of the droplet, and surface tension holding a droplet intact. He found that the upper limit of charge that a droplet of fluid can hold prior to splitting is (2.12).[29]

$$q_D^{max} = 8\pi \sqrt{\gamma \varepsilon_0 R_D^3} \tag{2.12}$$

Termed the Rayleigh limit, (2.12) can be rearranged to determine the droplet diameter,

$$R_D = \left(\frac{1}{64\pi^2} \frac{q_D^2}{\gamma\varepsilon_0} \right)^{1/3} \qquad (2.13)$$

As mentioned previously, the droplet diameter was found to scale as (2.5). Therefore, the flowrate and Rayleigh limit are useful in determining the size of emitted droplets in electrosprays, which becomes relevant when comparing their size to the size of nanoparticles in the ILFFs introduced in Section 2.2.

In summary, onset potential, emission current, and droplet size of electrosprays are all functions of the fluid parameters of the propellant, such as conductivity, surface tension, viscosity, and volatility. Ionic liquids (ILs) comprise a large family of fluids which are defined by their composition, i.e. equal parts anions and cations. With a vast selection of combinations of anion-cation pairs to choose from, the properties of an IL can be tailored to fit different electrospray applications. [20] For example, high conductivity fluids produce small jets and small droplets or even ions.[18, 30] It is also possible to produce ILs with both high conductivity and negligible volatility, which would be suitable for electrosprays in a vacuum environment; *e.g.* electrospray propulsion.[1, 3, 18, 31-33]

2.1.1. Ionic Liquid Electrospray Propulsion

Gamero-Castaño and Hruby were the first to demonstrate the use of a high-conductivity, low-volatility IL as an electrospray propulsion propellant.[18] Their system, termed capillary electrospray, fed the IL 1-ethyl-3-methylimidazolium bis(trifluoromethylsulfonyl)imide (EMIM-NTf2) through a 50-μm inner diameter fused-silica capillary tube to a needle apex that was sharpened to a cone; the capillary was coated

with a conductive layer of tin-oxide. They found that the electrospray emitted with a relatively low I_{sp} of 126-171 seconds, an average mass-to-charge ratio of 100,000-150,000 amu/e, and with a mixture of ions and droplets. Furthermore, they determined that large polydispersity of emission effectively lowered thruster efficiency by 25-percent.

Hruby and Gamero-Castaño continued expanded on this original by fabricating and demonstrating a 9-emitter array for Busek Co. Inc, which provided 5-30 µN of thrust using the EMIM-NTf2 propellant. They are the first flight electrospray thrusters, launched on the NASA/ESA LISA Pathfinder mission, ST7 in 2015.

Since these first demonstrations of electrospray used for propulsion, other groups have developed their own method to produce and extract various propellants via electrospray. Romero-Sanz, Bocanegra, Fernandez de la Mora and Gamero-Castaño also used a capillary needle electrospray source (20- or 40- µm inner diameter), but the propellant was a higher conductivity IL, 1-ethyl-3-methylimidazolium tetrafluoroborate (EMI-BF$_4$).[34] Lozano's group at Massachusetts Institute of Technology developed both planar and rectangular arrays of porous emitters through a myriad of MEMS processes using materials such as tungsten, silica, and carbon xerogel.[2, 35-38]

Though the heritage of these types of thrusters appears sound, they do have obstacles, including clogging,[1] emitter or propellant degradation,[30, 39] and arcing events,[9, 10, 40, 41] each of which could prove disastrous for multi-year in-space missions. Researchers have accounted for most of these obstacles, (prepping procedures to prevent clogging of foreign materials, and alternating bias and distal electrodes to mitigate degradation), but the underlying cause of them stems from the emitter structures necessary for the

electrospray process. They are typically small, relatively sharp features, which provide geometric enhancement to an applied electric field, and lower the electric field strength required for extraction. Due to the complexity in their fabrication, these emission structures are time-consuming and costly to produce. Furthermore, their size and aspect ratio makes them inherently fragile to contact or arcing. While the time and cost to fabricate these arrays have been reduced by an order of magnitude thanks to newer technologies, the fragility remains an issue. The new technology developed at Michigan Tech uses ILFF as both the propellant and support structure that could provide an alternative technique which may avoid the inherent fragility of emitters in literature. However, a sound comparison between the neat IL and ILFF electrosprays technologies is necessary to understand the impact that ferrofluids would have on current techniques; this is the primary motivation for this research.

2.1.2. Angular Divergence of Electrospray Beam

A beam of charged particles has inherent self-repulsion forces which induces uniform radial spreading away from the central axis of the electrospray, Figure 2.2. Beam spreading is undesirable for an electrospray thruster as the resultant radial components of thrust cancel, while the process of accelerating the particles still consumes power. The radial component of thrust, T_r, is easily related to the angle of the beam divergence, θ_B, via

$T_r = \sin\theta_B \dfrac{d(m\mathrm{v})_i}{dt}\hat{e}_r$, where the derivative term is the time-rate of momentum change of

the particles in the electrospray beam; θ_B is also a dependent term in the beam divergence

efficiency of a thruster.[42] As such, the measurement of θ_B is of interest to any research related to propulsion.
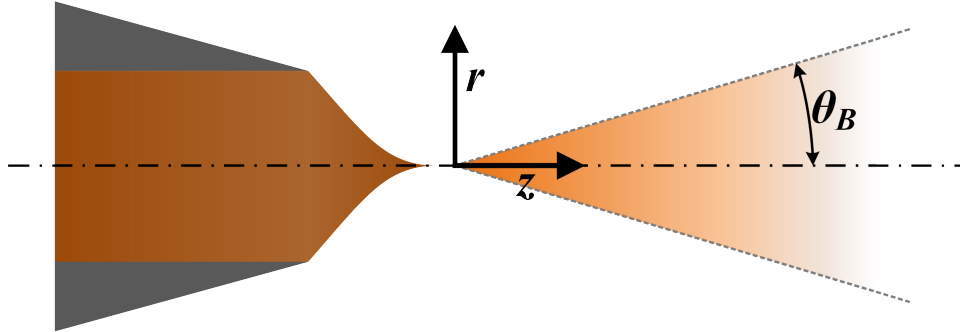
Figure 2.2. Divergence of the emitted beam in a uniform electrospray.

Multiple diagnostic tools exist to measure beam divergence ranging in collection method and angular resolution. Lozano developed a current collector comprised of 10 concentric rings (largest had a 6-cm diameter) and a one center circular plate to measuring beam spread and focusing.[1] He found that the collector needed to be positioned relatively close to the source (within 7-cm) to collect the majority of the electrospray beam. Prince's group at the Air Force Research Laboratory attached their capillary electrospray source to a rotatable platform such that it could rotate ±45° in the vertical plane.[43] Similarly, a Massachusetts Institute of Technology team led by Gassend developed a method of rotating their array of electrospray emitters to measure divergence of the beam.[7] The advantages of these setups over Lozano's was their ability to gather current profiles over a large angular range without requiring the close proximity of the diagnostic tool to the source. However, rotation requires a dynamic device that can be cumbersome. Therefore, the device used for experiments presented in this dissertation had a design similar to Lozano's setup to reduce complexity.

2.1.3. Energy of Electrospray Beam

Another important characteristic of an electrospray is the kinetic energy of the charged particles (hereon referred to as ions) that comprise the beam. In a perfectly accelerated electrospray beam, the kinetic energy of any ion, $\frac{1}{2}m_i v_i^2$, is equal to the input electric energy of the extraction region, eV_{ext}. However, it is well known that perfect acceleration of all particles in an electric propulsion device does not occur.[42] This excess power to the system results in what is defined as the voltage utilization efficiency, η_V, and is actual energy imparted to ion during their birth and acceleration to the total input energy of the electrospray extraction region,

$$\eta_V = \frac{\frac{1}{2}m\langle v^2 \rangle}{eV_{ext}} = \frac{\langle \epsilon_{ion} \rangle}{eV_{ext}}. \tag{2.14}$$

In (2.14), $\langle \epsilon_{ion} \rangle$ is the most probable ion kinetic energy. Since kinetic energy is directly related to the distance the ion travelled through the extraction field, (which has a maximum potential of V_{ext}), $\langle \epsilon_{ion} \rangle$ will always be less than or equal to V_{ext}.

The quantity $\langle \epsilon_{ion} \rangle$ is typically measured using what is called a retarding potential analyzer (RPA). A description of RPA function is presented in Section 5.2.2. Variations of RPAs have been designed and tested for electrospray devices. Miller *et al.* used a set of three grids each in line with the far-field electrospray beam axis and measured the potential required to block ions from entering the main detection unit of their time-of-flight (TOF) mass spectrometer.[43] Lozano used a similar method in a linear TOF mass spectrometer wherein two parallel grids were placed before the TOF collector and biased to an increasing

potential until zero current was measured.[1] Most recently a spherical RPA was developed by Miller *et al*. to measure the fragmentation rates of ion clusters.[44] Her design was specifically crafted to simultaneously capture particles emitted at high-angles by using large-diameter, curved grids, while also mitigating IL buildup on the RPA grids (a common failure mechanism of RPAs when measuring IL electrosprays) by using grids with large open-areas. Therefore, the RPA designed for experiments presented in this dissertation followed Miller's approach to mitigate IL buildup, but used small grids that only measured the center axis due to space limitations.

2.1.4. Polydispersity of Electrospray

Polydispersity *i.e.* multiple ion species and droplet populations, of the products created by an electrospray thruster is reportedly the most influential to thrust efficiency.[1] However, an electrospray that emits polydisperse particles, is not inherently undesired. Having an ability to throttle the emission from an electrospray from pure ion (few ion species) to mixed ion/droplet (polydisperse) to pure droplet (one or two droplet populations) provides flexibility in the amount of thrust (or specific impulse) the source can provide.[1, 3, 33] Therefore, a measurement of the polydispersity of an electrospray beam is of interest when developing source with new propellants or, in the case of this study, added body forces (magnetic field).

A stepping stone in determining polydispersity is measuring the size of particles within a part of an electrospray beam. One method to determine just that is called mass spectrometry. In this technique, the m/q values of an electrospray are measured using a

couple different types of mass spectrometers (time-of-flight or quadrupole), which results in spectra denoting the relative fraction of the emitted ion and droplet species within the beam. As such, mass spectrometers are well established in the electrospray community.[2, 4-7, 33, 45-51]

Within the field of electrospray propulsion, time-of-flight mass spectrometers (TOF-MS) are most common, though their design and function vary. Gamero-Castaño and Hruby used a linear TOF-MS setup which measured the current of the electrospray beam using a collector-plate read by a fast electrometer and recorded via an oscilloscope that was triggered by the voltage signal of the electrospray needle to measure EMIM-NTf2 and formamide and tributyl phosphate.[18] The same device was used by Romero-Sanz *et al.* and Garoz *et al.* to study 1-ethyl-3-methyl-imidazolium tetrafluoroborate (EMI-BF4) and high surface tension ILs, respectively.[34, 52] K. L. Smith and J.P.W. Stark at Queen Mary University have a similar TOF-MS setup and have collected spectra from several types of sources running the IL EMI-BF4.[40, 53, 54] While these devices were useful in confirming the polydispersity of IL electrospray beam, the resolution is limited to the energy spread of the emitted particles. Furthermore, larger m/q species are often indiscernible due to the low signal relative to lighter ions and droplets.

Lozano built a dual electrostatic-gate TOF-MS with an electrostatic mirror to correct for the energy spread observed in the previous devices.[1] The electrostatic gates were normally closed and opened for very short intervals to ensure the electrospray beam only entered the TOF drift tube during collection of spectra. The length of the pulse which opened the gates defined the resolution of the spectra. Also, the electrostatic mirror

provided the means to separate the particles based on their accelerating potential, further increasing the resolution of the detector by eliminating the energy spread of each ion/droplet species. The dual gate design allowed the instrument to collect only those particles within a select range of flight times by delaying the pulses of each gate by a known time. The device was capable of high-resolutions mass measurements ranging of single ion species (<1000 amu) as well as the collection of droplet distributions.[1, 55] Chui *et al.* used a similar TOF-MS that had a dual-gate sans the electrostatic mirror and realized similar capture of ion species in their mass spectra.[33] These devices, while an upgrade from those used by Gamero-Castaño and Hruby, and K. L. Smith and J.P.W. Stark, still lacked the capability of measuring of discriminating larger m/q particles (*i.e.* droplets distributions). The size of the NPs in the ILFFs developed for this research are similar to typical IL droplets sizes expected in capillary IL electrospray (30-nm-diameter and 10- to 100-nm-diameter, respectively), which are in the range of 40,000-200,000 amu/e.[26, 56] Therefore, since a goal of this research was to discern the NPs from other species within the electrospray beam (IL ions and/or droplets), a different mass spectrometry technique was required.

In 2014, Prince's group at the AFRL at Kirtland AFB developed a method to measure the m/q >10,000 amu/e using their orthogonal TOF-MS.[57] The device is unique compared to the others previously described; instead of pulsing an electrostatic gate and measuring the TOF of the electrospray beam that makes it through in the pulse-time, the AFRL device slows the emitted electrospray to thermal velocities within a set of pulsing plates orthogonal to the electrospray beam axis, where they are then extracted into the flight tube located orthogonal to the beam axis by pulsing one of the two plates (see Figure 3.8.

of 3.6). The device could discriminate multiple droplet distributions within an BMIM-DCA and EMIM-NTf2 electrospray in the mass range of 10,000 amu/e to 200,000 amu/e while maintaining high resolution collection of ion species in the sub-5,000 amu/e range.[58] The functionality of the AFRL orthogonal TOF-MS was what prompted its use for measuring the new ILFF electrosprays, which were believed to have both ions, droplets, and NPs.[46]

Having reviewed electrosprays used in space propulsion, the parameters that drive them, and the methods to test their performance in a laboratory setting, I will now review the necessary material that pertains to the new ILFF propellants used in this research. This includes an overview of ferrofluids and their synthesis, the basic physics attributed to electromagnetic interaction with the surface of these fluids, and the potential for their use in spacecraft propulsion.

2.2. Ferrofluids and the Rosensweig Instability

The first ferrofluids were developed by S.S. Papell in 1965, though the materials and technology have been available for millennia.[59] They are formed by suspending single-domain magnetic nanoparticles in a carrier liquid; the resulting fluid is susceptible to magnetic fields. The particles are of such small size—on the order of 10 nm—that Brownian motion prohibits sedimentation caused by external body forces.[45] Additionally, the are coated with a polymer surfactant to prohibit clumping. These qualities make ferrofluids applicable in multiple arenas including engineering (for damping in speakers, heat transfer, and bearings);[45, 60, 61] biomedical (for drug delivery,

hyperthermia, in vitro applications and within MRI machines);[62-64] and more recently propulsion, specifically, ionic liquid ferrofluid (ILFF) electrosprays.[13, 46]

The following subsections describe the techniques used to create ferrofluids, including the synthesis of our unique ILFF. This is followed by an overview of Rosensweig's work on the physics that govern ferrofluid that has been placed in a within a magnetic field. Both are necessary to understand our motivation to use ILFF in space propulsion applications, which is discussed in the concluding subsection of this chapter.

2.2.1. Synthesis of Ferrofluids

To prepare a suitable ferrofluid for specific applications involves two components, the creation of monodomain and monodisperse nanoparticles, and the selection of a carrier fluid and polymer coating which stabilize the particles in the fluid. Two primary methods are used to create a ferrofluid, size reduction and chemical precipitation.[11] The first method of size reduction was discovered by Papell and was accomplished through wet grind of material using a surfactant for 100s of hours. Rosensweig, Nestor, and Timmins enhanced the process by perfecting a way to create a monolayer surfactant coating, definitively measuring the particle size, and developed a method to remove oversized particles.[65] Rosensweig and Kaiser went a step further by developing a method to disperse particles in other solvents including water and hydrocarbons.[66] A benefit of the size reduction process is bulk synthesis of ferrofluids. The method for chemical precipitation to create ferrofluid typically requires a soluble metal salt and a coprecipitate (NaOH or NH_4OH) to be mixed to start precipitation, followed by a peptization step to exchange particles from an aqueous phase to an organic phase using a dispersant.[11]

Multiple groups have produced fluids with water and oil as the carrier liquid using both methods of synthesis.[60, 67-70] Also, Jain *et al.* was the first to demonstrate aqueous ferrofluids that would 'spike' when subjected to a magnetic field.[70] All of these fluids were decent for simple demonstrations at atmosphere, but lacked a critical requirement to use them as electrosprays in a vacuum: low vapor pressure.

In the early 2010s several groups produced viable fluids with low vapor pressures by using an ionic liquid as the carrier fluid; Hawkett *et al.* and Mestrom *et al.* used iron oxide particles,[12, 71, 72] and Huang and Want used cobalt ferrite particles.[73] Hawkett and Jain of the University of Sydney demonstrated sterically-stabilized ionic liquid ferrofluid by incorporating a thin coating of short acrylic acid-b-acrylamide copolymer (AA10-b-AM14) on ~10-nm diameter γ-Fe_2O_3 particles in 1-Ethyl-3-methylimidazolium acetate, EMIM-Ac, and Ethylammonium nitrate, EAN.[12] This led to a collaboration between Hawkett and Jain of the University of Sydney, and Meyer, Hopkins, and King of Michigan Technological University that resulted in a similar ionic liquid ferrofluid using 1-Ethyl-3-methylimidazolium bis(trifluoromethylsulfonyl)imide, EMIM-NTf2 as the carrier fluid.[13] Multiple batches of the EMIM-NTf2 ferrofluid were prepared using Sirtex maghemite nanoparticles and the block copolymer poly(MAEP10-b-DMAm60) at varying weight-percent of components. Table 2.1 lists four of the batches labelled NJ397028, NJ397047, NJ397074, and NJ397091 created for the Ion Space Propulsion Laboratory.

The significance of the ILFFs in Table 2.1 is their ability to produce 'spikes' along the surface when subjected to an external magnetic field. The phenomenon is essential to their use as emission sites for electrospray propulsion, and would replace the state-of-the-art

solid backbone emission sites. The phenomenon was studied extensively by R. E. Rosensweig and will be reviewed in the next subsection.

Table 2.1. Properties of Ionic liquid ferrofluid batches synthesized by Hawkett and Jain. All ferrofluids use EMIM-NTf2 as the carrier liquid.

Batch No.	Fe_2O_3 % (w/w)	Polymer % (w/w)	Ionic Liquid % (w/w)
NJ397028	27	3.9	69.2
NJ397047	27	4.5	68.5
NJ397074	26.3	3.9	69.8
NJ397091	26	4.6	69.4

2.2.2. The Rosensweig Instability and Ferrohydrodynamics

Subjecting a ferrofluid to a strong magnetic field causes the magnetization of the nanoparticles to align with the magnetic field. Perturbations along the surface of the colloid cause local concentrations of the magnetic field. The concentration of the magnetic field attracts the nanoparticles and an instability forms that causes the liquid to bulge at the locations of concentrated magnetic field known as the Rosensweig instability.[11, 67] The instability is balanced by the surface tension of the fluid which pulls against this change in the liquid surface. The result is an arrangement of static fluid peaks on the surface of the ferrofluid, Figure 2.3. R. E. Rosensweig studied the physics behind the instability shown in Figure 2.3. along with the physics of other fundamental phenomena observed when using ferrofluids in his book *Ferrohydrodynamics*.[11] I will detail some of his findings below as they pertain to the ILFFs used and experiments conducted in this research.
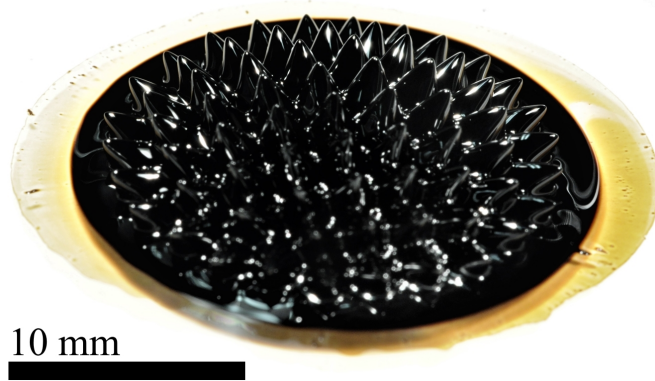
Figure 2.3. The surface of a hydrocarbon-based ferrofluid after application of a divergent magnetic field. The magnetic field induces Rosensweig instability forming an arrangement of static liquid peaks along the liquid surface.

In his text, Rosensweig determined the magnetic stress tensor, $\mathbf{T}_m$, that acts on a ferrofluid due to the magnetic field.

$$\mathbf{T}_m = -\left[\mu_0 \int_0^H \upsilon \left(\frac{\partial M}{\partial \upsilon} \right)_{H,T} dH + \mu_0 \int_0^H M dH + \frac{1}{2}\mu_0 H^2 \right] \mathbf{I} + \mathbf{BH} \qquad (2.15)$$

In (2.15) he defined two terms which will elucidate the stress balance that forms the peaks of the Rosensweig instability. The first is termed the magnetostrictive pressure, p_s, and is equal to,

$$p_s = \mu_0 \int_0^H \upsilon \left(\frac{\partial M}{\partial \upsilon} \right)_{H,T} dH \;. \qquad (2.16)$$

The second term is the fluid-magnetic pressure, p_m, which is equal to,

$$p_m = \mu_0 \int_0^H M dH \;. \qquad (2.17)$$

Using the terms of (2.15) Rosensweig developed an augmented form of the Bernoulli equation which includes the terms for an ferrofluid within a magnetic field:

63

$$\rho\left(\frac{\partial \mathbf{v}}{\partial t} + \mathbf{v} \cdot \nabla \mathbf{v}\right) = -\nabla(\hat{p} + p_s + p_m) + \mu_0 M \nabla H + \mu \nabla^2 \mathbf{v} + \rho \mathbf{g}. \qquad (2.18)$$

Reexamining the fluid meniscus of Figure 2.1 and substituting the magnetic field for the electric is useful in determining the boundary conditions for (2.18) to complete the definition of the ferrohydrodynamic Bernoulli equation. The stress tensors express the stress of the volume on either side of the interface, the boundary conditions for the ferrofluid meniscus is found to be,

$$\hat{p} + p_m + p_s + p_n = p + p_c. \qquad (2.19)$$

p_c is the capillary pressure equivalent to $\sigma_{SurfaceTension}$ of (2.2), and p_n is a newly derived term called magnetic normal traction which is induced by the magnetic field stressing the boundary, $p_n = \mu_0 M_n^2/2$; this boundary condition provides an avenue to examine the stresses acting on a ferrofluid surface specific to a magnetic field. Combining electrohydrodynamics and ferrohydrodynamics reviewed in this chapter results in a unique stress balance that illustrates the complimentary nature of the two fields, Figure 2.4.
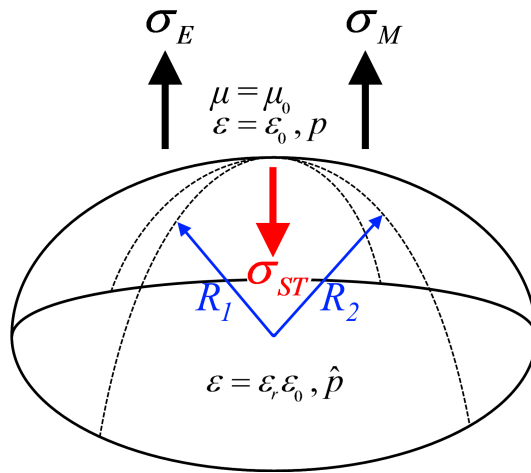
Figure 2.4. Force balance on the meniscus of a fluid-vacuum interface in both an electric field and a magnetic field.

The specific stresses related to $\sigma_{Electric}$, $\sigma_{Magnetic}$, $\sigma_{SurfaceTension}$, and pressure are combined into a single stress balance for a static meniscus,

$$\hat{p} + \frac{1}{2}\varepsilon_0 E^2 + \mu_0 \int_0^H M dH + \mu_0 \int_0^H \boldsymbol{v}\left(\frac{\partial M}{\partial \boldsymbol{v}}\right)_{H,T} dH + \frac{1}{2}\mu_0 M^2 = p + \frac{2\gamma}{R}. \qquad (2.20)$$

Studies on the combined effects of electric and magnetic fields on ferrofluids include examinations of dielectric micro-drops within magnetic fluids,[74, 75] and droplet shapes of the ferrofluid.[13, 76-78] Other studies which used the combined fields to induce electrospray were completed by King's group at Michigan Tech, F. de la Mora's group at Yale University, and Dikansky's group at Stavropol State University. The findings in each of these studies hint at the complexity of electromagnetically-manipulated ferrofluid. As such, to properly understand the nature of these systems the specific effects that the two EM fields have on a ferrofluid must be isolated and individually analyzed. This was the primary motivator for research completed in this study.

2.2.3. Potential of Ionic Liquid Ferrofluids in Electrospray Propulsion

The initial motivation to use ILFFs for electrospray propulsion came from a manufacturing standpoint; as shown in Figure 2.3. the Rosensweig instability creates peaks that are remarkably similar in size and layout of the multi-tip arrays used by several electrospray groups.[32, 35, 36, 53, 79, 80] A case can be made that the nearly instantaneous formation of a Rosensweig instability could eliminate the time and cost associated with fabricating the arrays of emitters typically used in electrospray.

The potential of ionic liquid ferrofluids as electrospray propellants in traditional sources will depend on how the magnetically-susceptible fluid influences the specific characteristics of performance as discussed in Sections 2.1.2. - 2.1.4. The fluid itself presents a feature that is new to electrospray propulsion: suspended magnetic nanoparticles. The size of the NPs are known to be on the order of droplet populations, and Taylor jet diameter of IL electrosprays.[3, 13] As such, ferrofluids produced using these NPs in a magnetic-field-free spray could influence both formation of and emission from the cone-jet structure, and consequently the electrospray beam structure and composition. Furthermore, because the NPs could potentially be emitted in the electrospray, tailoring the NPs in either size or concentration would provide a direct means to vary the thrust-to-power or specific impulse of a device using the fluid.

The magnetic susceptibility of ILFFs is the other characteristic that is potentially useful to traditional electrospray propulsion devices. Applying a magnetic field to a ferrofluid is already known to influence the shape of the surface, which could be beneficial if the shape change complimented the formation of the Taylor cone, thus reducing the electric field necessary to induce electrospray. The magnetic influence on the surface of the emission structure could also influence the electrospray beam structure and composition, thus providing another means to alter the performance of the source (for better or worse) by changing beam divergence, beam energy, and/or polydispersity of the emitted particles. Additionally, an applied magnetic field could affect the post-emission products of the electrospray. For example, the trajectory of magnetic NPs would be more susceptible to Lorentz force caused by an axial magnetic field than a normal charge particle of similar

size; furthermore, an axial or radial field could also reduce the effects of the surface instabilities on the electrospray jet, potentially changing the size of droplets.[11, 81]

Presented with the potential for ILFFs in electrospray propulsion illuminates the motivation for research presented in the remaining chapters of this dissertation.

Chapter 3

Equipment and Facilities for Capillary

Electrospray Source Experiments

This chapter describes the electrospray propellants, the capillary electrospray source, and the general facilities and equipment used in experiments on the capillary source. Note: specific equipment and diagnostics used in individual experiments are presented in chapters respective to the experiments (Chapters 4 through 6). Also, the ILFF source using Rosensweig instability is described in Chapter 7.

3.1. Propellant Properties

Eight fluids were used throughout the experiments reported in Chapters 4-7. They are the neat IL EMIM-NTf2, two batches of EMIM-NTf2-based ILFF (batch NJ397074 and NJ397091), and five solutions of the ILFF with varying concentrations of magnetic nanoparticles produced from batch NJ397091. The ferrofluid solutions are henceforth called ILFF-10, ILFF-20, ILFF-30, ILFF-40, and ILFF-50 based on the volume percent of the parent ILFF that was mixed with neat IL. Batch NJ397091 contained 26.0 wt% iron oxide nanoparticles which led to nanoparticle concentrations in the four solutions of 3.04, 5.98, 8.80, 11.52, and 14.15 wt% for ILFF-10, ILFF-20, ILFF-30, ILFF40, and ILFF-50, respectively. The volumes of neat IL and ILFF, and nanoparticle concentrations that comprised each ILFF solution are tabulated in Table 3.1.

Table 3.1. Properties of all propellants used in the experiments.

ILFF Dilution	Ratio ILFF:neat IL	NP in ILFF (% wt/wt)	NP in ILFF (% v/v)	NP and Polymer in ILFF (% v/v)	Density (g/ml)
Neat IL (EMIM-NTf2)	0:1	0.00	0.00	0.00	1.523
ILFF-10	1:9	3.04	0.91	1.63	1.55
ILFF-20	1:4	5.98	1.82	3.26	1.58
ILFF-30	3:7	8.80	2.73	4.88	1.61
ILFF-40	2:3	11.52	3.65	6.51	1.63
ILFF-50	1:1	14.15	4.56	8.13	1.64
ILFF (NJ397074)	1:0	26.30	9.26	15.37	1.824
ILFF (NJ397091)	1:0	26.00	9.11	16.27	1.815

The NPs changed the viscosity, conductivity, and surface tension of the neat IL carrier fluid. The viscosity of the parent ILFF was previously reported to have similar viscosities as the neat IL.[46] However, measured values for the vial pressure required to produce the similar volumetric flowrate using different propellants, shown in Table 4.1, suggests that this is not correct. Fluid viscosity, η_{fluid}, can be calculated from the Hagen-Poiseuille equation given a known flowrate, Q, supply pressure, P, and feed-tube geometry (radius, r_c, and length, L_c) as shown in (2.1).

$$\eta_{fluid} = \frac{\Delta P \pi r_c^4}{8 L_c Q} \tag{2.1}$$

Note that even small variations in the r_c will greatly affect the calculated viscosity; the capillaries used in this research had dimension ±4% of their 37.5-μm-radius, which would result in an error of ±16% in η_{fluid}. Figure 3.1 a) shows the values of η_{fluid} for each propellant determined using (2.1); also plotted is the published viscosity of neat IL EMIM-

70

NTf2.[82] The addition of 14.15 wt% NPs approximately triples the viscosity of the neat IL.

While the viscosity was proportional to the wt% NPs in the neat IL, the conductivity and surface tension of the propellant decreased when NPs were added, as seen in Figure 3.1.b). The parent ILFF has a measured conductivity of 0.57 S/m and measured surface tension of 32.39 mN/m, compared to 0.91 S/m and 36.28 mN/m, respectively, for the neat IL.
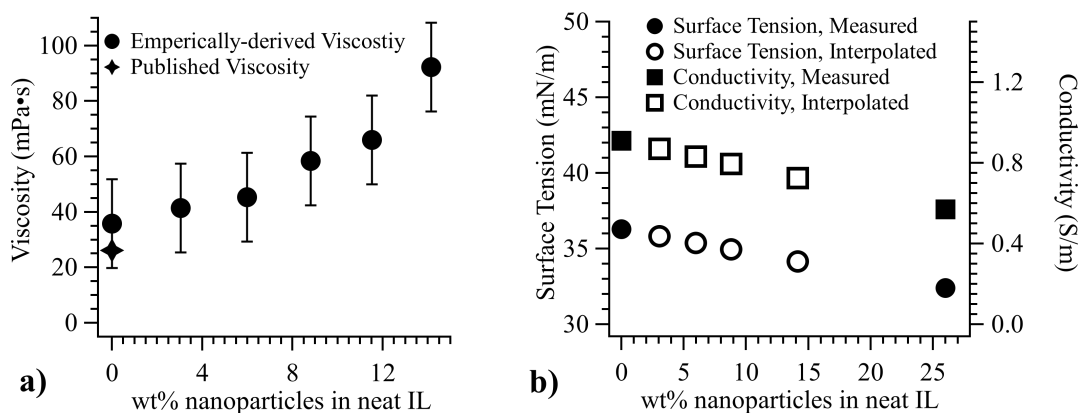
Figure 3.1. (a) Viscosity of ILFF solutions based on the weight percent of nanoparticles in each solution. The published viscosity of neat EMIM-NTf2 is also plotted and used as the zero of the linear fit. (b) Measured surface tension (solid circles) and conductivity (solid squares) of neat IL and parent ILFF and interpolated surface tension (open circles) and conductivity (open squares) of IL solution as a function of wt% nanoparticles added to the neat IL.

Literature has shown that the effects of NPs on fluid properties varied; specifically, two groups demonstrated that surface tension increases with the decrease in NP concentration,[83, 84] while several other groups observed a decrease in surface tension with increase in concentration of NPs,[85-87] with one that showed a decrease followed by an increase in surface tension with an increase in NP concentration.[88] (NPs in literature were Al_2O_3, TiO_2, ZrO_2, and SiO_2). The lack of a conclusive trend between NPs

71

on surface tension meant that extrapolating the both properties shown in Figure 3.1.b). would be unjustified, but it is reasonable to assume a linear interpolation between that of the parent ILFF and the neat IL, as shown in Figure 3.1 b).

3.2. Capillary Electrospray Source

The capillary electrospray source (CES), shown in Figure 3.2, was based on apparatuses used by Chiu *et al*.,[19, 33] Lozano *et al*.,[1] and Miller *et al*.[43, 58, 89]. The apparatuses in these studies had ionic-liquid propellant fed to the apex of a glass capillary needle using either a syringe pump or pressurized vial. The CES included a 0.50-m or 0.75-m long, 75-µm-inner-diameter capillary needle, with a wall thickness of ~5 µm at the apex. The capillary needle had a constant inner diameter, in contrast to tapered-inner-diameter needles used in literature, which helped to avoid blockage issues observed in preliminary tests.
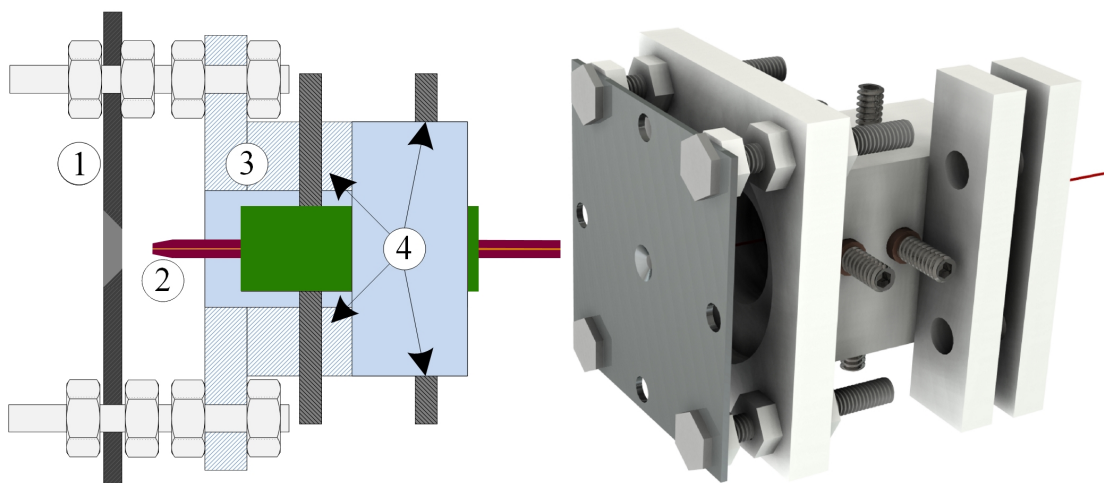
Figure 3.2. a) Capillary electrospray source comprised of (1) extractor plate, (2) capillary needle, (3) PTFE isolation block, (4) alignment set screws. b) CAD model of the CES.

The pressure-feed system described in Section 3.3. fed the IL or ILFF propellant to the capillary needle apex. An aluminum extractor plate with a 1.5-mm-diameter aperture to induce electrospray emission was placed downstream of the capillary needle apex, a PTFE block both held and isolated the needle, and set screws aligned the needle with the extractor aperture.

3.3. Pressure Feed System and Calibration

The propellant feed-system for the CES consisted of a vial of propellant with two inlet- and one outlet- capillary tubes. The openings of the inlet tubes where within the gaseous region of the vial, while the outlet capillary tube was inserted into the propellant. Nitrogen gas, fed through one inlet, pressurized the vial and induced propellant flow in the outlet capillary which fed directly to the needle apex. A mechanical pump attached in-line with the nitrogen feed, was used to evacuate the vial. A pressure transducer was attached to the second inlet capillary to measure the vial pressure. The desired pressure was achieved by systematically opening and closing two precision valves located on the nitrogen line and mechanical pump line. A diagram of the system is shown in Figure 3.3. The flowrate of the liquid being fed to the capillary source was determined via the bubble method, wherein the velocity of a bubble introduced in the feedline was measured for a given vial pressure, Figure 3.4. The velocity was then converted to volumetric flowrate using the known dimensions of the capillary tube.
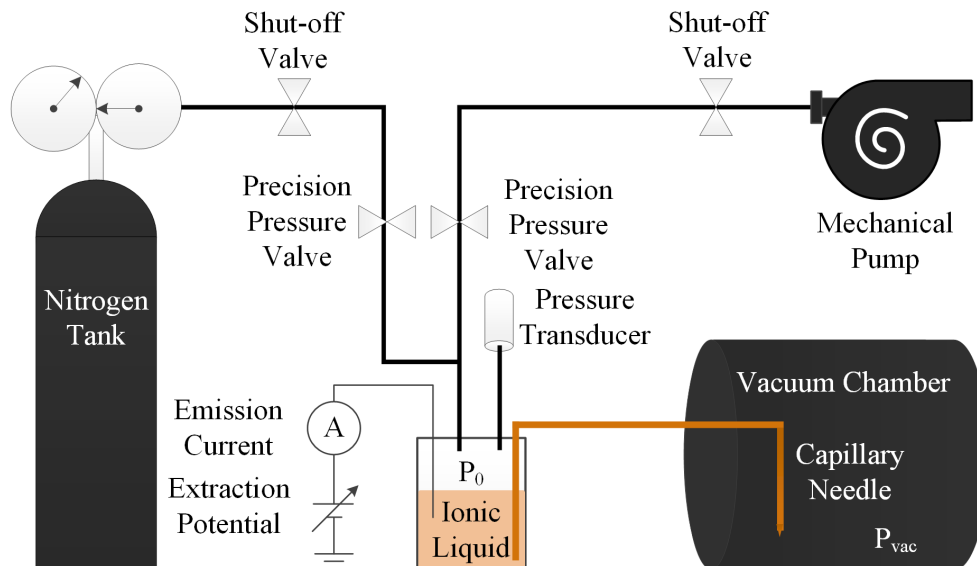
Figure 3.3. The pressure-feed system used to provide propellant to the capillary electrospray source. A propellant vial located outside the vacuum chamber is evacuated using a mechanical pump. Pressure is set to be within ±0.1 Torr by filling the vial N2 gas with the precision valves. The propellant is biased using an electrode inserted into the vial.
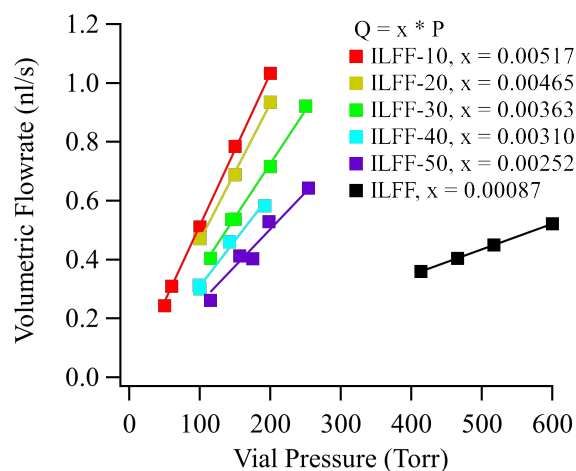
Figure 3.4. Volumetric flowrate of the six propellants used in this research plotted against the pressure of the propellant vial. The flowrate was determined via the bubble method. 'x' is the slope for the linear fits to the measured data, such that Flowrate (Q) = x * Pressure (P).

3.4. Helmholtz Coil – Theory and Apparatus

The need for a variable magnetic field was paramount for the experiments conducted in Chapter 4, Chapter 5, and Chapter 6. The testing facilities inhibited quick movement or

74

removal of permanent magnets which would provide the variable magnetic field, therefore the only option was to construct an electromagnet. A Helmholtz coil is a unique type of electromagnet that provides a uniform, non-divergent field in the volume located between to coils, Figure 3.5.

The field within a Helmholtz coil is easily determined through an examination of the Biot-Savart Law for the case of a point in space some distance away from a circular current loop. A Helmholtz coil is effectively two identical current loops, or coils, separated by a distance, b, along a common axis. As such the magnetic field **H** at the center point of the coil, $z = b/2$, is defined as twice that of a single current loop at the same distance, z.
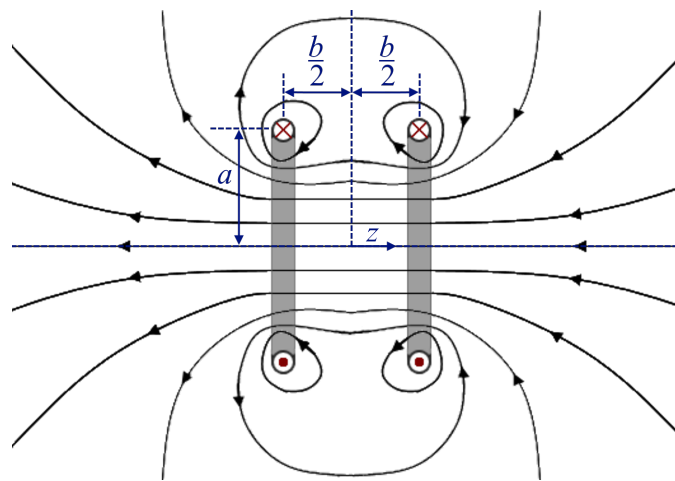
Figure 3.5. Geometry of a Helmholtz coil showing the resulting magnetic field lines created by the two collinear current loops.

Considering that each coil is comprised of n number of loops, the equivalent current in each coil is $I_T = n_H I_H$. Also, the magnetic field strength of the coil, **B**, is equal to $\mu_0 H$. As we've already determined that z is the only significant component of the field, the magnetic field strength is defined as the magnitude,

$$B = \frac{2\mu_0 n_H I_H a^2}{\left(a^2 + (b/2)^2\right)^{3/2}} . \tag{2.2}$$

A uniform field is generated when the two coils are separated by a distance equal to half the radius of the coil, a, as determined by the expanded Taylor series of the field strength with $x = 0$ located at the central point of the two coils. With $b = a$, (2.2) is reduced to,

$$B = \left(\frac{4}{5}\right)^{3/2} \frac{\mu_0 n_H I_H}{a} \tag{2.3}$$

Two Helmholtz coils, HC-A and HC-B, were designed for the onset and stability experiments using (2.3), and were also utilized for the experiments reported in Chapter 5 and Chapter 6. The radii of the coils were chosen based the facilities (HC-A which needed to fit inside the UHV facility, whereas HC-B fit over a 6-inch-flange that enclosed the CES that was attached to either the UHV or TOF-MS facilities). Coil separation of both HC-A and HC-B was larger than the coil radii. The current, I_H, was bound by the power supplies available for use in the experiments. Therefore, n_H was determined by selecting a maximum magnetic field strength and rearranging (2.3). Excess heat was an expected issue for both HC-A and HC-B, and necessary measures to cool the coils were included in the design. HC-A was lined with multi-layer insulation to reduce radiative heat to the CES, and the coil was only powered for short periods of time (on the order of 10 seconds). HC-B was either water-cooled using a copper-pipe sleeve that fit between the coil and the flange, or cooled via forced-air convection using a box fan. HC-B could be powered for

minutes at a time. Table 3.2 details the specifications for the final design of the two Helmholtz coils.

Table 3.2. Specifications for the Helmholtz coils used in CES experiments.

Helmholtz Coil	Maximum B-field (Gauss)	Maximum Current (Amps)	Maximum Power (Watts)	Coil radius (cm)	Number of wraps	Separation (cm)
HC-A	200	29.6	450 to 600	4	75	10.5
HC-B	199	5.5	650 to 900	9.5	490	10

3.5. Ultra-High-Vacuum Facility

The ultra-high vacuum (UHV) facility at Michigan Technological University, Figure 3.6, is approximately 0.5 meters in diameter and 0.5 meters in length, with a base pressure of 10-9 Torr. High vacuum pressures were achieved using a 280 L/s turbo-molecular pump with a 110 L/m backing dry scroll pump; ultra-high vacuum pressures were achieved using a 300 L/s combination ion-sublimation pump. Attached to the facility was a 90x trifocal stereo microscope with a digital color camera that was used for in-situ imaging and video capture. Other test equipment accessible in the facility included a Matsusada AMT-5B20 high voltage amplifier capable of ±5 kV output at 20 mA, a Rigol DG4162 arbitrary function generator, EEVBlog μCurrent micro-ammeters, an in-house-built high-voltage uAmmeter, and a Keithley 2410 Sourcemeter. The signals from each piece of test equipment were recorded through an NI PXI-1033 data acquisition chassis via a SCB-68 connector block, or a NI USB-6361 multifunction input-output device.
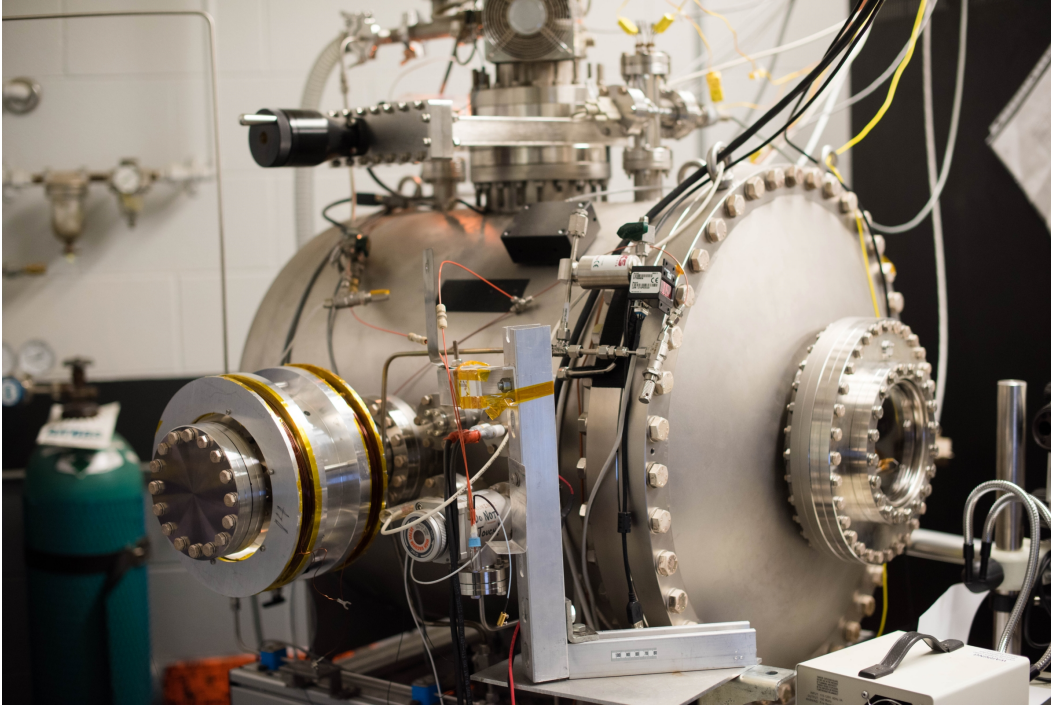
Figure 3.6. The ultra-high vacuum facility in the Ion Space Propulsion Lab at Michigan Technological University

3.6. Time-of-Flight Mass Spectrometry

TOF mass spectrometers use the inherent fact that charged particles and droplets extracted from a source using a constant potential will have a unique velocity proportional to each particle's mass-to-charge ratio. To do this, the mass spectrometer pulses an extraction electrode V_i placed perpendicular to the axis of the electrospray beam to capture a volume of the beam and accelerate it toward a charge-exchange multiplier (CEM). Each particle's time-of-flight is defined as the difference between the time at which the extraction plate is pulsed and the time at which the particle is recorded by the CEM. A particle's time-of-flight can be directly related to its mass-to-charge ratio m_i/q_i through the relationship between electrical and kinetic energy of the particles, shown in (2.4),

$$E_i = \frac{m_i u_i^2}{2} = q_i V_i.$$ (2.4)

Rearranging (2.4), and substituting the length of the TOF chamber, L_{TOF}, divided by the time-of-flight, t_{flight}, for the velocity, the mass-to-charge ratio of a species of particles as a function of their t_{flight}, and vice versa are defined as,

$$m_i/q_i = 2V_i \left(\frac{t_{flight}}{L_{TOF}}\right)^2$$ (2.5)

$$t_{flight} = L_{TOF} \sqrt{\frac{1}{2V_i}\frac{m_i}{q_i}}$$ (2.6)

The output of the mass spectrometer used in this research (AFRL TOF-MS) was the CEM intensity plotted against the time after the pulsing plates were activated (see Figure 3.8.). To convert the time axis to m/q, the peaks with flight times that closely matched the t_{flight} of the known EMIM-NTf2 ion species were assigned to their respective m/q, (all ions assumed to be singly charged), and a scale between t_{flight} and $\sqrt{m_i/q_i}$ was defined via a linear fit with the slope equivalent to $L_{TOF}\sqrt{0.5V_i^{-1}}$.

3.7. Air Force Research Laboratory Time-of-flight Mass Spectrometer Facility

The Air Force Research Laboratory at Kirtland Air Force Base housed the orthogonal TOF mass spectrometer facility used for this research, Figure 3.7. The mass spectrometer that comprises the bulk of the facility, is briefly described later; a full description of the

instrument is well documented by Miller *et al.*[58] The facility has the capability of detecting particles in the range of a couple amu/e to 200,000 amu/e; and is comprised of a 1-meter long by 0.254-meter wide by 0.254-meter tall reflectron flight-tube detection chamber that is situated orthogonal to a 0.5-meter long source chamber. A multichannel plate (MCP) is used as the detector and is positioned at the end of the reflectron flight-tube. The MCP signal was directed into two amplification stages of a 300 MHz Stanford Research pre-amplifier and then read by a multichannel scaler or a TOF card to produce TOF spectra. The source chamber was maintained at a pressure of 10^{-7} Torr, while the detection chamber was maintained at approximately 2×10^{-8} Torr. The pressures were achieved using two 250 l/s turbo-molecular pumps backed by one 600 L/min dry scroll pump.
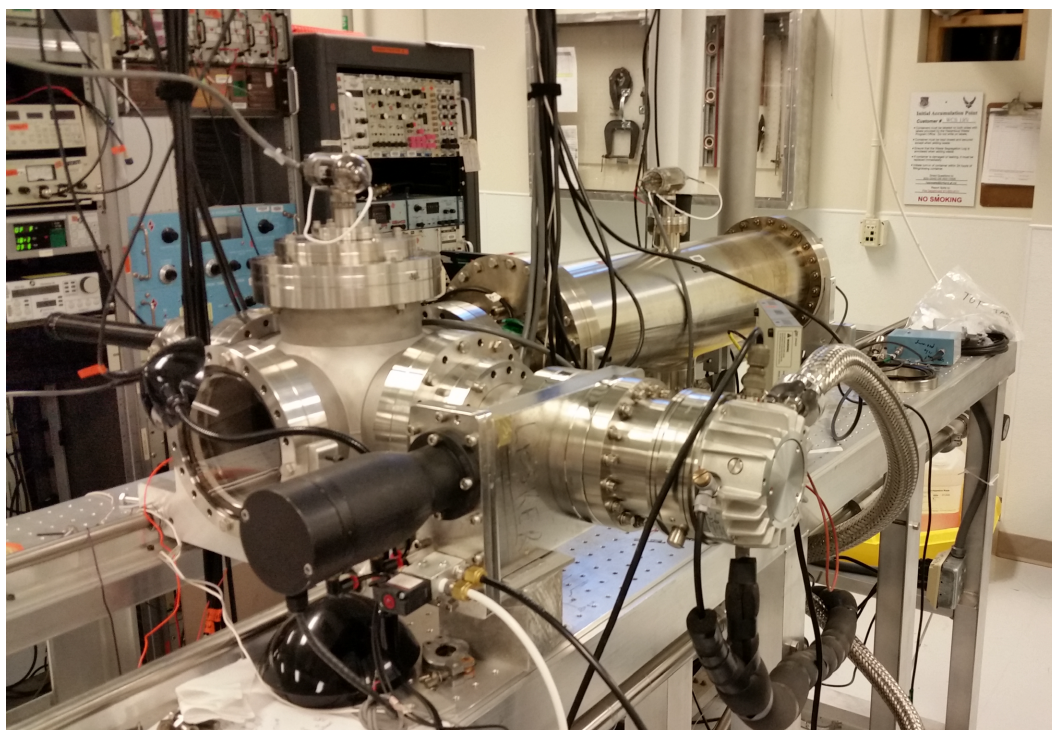
Figure 3.7. The time-of-flight mass spectrometer facility in the Air Force Research Laboratory at Kirtland AFB. The facility was capable of linear and reflector TOF-MS.

Multiple lenses, grids and deflectors were also attached at the end of the CES used to maximize the intensity of the beam that entered the TOF extraction region. The extraction region consisted of a pair of parallel pulsing plates which are parallel to, but offset from, the beam axis. Each plate had a gridded aperture to allow orthogonal transmission of ion species when the voltages on the plates are pulsed. If the parallel pulsing plates were off, the beam would pass through a 6-mm aperture where a quartz crystal microbalance (QCM), used to quantify the mass flow rate, and a Faraday cup, used to measure the current of the beam, were located. These devices were positioned by means of a linear translation stage allowing rapid switching of the two devices. The QCM measured the mass flow rate of electrospray by measuring the accumulation of a uniform layer of the condensed beam products on a quartz crystal. The additional layer changed the natural frequency of the crystal, which translated to thickness-, or mass accumulation-, per-second. The maximum detectable mass flow rate on the QCM was on the order of 100 ng/s.

The transverse axis began beyond the parallel extraction plates with an Einzel lens located 6 mm from the time-of-flight extractor pulsing plate, with the front and back lens potential of the Einzel fixed at ground. Beyond the Einzel lens was a simple horizontal deflector that allowed the ion beam into the main field-free flight tube. At the end of the tube, a series of grids turned the ion beam around and directed it to the MCP.
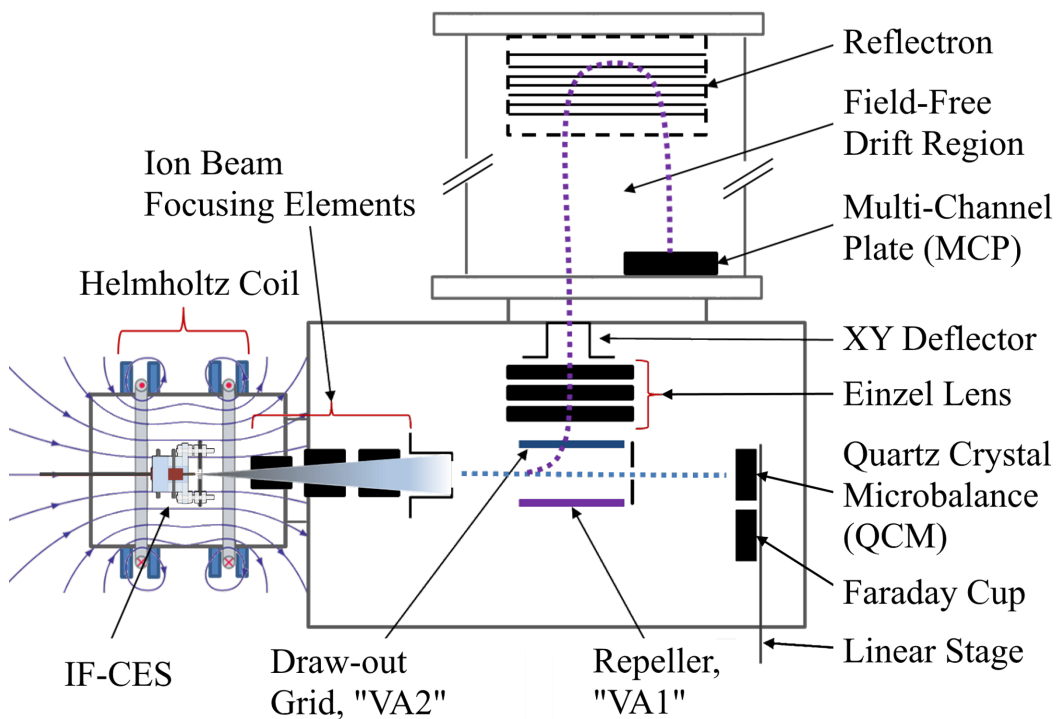
Figure 3.8. Schematic of TOF-MS facility showing the relative locations of the spectrometer, CES and other components of the facility.

The collection of a time-of-flight spectrum constituted the accumulation of signal from the MCP over a series of pulse cycles. In each pulse cycle, the plates are first given a base DC offset that serves to retard the ions in the middle of the extraction zone. When the pulse was active, the repeller plate (VA1) had a greater potential than the draw-out grid (VA2), which serves to repel the ions toward VA2. Particles which passed through the aperture of the draw-out grid yielded additional acceleration as the front component of the Einzel lens was held at ground. For example, consider the emission source being biased at +900 V, and with the pulsing plates initially at a potential of +880 V. Ions in the middle of the extraction region will have had approximately 20 eV axial kinetic energy at the center of the extraction region, assuming they were emitted at the nominal bias potential. If these ions were in the center of the extraction region during an active pulse event of +400 V,

VA1 would have been at a +1280 V potential, while VA2 maintained +880 V. If an ion successfully passed VA2, it will have netted approximately 1080 eV of transverse kinetic energy by the end of the Einzel lens, which it then used to travel along the flight-tube to the MCP.

Chapter 4

Onset and Stability of the Capillary Electrospray Source

Two basic parameters of standard electrospray operation are emission onset and its stability island. Examining how the magnetic NPs and magnetic stress alter these parameters was a good introduction into how the ILFF electrosprays compare to neat IL electrospray. Chapter 4 defines and discusses the three experiments conducted on the CES described in Section 3.1. to measure the two parameters; specifically, there was an onset experiment (ON-Exp), and two experiments to define the stability island, one for positive-polarity emission (PSI-Exp) and one negative-polarity (NSI-Exp). It begins with the motivation behind the experiments and research goals which they were expected to achieve. The remaining sections of Chapter 4 were partially collated by experiment in the following format: apparatus and experimental setup, experiment procedure, and results of experiment. A discussion on the influence that magnetic field on the onset experiment immediately follows its results, while discussing on the influence both NPs and magnetic field had on the stability island were completed for both stability island experiments concurrently. The chapter ends with conclusions which relate the findings to the overall goals of the research.

4.1. Motivation and Goal

The potential required for onset of electrospray is a necessary component of the stability island as it defines the power required to operate the electrospray. Literature shows that the onset potential is between 5- and 20-percent greater than the extraction potential required for stable emission.[1, 90] The onset potential is dependent on surface tension of the propellant, as shown by (2.3), and the NPs within the ILFF propellant were shown to increase the surface tension of the neat IL (Figure 3.1). Furthermore, the study by Madden et. al also showed that the onset potential was highly influenced by an applied magnetic field. These three combined observations/studies motivated the experiments to determine onset potential of the CES using the ILFF propellant.

Another integral measurement of electrospray performance is the what has become known as the electrospray stability island required. Cloupeau and Prunet-Foch were some of the first researchers to attempt systematic studies of the stability island (termed the "functioning domain" in their work) for a given electrospray fluid.[90] Their findings on the matter discerned the influences of conductivity, capillary geometry, and wettability on the stability island, and also discussed several phenomena including coronal discharge effects and hysteresis induced by the direction of extraction potential change. Jaworek and Krupa also used a systematic approach to measure the operating modes of electrosprays based on different flowrates and extraction potentials.[91, 92] Several of these modes came when an electrospray operated outside of its stability island; I have illustrated these modes, along with the stable cone-jet mode, with respect to Q vs. V_{ext} in Figure 4.1.
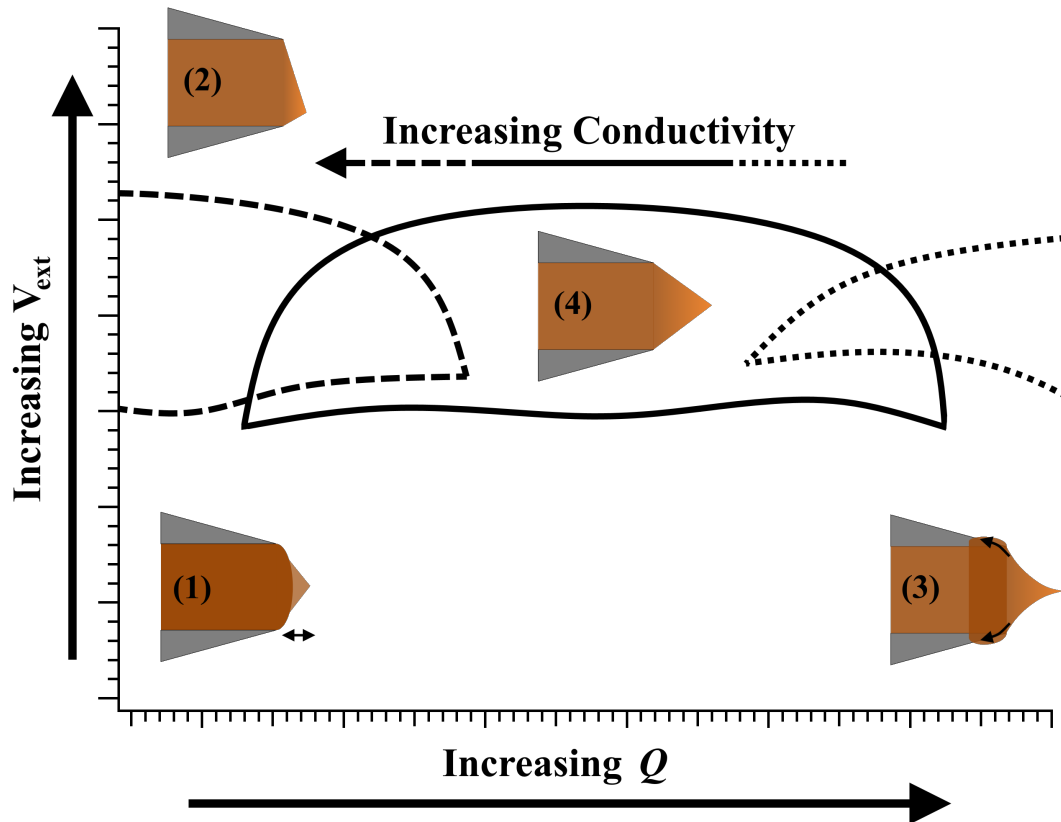
Figure 4.1. General shapes (dotted, solid, and dashed curves) of the stability island (Q, V_{ext}) for capillary electrosprays based on literature.[90] The conductivity of the operating propellant increases from the dotted (right) curve to the dashed (left) curve. The general shape of a Taylor cone operating within the stability island, *i.e.* stable cone-jet (4), and outside of the stability island, *i.e.* pulsating-cone (1), asymmetric cone-jet (2), and overflowing cone-jet (3), are shown relative to the solid (center) stability curve.

The different modes are (1) pulsating cone caused by either a lack of propellant-flow or low extraction potential, (2) asymmetric cone-jet caused by overly-high extraction potentials, (3) overflowing cone-jet caused by an excess of propellant-flow, and (4) a stable cone-jet. The latter mode produces a consistent electrospray beam that is symmetric along the center beam-axis and is desired when using diagnostic tools described in Section 5.2. The desire to operate in the stable cone-jet mode spurred the motivation to determine the stability island of the CES using the new ILFF propellants, which were already shown to have significant changes in conductivity from the NPs within (Figure 3.1). Furthermore, a

87

study by Madden et. al using a low-conductivity ferrofluid electrospray showed that the envelope of stable flowrates and extraction potentials was increased by applying a magnetic stress to the electrospray. This provides motivation to also determine the stability island of the CES using the ILFF propellants while it is subjected to a magnetic field.

The motivation outlined above led to three goals for the experiments presented in this chapter. One was to determine the stability island of CES producing magnetic-field-free electrosprays of the five diluted ILFF propellants described in Table 3.1. Another goal was to determine the effect a gradient-free magnetic field has on the stability island of the CES emitting electrosprays of the five diluted ILFF propellants. The final goal was to determine the effect a gradient-free magnetic field had on the onset potential of the CES running the parent ILFF. The following sections detail the setup, procedure, results and analyses specific to each of the three experiments used to achieve these goals, starting with the ON-Exp and followed by the stability island experiments (PSI-Exp and NSI-Exp).

4.2. Electrospray Onset Experiment

The electrospray onset experiment (ON-Exp) was completed to determine how the onset potential of the CES was influenced by the combined effect of the magnetically susceptible NPs and an applied magnetic field. First, the experiment setup and apparatus are presented and followed by the procedures used to measure onset with and without the magnetic field.

4.2.1. Experimental Setup

The setup for the ON-Exp is shown in, Figure 4.2. The experiment was conducted at atmosphere, although the setup was mounted within the UHV facility. The setup used a feed system in which the propellant vial was open to atmosphere and the capillary tube fed from the vial directly to the CES, as shown in Figure 4.2. A Matsusada AMT-5B20 high-voltage amplifier in direct DC output mode was used to apply the extraction potential, and the µA2 HV microammeter for was used to measure emission current. The data channels were recorded via LabVIEW using a NI-6361 USB DAQ. A 90x trifocal, stereo microscope with a digital color camera was used to capture the video and still images of the emission site. HC-A was used to provide the magnetic field when necessary.
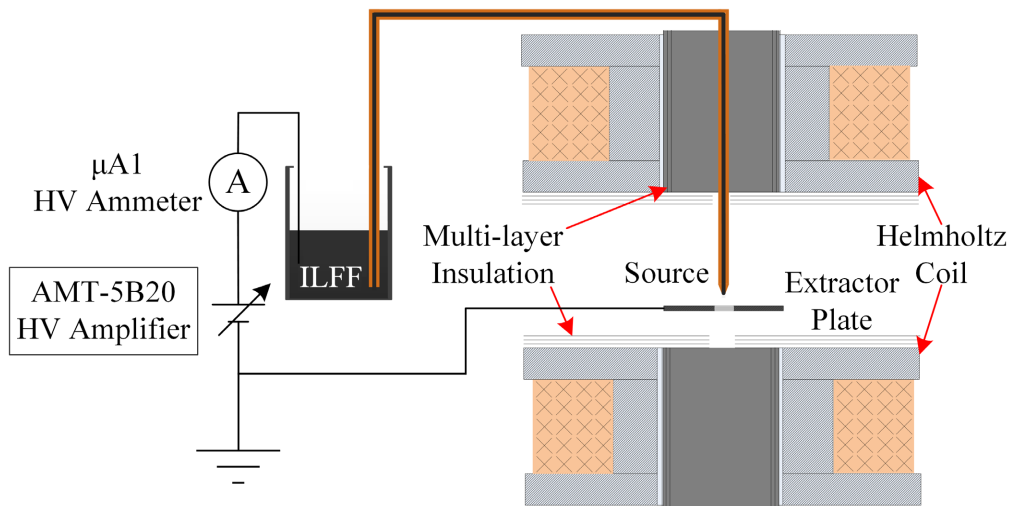
Figure 4.2. Setup used in ON-Exp. The experiment was conducted at atmosphere.

The µA1 HV microammeter, and the µA2 HV microammeter used in PSI-Exp later, were a custom-built by Washeleksi and Makela[93] to measure 0 to 100 µA through a cable that was floating 0 to 10 kV. A block diagram and further description of the device is provided in Makela's dissertation. Both devices required a warm-up period of ~30 minutes

to remove transient signals. When the devices were at steady-state a Keithley 2410 Sourcemeter was used to calibrate the output signal; multiple calibration curves are shown for both devices in Appendix A.

4.2.2. Procedures

In ON-Exp the extractor plate was fixed 1.32 mm downstream of the capillary apex. The CES was inserted into HC-A and placed into the UHV facility. The experiment was conducted at atmosphere environment with hydrostatic pressure since flow rates or post-onset behavior were not a concern of this study. The ILFF propellant was inserted into the vial, which was positioned 65 mm above the needle tip such that hydrostatic pressure would form a meniscus at the needle exit. The propellant vial bias was swept from 0 V to V_{onset} at a slew rate of 100 V/s, while the extraction electrode was kept at ground. The voltage bias on the propellant vial was removed once onset was observed. The procedure was repeated five times with zero magnetic field applied to the source. 50-, 100-, 150-, and 200-Gauss magnetic fields were then applied to the source, and the procedure was repeated three times for each magnetic field strength. The needle was cleaned after each increase in magnetic field strength. Note: the atmosphere environment and the propellant used in ON-Exp (parent ILFF) differed from the vacuum environment and ILFF-based propellants of the stability island experiments.

4.2.3. Results and Discussion – Magnetic Influence on Onset

Results from the onset potential experiment (Figure 4.3.) were the telemetries of emission current and extraction potential for the CES operating with a) 0 and b) 200 Gauss

magnetic fields. Comparing the extraction potential telemetries of the two plots illustrates that an application of a 200-Gauss magnetic field to the source reduced the extraction potential required for onset (defined as the point which emission current became non-zero).
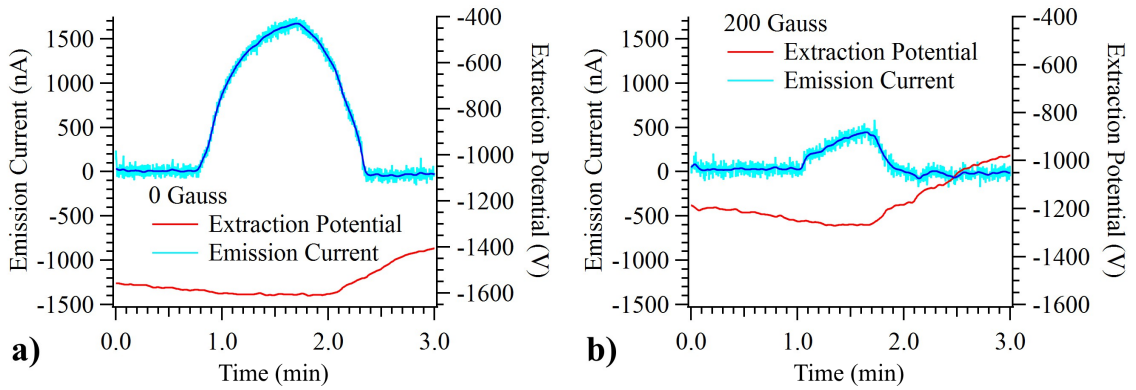
Figure 4.3. Telemetry of CES emission current and the extraction potential applied to the source collected during onset potential experiment while in atmosphere environment. Applied magnetic field is (a) 0 Gauss, (b) 200 Gauss

Onset potentials were extracted from the emission current and extraction potential telemetries collected for 0-, 50-, 100-, 150-, and 200-Gauss magnetic fields and are shown plotted against time for five discrete steps in magnetic field strength in Figure 4.4.
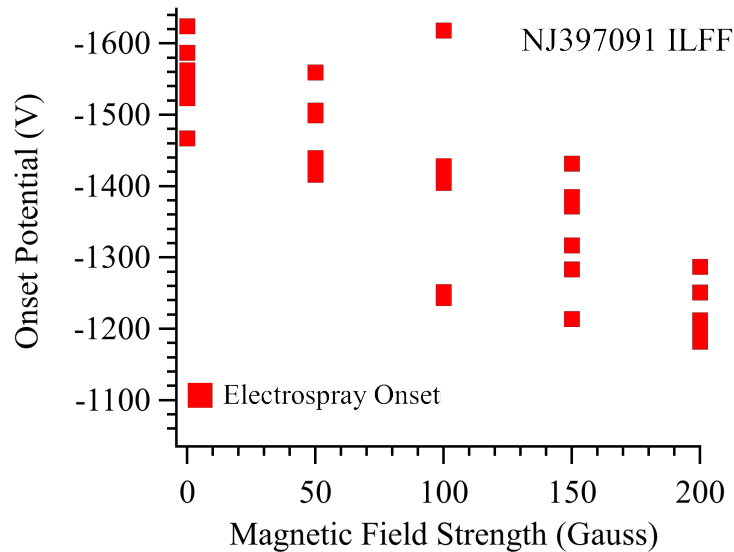
Figure 4.4. Onset potential of CES plotted against the strength of the magnetic field applied to the source.

91

The onset potential appeared to follow a negative trend which was proportional to the magnetic field strength. Specifically, a 200-Gauss magnetic field induced a 22-percent drop in the onset potential of the CES operating on the parent ILFF. The behavior was likely a result of the magnetic pressure acting on the meniscus at the emission site. As described in the Section 2.2.2., the magnetic pressure will act to stretch a meniscus in the direction of the magnetic field, which was along the electrospray beam axis of the source in the Helmholtz coil setup. The additional stress from the magnetic field aides the electric stress in inducing the formation of the Taylor cone and subsequent ion/droplet emission.

The change in shape of the meniscus could have caused the reduction in the onset potential. *In-situ* observation of the parent ILFF electrospray during the application of magnetic field, shown in Figure 4.5., suggests the Taylor cone undergoes significant increase in the cone angle, from 44.5° to 50.4° as a reaction to the magnetic stress. Krpoun and Shea suggested that an increase in half-angle of the emission cone reduces the onset potential. Therefore, the onset potential reduction is possibly the result of an increase in cone half-angle caused by the applied magnetic field application.

0 Gauss
$\alpha_1 = 44.5°$
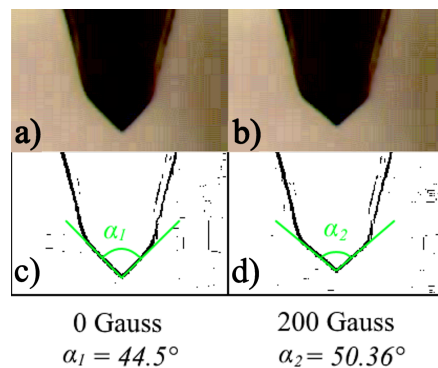
200 Gauss
$\alpha_2 = 50.36°$

Figure 4.5. Images of the Taylor cone geometry at the emission site of CES operating on the parent ILFF with an applied magnetic field strength of a) 0 Gauss and b) 200 Gauss. Image enhanced using an edge detector and the cone angle was measured for a magnetic field of c) 0 Gauss and d) 200 Gauss.

Evidence that the combined stresses were the physical mechanism that reduced the onset potential was in a numerical simulation conducted by Jackson, Terhune, and King.[94] The study was on the deformation of magnetically susceptible meniscus under electric and magnetic fields, and showed agreement to the trend observed in this experiment, albeit predicting only a 10- to 15-percent drop in onset potential induced by a magnetic field.

To end this section I would like to note that there was another interesting observation made when I attempted to complete the onset experiment at vacuum. During the test, stable electrospray onset was not achievable; however, the results showed a trend between the frequency of electrospray onset and cessation and the magnetic field strength. A discussion on the findings can be found in Appendix B.

4.3. Stability Island of the Capillary Electrospray Source

The stability island of the CES was partially defined in this research. The purpose was to determine the influence of NPs and the applied magnetic field on the lower bounds of the stability island, as well as defining multiple stable points within the stability island. Because the CES was operated in both positive and negative polarity for the extraction potential, an experiment was conducted in each polarity (PSI-Exp and NSI-Exp, respectively). The following sections describe the experimental setup, procedures, and results of the experiments, first for PSI-Exp and then for NSI-Exp. This is followed by analyses on the influence that NPs and magnetic field had on the stability island, which are presented in parallel for both experiments.

4.3.1. Positive-Polarity Stability Island Experiment

4.3.1.a. Experimental Setup

The setup for the PSI-Exp is shown in Figure 4.6. It used the same pressure feed system described in Section 3.3., and the HC-B Helmholtz coil to provide magnetic field when necessary. A Matsusada AMT-5B20 high-voltage amplifier in direct DC output mode was used to apply the extraction potential, and the µA1 HV microammeter was used to measure emission current. The data channels were recorded via LabVIEW using a NI-6361 USB DAQ.
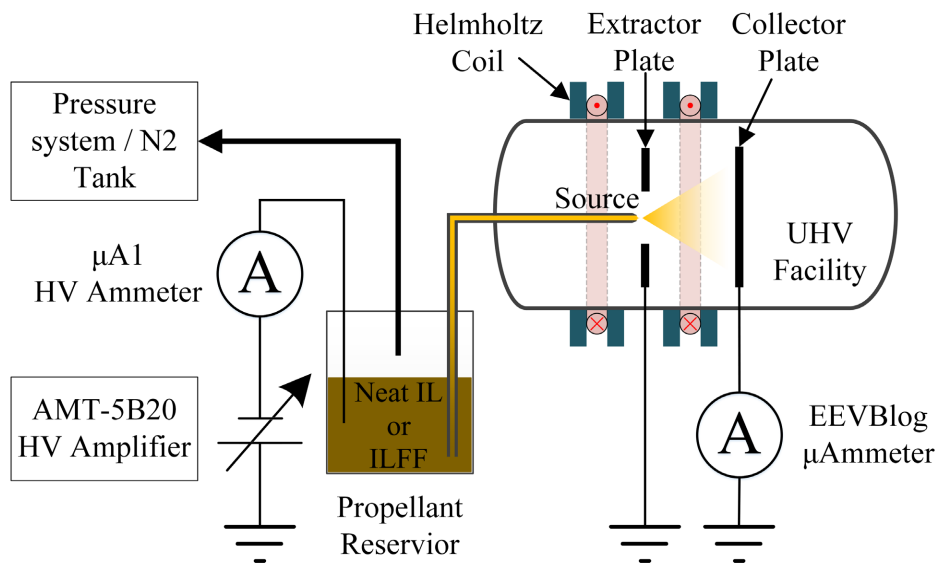
Figure 4.6. Setup for stability island experiments conducted in the UHV Facility.

4.3.1.b. Procedures

PSI-Exp was completed using the following procedures. The procedures to measure the emission current at various Q and V_{ext} within the stability island are described first, followed by those used to measure minimum flowrate. The initial conditions of the stability

island for electrospray emission using the CES were unknown; Instead, the initial extraction potential was chosen based on the theoretical onset potential calculated from (2.3). The extraction distance of the source, d_{ext}, was 1.22±0.03 mm throughout the testing, R was 0.0375 mm and ε_0 is a known constant, leaving the surface tension of the fluid, γ, as the only dependent variable. γ varied from 36 mN/m for neat IL to 32 mN/m for the parent ILFF. Inputting these values into (2.3) results in the theoretical onset potential of 1541±10 V for the CES operating on the parent ILFF (note this matches the onset potential measured in Figure 4.4.), and 1634±10 V for neat IL. Therefore, 1700 V was chosen as the initial extraction potential. The initial flowrate was selected as the vial pressure that induces a nominal 0.5 nl/s which was based on the reported range of 0.1 nl/s to 2.18 nl/s from studies by Gamero-Castaño and Hruby,[18] Lozano,[1] and Miller[95].

Based on these initial conditions, the following procedure was taken to determine the lower boundaries of the positive-polarity stability island of the propellants listed in Table 4.1. The CES was inserted into the UHV facility which was pumped to high-vacuum. The propellant vial was filled with one of the propellants and the vial was pressurized to the absolute pressure corresponding to known flowrates of the specific propellant (pressures and flowrates are listed in Table 4.1). The propellant vial was then biased to -1700 V, while holding the extractor plate at ground potential, to establish a magnetic-field-free electrospray; the emission current was recorded concurrently. A 200-Gauss magnetic field was then applied to the source, while maintaining the same flowrate and extraction potential, and the emission current was recorded concurrently. The magnetic field was then removed to return the CES to magnetic-field-free electrospray emission.

The magnitude of the extraction potential was then increased by 100-V and the procedure was repeated. The number of times the extraction potential was increased depended on whether the emission current substantially increased or decreased after the change in extraction potential (±100% the magnitude of the previous emission current). Both are indicative of other, undesired, modes of emission (multiple jets or off-axis emission). The number of steps was limited to a maximum of four as the upper range of the stability island was not in the scope of this work. The magnitude was then decreased one or two 100-V increments, depending on the whether the electrospray ceased emission and the procedure was repeated. The CES was removed from the UHV facility, cleaned and returned each time there was a change in propellant.

Table 4.1. Vial pressures (absolute) and corresponding flowrates for each of the propellants used in the CES.

ILFF Solution	Vial Pressure (Torr)	Flowrate (nl/s)
Neat IL	50	0.32
	100	0.63
	150	0.95
	200	1.26
ILFF-20	100	0.47
	150	0.71
	200	0.94
ILFF-30	125	0.45
	175	0.64
	225	0.82
ILFF-40	150	0.47
	200	0.62
	250	0.78

The minimum flowrate of the positive stability island was determined using a separate procedure from the rest of PSI-Exp. The CES was inserted into the UHV facility and

operated on one of the ILFF-based propellants listed in Table 4.1. at its lowest stable flowrate. The initial extraction potential was selected as the minimum potential used in the first part of PSI-Exp. After a stable magnetic-field-free electrospray was established, the vial pressure was reduced at a slew rate of approximately 0.5 Torr/s until the emission became erratic or extinguished. The vial pressure was then reset to the starting pressure and a 200-Gauss magnetic field was applied to the source. The same procedure was then followed to determine the minimum flowrate with a 200-Gauss magnetic field. The entire procedure was repeated for each of the extraction potentials determined in the first part of PSI-Exp, in 100-V increments. The procedure was repeated for all ILFF-based propellants in Table 4.1. and ILFF-50 propellant at V_{ext} of -2000, -2100, -2200, and -2300 V. The CES was removed from the UHV facility, cleaned and returned each time there was a change in propellant. The minimum flowrate for neat IL was not determined as the interest of the measurement was to determine if any magnetic influence existed for ILFF-based electrosprays. However, the minimum flowrate of neat IL during negative-polarity electrospray emission was much lower than that of any of the ILFF-based propellants (Section 4.3.2.c.) and the same should be expected during positive-polarity electrospray emission.

4.3.1.c. Results

The results from PSI-Exp include the lower range of the stability island for ILFF-20, ILFF-30, ILFF-40, and ILFF-50 propellants, and the emission current at each (Q, V_{ext}) data point of all the propellants in Table 4.1. Examples of the emission current and vial pressure telemetries used to determine minimum flowrate from a ILFF-20 electrospray with and

without a 200-Gauss magnetic field are shown in Figure 4.7. In the plot, the emission current (red curve) remained stable until a critical vial pressure was reached (blue curve), at which time the magnitude drops to zero; the vial pressure at that moment converted to flowrate was considered the minimum flowrate for this Q, V_{ext}.
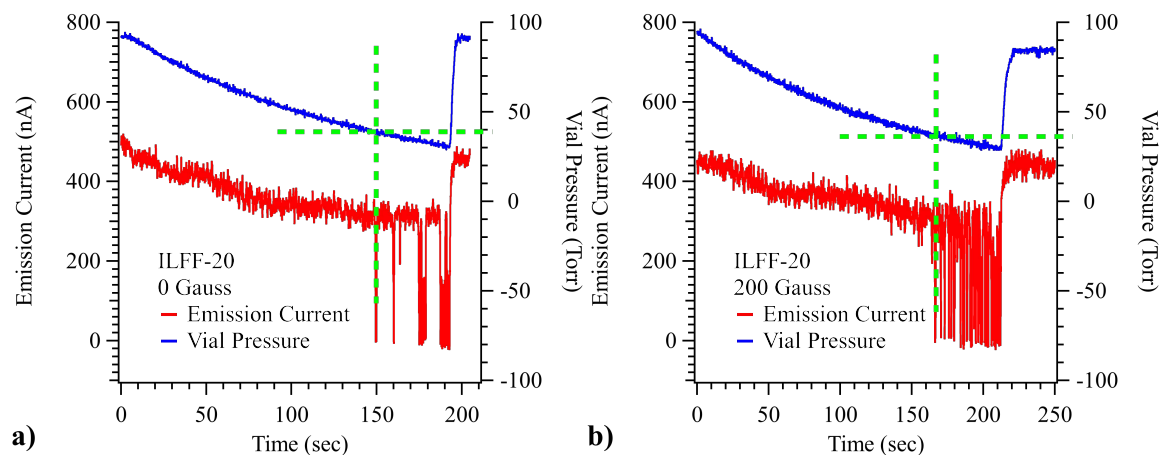
Figure 4.7. An example of the vial pressure and emission current histories for the minimum flowrate test of PSI-Exp using ILFF-20 with a) zero magnetic field, and b) a 200-G magnetic field. The green dashed lines highlight the vial pressure at the point emission becomes erratic, indicating the minimum flowrate.

The lower range of the stability island four ILFF-based propellants are included in Figure 4.8. The left-most (low flowrate) data points in the plot define the lower Q boundary of the stability island for the respective extraction potentials. The bottom-most (low extraction potential) data-points were not strictly the lower V_{ext} boundary, however, they are within 100 V of the lowest potential at which the CES could operate. Figure 4.8. illustrates that the extraction potential required for stable emission correlated to the wt% of NPs within the neat IL. For example, given the nominal flowrate 0.33 nl/s, the required extraction potential to produce stable emission was only 1600 V for the ILFF-20 propellant. However, increasing the wt% NPs in the neat IL by approximately 2, 6, or 11% and the required extraction potential becomes 1800, 1850 and 2000 V, respectively. The emission

current (results presented in Section 4.3.3.a.) followed a similar trend, wherein the propellants with increasing wt% NPs had increasing magnitudes of emission current (for a given Q). Both trends related to wt% NPs in neat IL, along with the magnetic influence on the electrosprays, will be discussed in Section 4.3.3.
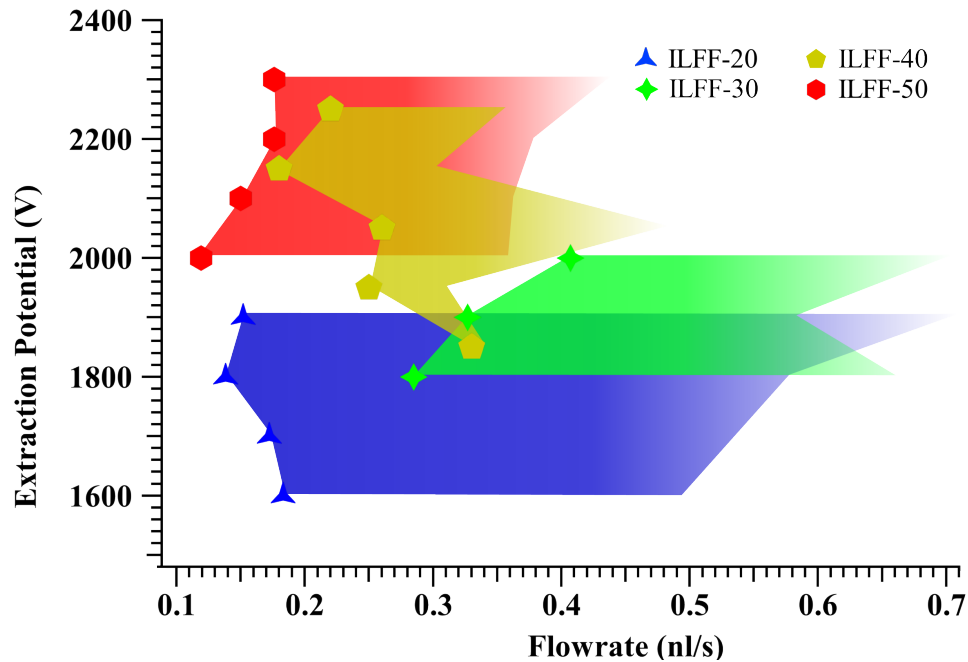
Figure 4.8. Lower region of the positive-polarity stability island for the CES operating on ILFF-20, ILFF-30, ILFF-40, and ILFF-50 propellants. The data points at the lowest flowrates for a given extraction potential were determined to be the minimum flowrate for the CES operating on each propellant. The remaining boundaries (higher flowrate and higher extraction potentials) were not completely defined; no boundaries for the neat IL stability island were defined.

4.3.2. Negative-Polarity Stability Island Experiment

4.3.2.a. Experimental Setup

The negative stability island experiment (NSI-Exp) was conducted in the AFRL TOF-MS facility and used a pressure feed system like the one described in Section 3.3. for propellant delivery, Figure 4.9. Two Matsusada AMT-5B20 HVAs (one to bias the

propellant vial, one to bias the extraction electrode) amplified DC signals from external generators to extract electrospray from the CES. Emission current was measured using via either a Fluke 179 Multimeter or a calibrated Keithley 617 electrometer which was input into LabVIEW via a NI USB-6008 DAQ. HC-B was utilized for the operation characterization and the minimum flowrate experiment.
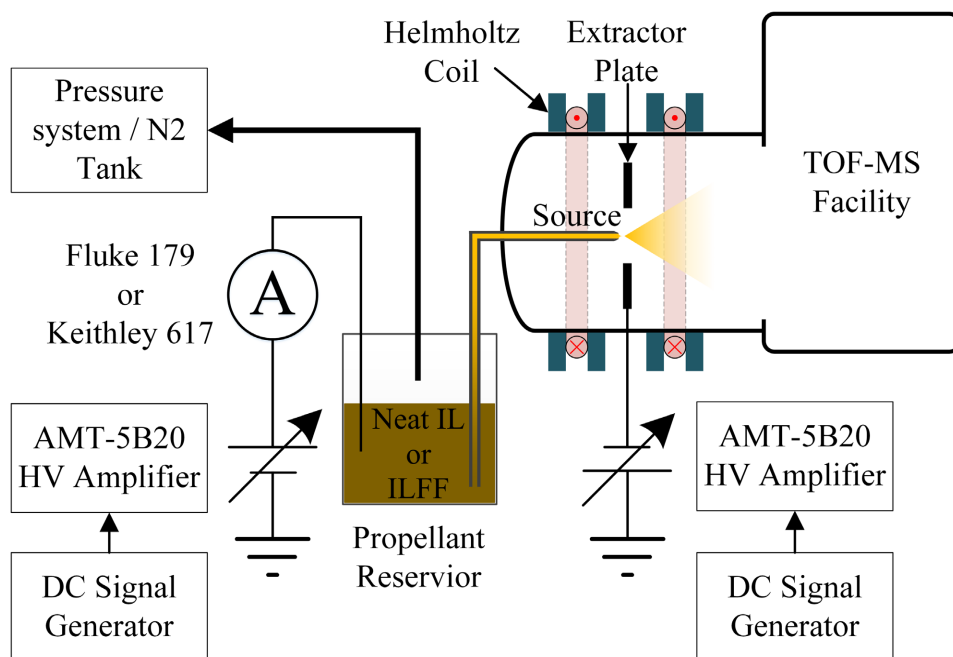
Figure 4.9. Setup for experiments conducted in the AFRL-TOF Facility.

A Fluke 179 Multimeter placed in-line with the propellant vial biasing cable would measure the voltage drop, which could be converted to emission current of the source. The equivalent impedance of the multimeter in-line with the biasing cable was 4.444 MΩ. This meant readout on the multimeter display could be converted to emission current using the conversion factor 0.225 µA/V. The signal was recorded every 5 minutes unless there was a change in extraction voltage or flowrate, in which case the current was recorded immediately after the change. Using the Fluke multimeter was necessary due to a lack of a HV microammeter like those available at Michigan Tech.

4.3.2.b. Procedures

NSI-Exp was completed in conjunction with time-of-flight mass spectrometer experiment presented in Chapter 6. As such, mapping the stability island was not rigorous. However, the goal to determine the Q and V_{ext} that produced stable electrospray using the CES and the ILFF propellants was achieved. The procedures used to measure the emission current at various Q and V_{ext} within the stability island are presented first, followed by those used to measure minimum flowrate. The initial conditions were determined using the same method as the PSI-Exp. The specific geometry of the CES changed, specifically the extraction distance was 1.2±0.10 mm, but the propellant properties remained the same. Therefore, the initial extraction potential and flowrate were different, *e.g.* $V_{ext} = 1750$ V and $Q = 0.63$ nl/s for neat IL.

The propellant vial was filled with one of the propellants listed in Table 4.2. and the vial was evacuated. The CES was then inserted into the AFRL TOF-MS facility which was pumped to high-vacuum. When the desired vacuum was achieved the propellant vial was pressurized to the absolute pressure corresponding to known flowrates of the specific propellant (pressures and flowrates are listed in Table 4.2). The source was concurrently biased to the initial extraction potential as determined above. The bias to create the extraction field for tests in TOF-MS facility was split between the propellant vial electrode and the extraction plate. As the TOF-MS pulsing plates required the particles to be a constant energy, the vial electrode had a constant 900-V bias and the extraction plate varied from -600 V to -1100 V, depending on the propellant and flowrate. Once a stable electrospray was established the emission current was recorded. A 200-Gauss magnetic

field was then applied to the source, while maintaining the same flowrate and extraction potential, and the emission current was again recorded. The magnetic field was then removed to return the CES to magnetic-field-free electrospray emission.

The magnitude of the extraction potential was varied by either ±50 or ±100 V depending on the propellant and flowrate and procedure was repeated (the procedure was only completed for one (Q, V_{ext}) using the ILFF-40 propellant). The CES was removed from the ARFL TOF-MS facility, cleaned and returned each time there was a change in propellant.

Table 4.2. Vial pressure and corresponding flowrates for each of the propellants used in the CES.

ILFF Solution	Vial Pressure (Torr)	Flowrate (nl/s)
Neat IL	50	0.32
	100	0.63
	150	0.95
	200	1.26
ILFF-10	100	0.52
	150	0.78
	200	1.04
ILFF-30	125	0.45
	150	0.55
	175	0.64
	200	0.73
	225	0.82
	250	0.91
ILFF-40	175	0.54
ILFF-50	150	0.54

The minimum flowrate of the positive stability island was determined using a separate procedure from the rest of NSI-Exp. The CES was inserted into the AFRL TOF-MS facility and operated on either neat IL, ILFF-10, ILFF-30 or ILFF-50 at its lowest stable flowrate.

The initial extraction potential was selected as the minimum potential used in the first part of NSI-Exp. After a stable magnetic-field-free electrospray was established, the vial pressure was reduced at a slew rate of approximately 0.5 Torr/s until the emission became erratic or extinguished. The vial pressure was then reset to the starting pressure and a 200-Gauss magnetic field was applied to the source. The same procedure was then followed to determine the minimum flowrate with a 200-Gauss magnetic field. The entire procedure was repeated each of the remaining propellants (either neat IL, ILFF-10, ILFF-30 or ILFF-50) at multiple extraction potentials determined via the method as used in PSI-Exp (Section 4.2.2.). The CES was removed from the UHV facility, cleaned and returned each time there was a change in propellant. The minimum flowrate for neat IL was only determined for one extraction potential -1600 V.

4.3.2.c. Results

The results from NSI-Exp include the minimum flowrates for each ILFF-based propellant for several extraction potential magnitudes, and emission currents for each of the (Q, V_{ext}) point for all propellants listed in Table 4.1. An example of emission current and vial pressure telemetries used to determine minimum flowrate from a ILFF-30 electrospray with and without a 200-Gauss magnetic field are shown in Figure 4.10. The result of applying the 200-Gauss magnetic field to the ILFF-30 electrospray is a lower required vial pressure (*i.e.* flowrate) to maintain a stable emission. This will be investigated further in Section 4.3.3.c.
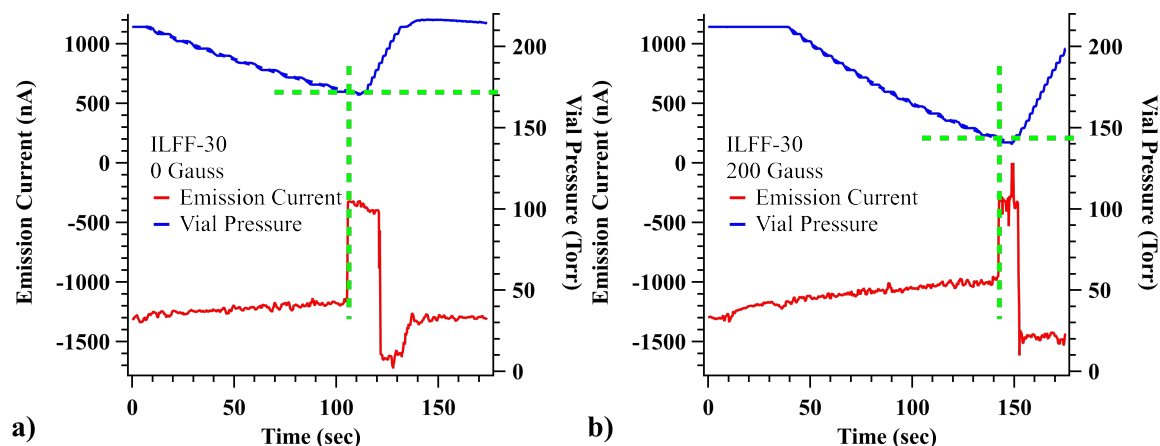
Figure 4.10. An example of the vial pressure and emission current histories for the minimum flowrate test of NSI-Exp using ILFF-30 with a) zero magnetic field, and b) a 200-G magnetic field. The green dashed lines highlight the vial pressure at the point emission becomes erratic, indicating the minimum flowrate.

The lower range of the negative-polarity stability island for ILFF-10, ILFF-30, and ILFF-50 propellants are shown in Figure 4.11. Only the lower Q boundary for the stability island was determined, while the lower V_{ext} boundary was within 100 V of the lowest potential included in the plot. Boundaries of the neat IL, ILFF-20, and ILFF-40 negative-polarity stability islands were undefined and therefore not included in Figure 4.11. However, the minimum flowrate for neat IL was measured at $Q = 0.19$ nl/s for $V_{ext} = -1600$ V. The magnetic influence was significant on the negative stability island for ILFF-30 and ILFF-50 propellants; a discussion on the influence is included in Section 4.3.3.c.
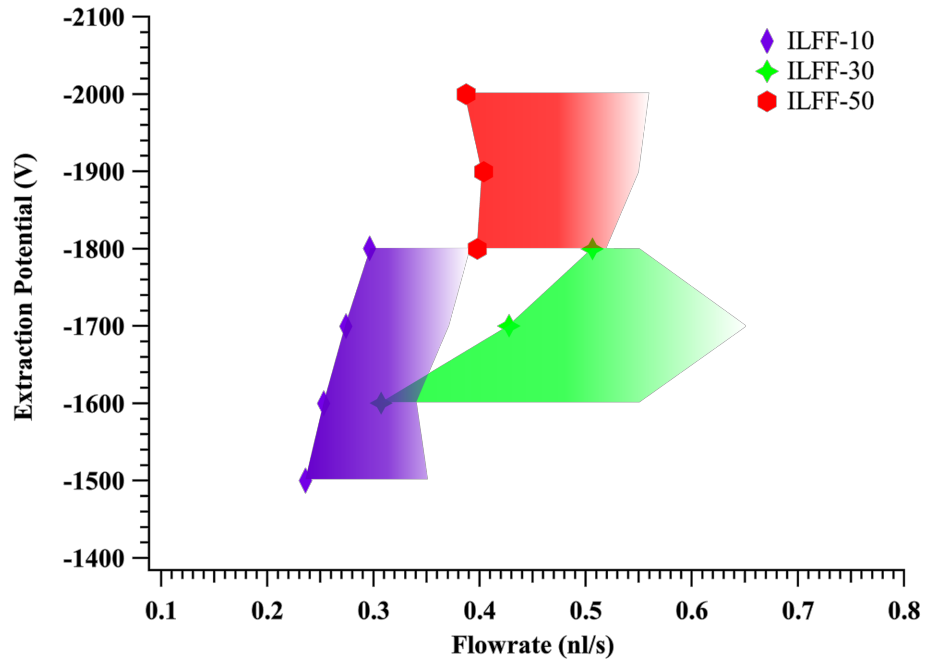
Figure 4.11. Lower region of the negative-polarity stability island for the CES operating on ILFF-10, ILFF-30, and ILFF-50 propellants. The data points at the lowest flowrates for a given extraction potential were determined to be the minimum flowrate for the CES operating on each propellant. The remaining boundaries (higher flowrate and higher extraction potentials) were not completely defined.

4.3.3. Analysis and Discussion of Stability Island

The results presented in the previous section successfully defined multiple (Q, V_{ext}) points within the stability island for both negative- and positive-polarity emission for the neat IL and ILFF-based propellants described in Table 3.1, along with the lower Q boundary for many of the propellants. The results also revealed that both the magnetic field applied to the electrospray and the magnetic NPs in the electrospray propellant affected normal electrospray operation. While the influence the NPs had on emission current did not fall in the experimental goals of this chapter, it was within the overall goals of the research, and as such warranted the discussion presented here. Therefore, I have split the

discussion section into four subsections with each focusing on how either the magnetic NPs or magnetic stress affected the stability island, emission current.

4.3.3.a. Nanoparticle Influence on the Stability Island

As mentioned in the results of the positive-polarity stability island, there appeared to be a correlation between the extraction potential of the electrospray and the wt% NPs in the propellant. Specifically, and increase in the lower extraction potential boundary with an increase in wt% NPs in the propellant. The effect of the NPs to the negative-polarity stability island was similar, wherein the lower extraction potential boundary of CES was $V_{ext} = -1500\pm^0_{100}$ V operating on the ILFF-10, $V_{ext} = -1600\pm^0_{100}$ V operating on the ILFF-30, and $V_{ext} = -2000\pm^0_{100}$ V operating on ILFF-50. While the trend is interesting, the mechanism behind it is unknown. Theoretically, if the Prewett-Mair or Krpoun-Shea models for onset potential holds true, (2.3) and (2.4), respectively, changes in surface tension, permittivity and/or the meniscus apex radius could induce the increase extraction potential observed in the results. However, surface tension differed by only 10% between neat IL and ILFF and therefore is unlikely to be the cause of any change in onset potential. Alternatively, permittivity would induce the onset potential increase, if it increased proportionally with weight-percent of the NPs in the propellant. Literature has shown that NPs can change the permittivity of its carrier fluid;[96, 97] however, permittivity was unknown for any of the ILFF-based propellants as its measurement was out of the scope of this work (the effects permittivity has on electrospray as seen in literature is discussed more in the next section). Potentially, the NPs could influence the apex radius since they are non-deformable and

therefore define a minimum radius when they are located at the apex. However, a larger apex radius should induce a reduction in onset potential; as such more NPs in the propellant should lower necessary extraction potential, which is the opposite trend of that observed in Figure 4.8 and Figure 4.11. Therefore, the physical mechanism for the increase in necessary extraction potential when using ILFF propellants remains uncertain, though it appears the NPs are at least partially responsible.

The lower bound of flowrate for the CES stability island did not appear to correlate to the weight-percent of suspended nanoparticles. Comparison between the minimum flowrate that produces stable electrospray using neat IL to that using ILFF-based propellants reveals that adding NPs to the neat IL increases the lower Q boundary; apart from this, there was no apparent trend between the NPs and the minimum flowrate of the propellants.

Overall, the influence colloidal particles had on the electrospray stability island was likely the result of changes in fluid and electrical properties of the neat IL due to the inclusion of NPs. Section 3.1. showed that the NPs induced significant changes to the properties of the of its neat IL carrier fluid. Literature has shown that the suspension of colloidal particles elicits a change in the electrospray through changes in fluid and electrical properties of the spraying liquid. Jayasinghe and Edirisinghe sprayed a suspension of 20-volume-percent alumina ceramic powder (0.5-micron-diameter particles) in ethanol and measured the size of droplet relics on a substrate finding a dependence on relic size to extraction potential and flowrate.[98] Suh *et al.* electrosprayed a 50-volume-percent mixture of either 4.2-, 10.5-, or 25-nanometer-diameter gold particles suspended in

methanol to produced highly-charged-monodisperse spray of nanoparticles.[99] Studies by Zhu *et al.* and Halimi *et al.* focused on electrospraying suspensions of titanium oxide (TiO_2) nanoparticles for deposition; the former used a 40 weight-percent solution of 25-nanometer-diameter particles in ethylene glycol to create dye sensitized solar cells,[100] whereas the latter deposited a 0.05-weight-percent solution of ~1-micron-diameter particles in deionized water to measure the effect deposition distance had on the deposited TiO_2 droplet size.[101] However, each of the studies used volatile liquids or liquids with low electrical conductivity, so comparison to the results in this research, which used non-volatile, high-conductivity propellants, was not completed.

A final point about the stability island of the CES was during its operation using the ILFF propellants with higher wt% NPs. During several tests, the source operated with less than ideal performance when using propellants with higher weigh-percent NPs. For example, running the CES on ILFF-50 resulted in fluctuations in the emission current that were as large as 25% of the mean, Figure 4.13. These fluctuations were included as error bars in emission current data (*e.g.* Figure 4.14.) to ensure their significance was not ignored. Also, the exterior surfaces of the capillary needle would wet with propellant if it had higher wt% NPs (Figure 4.12) that could not be removed during testing. These non-ideal conditions were avoided by maintaining the ideal extraction field from the moment flow was induced to ensure overflow doesn't occur, reducing flowrate when wetting begins, and cleaning the emitter after each emission test.

108

a)	b)	c)
Ideal Operation	Needle Wetting	10 Minutes after Needle wetting
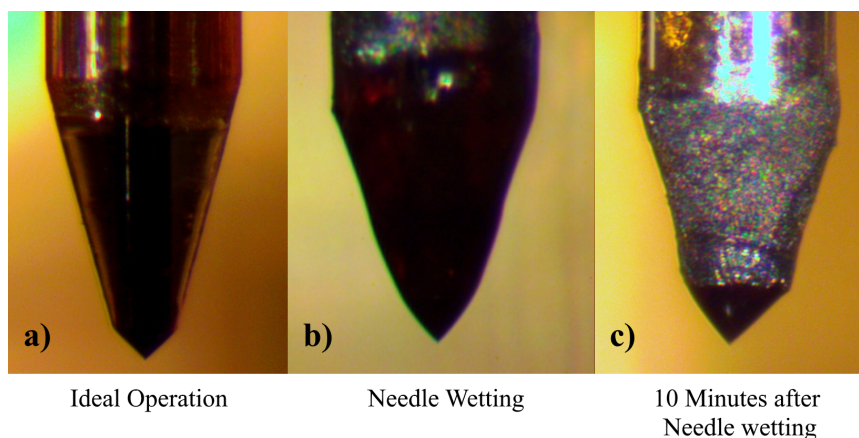
Figure 4.12. Image of CES operating on the parent ILFF showing a) ideal operation, b) the wetting and c) subsequent carbonization of ILFF on the external surface of the needle that may occur during operation of the source. Note, the needle in image a) was different than that in images b) and c)
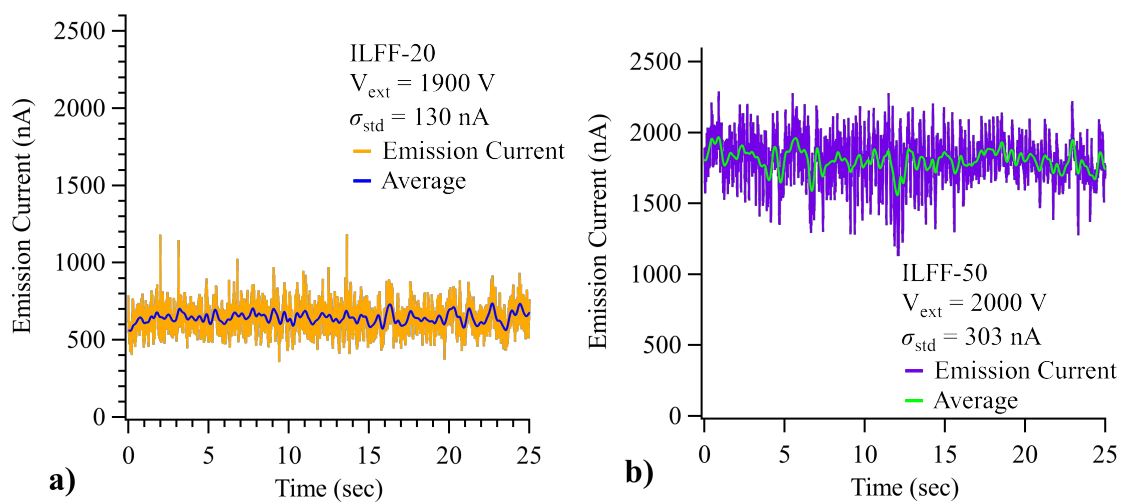
Figure 4.13. Fluctuations in emission current of CES operating on a) ILFF-20 and b) ILFF-50 propellants. In each plot includes a smoothed time-resolved average of the emission current. The standard deviation was based on the average over the entire period.

4.3.3.b. Nanoparticle Influence on the Emission Current

During ideal operation within the stability island, the emission current magnitude of the source was correlated to the wt% NPs in the propellant. However, a direct comparison of the current magnitude for the CES operating on each propellant does not account for the changes in fluid or electrical properties previously mentioned. Therefore, a term that relates

109

the properties of the fluid to flowrate and emission current was sought. A model that accomplishes this was developed by Fernandez de la Mora and Loscertales (Eq. (2.6) discussed in Section 2.1.), and is repeated here for convenience: $I = \left(f(\varepsilon_r) \middle/ \varepsilon_r^{1/2} \right) \sqrt{KQ\gamma}$. This model scales emission current as a function of $Q^{1/2}$, and is known to hold for propellants with relatively high viscosity and conductivity, by relating them to an empirically derived F. de la Mora constant, $f(\varepsilon_r)$. [26, 52, 102-105] Fernandez de la Mora and Loscertales determined $f(\varepsilon_r)$ by taking the slope of the nondimensionalizing emission current, (2.8) and flowrate, (2.9) of multiple pure electrospray propellants. Based on the empirical data, they determined $f(\varepsilon_r) \approx \frac{1}{2}\varepsilon_r$ for $\varepsilon_r \leq 40$ and $f(\varepsilon_r) \approx 18$ for $\varepsilon_r > 40$, and $\xi \approx f(\varepsilon_r)\eta$, the dimensionless counterpart to (2.6).

However, measuring the relative permittivity of the propellants was out of the scope of this research, and as the unknown $f(\varepsilon_r)$ is dependent on ε_r, the results of this data could not be fit to the model in (2.6). As literature has shown that permittivity of the solution is proportionally and/or inversely-proportionally effected by the weight percent of nanoparticles, it was not correct to assume that the permittivity of the ILFF-based propellants was the same as their carrier IL.[96, 97] Instead the spray current from the ILFF electrosprays was analyzed based on whether the liquids fell into the $Q^{1/2}$ scaling law or $Q^{1/4}$ scaling law defined by Gañán-Calvo et al.[27] To determine which scaling law best models the spray current from ILFF electrosprays, the dimensionless parameter $\delta_\mu \delta^{1/3}$ was calculated. For ILFF (NJ397091) using the properties outline in Section 3.1., and a nominal

flowrate of 1 nl/s, the result was $\delta_\mu \delta^{1/3} = 8.30E\text{-}05$, which is much less than 1. This means that the spray current should scale as $I \sim Q^{1/2}$, like the model set in by (2.6).

Since the permittivity of the ILFF propellants was unknown, the permittivity dependent parts of (2.6) were combined into a single constant $g(\varepsilon_r) = f(\varepsilon_r)/\varepsilon_r^{1/2}$, and ignored such that a scaling relationship between the emission current and remaining variables was created: $I \sim \sqrt{KQ\gamma}$. Using the properties of the propellants defined in Section 3.1., the emission current for each propellant is plotted against $\sqrt{KQ\gamma}$ in Figure 4.14.
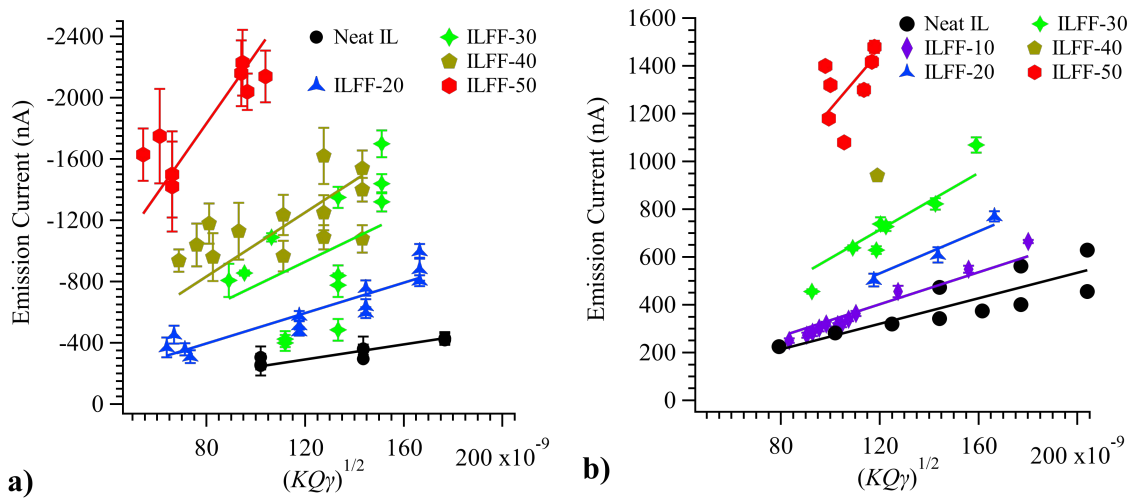
Figure 4.14. Measured emission current of the magnetic stress-free CES plotted against $\sqrt{KQ\gamma}$. a) CES operating in positive polarity using neat IL and four of the ILFF propellants; b) CES operating in negative polarity using neat IL and the five ILFF solutions. Linear fits for each electrospray (solid) follow $I = g(\varepsilon_r)\sqrt{KQ\gamma}$.

The plots reveal that an increase in the weight-percent of Fe_3O_2 is proportional to the slope of the I vs. $\sqrt{KQ\gamma}$ line. As $g(\varepsilon_r)$ is the constant that relates I to $\sqrt{KQ\gamma}$, Figure 4.14 shows that $g(\varepsilon_r)$ for each propellant, and, correspondingly, the permittivity of each propellant must be correlated to the wt% NPs in the neat IL. This is of course assuming

that the ILFF propellants follow the $Q^{1/2}$ scaling law, which is best verified by measuring the permittivity of the ILFF propellants. I would like to note that even if the permittivity varied by an order of magnitude in either direction, the electrosprays would still follow this scaling law.

As a propellant that follows the $Q^{1/2}$ scaling law (with high viscosity and conductivity), ILFF emits electrosprays with a current that does not scale with the electrostatic variables (*i.e.* electric field and the resulting electric stress). Instead, the emission current depends on the flowrate and liquid properties of the ILFF propellant. Also, in following the $Q^{1/2}$ scaling law, an ILFF electrospray emits a jet with a flat velocity profile across its radius, and charge is carried by both conduction in the bulk of the jet and convection along the jet surface. This is opposed to propellants with low viscosity/low conductivity in which charge is by surface convection.[27] This means that when electrospraying an ILFF propellant, the tangential electric stress of the electric field is transmitted across the entire jet due to the propellant's high viscosity, *i.e.* viscosity is the driving variable in determining charge advection and fluid velocity within an electrospray jet.

An observation unrelated to NPs in the propellant was the influence the extraction potential polarity had on the magnitude of emission current for all the propellants. The polarity-dependence on magnitude of emission current is observed in literature.[2, 3, 9, 106] It is an expected consequence of size difference between the anion and cation of the IL (m/q is 111 amu/e and 280 amu/e for $EMIM^+$ and $NTf2^-$, respectively). As the ions are the sole charge carrier of an IL electrospray, the difference in m/q of the cation and anion resulted in larger magnitudes of emission current from an $EMIM^+$ electrospray, Figure

4.14. a), compared an NTf2⁻ electrospray, Figure 4.14. b). This is not remarkable as it follows the expected trend according to literature, but it does provide evidence that electrosprays of ILFF propellants have similarities to their neat IL counterparts.

4.3.3.c. Magnetic Influence on Stability Island

The magnetic stress affected the stability island of several of the ILFF propellants, specifically the lower Q boundary. This was illustrated by comparing the minimum flowrates of the electrosprays without a magnetic field (previously shown in Figure 4.8 and Figure 4.11) to the electrosprays of the same propellants at the same extraction potential, but with a 200-Gauss magnetic field applied to the source, Figure 4.15. In the figure, the application of the magnetic field appears to have reduced the minimum flowrate of the electrospray, for most of the propellants and extraction potentials.
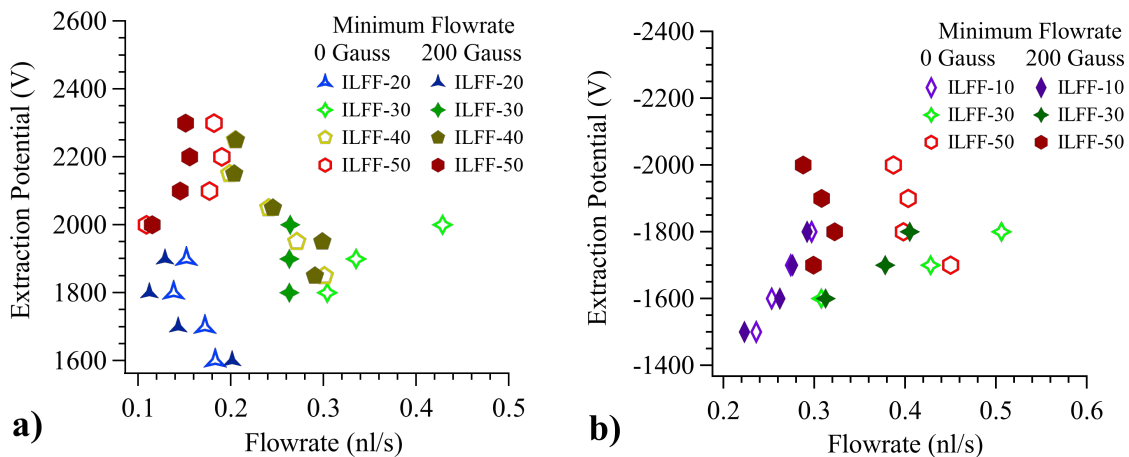
Figure 4.15. Minimum flowrate with and without a 200-Gauss magnetic field. Propellants were a) ILFF-20, ILFF-30, ILFF-40, and ILFF-50 propellants in positive-polarity operation. Changed induced by the application of a 200-Gauss magnetic field. Extraction field during operation was a) positive and b) negative.

The change in minimum flowrate for five of the propellants induced by the magnetic field is quantified in Figure 4.16 as a percentage of the minimum flowrate measured with no magnetic field. The error defined in the plots is derived from a single standard deviation of the mean minimum flowrate converted into percent of 0-Gauss minimum flowrate. In Figure 4.16 the minimum flowrate of electrosprays using propellants with higher wt% NPs and operating with positive extraction potentials is seen to be reduced by the magnetic field, albeit not correlated with wt% of NPs. A similar observation is seen for the minimum flowrates of ILFF-20 and ILFF-30 electrosprays operating with negative extraction potentials; however, the error negates any correlation of minimum flowrates for ILFF-40 and ILFF-50 electrosprays operating with the same polarity. The error included in minimum flowrate results was likely a consequence of fluctuations at the emission site, which explains the variability that was also observed in the emission current while the magnetic field was applied (Section 4.3.3.a.). These fluctuations significantly affected the spray when the concentration of nanoparticles was above 30 wt%, *i.e.* ILFF-40 and ILFF-50. Specifically, the emission current of the ILFF-50 electrospray during application of the magnetic field began would fluctuate by >10-percent of the mean emission current, and persisted for several minutes after removal of the field.
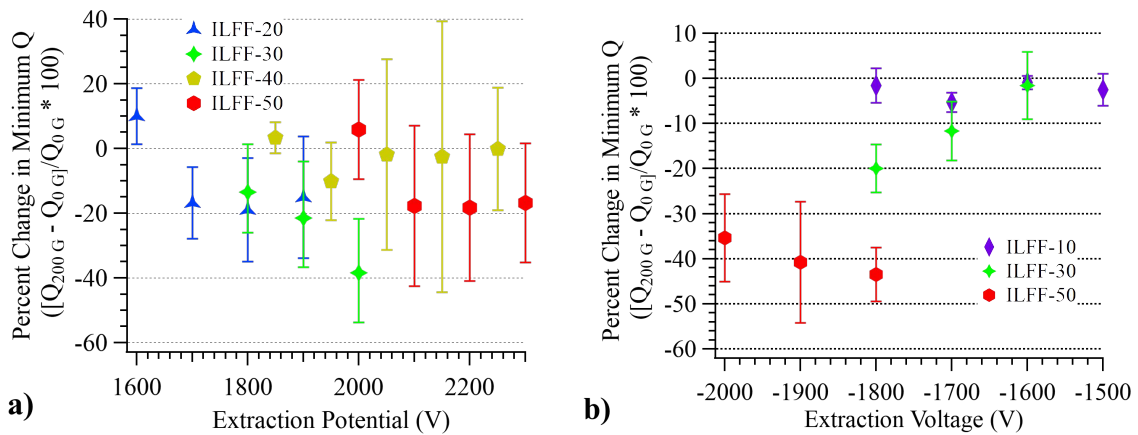
Figure 4.16. Percent change in the minimum flowrate from a zero-magnetic-field case for ILFF-10, ILFF-30, ILFF-40, and ILFF-50 propellants. Changed induced by the application of a 200-Gauss magnetic field. Extraction field during operation was a) positive and b) negative. Error bars are one standard deviation of the mean percent change in flowrate.

This magnetic-field induced reduction of the minimum required flowrate for ferrofluids has also been observed by Madden *et al.*[107] In their work, two low-conductivity, sulfolane ferrofluids were used, one with 15% (v/v) ethyl ammonium nitrate (EAN), and the other with 0.1% (v/v) EAN. With the application of a 300-Gauss magnetic field they saw a 40-percent and 30-percent drop in minimum flowrate for the 15-percent EAN and 0.1-percent EAN solutions, respectively. Furthermore, the minimum extraction at which a Taylor cone formed was reduced by 23-percent and 24-percent for the 15-percent EAN and 0.1-percent EAN solutions, respectively. They did not ascertain the physical mechanism behind the reduction of either minimum flowrate or minimum potential. A couple possibilities exist and are related to the emission structure; these are discussed at the end of the following section.

115

4.3.3.d. Magnetic Influence on the Emission Current

The measurement of magnetic field influence on the emission current was not a goal of this experiment, however, it was within the overall goals of the research and is presented here. The magnetic field influence on electrosprays of the ILFF-based propellants was readily observed in the change in emission current from the source. During application of the field, the emission current from the CES was significantly reduced; this was true for all ILFF-based propellants. The emission current collected from the CES during application of a 200-Guass magnetic field plotted against the quantity $\sqrt{KQ\gamma}$ in shown in Figure 4.17.
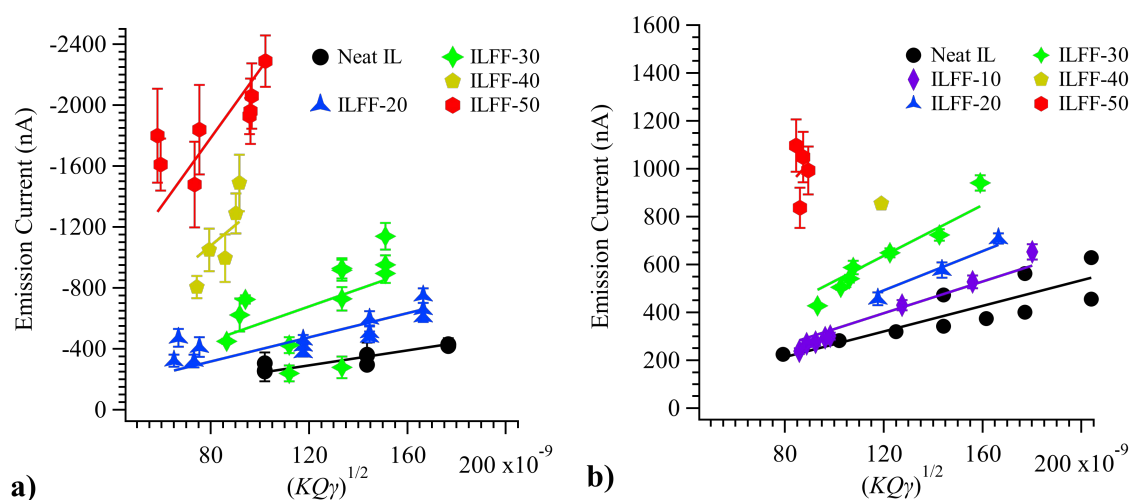
Figure 4.17. Measured emission current of the CES operating within a 200-Gauss magnetic field plotted against $\sqrt{KQ\gamma}$. a) CES operating in positive polarity using neat IL and four ILFF propellants; b) CES operating in negative polarity using neat IL and the five ILFF solutions. Linear fits for each electrospray (solid) follow $I = g(\varepsilon_r)\sqrt{KQ\gamma}$.

By comparing the emission current of the source with (Figure 4.17) and without (Figure 4.14) an applied magnetic field for all the propellants, the extent of the reduction was quantified as a percentage change in the emission current of the zero-magnetic-field electrospray in Figure 4.18. While the effect was more significant for higher concentrations

of nanoparticles, it was not proportional to the wt% NPs; e.g. a reduction of ~5 percent, 10 to 40 percent, and 10 to 20 percent of the zero-magnetic-field magnitude when a 200-Gauss magnetic field was applied, for propellants with 3.04-, 8.80-, and 11.52-wt% nanoparticles, respectively. The flowrates of the source running on ILFF-50 with the 200-Gauss magnetic field did not match the flowrates while operating with no magnetic field. Therefore, the influence of magnetic stress on emission current was not precisely calculated and does not appear in Figure 4.18. However, for similar flowrates (within +/- 0.01 nl/s) a reduction in the emission current was on the order of 200 nA, or 15-percent of the mean emission current of the negative-polarity magnetic-field-free electrospray.
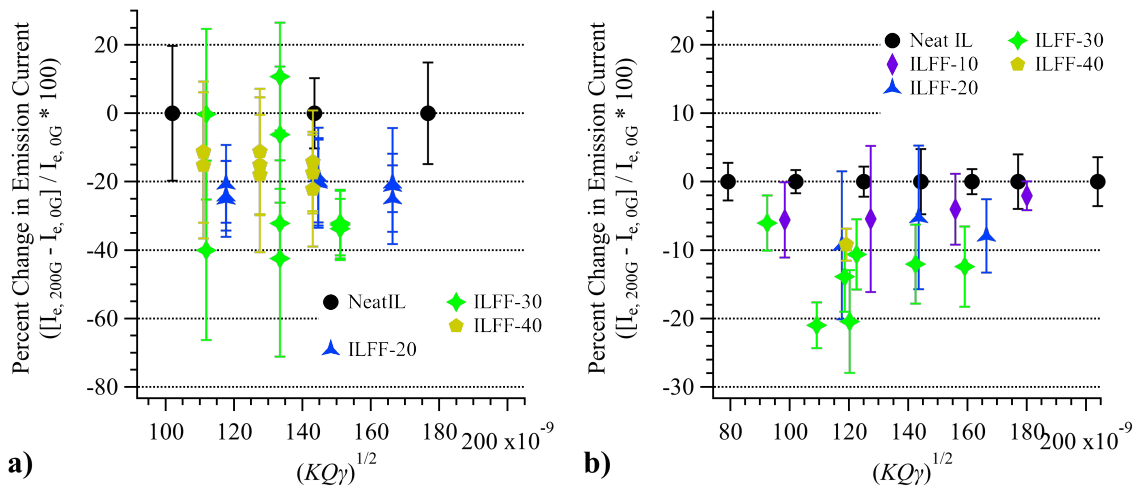
Figure 4.18. Percent change in emission current measured before and after application of a 200-Gauss magnetic field during a) negative extraction, b) positive extraction.

The reduction in emission current (and the minimum flowrate and fluctuation of the emission current induced by the application of a magnetic field discussed in the previous sections) may be the product of the magnetic stress interacting with the emission site geometry. As noted in Section 2.2.2., perturbations, such as Taylor cones, on the surface of magnetic liquid are known to increase the gradient of the magnetic field (∇B).[11, 13,

117

45, 67] This would lead to a larger Kelvin force, $f_B = M \nabla B_0 / \mu_r$, at the apex of the emitter attracting the fluid to that location, which may change the mobility dynamics of the nanoparticles, and/or the formation of the Taylor cone at the emission site. Literature on how the latter affects emission current magnitude exists for many propellants. Driesel, Dietzsch, and Möser report that when operating externally wetted, liquid-metal electrosprays the Taylor cone half-angle was inversely proportional to emission current.[108] Fernandez de la Mora reported that the Taylor cone angle for stable emission of a solution of 5-percent H_2SO_4 in 1-octonol influenced the emission current via the function $I = 2\pi\gamma KqG(\alpha)$, where $G(\alpha)$ is dimensionless current. In his work, he determined that a proportionality between cone angle and emission current existed for the cone-angle range of $46° > \alpha > 32°$.[109] Figure 4.5 showed that the magnetic field application did increase the half-angle of the emission cone. However, empirical results presented previously show a reduction in current with the application of magnetic field, which is opposite of the trends observed by Driesel, Dietzsch, and Möser, and F. de la Mora. As such, the results of this form an incomplete picture, though it is possible that the change in Taylor cone shape induced the observed change in emission current. However, measurement of the Taylor cone geometry during the application of a magnetic field was out of the scope this research and not rigorously studied; these results should spur future investigations on CES cone geometry while magnetically stressed.

Another possibility for the changes observed in the emission current and stability of the CES electrospray was the change in the nanoparticle mobility at the emission site. As Rosensweig states, steric-stabilization of nanoparticles in a ferrofluid is dependent on the

magnetic attractive energy in the ferrofluid, $W = -\int_H^0 \left(\mu_0 M \dfrac{dH}{ds} V \right) ds.$ [11] The magnetic

field gradient at the emission site is much larger than a planar ferrofluid surface due to the

emitter geometry. A substantial increase in field gradient could increase the magnetic

attractive energy to a point that it overcomes opposing steric repulsion energy between the

nanoparticles, increasing the local number concentration and impeding their mobility at the

emission site. However, this mechanism is not fully understood, and without further

investigation it is difficult to state whether it will have any significant effect on electrospray

emission.

4.4. Conclusions: Electrospray Onset, Emission Current and Stability Island

The goals of this chapter were to measure the onset potential of an ILFF electrospray,

and to define the stability island of extraction potentials and flowrates of the propellant

used in this research, and measure the influence a magnetic stress had on the onset and the

stability island. First-off, as Figure 4.4. shows, the magnetic stress significantly reduced

the require onset potential for a 26-wt% NPs ILFF electrospray; *i.e.* the onset potential

when a 200-Gauss magnetic field was applied to the source was ~15% less than that when

no magnetic field was applied. This observation was of great interest as it ultimately means

lower power requirements to run an ILFF electrospray that is magnetically-stressed;

however, I should note that there will be trade-offs between this reduction in power and

extra mass and volume of the required magnet when using the ILFF electrospray as a space

propulsion device.

During the stability experiments, the influence of the NPs within the ILFF-based propellants was most apparent, as the addition of the NPs increased both the range of usable extraction potentials and significantly increased the emission current of the ILFF electrosprays (compared to neat IL); both the necessary extraction potential and subsequent emission current correlated to the wt% NPs in the ILFF propellants. The influence of the magnetic field on neat IL electrospray was negligible; this was expected and confirmed that changes observed on electrospray process due to the application of a magnetic field were caused by the magnetic susceptibility of the NPs. The magnetic stress had a significant effect on the electrospray stability island and emission current of ILFF-based propellants; qualitatively, it appeared to decrease the emission current of the electrosprays, decrease the lower Q boundary of the stability island.

However, some undesired results were observed. The emission current fluctuated more when using propellants with higher wt% NPs; furthermore, the magnetic field did not lessen the fluctuations, and frequently increased the fluctuations directly after its application. Also, the ILFF propellants began to coat the capillary needle after 10s of minutes of emission, which could not be removed via application of higher extraction field. Understanding the stability island of each of the propellants, with and without a magnetic field applied to the source, was pertinent to conduct the remaining experiments of this work.

Chapter 5

Beam Diagnostics of the Capillary Electrospray Source

Beam diagnostics of the CES were completed using the source stability island defined in Chapter 4. Two specific diagnostics were completed in this chapter using three ILFF propellants: beam energy and beam divergence of electrospray beam. The chapter begins with the motivation for the diagnostics and goal of the experiment, followed by the apparatuses and procedures used to acquire both beam energy and beam divergence of the CES. The chapter continues with a discussion of the results from the experiment, beginning with the those collected using neat IL propellant, then followed by those collected using the ILFF propellants. The latter is split into two parts to analyze the unique effects of NPs and magnetic stress to each of the beam attributes. Concluding remarks end the chapter.

5.1. Motivation and Goal

Electrospray performance on a source is measured through the operating parameters described in Section 2.1.2. These parameters defined how well the spray is extracted, including efficiency losses related to the cosine losses of the extracted beam, and power losses from partially accelerated particles. Therefore, producing a highly-collimated spray at the maximum possible energy provided by the extraction field is desired. Literature exists on the measurement of beam energy and divergence for multiple electrospray sources and propellants. [43, 44, 89, 95]. However, literature does not appear to exist on

how colloidal NPs affect these characteristics. There exists some research on magnetic influence the divergence of an emitted electrospray beam including an empirical study by Jackson and King,[110] and a theoretical analysis of coaxial magnetic field influence on electrospray jets and droplets by King.[81] To date, the only empirical study conducted on capillary electrosprays using a superparamagnetic propellant of suspended nanoparticles was conducted in the TOF-MS experiments of this research, Appendix D. which used the TOF pulsing plates to selectively measure the fraction of the electrospray beam current at different energies. This study, combined with the absence of other empirical data on beam diagnostics using super-paramagnetic propellants provided motivation for these experiments presented in this chapter.

The goals of the experiment in this chapter aligned with the overall goals of this research. Specifically, the experiment aimed to 1) quantify how or if the presence of solid nanoparticles within an ionic liquid affect the divergence and energy of an ILFF electrospray beam; and 2) measure the influence of magnetic stress on the divergence and energy of an ILFF electrospray beam. The next section describes the specific apparatuses designed for this experiment and the procedures used to complete it.

5.2. Apparatuses and Procedure

The experiment consisted of two beam diagnostics of the CES per the procedures outlined in Section 5.2.4. The divergence of the beam was measured using the Faraday stack described in Section 5.2.2. The energy of the beam was measured using the retarding potential analyzer described in Section 5.2.3. Both diagnostics of the CES were performed

in the UHV facility, described in Section 3.5. and employed the HC-B Helmholtz coil to apply a magnetic field to the source.

5.2.1. Helmholtz Coil

The HC-B Helmholtz coil described in Section 3.4. was operated at its maximum output current of 5.5 Amps when the magnetic field was required. The coil was only operated for periods of maximum 60 seconds, and powered off following each period for approximately 5 minutes to allow the it to cool down.

5.2.2. Faraday Stack

The Faraday stack diagnostic built to measure beam divergence of CES consisted of three concentric stainless-steel plates placed along the downstream axis of the electrospray beam, Figure 5.1. The design was based on Lozano's,[1] as described in Section 2.1.2., albeit fewer concentric plates, and the plates were separated by centimeters to avoid shorting caused by the buildup of IL. It was chosen over a rotatable stage (like that used by Prince's group) since the Helmholtz coil fixed to the facility and could not be rotated with the source. The large-aperture Faraday plate (LRP) was placed 28.2-mm downstream of the extractor plate and had an 18.1-mm -diameter of aperture; the small-aperture Faraday plate (SMP) was 41.75-mm downstream of the extractor plate and had a 12.75-mm-diameter aperture; the solid Faraday plate (SFP) was 54.9-mm downstream of the extractor plate. Changes in the current fraction measured on each plate indicate potential tightening or broadening of the beam. The half angle of the electrospray beam that interacted with each Faraday plate was determined by geometry of the setup, *i.e.* the radii of the apertures

in the extractor plate, LRP and SMP, and the distance each was from the source. The emission current was measured via the μA1 HV ammeter, and the current measured on each Faraday plate was measured through three individual EEVBlog μCurrent microammeters; the output signals of each ammeter were recorded via an input into a NI-6361 USB DAQ and recorded via a LabVIEW VI.
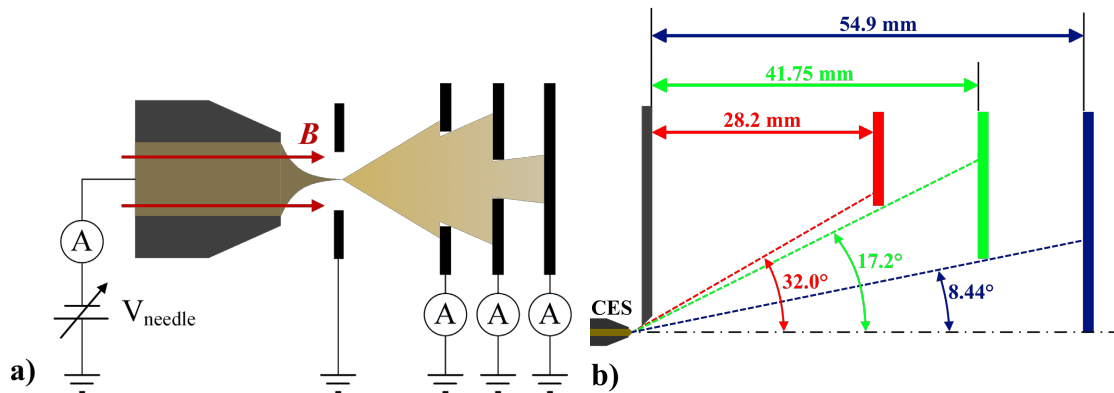
Figure 5.1. a) Schematic of the Faraday stack used as the beam divergence diagnostic illustrating relative position of the Faraday stack and the circuit design. b) Drawing of Faraday stack with dimensions. The denoted distances are measured from the extractor plate to the LRP (red), from the extractor plate to the SMP (green), and from the extractor plate to the SFP (blue). The denoted half-angles represent the portion of the electrospray beam that interacts with each Faraday plate.

5.2.3. Retarding Potential Analyzer

Three factors are typically used in the design of a retarding potential analyzer (RPA) used to measure ion energy in plasma devices: Debye length, grid spacing, and mesh size.[111-115] However, following these three criteria when designing an RPA for IL electrosprays is unnecessary and problematic for several reasons. An IL electrospray plume is comprised of ions and liquid droplets. The ions were assumed to be entirely species of one polarity (either anion or cation) depending on the extraction potential. Therefore, the Debye length is related only to the mobility of the ions. Furthermore, the electrospray tends to coat any surface downstream of the emission site with non-volatile, conducting film.

124

This will cause the small mesh grids to become impassible, as the liquid fills the gaps of the mesh. Also, if a film makes contact between the two grids it will form an electrical short, making the grids ineffective, which can only be removed via a chemical cleaning process.

Therefore, the RPA was designed and built for this experiment to measure the beam energy of the CES electrospray beam, while based on the criteria of plasma RPAs, needed to account for the differences and obstacles inherent to IL and ILFF electrospray. The final design is illustrated in Figure 5.2.
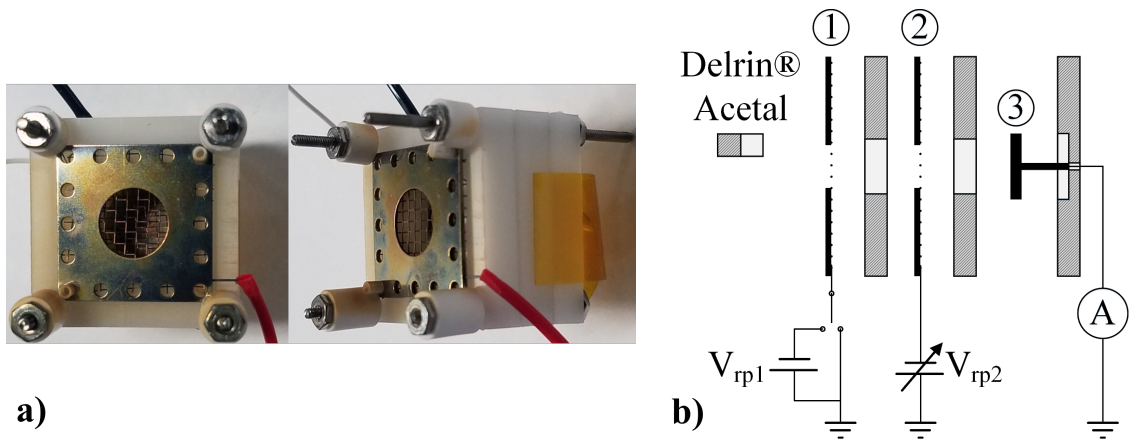
Figure 5.2. a) Image of the RPA design as a diagnostic of IL and ILFF electrospray b) Circuit schematic of the RPA used in the beam energy diagnostic (exploded view); (1) Front grid, (2) Repeller grid, (3) Faraday plate.

Only two electrostatic grids were used in the design as an electron repeller is not necessary and the secondary electron repeller grid was not included. The grids constructed from stainless-steel plates with 0.375-in apertures and 20-by-20 wires-per-inch, 0.0118-diameter tungsten wire mesh welded to the back face of each. A 0.50-inch disk was used as the Faraday plate. The two grids and Faraday plate are isolated from each other using 0.175-inch-thick blocks of Delrin® Acetal plastic. The Faraday plate was also seated in a

block of Delrin to electrically isolate it from the plasma environment. The assembly was aligned via alumina rods, and fastened together via stainless-steel rods and nuts sleeved in alumina. The entrance plane of the RPA was 28.3 mm downstream of the CES. The grids were biased using two high-voltage amplifiers with potential signals outputted from a NI-6361 USB DAQ. The input signals for the grid potential, and the output signal from the Faraday plate were input into and recorded through an Oscilloscope.

5.2.4. Experiment and Procedures

The procedure for the experiment was split into two parts; first a description of those used for the beam divergence diagnostic, these are followed by the procedures used to complete the beam energy diagnostic.

The beam divergence of the CES was measured through the following procedure. The CES, with the Faraday stack attached, was inserted into the UHV facility and a stable electrospray was established using the neat IL propellant with a flowrate of 0.315 nl/s and an extraction potential of 1400 V. A 200-Gauss magnetic field was then applied to the source for 20 seconds and then removed. The collected-current telemetries on the LRP, SMP, SFP were measured and recorded throughout testing. The entire procedure was repeated for select combinations of Q and V_{ext} using the neat IL, ILFF-20, ILFF-30 and ILFF-40 propellants, Table 5.1.

The beam energy in the center axis of the electrospray was measured through the following steps. The CES, with RPA attached downstream concentric with the beam axis, was inserted into the UHV facility. The front grid and repeller grid of the RPA were

initially biased to 2000 V to prohibit the electrospray beam from coating the device interior causing electrical shorts (this is also the state of the plates during non-measurement periods).

Table 5.1. Flowrates (nl/s) for given operating parameters for the beam divergence experiment.

Propellant	Extraction Potential (V)						
	1400	1500	1600	1700	1800	1900	2000
neat IL	0.315	0.315	0.315				
	0.63	0.63	0.63				
		0.945	0.945				
ILFF-20				0.47	0.47	0.47	
				0.705	0.705	0.705	
					0.94	0.94	
ILFF-30			0.454	0.454	0.636	0.636	0.636
				0.636	0.818	0.818	0.818
ILFF-40				0.47	0.47	0.47	
					0.62	0.62	0.62
					0.78	0.78	0.78

A stable electrospray was then established using the neat IL propellant at a flowrate of 0.315 nl/s and an extraction potential of 1400 V. Two energy traces were collected by grounding the front RPA grid, and then sweeping the repeller grid from 2000 V to 0 V at a slew rate of 200 V/second. After the sweep, the bias of both RPA grids was returned to 2000 V. A 200-Gauss magnetic field was then applied to the source using the Helmholtz coil, two energy traces were recorded, and then the magnetic field was removed. A total of 10 energy traces for this flowrate and extraction potential were captured, in the sequence of two with a 0-Gauss magnetic field applied to the source, two with 200 Gauss, two with 0 Gauss, two with 200 Gauss, and two with 0 Gauss. The entire procedure was repeated for select combinations of Q and V_{ext} using the neat IL, ILFF-20, ILFF-30 and ILFF-40

propellants. The combinations of Q and V_{ext} for each propellant, along with the maximum front grid potential and the maximum repeller potential are given in

Table 5.2. The maximum front grid and repeller potentials varied and were at least 100 V greater than V_{ext}.

Table 5.2. Operating parameters of the CES during beam energy diagnostics. Repeller potential is the electrical bias potential for both the front grid and repeller plate prior to collecting an RPA sweep.

neat IL

Extraction Potential (V)	1400	1500	1600	1700
Repeller Potential (V)	2000			
Flowrate (nl/s)	0.315 0.63	0.315 0.63 0.945	0.315 0.63 0.945	0.945

ILFF-20

Extraction Potential (V)	1500	1600	1700	1800	1900
Repeller Potential (V)	2000			2100	
Flowrate (nl/s)	0.47	0.47 0.705	0.47 0.705 0.94	0.47 0.705 0.94	0.94

ILFF-30

Extraction Potential (V)	1600	1700	1800	1900	2000	2100
Repeller Potential (V)	2000			2100		2200
Flowrate (nl/s)	0.454	0.454	0.454 0.636 0.818	0.454 0.636 0.818	0.454 0.636 0.818	0.818

ILFF-40

Extraction Potential (V)	1700	1800	1900	2000	2100
Repeller Potential (V)	2100			2200	2300
Flowrate (nl/s)	0.47	0.47 0.62 0.78	0.47 0.62 0.78	0.62 0.78	0.78

5.3. Results and Discussion

Results of the beam diagnostics experiment, and a discussion on the relevant observations and findings are presented below. The section begins with the results from the beam divergence experiment, beginning with those from neat IL control tests, and followed by those concerning the influence of nanoparticles and then magnetic stress. The section ends with results from the beam energy experiment following the same structure.

5.3.1. Neat Ionic Liquid Electrospray Beam Divergence

Figure 5.3.a) provides an example of the telemetries collected from the beam divergence experiment using neat IL as the propellant. The telemetries are for the emission current of the source and the currents intercepted by each of the Faraday plates, and include operation of the CES with and without a 200-Gauss magnetic field. The extractor plate current was not collected for the experiment; instead the fraction of emission current that was not collected on the three Faraday plates was assumed to have been stopped by the extractor plate.

Figure 5.3.b) shows the current that was not intercepted by the extraction plate and a percent of the emission current. It showed that 85 to 100 percent of the emitted current of a neat IL electrospray was within a $32.0°$ half-angle. While this is not very well collimated it still meant that at least 85 percent of the emitted products were useful beyond the extraction region; it also set a control that was used later to compare to ILFF electrospray beam divergence results. Error bars shown in Figure 5.3.b) are one standard deviation of the mean current.
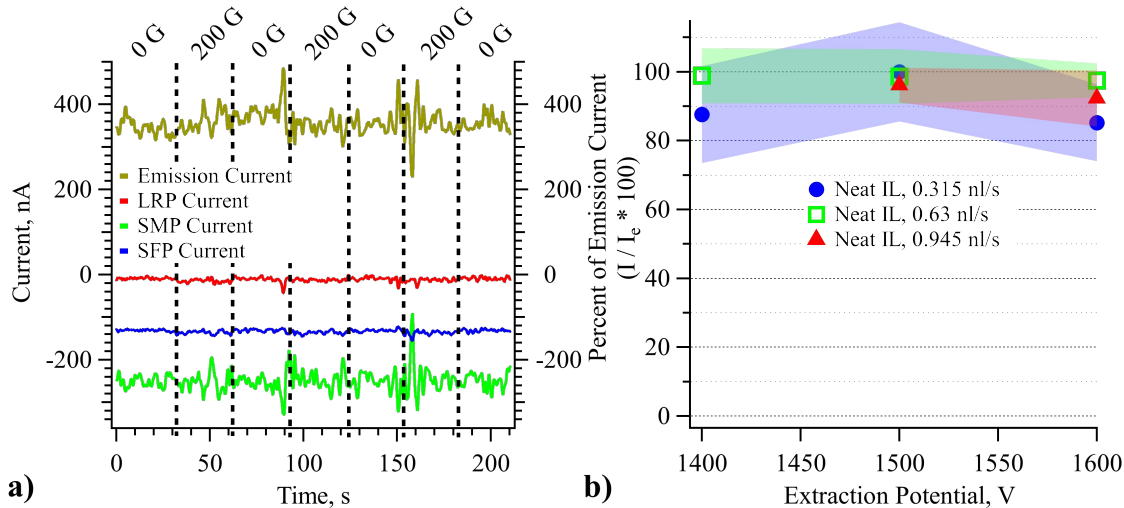
Figure 5.3. a) Telemetries of the emission current and the intercepted currents measured on the downstream Faraday plates of the CES operating on neat IL at Q = 0.63 nl/s and V_{ext} = 1500 V. The magnetic field strength applied to the CES is denoted at the top of each plot; dashes lines indicate temporal bounds of the applied magnetic field. b) The mean measured current collected on the LRP (red), SMP (green), and SFP (blue) as a percentage of the total emission current plotted against the extraction potential of the CES operating on neat IL at three flowrates. Error is one standard deviation of the percent of emission current.

As the surface areas of each of collector plates LRP, SMP, and SFP were not equivalent, angular-resolved profiles were not an appropriate measure of divergence. Instead the current density as a function of angle was determined by dividing the measured currents on each plate by their respective collection surface area, Figure 5.3. The collection surface area was defined as that visible from the source via line-of sight, thus the outer radii of the surface area are at half-angle 32.0°, 17.2°, and 8.44° as shown in Figure 5.1.b). The resultant current density profile was then normalized by the current density measured on the SFP, since this research was only interested in changes in divergence.

Figure 5.4. provides the current density profiles measured during CES operation plotted against the beam half-angle. The stepped-shape of them is the result of only recording a

single current across the angular range of each Faraday plate; the SFP is between half-angles of 0° – 8.44°, the SMP is between half-angles of 8.44° – 17.2°, and the LRP is between half-angles 17.2° – 32.0°. Error bars shown in Figure 5.4. are on standard deviation of the mean current density.
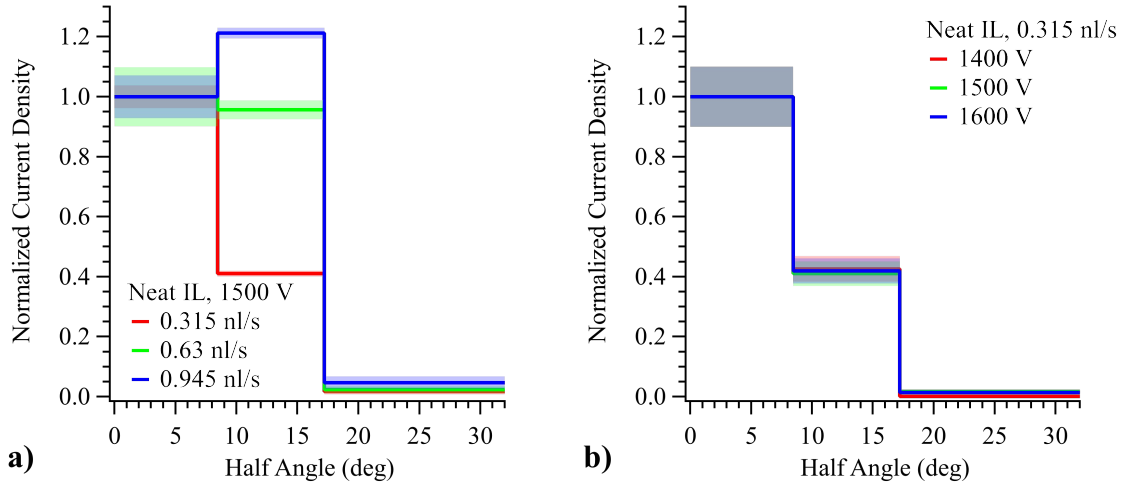
Figure 5.4. Normalized current density profile of the CES operating on neat IL with a) V_{ext} = 1500 V and Q = 0.315, 0.63, and 0.945 nl/s, b) with a Q = 0.315 nl/s and V_{ext} = 1400 V, 1500 V, and 1600 V. The SFP, SMP, LRP are between half-angles 0° - 8.44°, 8.44° - 17.2°, and 17.2° - 32.0°, respectively. Error is one standard deviation of the mean normalized current density.

Figure 5.4.a) illustrates an increase in the current density between half-angles of 8.44° and 32.0° (corresponding to the collection areas of the SMP and LRP Faraday plates) when the flowrate is increased. Figure 5.4.b) illustrates that the extraction potential of the CES has no significant influence over the beam divergence. The combined observations in Figure 5.4. suggests that the beam broadens only during an increase in flowrate. Similar observations are reported for electrospray sources running, [EMIM][NTf2] propellant,[3] [BMIM][DCA] propellant,[43] and [EMIM][EtSO4]-HAN propellant.[116]

Lastly, a 200-Gauss magnetic field was also applied to the neat IL electrospray, and through the comparison between the current density curves with and without the magnetic

field it was concluded that the magnetic field garnered no significant influence on the beam divergence, Figure 5.5. Therefore, any subsequent change in beam divergence of ILFF electrosprays can be attributed to the magnetic susceptibility of the propellants. Error bars shown in Figure 5.5. are one standard deviation of the mean current density.

Based on the combined results of Figure 5.4. and Figure 5.5., that the CES operating on neat IL propellant was concluded to behaved similarly to other capillary electrospray sources in literature. Therefore, they were used as a control source for the results presented in the Sections 5.3.2. and 5.3.3., which discuss if/how the new magnetically susceptible propellants changed the beam divergence of the control CES electrospray.
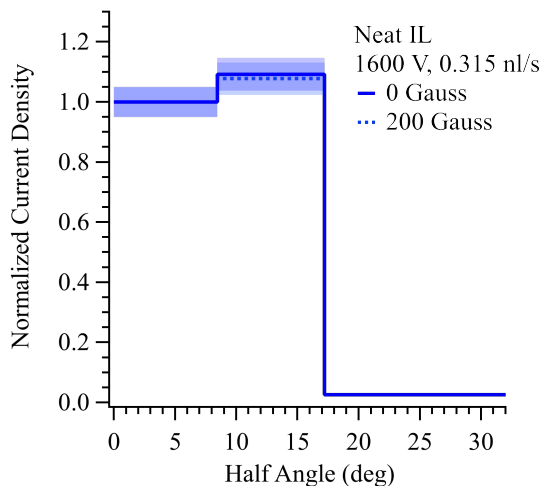
Figure 5.5. Normalized current density profiles of the IF CES operating on neat IL with a $Q = 0.945$ nl/s and $V_{ext} = 1600$ V, with (dashed line) and without (solid line) a 200-Gauss magnetic field applied. Error is one standard deviation of the mean normalized current density.

5.3.2. Nanoparticle Influence on Beam Divergence of Magnetic-Field-Free ILFF Electrospray

As mentioned previously, no literature was found that addressed the effect colloidal particles have on the divergence of an electrospray beam. However, the ILFF propellants used in this research are known to have different electric and liquid properties induced through the addition of NPs to EMIM-NTf2. Specifically, an increase in wt% NPs was correlated to an increase in density and viscosity, and a decrease in the surface tension and conductivity of the propellant, Section 3.1. In a study by Gamero-Castaño which examined the temperature effects on the expansion of an EMIM-NTf2 electrospray beam, he showed that an increase in 20°C increased the half-angle of the electrospray beam by 85.7% (21- to 39-degrees).[117] He concluded that the temperature induced beam expansion by changing both the electrical and liquid properties of the EMIM-NTf2. Other researchers have shown that the temperature of the fluid inherently changes properties of an IL propellant. Specifically, a 20°C increase in temperature from RT induces a 1.3% drop in density, a 49.7% drop in viscosity, a 1.6% increase in surface tension, and a 134.8% increase in conductivity of EMIM-NTf2.[118] However, the effects related to specific liquid properties were not determined in any of these studies. Given this and the added variable of NPs used in this research, the results in this study could not be compared to literature. As such, the results on the measured effects of the beam divergence in this section are only comparable between the propellants used in this experiment.

Current telemetries collected from beam divergence experiment using the ILFF propellants were analyzed in a similar manner as those from the neat IL. As with neat IL, the extractor plate current was not collected for the experiment, but instead the fraction of

emission current that was not collected on the three plates was assumed to have been stopped by the extractor plate. The results from the beam divergence experiment reveal that an addition of, and subsequent increase in concentration of NPs in neat IL significantly changed the fraction of emission current that was measured on each downstream plate, Figure 5.6. and Figure 5.7.
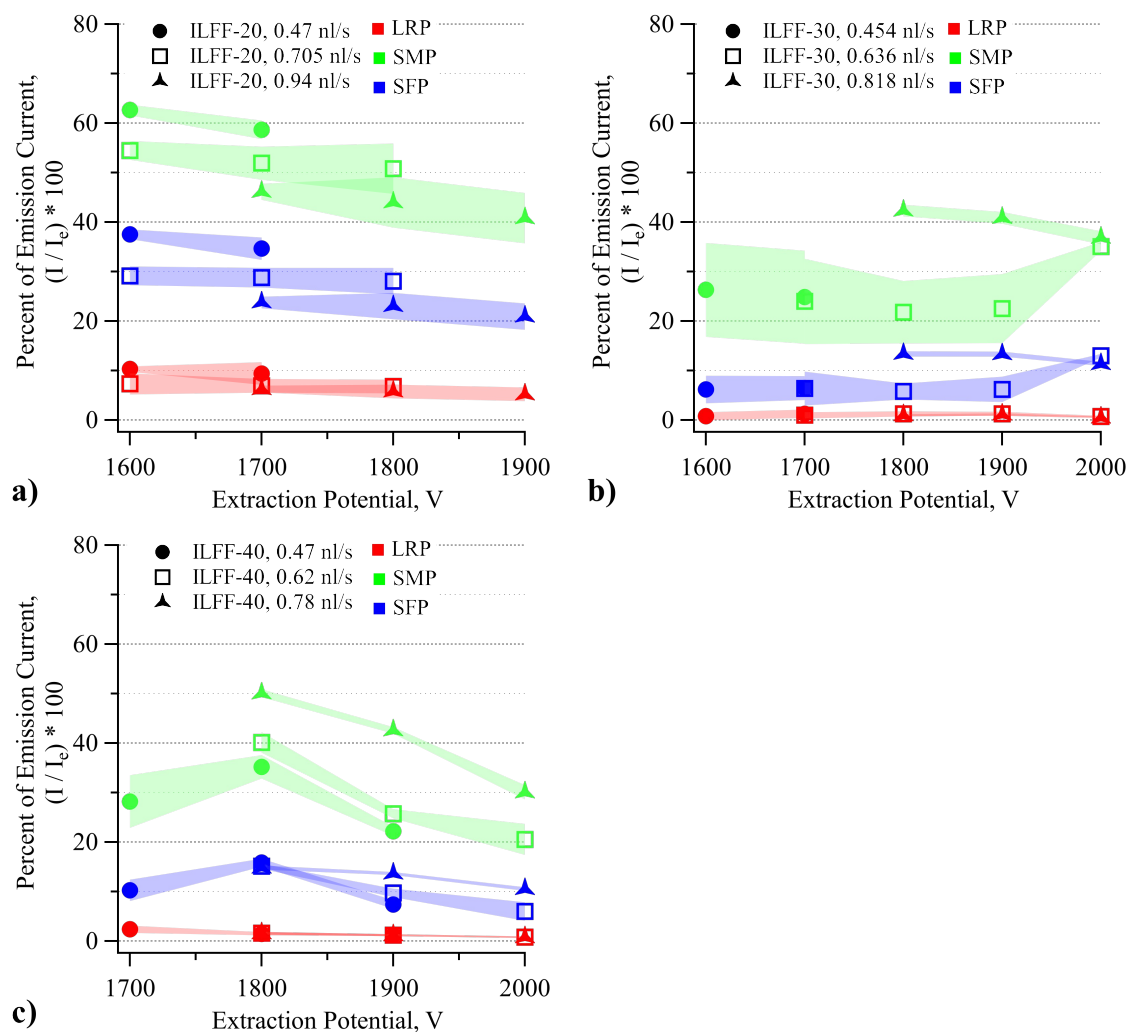
Figure 5.6. The mean measured current collected on the LRP (red), SMP (green), and SFP (blue) as a percentage of the total emission current plotted against the extraction potential of the CES operating at three flowrates operating on a) ILFF-20, b) ILFF-30, and c) ILFF-40. Error is one standard deviation of the percent of emission current. The electrosprays were not subjected to a magnetic field.

The mean current collected on each of the Faraday plates as a percent of emission current for all ILFF propellants shown in Figure 5.6. and Figure 5.7. reveals that the flowrate also had significant influence on magnetic-field-free ILFF electrosprays. Furthermore, unlike analogous neat IL results (Figure 5.3.b)), the extraction voltage also affects the percent of the emission current collected on the Faraday stack. Whereas the total fraction of the emission current intercepted by the Faraday plate during neat IL electrospray operation was invariant of the extraction potential, an increase in extraction potential of the source running on ILFF-20 or ILFF-40 corresponded to a decrease in the total fraction of emission current from all three plates; ILFF-30 propellant was invariant to extraction potential. Quantitatively, the total amount of current intercepted by all three Faraday plates when the source operated on neat IL was approximately 100-percent of the emission current, while the total amount of current intercepted by the three Faraday plates when the source operated on the ILFF propellants was typically less than 100-percent of the emission current. Note: at times the data reports over 100-percent on the emission current, however it was always less than 110-percent of the emission current and is most likely a systematic error of the high voltage ammeter.
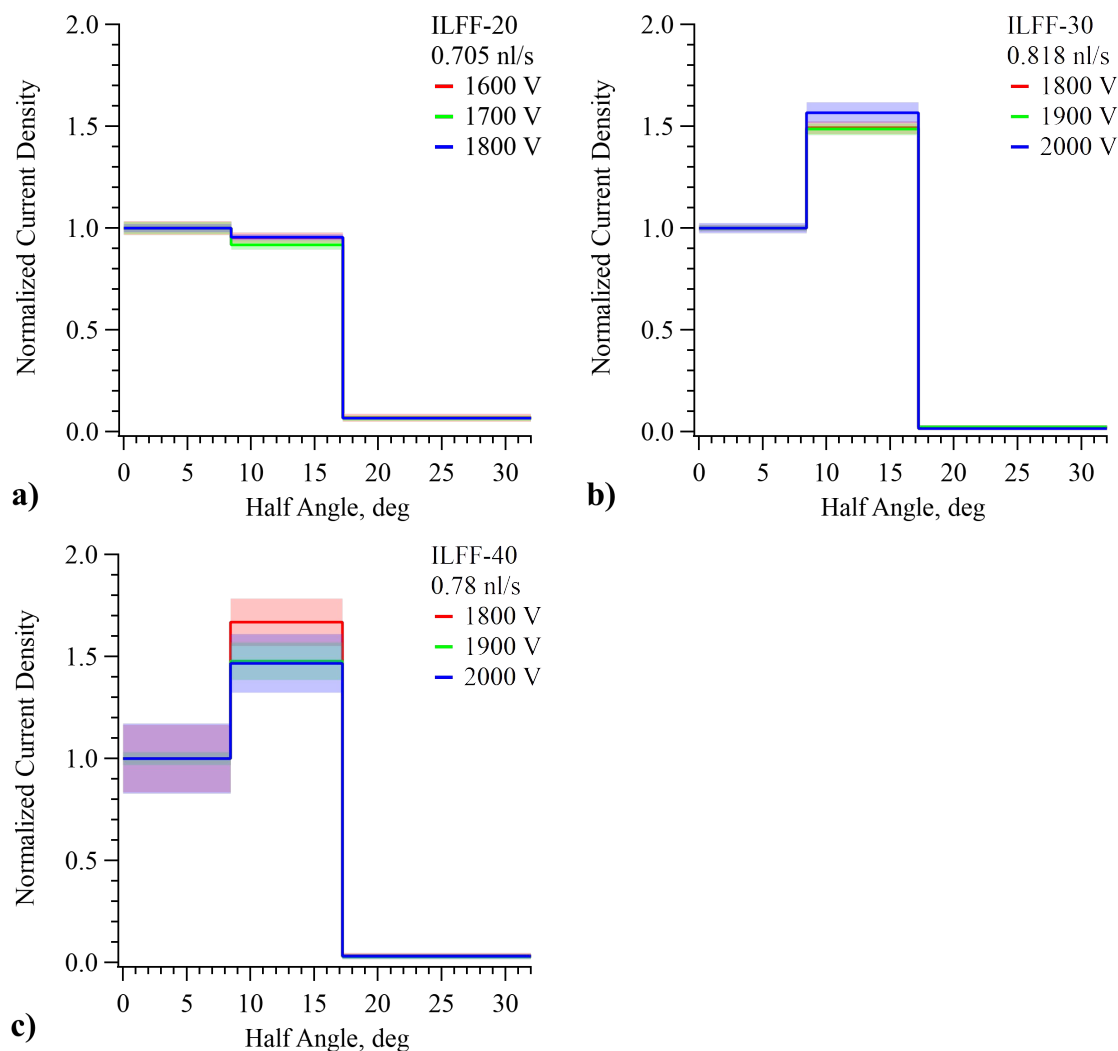
Figure 5.7. Normalized current density profile of the CES plotted against the half-angle of downstream beam, where 0-degrees is the electrospray beam center axis. a) ILFF-20, b) ILFF-30 and c) ILFF-40 propellants. The increase in wt% NPs in the neat IL from a) to c) is correlated to an increase in beam divergence, i.e. the relative current density at higher half angles increases from a) to c). Error is one standard deviation of the mean normalized current density.

A change in flowrate affected each ILFF propellant differently. As seen in Figure 5.6.a), the fraction of the emission current intercepted by the LRP, SMP, and SFP using the ILFF-20 propellant decreased with an increase in flowrate. The fraction of emission current intercepted by the LRP, SMP and SRP using ILFF-30 and ILFF-40 propellants (Figure 5.6.b) and c), respectively) either remain constant or decreased with an increase in

flowrate. Quantitatively, the current intercepted by the Faraday stack when the source operated on ILFF-20 at $Q = 0.47$ nl/s was approximately 100-percent of the emission current; at $Q = 0.94$ nl/s the total current measured on the Faraday stack was between 68 and 76 percent of the emission current. When the source operated on ILFF-30 or ILFF-40 propellants the total current on the Faraday stack as a percent of emission current was considerably reduced; it was 29- to 57-percent for ILFF-30 at flowrates of 0.47 and 0.818 nl/s respectively, and between 27- to 67-percent for ILFF-40, for flowrates of 0.47 and 0.78 nl/s, respectively.

The significant decrease in the total fraction of the beam intercepted by the three Faraday plates is indicative of a reduction in the current traveling within the portion of the electrospray beam intercepted by the Faraday stack. This reduction may be the consequence of an increasingly divergent electrospray beam wherein a larger fraction of the current was at half-angles greater than those collected by the LRP ($\theta > 32.0°$). Alternatively, the beam may be increasingly blocked by the extractor plate. However, each of these possibilities cannot be confirmed as the current was not measured on the extraction plate, and the largest half-angle captured by the LRP is 32.0°.

The fraction of the emission current of the source that was not intercepted by the extractor plate (un-intercepted current fraction) was not directly tied to the weight-percent NPs in the IL, *i.e.* the un-intercepted current fraction was the smallest for the source operating on the ILFF-30 propellant, not ILFF-40. The cause of this observation was not determined, though it may be the result of the NPs interfering with the emission process differently for each of the solutions.

The current density profiles for each ILFF electrospray at various operating settings (V_{ext}, Q) were calculated using the same method used for the current density profiles of the neat IL, Figure 5.4. and Figure 5.5., to compare and quantify the nanoparticle influence on beam divergence. A selection of them for constant Q and three V_{ext} for each ILFF propellant are shown in Figure 5.7. to illustrate the effect of the V_{ext} on the beam divergence. Figure 5.7. a) and b) show that V_{ext} was insignificant to the beam divergence of ILFF-20 and ILFF-30 electrosprays. However, Figure 5.7.c) shows that an increase of 100-V in V_{ext} shifted the current density profile of ILFF-40 electrosprays towards the center of the beam; this may come from the extraction potential changing the cone shape, as described by Morad *et al.*,[119] but no images of the Taylor cone were taken during the experiment to verify this hypothesis. No other statistically significant results exist that show a dependence on V_{ext} but, this could be due to the uncertainty in the current density profile (error shading in Figure 5.7.) which stemmed from fluctuations in the emission current, Figure 5.8.a).

5.3.3. Magnetic Influence on Beam Divergence of Ionic Liquid Ferrofluid Electrospray

The current telemetries of the ILFF-20 electrospray operating at 0.47 nl/s reveal that the magnetic field has significant influence on the emission current and the SMP current, Figure 5.8. a). A possible reason that only the SMP was affected by the magnetic field application was that it had a larger collection area than the SFP, and was located at lower half-angles than the LRP. This meant the SMP collected the highest current fraction of the electrospray beam relative to the emission current. Thus, any change in emission current is most readily seen in the SMP. Furthermore, the SMP current appears to be the most

affected in the current density profiles of Figure 5.8.c) and d), due to the normalization of each profile to the current density of the SFP.
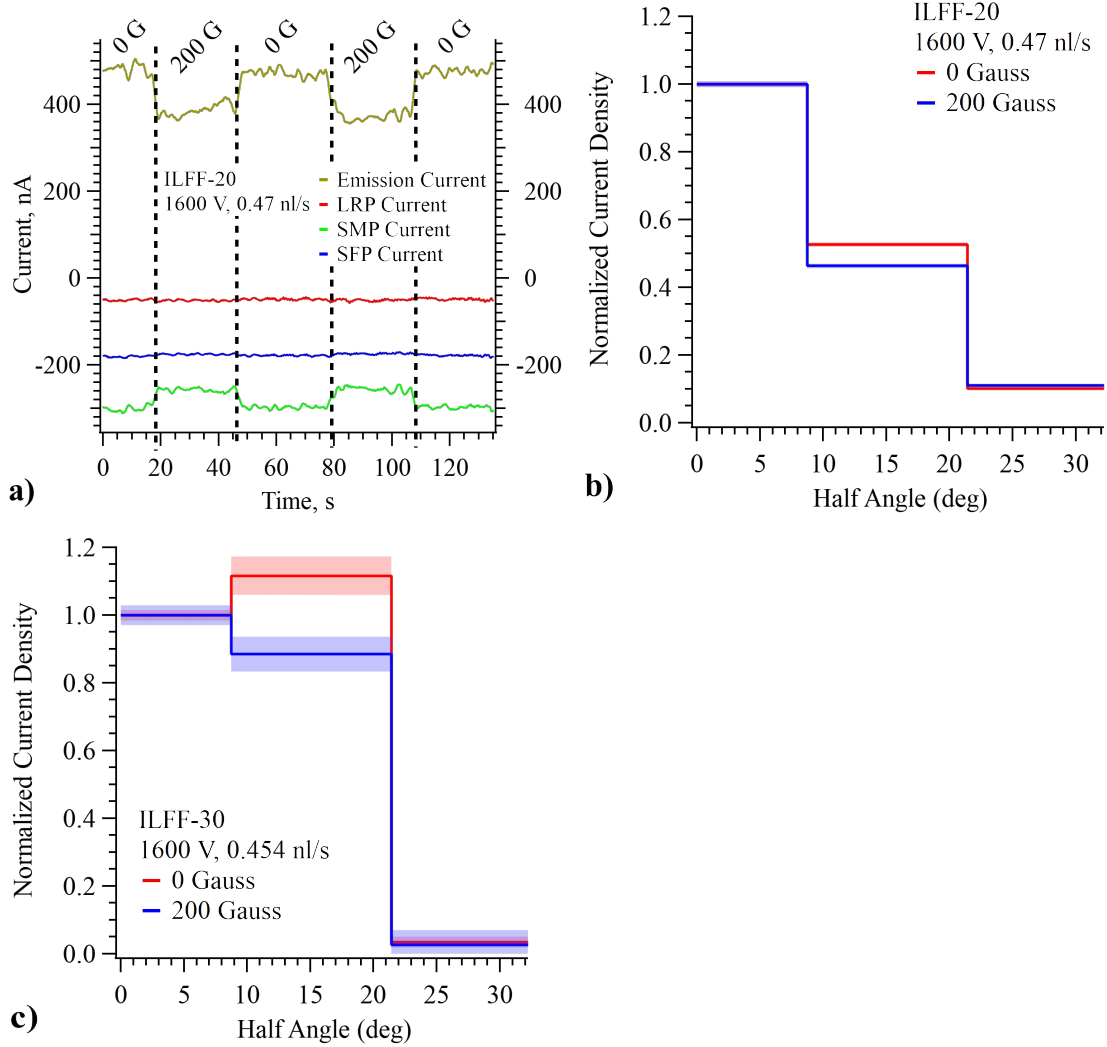
Figure 5.8. a) Telemetries of the emission current and the intercepted currents measured on the downstream Faraday plates of the CES operating on ILFF-20 at $Q = 0.47$ nl/s and $V_{ext} = 1600$ V. The magnetic field strength applied to the CES is denoted at the top of each plot; dashes lines indicate temporal bounds of the applied magnetic field. b) Normalized current density profiles of the IF CES plotted against the half-angle of an ILFF-20 electrospray running at $Q = 0.47$ nl/s and $V_{ext} = 1600$ V, and c) Normalized current density profiles of the IF CES plotted against the half-angle of an ILFF-30 electrospray running at $Q = 0.454$ nl/s and $V_{ext} = 1600$ V. Error is one standard deviation of the mean normalized current density. 0-degrees is the electrospray beam center axis.

The magnetic field influence on beam divergence was quantified by analyzing the current densities of the ILFF-20 and ILFF-30 electrosprays with and without a 200-Gauss magnetic field applied to the source. As Figure 5.8.b) and c) show, subjecting the electrospray to the magnetic field acts to constrict the electrospray beam, *i.e.* the current density at larger half-angles is reduced relative to the current density at smaller half-angles when 200 Gauss is applied to the electrospray. This is only statistically evident for several (Q, V_{ext}) settings of the CES running on ILFF-20 and ILFF-30. Statistically insignificant results at these operational settings were believed to stem from the fluctuations in emission current described in Section 4.3.3.a. The complete set of plots of current densities collected for the CES operating on the neat IL, ILFF-20, ILFF-30, and ILFF-40 propellants are included in Appendix C.

Literature on the divergence of a ferrofluid electrospray beam completed by Jackson and King found that a non- uniform magnetic field applied to an electrospray of IL with magnetic nanoparticles tightened the beam.[110] Therefore, the expectation was for the beam to tighten. However, further analysis by Jackson and King showed that the free space trajectory perturbation by magnetic forces was inconsequential; [120] this was complimented with a similar analysis of Lorentz force on charged particles and their subsequent Larmor radius that is included in Appendix E. Another potential cause of the beam tightening could be the Kelvin force density, $\mu_0 M \nabla H$. However, as the testing was conducting along the center z-axis of a Helmholtz coil, $\partial H / \partial z \simeq 0$ and $\partial H / \partial r \simeq 0$, and consequently $\mu_0 M \nabla H = 0$.

If the Lorentz and Kelvin forces on the particles of the emitted beam are not the mechanism for the change in beam divergence, then a change in emission site geometry induced by the magnetic field may be the cause of the change. A separate study by Jackson *et al*. which examined the onset potential of the parent ILFF demonstrated that a magnetic force changes the geometry of the Taylor cone during capillary emission;[94] an image of this shape change is shown in Fig. 11. This was a consequence of the magnetic normal traction and the fluid magnetic pressure simultaneously acting to change the shape of the cone-jet region of the meniscus. However, in-situ imaging was not feasible during this study due to the Helmholtz coil location, so the effect was not verified for the ILFF solutions. While in-situ imaging was not in the scope of this research, it is likely that the cone-jet region of the magnetically enhanced sprays differed from that of the purely electric.

5.3.4. Neat Ionic Liquid Electrospray Beam Energy

A set of the results from the RPA diagnostic experiment on a magnetic-stress-free neat IL electrospray from the CES are presented in Figure 5.9. Figure 5.9.a) shows the normalized RPA traces of the source emitting a neat IL electrospray at three flowrates, while Figure 5.9.b) shows dI/dV of the RPA current traces; *i.e.* the first derivative of the traces in Figure 5.9.a). Figure 5.9.b) reveals that the CES IL electrospray emits ions with energy that fall within a single energy distribution, regardless of flowrate and extraction potential. These results agree with those of other capillary electrosprays presented in literature.[1, 55, 95] Another observation from Figure 5.9. is that the tails of the dI/dV distributions had energies higher than V_{ext}. This is observed in literature and is suggested

to be the effect of the combined droplet collection from the beam and secondary electron emission.[56, 95] The complete set of RPA traces for neat IL electrosprays running at several combinations of Q and V_{ext} are provided in Appendix F.
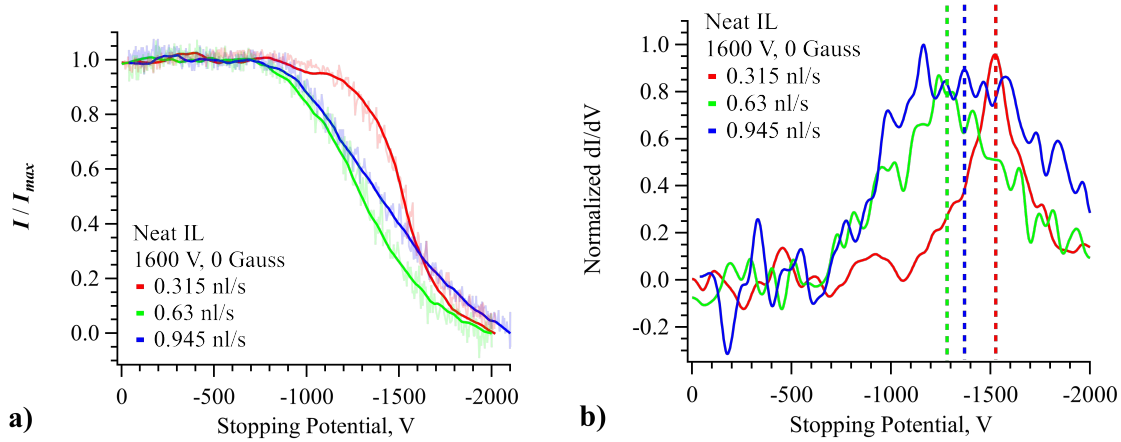
Figure 5.9. a) RPA traces of neat IL electrospray, and b) normalized derivatives of the same RPA traces; V_{ext} = 1600 V and Q = 0.315, 0.63, and 0.945 nl/s. There was no magnetic field applied to the source in either a) or b).

5.3.5. Nanoparticle Influence on Beam Energy of an Ionic Liquid Ferrofluid Electrospray

Several of the RPA traces of each of the ILFF propellants that were collected at combinations of Q and V_{ext} are provided in Figure 5.10. The remaining traces are included in Appendix F. From these traces, it was concluded that NPs were had a dramatic effect on the energy distributions of the electrospray beam. This was most easily illustrated by comparison of the most probable ion energy, $\langle \epsilon_{ion} \rangle$ for each of the electrosprays. $\langle \epsilon_{ion} \rangle$, as a percent of V_{ext}, was calculated for multiple (Q, V_{ext}) settings using each of the ILFF electrosprays subjected to zero magnetic stress, Figure 5.11. As shown in (2.14), this quantity was a good estimate of the voltage utilization efficiency, η_V, of the CES. The CES operated with the highest η_V during low flowrate and high extraction potential,

142

(Figure 5.11.). Similar results are observed in work by Miller *et al.*, wherein they found that the decrease in energy correlated to the cone extending further into the electric field during higher flowrates.[89] Lozano also observed a drop in energy correlated to an increase in flowrate.[1] In both studies the measured energy as a percent of the overall extraction potential is 85- to 90-percent.
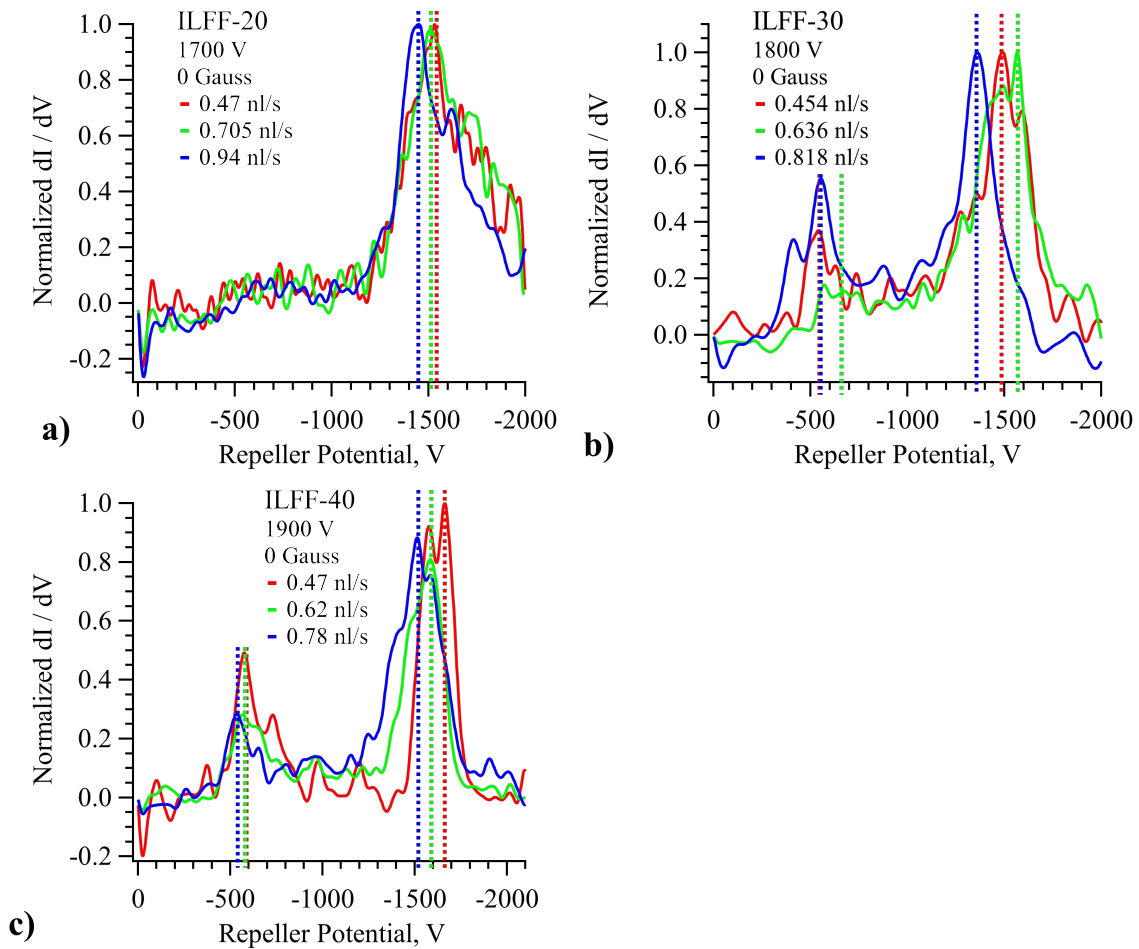
Figure 5.10. Normalized derivatives of the RPA traces collected from the IF CES operating on a) ILFF 20, b) ILFF 30, and c) ILFF 40 propellants. There was no magnetic field applied to the source.

The electrospray beam with NPs also appeared to be poly-energetic; *i.e.* two energy distributions existed for electrosprays of the ILFF-30 and ILFF-40 propellants, Figure 5.10. b) and c). One above 75-percent of the extraction potential and one below 50-percent of

143

the extraction potential, identified henceforth as the primary and secondary populations, respectively. The energy of the primary population of particles in ILFF electrosprays was similar to those in neat IL electrospray; as Figure 5.11. shows, η_V of the ILFF electrosprays was 0.75 to 0.9, depending on propellant and flowrate, which is identical to the range for neat IL η_V. Significant flowrate dependence was only observed in the η_V of the primary populations for ILFF-30 and ILFF-40 electrospray, and resulted in a general reduction in beam energy, (green and blue solid square of Figure 5.11.).
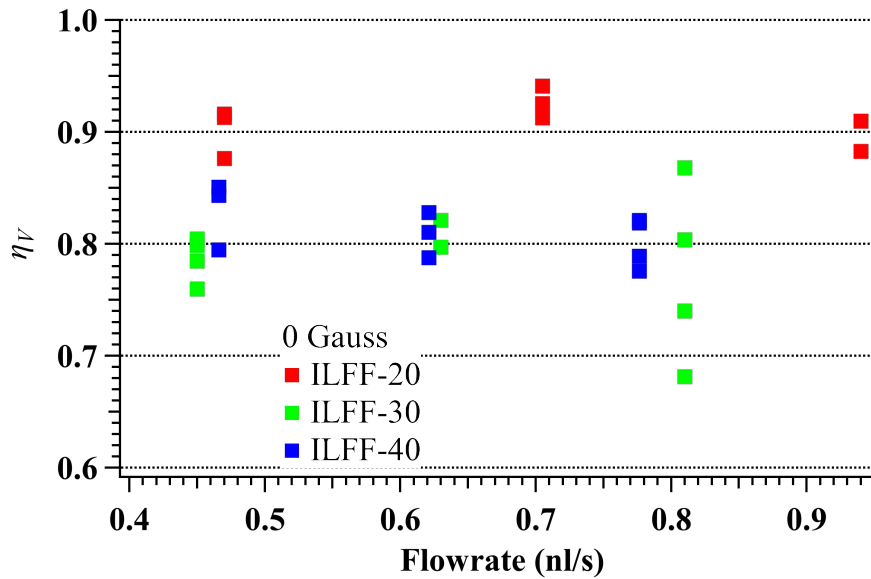
Figure 5.11. Voltage utilization efficiency for magnetic-field-free electrosprays from the CES operating on ILFF-20, ILFF-30, and ILFF-40 propellants plotted against the *Q*. Error-bars are removed for clarity but are 1 to 4.5 percent change for ILFF-20, 2 to 10 percent change for ILFF-30, and 1.5 to 6 percent change for ILFF-40.

The secondary population was distinguishing feature between the energy distributions of ILFF and neat IL electrosprays, and was only observed when using ILFF-30 and ILFF-40 propellants. These distributions were centered between repeller potentials of -500 to -700 V (or 30- to 50-percent of V_{ext}), Figure 5.10.b) and c). As the secondary populations only appeared when the CES was operating on ILFF-30 and ILFF-40, they were likely the

result of NPs. However, as noted in Section 3.1., the addition of NPs changed the density, surface tension, viscosity and conductivity of the neat IL, and were also a physical presence in the spray, therefore, the mechanism that produced low energy particles could not be differentiated from the other effects of the NPs. A mechanism that could produce the secondary population is the fragmentation of ions from the emitted NPs within the extraction field of the source. In a study on the beam energy of an externally wetted EMIM-BF4 electrospray source, Miller and Lozano concluded that similar poly-energetic RPA traces were the result of fragmentation of dimer ion species into monomer species within the extraction field.[44] Thus the lower-energy, secondary populations presented in Figure 5.10. could be the consequence of ion species fragmenting from droplets or off NPs partway through the extraction field of the source. Since this population does not appear in the RPA traces of neat IL or ILFF-20 electrosprays, this hypothesis is possible, but it would require future testing and/or modelling to confirm.

5.3.6. Magnetic Influence on Beam Energy

The magnetic influence on the beam energy of the neat IL electrospray was negligible. This was expected as the neat IL propellant was non-magnetic and the effect of the magnetic field on the moving ions emitted from the source was already found to be insignificant (Section 5.3.1.). This finding provided a baseline for adding magnetic stress to the electrosprays of ILFF propellants.

The magnetic stress significantly influenced the RPA traces collected from the CES operating on the ILFF propellants, Figure 5.12. Furthermore, by comparing the η_V of the

electrospray with and without a 200-Gauss magnetic field, Figure 5.11. and Figure 5.13., respectively, the application of a magnetic field was concluded to consistently increase the energy of the primary population for various flowrates and extraction potentials within the stability island of all ILFF propellants. The magnetic field also increased in the $\left\langle \epsilon_{ion} \right\rangle$ of the secondary population when it appeared in the RPA trace, Figure 5.12.

The beam energy of the primary population for the CES operating on the ILFF-30 propellant was most affected by the magnetic field compared to ILFF-20 or ILFF-40 propellants. At lower flowrates, the magnetic field consistently increased the primary population energy by more than 10-percent when compared to spray during a 0-Gauss magnetic field. The fact that the magnetic influence affected the beam energy of the ILFF-30 electrosprays the most was interesting as the magnetic influence on the beam divergence was also the largest when using the ILFF-30 propellant. This could mean for the specific wt% of NPs in ILFF-30 propellant the magnetic susceptibility of the nanoparticles dominates other potential influences caused by the addition of NPs, *i.e.* changes in density, surface tension, conductivity and viscosity.

The general increase in the energy of both populations caused by the magnetic field application suggests that the emission site location of all charged particles reacted to the application of the magnetic field. The shape of the Taylor cone that formed during ILFF electrospray emission was already observed to change significantly, Figure 4.5. Therefore, it was likely some effect related to this shape change that induced the increase in most probable ion energy, though the specific mechanism was not determined in this research.

146

Remaining RPA traces for propellants operating with a 200-Gauss magnetic field are provided in Appendix F.
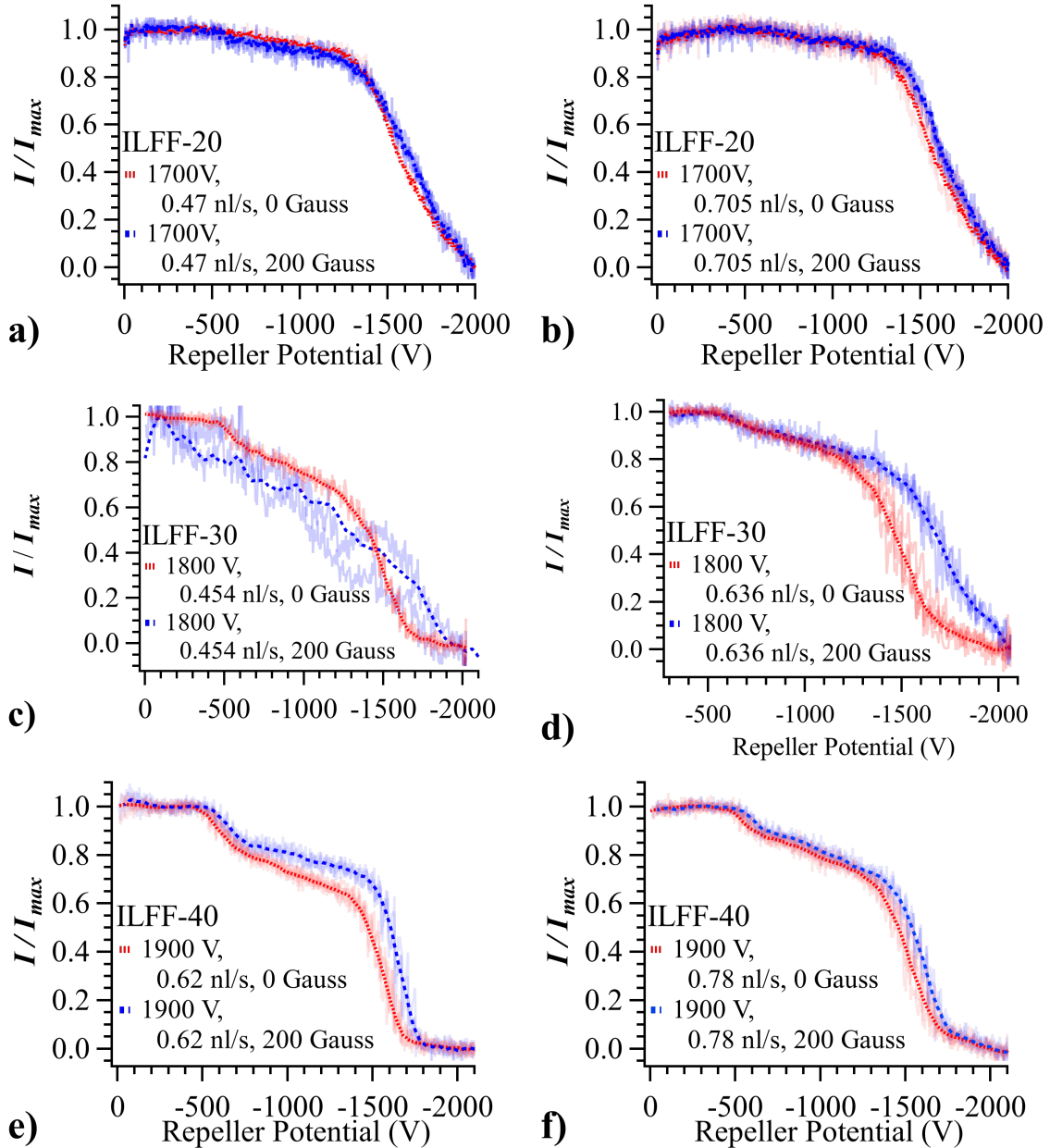
Figure 5.12. RPA traces of an electrospray acquired from the CES with (blue) and without (red) a 200-Gauss magnetic field applied. Each trace shown here was an average of two RPA sweeps (light blue and light red). The propellants used are ILFF-20 operating at with V_{ext} = 1700 V, and flowrates, Q, of (a) 0.47 nl/s and (b) 0.705 nl/s; ILFF-30 operating with an V_{ext} = 1800 V and Q of (c) 0.454 and (d) 0.636 nl/s; and ILFF-40 with an V_{ext} = 1900 V and Q of (e) 0.62 and (f) 0.78 nl/s.
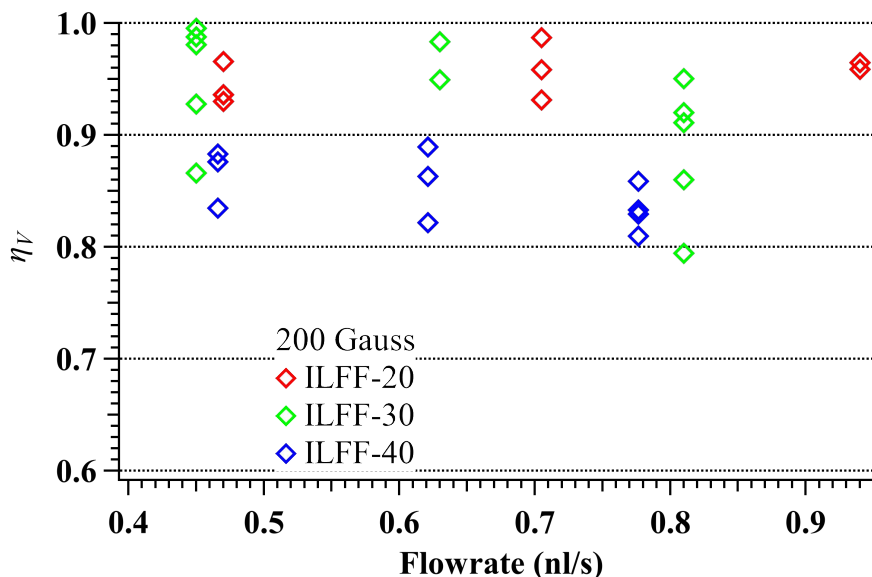
Figure 5.13. Voltage utilization efficiency for of magnetically-stress electrosprays from the CES operating on ILFF-20, ILFF-30, and ILFF-40 propellants plotted against the Q. Error-bars are removed for clarity but are 1 to 4.5 percent change for ILFF-20, 2 to 10 percent change for ILFF-30, and 1.5 to 6 percent change for ILFF-40.

5.4. Conclusions: Beam Diagnostics

The results presented in Chapter 5 showed that the magnetic NPs and magnetic stress had significant influence the divergence and energy of an electrospray beam from the CES operating on neat IL, ILFF-20, ILFF-30, and ILFF-40.

The NPs influenced both the beam divergence and beam energy of the neat IL electrospray. The current density at higher half-angles of the ILFF-30 and ILFF-40 electrosprays (higher wt% NPs) was significantly higher than electrosprays of neat IL or ILFF-20 propellants. Furthermore, the percent of the electrospray beam not intercepted by the extractor plate was significantly less for the ILFF-30 and ILFF-40 propellants. These two observations led us to conclude propellants with higher wt% NPs produced broader

electrospray beams. The electrosprays of ILFF-30 and ILFF-40 propellants also had $\langle \epsilon_{ion} \rangle$ that were consistently lower, relative to the extraction potential, than those of the neat IL and ILFF-20 electrosprays. Furthermore, a second energy population was recorded for the electrosprays using propellants with higher wt% NPs, and was 30 to 50 percent of the extraction potential.

The effect magnetic stress had on the beam divergence was only statistically significant for ILFF-20 and ILFF-30 propellants. When applied, the magnetic field either broadened or tightened the beam depending on the propellant, flowrate, and extraction potential. The most significant results were measured while running the ILFF-20 propellant at 0.47 nl/s and 1600 V, where the application of the magnetic field increased the fraction of the current in the center of the beam by a summed total of 25 percent.

Magnetic stress had a significant effect on the $\langle \epsilon_{ion} \rangle$ of the emitted species from the CES operating on the ILFF propellants, and was generally increased for all electrosprays. The electrosprays of ILFF-30 were most affected, increasing by upwards of 16 percent for multiple operating conditions.

An obstacle that was discovered during the beam diagnostics experiments was the poor angular resolution of the Faraday stack. This made it impossible to determine the beam divergence with any meaningful resolution when concerned with efficiency of the beam emission. This could be determined in a future investigation by using a Faraday stack with more plates, or creating a setup that provides rotation of both the electrospray source and magnetic field source relative to the diagnostic tools.

Chapter 6

Mass Spectrometry of An Ionic Liquid Ferrofluid Capillary Electrospray

The following chapter details the experiments in which mass spectra of the CES operating on the ILFF propellants were collected and analyzed to understand the influence that NPs and magnetic stress had on the composition of the emitted electrospray. The motivation and goal of the experiments presented in the chapter are described first, followed by the apparatuses, including the TOF-MS, and the procedures used to collect spectra from the source. The resulting spectra are then presented and analyzed to determine the composition of the beam, including the desired measurement of magnetic NPs, and how they affect the electrospray. The influence of magnetic stress on the spectra is then presented and followed by conclusions from the experiments to end the chapter.

6.1. Motivation and Goal

Mass spectrometry is a common technique for the measurement of IL capillary electrosprays.[3, 33, 49, 58, 121-124] Within, these studies researchers showed that the ion/droplet composition of IL electrosprays have dependence on the flowrate,[43, 58] propellant,[33, 124] and temperature.[3, 123] The ion/droplet dependence on the latter two are the consequence of differences in liquid and electrical properties caused by change in propellant or temperature. Literature which focused on magnetically influencing an electrospray source within mass spectrometry was not extensive. All the studies found on

the subject related to researchers that placed electrospray ionization sources into the strong magnetic fields (1 to 3 T) of Fourier transform ion cyclotron resonance (FTICR) mass spectrometers to extend the mass-range that the device can measure.[125-128] The electrosprayed fluids were low-conductivity, aqueous protein solutions.

Therefore, using the mass spectrometry technique to examine composition of ILFF propellants presented a unique study, owing to their superparamagnetic NPs, which were shown to influence both liquid and electrical properties owing to the addition of NPs to the carrier neat IL (Section 3.1.) and provided the means to be influenced by the magnetic field (Chapter 4 and Chapter 5.). Furthermore, because the magnetically susceptible NPs existed in a solid phase, (which have been observed to emit with the electrosprayed IL),[46] they must affect the emission products measured by a mass spectrometer. Multiple studies on nanoparticles within electrosprays of various propellants have been completed, including several that examined ceramic and gold NP suspensions in electrosprays and the relics from the electrospraying process,[98, 129, 130] one that examined how the nanoparticle diameter affected spray characteristics,[98] one that examined charge build-up on the surface of NPs in volatile propellants,[99] and the aforementioned studies on ILFFs by research teams at Yale University[107] and Michigan Tech.[13, 94, 131] However, only the latter two research teams used non-volatile liquids, and only Michigan Tech used propellants with high conductivities. Furthermore, none of these studies examined the colloids within a mass spectrometer to reconcile the m/q of the NPs, or generally number density within the electrospray beam.

As such, the desire of these experiments was to measure the NPs m/q and number density within the electrospray beam, and to understand how they impacted the composition of a magnetic-field-free and magnetically-stressed electrospray that motivated the TOF-MS experiments described in this chapter. The goals of the experiments were threefold: (1) determine the mass composition of an electrospray using an IL with suspended magnetic nanoparticles; (2) measure the NPs present in the magnetic-field-free and magnetically-stressed electrospray beam; (3) determine how an applied magnetic field changed the composition of an ILFF electrospray beam compared to magnetic-field-free spray. (Another experiment was conducted which examined the composition of the ILFF electrosprays operating at the lower bound of the stability island; this was not within the goals of this chapter, however, the results and discussion from the study are presented in Appendix G.)

6.2. Measuring Nanoparticles in a Mass Spectrometer

Prior to attempting the measurement of NPs in magnetic-field-free and/or magnetically-stressed electrosprays, some discussion on how the NP would appear in a TOF mass spectrum was required to determine if/how the measurement was possible. Specifically, several questions required attention: 1) What an emitted NP would look like? 2) What artifact/s would a population of NPs produce in a TOF mass spectrum?

To answer the first question literature on the ferrofluids designed for this research (Section 2.2.1.) was revisited.[12] During the synthesis of their ILFFs Jain *et al*. determined the hydrodynamic diameter of the NPs before and after coating the NP with the block

copolymer to stabilize the NPs in the carrier IL. Comparison of the diameters of the coated and uncoated NPs revealed that the copolymer chains extended ~15 nm from the NP surface. Therefore, coated, 30-nm-diameter NPs in the ILFF propellants of this research would have hydrodynamic diameters of 60 nm while in the carrier IL. How the electrospraying process affects this diameter was unknown; however, since the copolymer coating was selected for its solubility in the neat IL EMIM-NTf2, it was assumed that neat IL would remain with the NP during emission, at least to the extent that it solvated the copolymer chain, *i.e.* the hydrodynamic diameter of a coated NP. Therefore, the smallest form that a single emitted NP would take was the summed mass and charge of a 30-nm-diameter NP coated in a 15-nm layer of IL.

The range of m/q for this hypothetical emitted NP was determined using two assumptions, (1) the charge of the Neat IL coating the NP followed the Rayleigh-limit model, (2.12), (2) the only charge carriers were the ions of the neat IL; *i.e.* the solid NP was neutral. The mass of the of the IL-coated NP was calculated to be 6.14E-19 kg, or 370 million amu, using the densities of the NP, $\rho_{Fe3O2} = 5242$ kg/m^3, and the neat IL EMIM-NTf2, $\rho_{IL} = 1532$ kg/m^3, (The density of IL was used to determine the mass of the entire IL/copolymer coating density since there was little difference between the densities of PMMA, $\rho_{PMMA} = 1180$ kg/m^3, and neat IL, and the fraction of each in the NP coating was unknown). The charge of the emitted NP was estimated via the Rayleigh limit, which is only dependent on the stress balance across the surface the neat IL. Therefore, the solid NP was inconsequential to the calculation, the 60-nm-diameter, IL-coated NP was treated as a 60-nm-diameter neat IL droplet. The Rayleigh limit for this sized EMIM-NTf2 droplet,

given the properties presented in Section 3.1., was 5.76E-16 Coulombs, or approximately 1437 e. Prior literature shows that nanodroplets emitted from electrospray have charge 44% of the Rayleigh limit, or in this instance 632 e.[58] The ratio of the estimated mass and charge of the emitted NP set a lower bound of the m/q range in which a signal identifying the NP in the TOF spectrum would begin to appear, ~600,000 amu/e. Potentially, the emitted NP, could have a larger mass and/or the lower charge, both of which would mean the NP would have large m/q.

Acknowledging the m/q range of an electrosprayed NP estimated from the above discussion the final question became straight-forward: was there a TOF system that could measure masses of electrospray products in an m/q range greater than 500,000 amu/e? As discussed in the literature review, Miller *et al*. developed a method to detect masses of >100,000 amu/e, while maintaining high resolution within the spectra. This meant that the measurement of NPs within the electrospray beam was technically feasible; the results presented in this chapter will verify whether this was the case.

6.3. Apparatus and Procedure

Three experiments were used to determine the mass composition of the electrosprays from the CES; the neat IL electrospray mass spectrometry (ILMS) experiment, the magnetic-field-free ILFF electrospray mass spectrometry (IFMS) experiment, and the magnetically-stressed ILFF electrospray mass spectrometry (IFMS-B) experiment. The procedures of each are outlined in Section 6.3.2. The facility used to measure the mass composition was the AFRL TOF-MS described in Section 3.6. The TOF-MS diagnostic

and equipment used to power the source and TOF optics are described below. The propellants used in the experiment Neat IL, ILFF-10, ILFF-20, ILFF-30, and ILFF-40 propellants were used. The HC-B Helmholtz coil applied a magnetic field to the source when necessary.

6.3.1. Summed Time-of-Flight Mass Spectrum

The DC offset potential on the pulse plates transformed the instrument into an energy sensitive analyzer. Simulations have shown that ions with residual axial kinetic energies of greater than 20 eV, regardless of m/q, cannot traverse the flight tube without collision with the instrument walls (Appendix H.). The wide range of axial kinetic energies at which ion and droplet species are emitted means that only those particles within a small energy difference from the pulsing plates are slowed properly for entrance into the flight tube, (see Miller *et al*. for further discussion on this topic[58]). To ensure the measurement of most of the emitted particles, spectra needed to be collected for varying pulsing-plate potentials corresponding to varying particle energies, *i.e.* particles with varying energy defects. (Energy defect was defined as the difference between the axial kinetic energy of a particle and electrospray bias potential.) This was achieved by decreasing the pulsing plate bias in 50-V increments from a maximum of 850 V (equal to an energy defect of 50 eV for a particle) to the bias that had a Faraday current of 50 percent of the maximum magnitude (*i.e.* 50 percent of the Faraday cup current magnitude when the pulsing plates were at ground) and/or provided a mass spectrum that had measurable droplet distributions. (Note: Neat IL spectrum were taken at 100-V increments as the focus of this study was the ILFF propellants). As this work was not focused on identifying those ions emitted at various

156

energy defects, the spectrum taken at each energy defect for a given flow rate were directly summed to approximate the entire mass spectrum of the emitter. Furthermore, the summed spectra would assist in observing distributions with relatively low intensity, (namely the desired NPs in the ILFF propellants). This summation was termed the *summed time-of-flight mass spectrum*. An example of how one of these was created, and a discussion on what may be omitted in the process, is provided in Appendix I.

6.3.2. Experimental Procedures

The procedures of the three experiments are described below. First, the source operation for each experiment is presented, including the settings for stable emission. Next the general procedure used operate the TOF-MS is detailed. The section ends with specific TOF-MS settings used in each experiment.

The ILMS experiment used neat IL as the propellant and followed the procedures outlined in Section 4.3.2.b. to establish electrospray emission. The experiment was split into two parts, ILMS-B which observed the effect a magnetic field had on the neat IL electrospray, and ILMS-Sum which examined the summed TOF mass spectra of magnetic-field-free IL electrospray. $V_{ext} = 1850$ V and Q = 0.315, 0.63, 0.945, and 1.26 nl/s for the magnetically-stressed IL electrospray, and $V_{ext} = 1800$ V and Q = 0.63 and 0.945 nl/s for the magnetic-field-free IL electrospray. The CES was rebuilt between ILMS-B and ILMS-Sum; the rebuilt source was used in the remaining two ILFF experiments. Both IFNB-Exp and IFB-Exp used ILFF-10, ILFF-20, ILFF-30, and ILFF-40 propellants and followed the procedures in Section 4.3.2.b. to establish electrospray emission. The flowrates and

extraction potentials used to produce electrosprays of each propellant are given in Table 6.1.

Table 6.1. Vial pressures, flowrates and pulsing plate potentials used in the ILFF mass spectrometer experiments.

ILFF Solution	Flowrate (nl/s)	Extraction Potential (V)
ILFF-10	0.52	1800
	0.78	1800
	1.04	1850
ILFF-20	0.47	1750
	0.705	1850
	0.94	1850
ILFF-30	0.54	1700
	0.72	1750
	0.9	1850
ILFF-40	0.54	1750

The general procedure with which TOF spectrum were collected was as follows: once stable electrospray emission was established the optics were optimized to provide maximum current signal on the Faraday cup. The parallel plates were then pulsed and ions were introduced into the TOF flight tube and subsequently recorded by the MCP. The pulse width greatly affects the size of particles gated into the chamber, as heavy particles must fully escape the extraction region before the end of the pulse to be recorded. As a result, the pulse length used for these experiments was 100 μs to allow particles up to 1,000,000 amu/e, which was an expected range of IL droplet distributions and the NPs within the ILFF propellants. The pulse width and magnitude were 10 μs and 400V, respectively, for the magnetically-stressed part of The ILMS experiment (which was not concerned with the

larger particles in the electrospray). The pulse width and magnitude were 100 μs and 400V, respectively, for the magnetic-field-free part of ILMS, IFNB-Exp, and IFB-Exp. For all experiments, a single mass spectrum consisted of 50,000 pulse cycles collected at a rate of 200 Hz.

In ILMS-B, four mass spectra of a magnetic-field-free electrospray for a specific flowrate were collected at a single pulsing-plate potential corresponding to an energy defect of 260 eV; this was followed immediately with the collection of a single spectrum while a 200-Gauss magnetic field was applied to the source. For ILMS-Sum, a single spectrum was collected for each energy defect between 600 eV and 100 eV, at 100-eV increments, and a final spectrum an energy defect of 50 eV; the was completed for flowrates of 0.63 and 0.945 nl/s.

The summed TOF mass spectra of IFNB-Exp and IFB-Exp were collected in sequence and were collected for energy defects between 350 eV to 50 eV, at 50 eV intervals and the flowrates listed in Table 6.1. The ion peaks necessary for converting the TOF axis to an m/q axis were absent in spectra collected for energy defects greater that 350 eV, and were not included in the summed TOF mass spectra. For each energy defect one mass spectrum was collected while the electrospray source operated without an applied magnetic field. This was followed immediately by a spectrum while a 200-Gauss magnetic field was applied to the source. A final spectrum was collected after the removal of the magnetic field to verify reproducibility of the mass spectra taken at the same operating conditions. Cooling periods for the HC-B were on the order of 10 minutes and were required between the collection of spectrum with the 200-Gauss magnetic field. As time was a limiting factor

in the experiment, the cooling time of the HC-B precluded acquisition of more than a single mass spectrum of magnetically-stressed electrosprays per operating condition.

6.4. Results and Discussion

The results of the mass spectrometry experiments included the mass spectra of a IL electrospray, which provided the control for the study, and the summed TOF mass spectra of magnetic-field-free and magnetically-stressed electrosprays of each ILFF propellant, which were analyzed with respect to the goals established at the start of the chapter. The section begins with a discussion the intensity axis and repeatability of TOF spectral measurements which were crucial to analyses of the mass spectra. This is followed by the discussion of results from control experiment (ILMS). Then a discussion about the NP within the summed TOF mass spectra collected in these experiments. Finally, the mass spectra of the ILFF electrosprays is presented, analyzed, and discussed with attention paid to the influences of the NPs within the propellants, and the magnetic stress applied to the electrosprays. For the remainder of the chapter ion species will be referred to as n = 0, 1, 2, 3, etc. to define the number of cation-anion pairs attached to a single $EMIM^+$ cation, i.e. $[EMIM][NTf2]_n EMIM^+$. For example, n = 2 is the $[EMIM][NTf2]_2 EMIM^+$ ion species.

6.4.1. Intensity Axis and Spectra Repeatability

The intensities of the peaks in mass spectra can be a reasonable method to compare multiple scans and realize changes within the beam of the electrospray. However, there is uncertainty on the repeatability of the peak intensities between individual spectra. Four spectra collected from a ILFF-10 electrospray operating 0.52 nl/s are presented in Figure

6.1. to illustrate an example of the variation in peak intensity for a specific ion species over multiple spectra collected at the same operating conditions. Variability in peak intensity between spectra meant the electrospray emission was not temporally constant, while variability in the ratio of primary peak intensities, (Intensity $n = 1$)**:**(Intensity $n = 0$), revealed whether the relative composition of the electrospray was temporally constant.
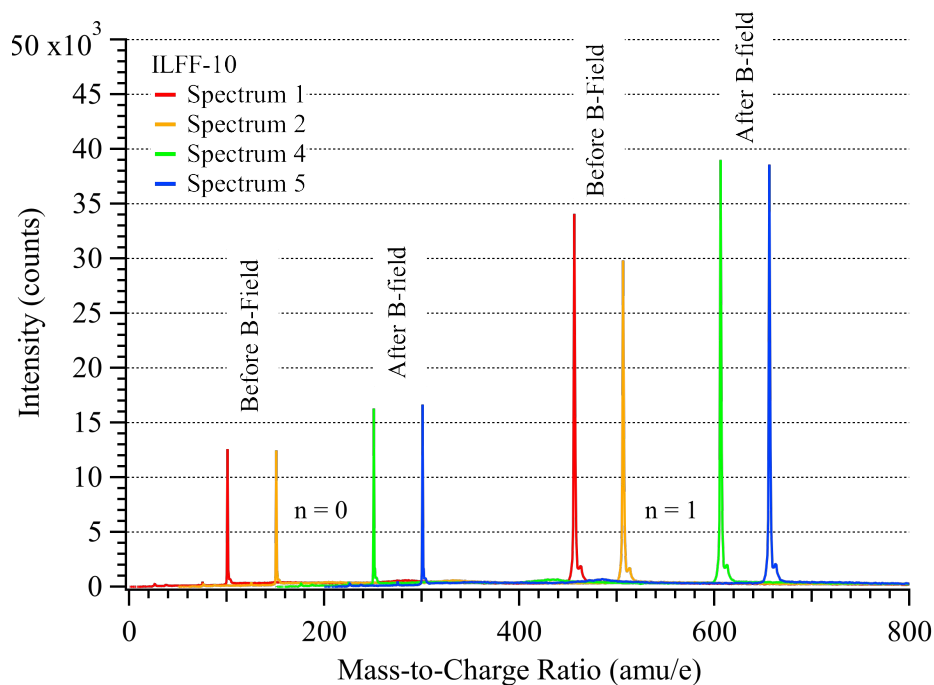
Figure 6.1. Individual scans of TOF-MS for an ILFF-10 electrospray operating at $Q = 0.52$ nl/s. Spectrum 1 and 2 were collected before a magnetic field was added to the source; Spectrum 4 and 5 were collected after the magnetic field was removed from the source. (Scan 3 was collected during magnetic field application and is not shown).

Therefore, repeatability between spectra was determined by collecting at least two full mass spectra (those consisting of 50,000 scans) for each energy defect while operating a magnetic-field-free electrospray and comparing the magnitude of the $n = 0$ peak intensities, and the ratio of peak intensities, of each mass spectrum. The variability of both the peak intensity and the peak intensity ratio between the two (or more) spectra collected at energy defect were calculated as one standard deviation from the average. Figure 6.2.a) and b)

give the standard deviation as a percentage of peak intensity and peak intensity ratio, respectively, for each ion energy at the lowest flowrate of each propellant. The standard deviations provide a measure of repeatability during collection of mass spectra. Therefore, the conclusions based on the comparisons of different spectra include this variability, and is illustrated as ±error in the subsequent figures that use the TOF-MS data.
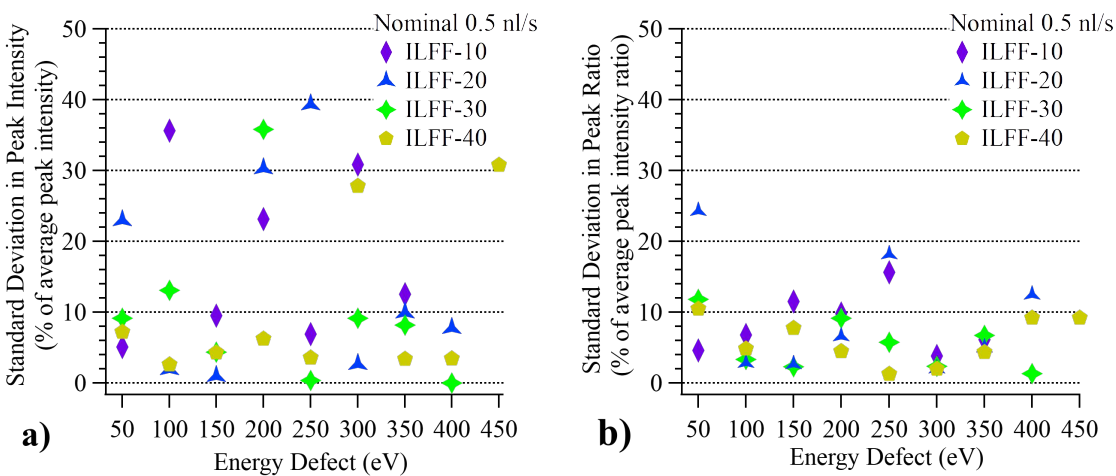
Figure 6.2. Standard deviation as a percentage of (a) average peak intensity, (b) average peak intensity ratio of mass spectra collected under the same conditions.

6.4.2. Mass Spectrometry of Neat Ionic Liquid Capillary Electrospray

The ILMS experiment produced two sets of TOF mass spectra of the CES neat IL electrospray and were used as the control during the analysis of ILFF mass spectra. ILMS-B produced a set of mass spectra collected for a single energy defect which corresponded to the pulsing-plate potential producing the highest signal on the Faraday cup prior to entrance into the TOF flight tube. The interest of ILMS-B was to measure the effect, if any, the magnetic field had on the spectra. The four spectra collected from a magnetic-field-free electrospray were averaged to produce a single spectrum for each flowrate ($Q = 0.315, 0.63, 0.945, 1.26$ nl/s), shown in Figure 6.3.a); the spectra collected

from magnetically-stressed electrosprays operating at each flowrate are shown in Figure 6.3.b). The mass peaks denoted in all the neat IL spectra are the cation species, $EMIM^+$ and $[EMIM\text{-}NTf2]^- EMIM^+_2 [EMIM\text{-}NTf2]^-_2 EMIM^+_3$, $[EMIM\text{-}NTf2]^-_3 EMIM^+_4$, $[EMIM\text{-}NTf2]^-_4 EMIM^+_5$, $[EMIM\text{-}NTf2]^-_5 EMIM^+_6$, and $[EMIM\text{-}NTf2]^-_6 EMIM^+_7$, denoted as $n = 0, 1, 2, 3, 4, 5$, and 6, respectively, in Figure 6.3.; heavier ion species also existed in the beam ($n = 12$ was the heaviest species observed). Large mass distributions also exist in each of the neat IL spectra and are presented as the inset plots of Figure 6.3.a). and Figure 6.3.b). The data in the inset plots were put through a binomial smoothing algorithm to ease comparison.

Comparison between the magnetic-field-free and magnetically-stressed spectra, Figure 6.3., revealed the insignificance that the magnetic field had on the m/q composition or intensity of the emitted masses. This meant that any differences in the m/q or intensity of masses of ILFF spectra with and without a magnetic field are only an effect of the magnetic field acting on the added nanoparticles, not the base IL, of the ferrofluid. Also observed in Figure 6.3. were trends in the peak intensity and droplet distributions which correlated to the flowrate of the neat IL electrospray. This was in line with studies on EMIM-NTf2 by Miller *et al.*, wherein a flowrate increase reduced the intensity of the ion peaks, and shifted the center m/q of the two droplet distributions.[58] Miller *et al.* concluded that the shift in the large droplet distribution was a consequence of the location of droplet birth and coincidently their energy.
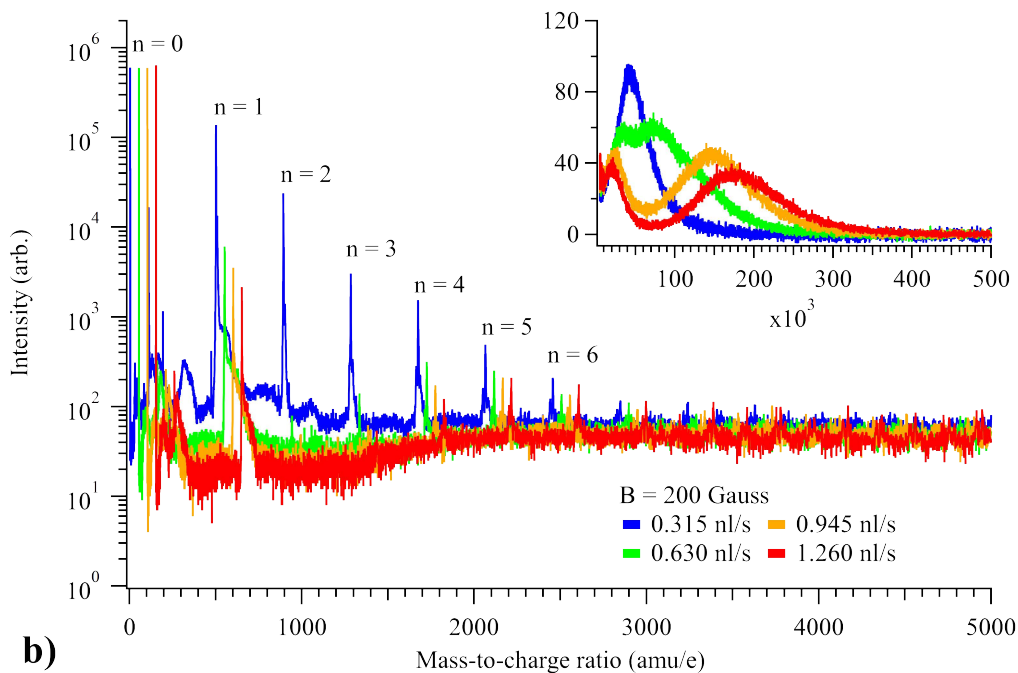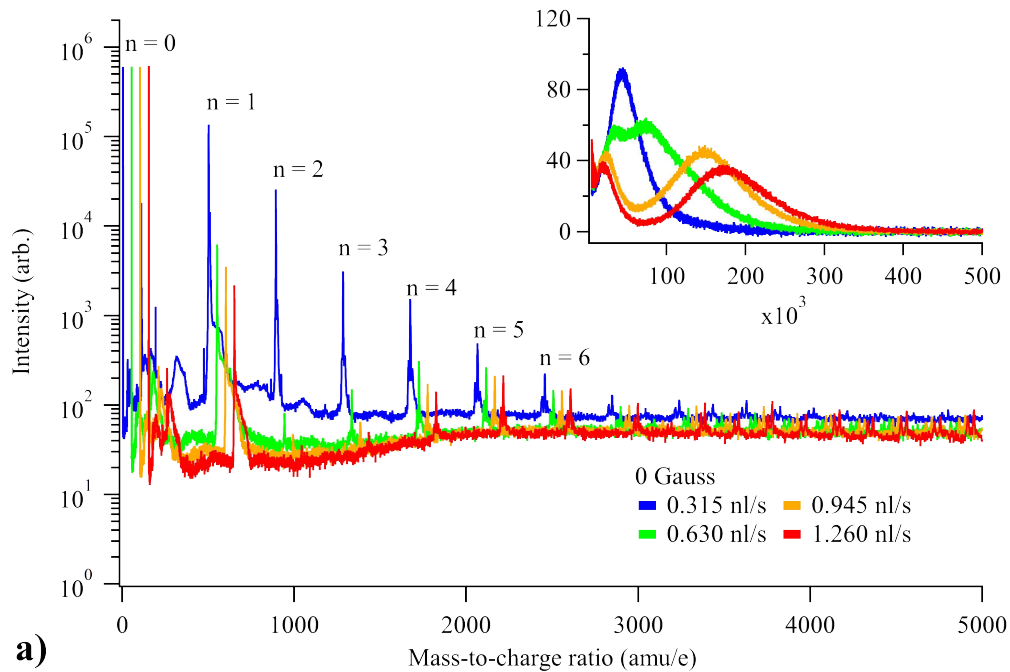
Figure 6.3. Neat IL summed mass spectra of the CES with an energy defect of 260 eV and a) zero magnetic field, b) a 200-Gauss magnetic field applied to the source. The spectra in the low-mass plot (0-5000 amu/e) were shifted by artificially adding 50, 100, and 150 amu/e to green, orange, and red curves, respectively, to ease comparison.

164

The ILMS-Sum experiment produced a set of summed time-of-flight mass spectra for magnetic-field-free IL electrospray operating at flowrates of 0.63 and 0.945 nl/s, Figure 6.4.
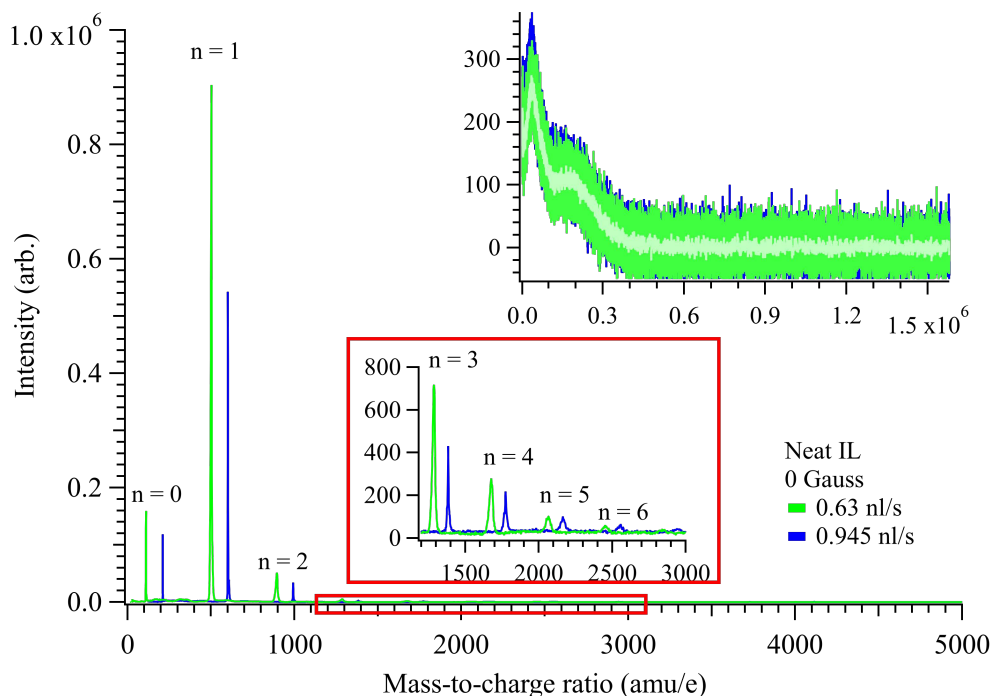
Figure 6.4. Neat IL summed mass spectra of the CES with zero applied magnetic field applied to the source. The spectra in the low-mass plot (0-5000 amu/e) and the inserted plot (red outline) have been incrementally shifted by artificially adding 100 amu/e to the blue curve to ease comparison.

The summed mass spectra of Figure 6.4. revealed that at least eleven ion species and several droplet distributions exist in the beam. Cation species that denoted in the Figure 6.4. were n = 0, 1, 2, 3, 4, 5, and 6; the droplet distributions were centered at 40,100 amu/e and 163,000 amu/e for 0.63 nl/s, and 36,700 amu/e and 160,000 amu/e for 0.945 nl/s. (A lower m/q distribution between 5,000-8,000 amu/e existed and was classified literature as a distribution of multiple ion species larger than n = 8 that emitted at lower intensities and often with multiple charges.)[43, 58] Furthermore, the flowrate increase appeared to reduce

165

the intensity of the ion peaks, which aligns with results of summed mass spectra presented by Miller *et al*.[58] The locations of the droplet distributions and the existence of 11 or 12 cation species defined the control used during analyses of the summed mass spectra of ILFF electrosprays. With respect to typical operation of electrosprays, the CES running neat IL appeared to operate in a mixed ion/droplet mode (eleven ion species and several droplet distributions). The mode of operation will be examined for each of the ILFF propellant to assess whether the addition of NPs influenced this characteristics of the CES.

6.4.3. Composition of An Ionic Liquid Ferrofluid Capillary Electrospray Beam

The collection of mass spectra from the CES using the ILFF propellants was the main goal of this chapter, and the results were expected to illustrate the influence from NPs and the applied magnetic field on the mass composition of neat IL electrospray beam. Furthermore, a primary expectation the mass spectrum collected of ILFF propellants would be the measurement of the NPs emitted during operation. First, the discussion review what the collected mass spectra of the ILFF propellants said about the operation of the CES running on the propellants.

The summed TOF mass spectra were collected for each propellant at the flowrates reported in Table 6.1. The range of energy defects used for individual spectra in the summed TOF mass spectra was 350 eV to 50 eV. An example summed TOF mass spectra collected from the CES running on each propellant at a nominal flowrate of 0.5 nl/s is presented in Figure 6.5.
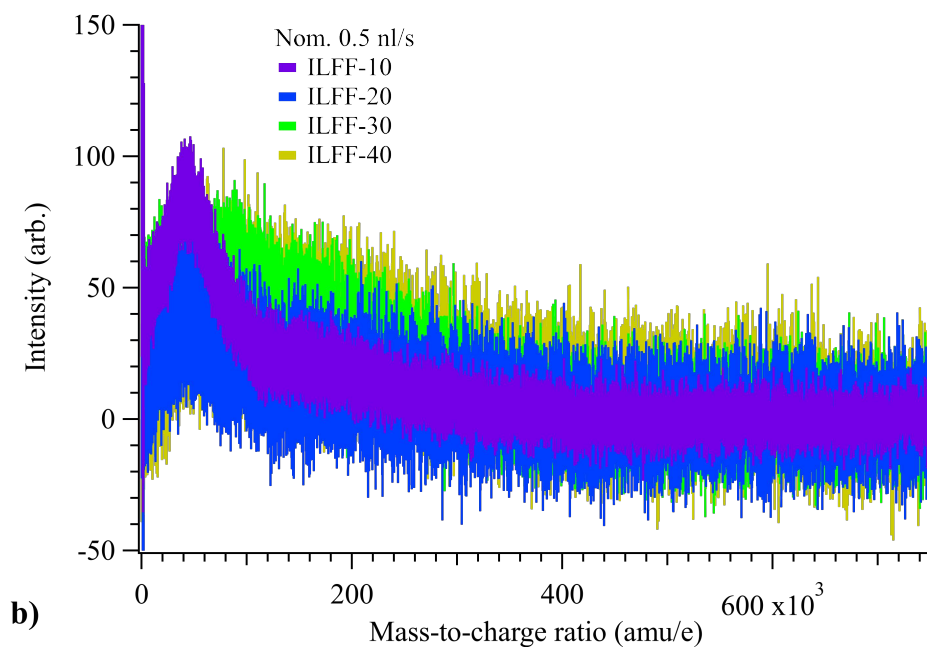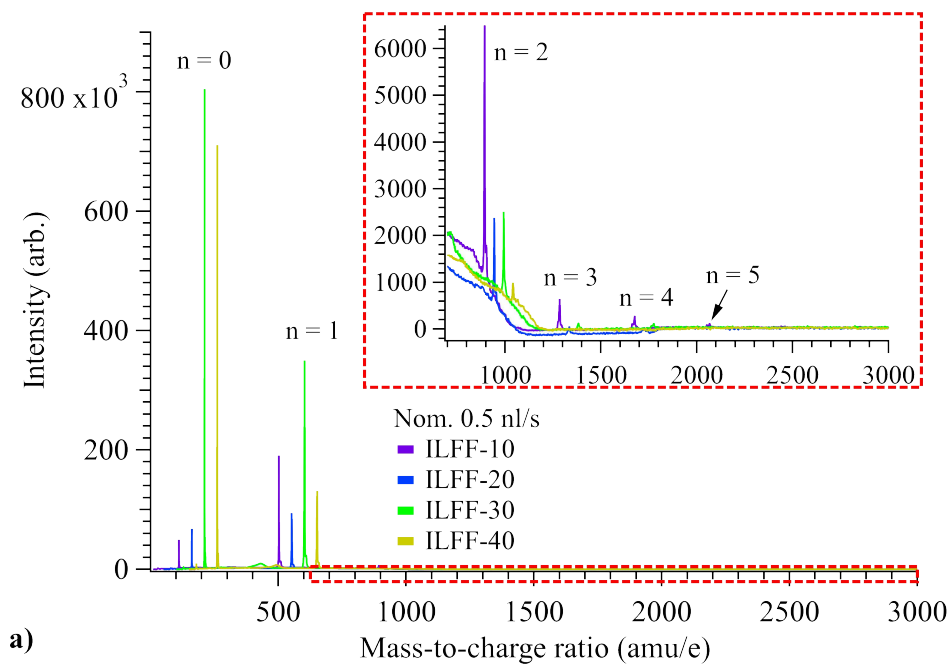
Figure 6.5. Mass spectra of an electrospray emitted from the capillary source using ILFF-10 under a zero and a 200-Gauss magnetic field. The 200-Gauss spectra in the background plot (0-3000 amu/e) and the lower inserted plot (red outline) have been incrementally shifted by artificially adding 50, 100, and 150 amu/e to the blue, green and yellow traces, respectively, to ease comparison.

An immediate observation from Figure 6.5. was that the ILFF electrosprays, while

highly ionic, all operated in mixed ion/droplet modes; All emitted ILFF electrosprays had

167

at least n = 0, 1, 2 ion species and one or more droplet distributions centered at m/q ranging from 30,000 amu/e to 150,000 amu/e. Similar observations were made on the summed spectra for higher flowrates of ILFF-10, ILFF-20, and ILFF-30 propellants, Appendix J. The finding begged the question: what fraction of the mass (and fraction of the charge) of the electrospray beam was transported by each type of particle (ion or droplet)?

The process to answer the question began by defining the specific m/q ranges of the beam that were of interest. These were used as the bins which would be filled with based on the intensity of a specific mass spectrum. For example, Figure 6.6. illustrates seven distinct ranges, three of which are the three lightest ion species, one is a range that includes the combined intensities of several heavier ion species, and the two others define portions of the beam transported by larger m/q distributions (*i.e.* droplets). The selection of the lightest ion species as bins was easiest as the peaks were distinct and the ion m/q was already defined. Combining the remainder of heavier ion species into a Bin 4 was done due to the relatively low intensity of their peaks in summed mass spectra for all the electrosprays (*i.e.* the mass or current fraction transported by the heavier ion species would have been inconsequential compared to the lighter ions or droplets). The ranges of m/q for Bin 5 and 6 were not distinct ions, but instead where selected based on distributions observed in the spectra denoted in Figure 6.6.c) with Maxwell-Boltzmann fits; (the use of this distribution will be discussed later). Bin 7 was defined as the m/q range that was greater than the tail end of the droplet distribution of Bin 6 to capture the tail end of the summed mass spectrum.
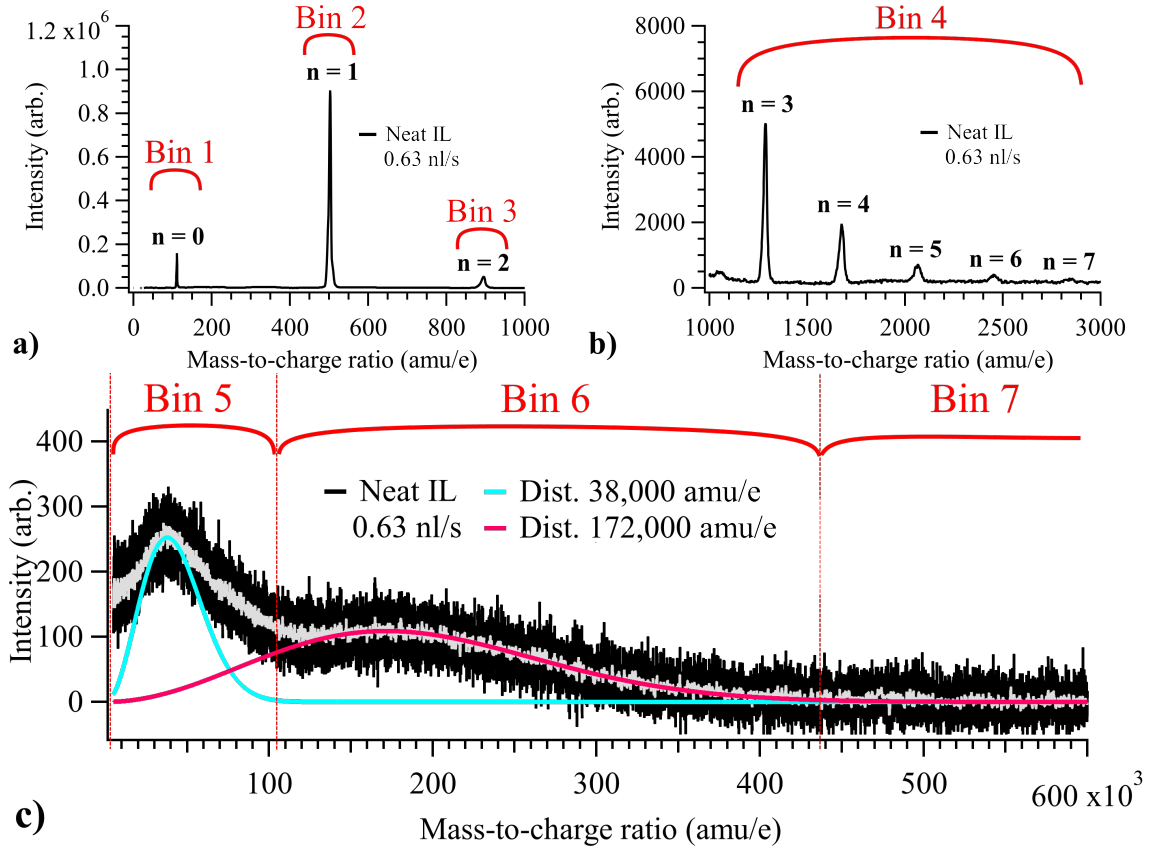
Figure 6.6. The summed mass spectrum of neat IL electrospray broken into 7 ranges of m/q that would be used as bins for the mass and current fractions of an electrospray beam. a) light ion species which comprise Bins 1-3; b) heavier ion species which combine to form Bin 4, c) Droplet distributions which were split into three bins based on the center m/q of each distribution.

    With the bins of low and high m/q ranges selected, the actual masses of the particles were needed to determine the fraction of the mass flow in the electrospray beam that was associated with each. This was accomplished by first assuming the distributions were comprised of polydisperse droplets with charge equal to 44% of the Rayleigh limit, (2.12) ; this definition for droplet charge is well established in literature.[1, 29, 58, 132] Using the definition for mass of a spherical droplet, $m = \frac{4}{3}\pi R_D^3 \rho$, and the Rayleigh limit, the radius of a droplet was easily solved to be function of m/q, ρ and γ (density and surface tension of EMIM-NTf2, respectively),

169

$$R_D = \left(\left\langle \frac{m}{q_D^{0.44}} \right\rangle \frac{6*0.44(\varepsilon_0\gamma)^{1/2}}{\rho} \right)^{2/3}.$$

(6.1)

The m/q axis of the summed mass spectra were converted to droplet radius via (6.1). Furthermore, the droplet radius was input into (2.12) to determine the particle charge of as function of m/q, and subsequently used to find the mass axis of the summed mass spectra, $m = \frac{m}{q} q_D^{0.44}$. Using the estimated droplet radius and particle mass, the fraction of the mass transported by the distributions was estimated by integrating the intensity curve of the summed mass spectra of five propellants with respect to the new mass axis. The results were separated based on the bins defined in Figure 6.6. forming the histogram presented in Figure 6.7. The bins from Figure 6.6. were defined by either the ion species (n = 0, 1, 2, 3…) or a range of droplet radii that form the distributions.
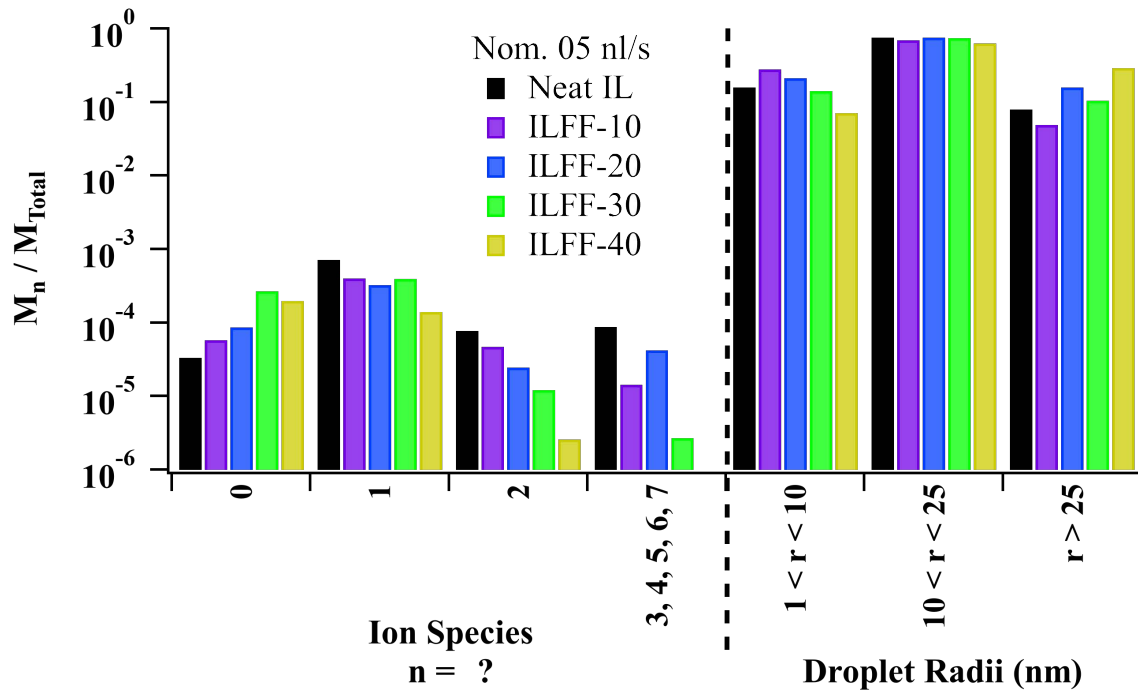
Figure 6.7. Mass fractions of all electrosprays running at a nominal 0.5 nl/s. The left axis is on a log scale to better illustrate the magnitude of the mass fraction for the ion species.

Figure 6.7. illustrates that the mass of the electrospray beam emitted from the CES is transported almost entirely by the droplet distributions. This is a known characteristic of capillary electrosprays stemming from the size of the orifice in the capillary and the flowrate required to maintain stable emission. Whether this is undesirable is dependent on the application, (*i.e.* are droplets or ions wanted). Several groups have had some success in using flow inhibitors to reduce the flowrate and increase the ion production of IL electrosprays.[10, 133] In the study of this dissertation, using the NPs did not appear to be a factor in the mass fraction of the electrospray beam. This is despite the assumed inclusion of NPs within an emitted ILFF electrospray, which were known to be five times the density of neat IL. This raised another question about the summed mass spectra: was a NP distribution detected and can it be distinguished from other artifacts in the electrospray beam?

6.4.4. Potential for Nanoparticle Distribution in Summed Mass Spectra

The discussion of Section 6.2. is revisited to determine whether a NP distribution was detected by the summed TOF mass spectra collected in this study. The NP m/q was estimated to be ~600,000 amu/e, but the mass and charge of a NP was expected to vary. This meant that the range of m/q in which a NP could produce a signal in a TOF mass spectrum began at the estimated m/q of the smallest NP at 44% Rayleigh limit and extended to a range beyond that measured using the AFRL-TOF instrument which maxed out at ~800,000 amu/e. Though this still implied that a NP could have been detected by the instrument. But the intensity of the NP signal in the mass spectrum may be an insurmountable hurdle in its detection. The volume fraction of NPs in the ILFF-40

propellant was only 3.65 %v/v, or 6.5 %v/v if copolymer was considered. This meant that if the electrospray is assumed to emit only droplets[1] of radius 17.5 nm (center radii of the bin with highest mass fraction in Figure 6.7.), a 30-nm-diameter IL-coated NP will appear only once for every 77 emitted IL droplets, Figure 6.8.
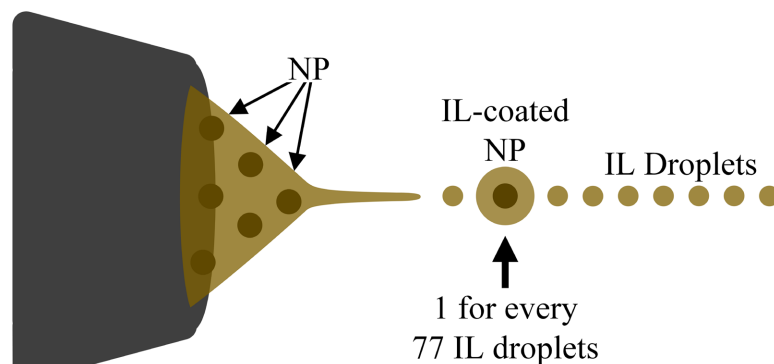
Figure 6.8. Graphic of an ILFF electrospray emission of NP and IL droplets.

As the MCP detector for the TOF-MS is an event-based device (*i.e.* 1 count on the intensity axis of a mass spectrum was equal to one impact event of the MCP which is independent of particle mass or charge) the intensity of a NP distribution relative to an assumed 17.5-nm IL droplet distribution nearly two orders of magnitude less. If the NP distribution was monodispersed and equally charged (1 amu/e distribution width at the estimated m/q of ~600,000 amu/e) its intensity peak would have a magnitude in the 1000s, well above the droplet distributions, and should be easily distinguished from other populations in a summed TOF mass spectra, Figure 6.9.a). However, the assumption that the emitted NPs had zero variation in mass or charge is unwarranted given the known variation in hydrodynamic diameter of the NPs (±5 nm). If the m/q of NPs within the population varied in diameter by ±1 nm (±4,000 amu/e) the resultant distribution would have an average intensity on the order of 10, Figure 6.9.b).
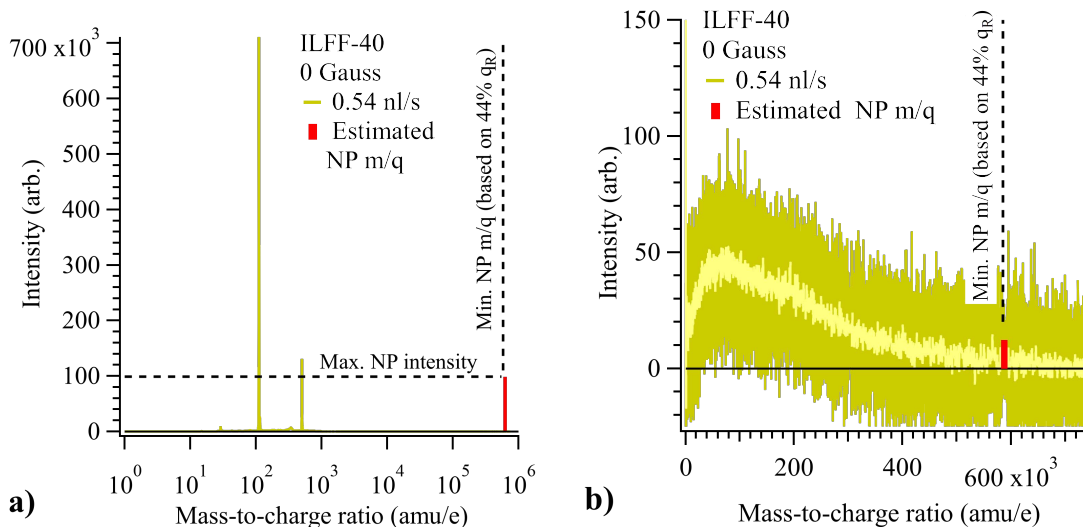
Figure 6.9. a) Summed TOF mass spectrum of CES running on ILFF at Q = 0.54 nl/s overlaid with the estimated NP peak (red) assuming its m/q was 585,400 amu/e with width of 1 amu/e. b) Summed TOF mass spectrum of CES running on ILFF at Q = 0.54 nl/s overlaid with an estimated NP distribution (red) given a center m/q of 585,400 and a width of 8,000 amu/e (±1 nm variation in NP diameter).

These observations were disconcerting as it meant that, if a NP distribution existed and had even a 1% variation in its m/q, it would be indistinguishable from the other artifacts/distributions in the summed TOF mass spectra. However, the estimation of an NP distribution does provide insight for future investigation; specifically, an initial estimation that can be used to develop a new TOF spectrometry technique to distinguish distributions with relatively small signals, or to determine if a different instrument exists that can separate/measure emitted NPs in an electrospray beam from similar sized droplet populations.

6.4.5. Magnetic Effect on Mass Spectra

The last goal of the mass spectrometry study was to measure how the magnetic field influenced the mass spectra collected from ILFF electrosprays emitted from the CES. As the electrospray from the CES operating on the ILFF propellants was shown to run in a

mix ion/droplet regime, one question would be, does the magnetic field change the primary

mass transport species, *i.e.* are 10 to 25-nm-radius droplets still the primary mass carrier of

the electrospray beam?

The only measured influenced the magnetic field had on the ion species was observed

in the ILFF-30 and ILFF-40 summed mass spectra. An example of the influence is shown

in the compiled summed mass spectra collected from both magnetic-field-free and

magnetically-stressed ILFF-30 electrosprays at flowrates of 0.54 nl/s, 0.72 nl/s, 0.90 nl/s

of Figure 6.10.
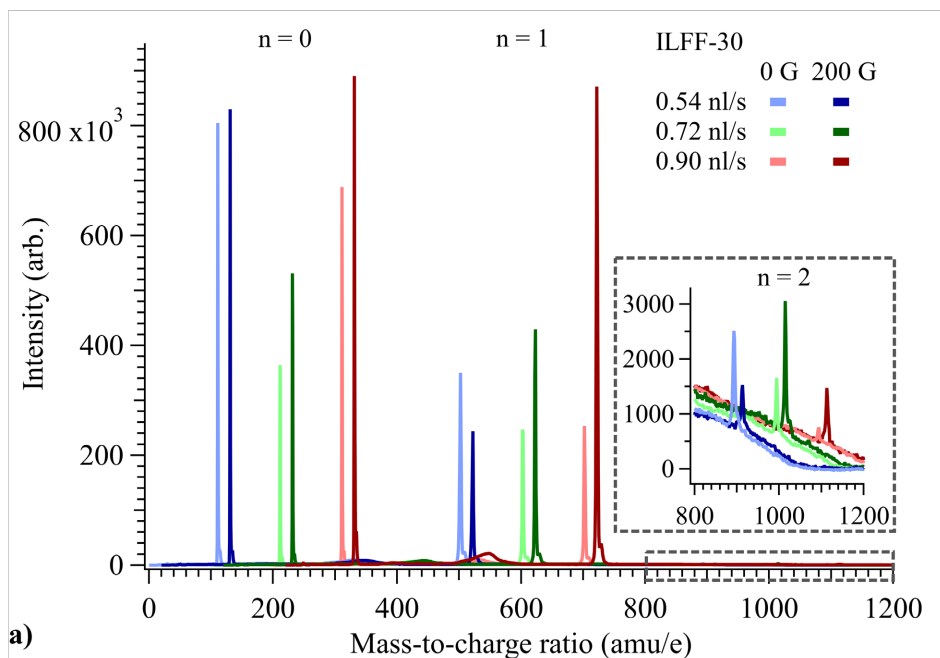
Figure 6.10. Mass spectra of an electrospray emitted from the CES using ILFF-30 under a zero and a 200-Gauss magnetic field for two flowrates. To ease comparison, the 0-Gauss spectra in both the main and inset plots have been shifted on the m/q-axis by artificially adding 100 and 200 amu/e to light-green and light-red traces, respectively, with an addition 20 amu/e adding to their 200-Gauss counterparts.

Following the procedure outlined in the previous section, the mass fractions were

calculated from spectra collected when using ILFF-30 and ILFF-40 propellants, and with

and without the 200-Gauss magnetic field, and are presented as histograms in Figure 6.11.

(The M_n/M_{Total} axis is $\log_{10}$ in a) and linear in b) but both include the same data). The mass fractions revealed several interesting observations: (1) the mass fraction of the ion species in magnetically-stressed electrosprays was still several orders of magnitude less than that of the droplet populations. (2) The particles estimated with radii between 10 and 25 nm still carried the largest fraction of mass, regardless of the magnetic stress state of the electrospray. (3) The combined mass fraction of the ion species and the combined mass fraction of the particles with estimated radii greater than 10 nm in a given electrospray increased after magnetic field application.

The last observation meant that the magnetic field had increased the mass flow of the largest m/q particles and lightest ion species; concurrently, the field also increased the intensity peaks of the lightest three ion species, Figure 6.10. The combined effect was disconcerting because the measured emission current of the source was reduced when the magnetic field was applied (Section 4.3.3.d.), however an increase in mass flow and intensity of the lightest ions species would suggest higher current in the electrospray beam. The mass spectra, and mass fractions thereof, were only collected in a small solid-angle of the center electrospray beam. In literature, the current density and mass flowrate change significantly at higher beam half-angles.[43] Therefore, any changes observed in the spectra due to the magnetic field may not appear to follow other magnetically-induced changes observed in electrospray operation.

The results suggest that while the magnetic field does have some influence on the composition of the electrospray, they are negligible when focusing on the general emission of the electrospray (ion/droplet mode, m/q range with highest mass fraction).
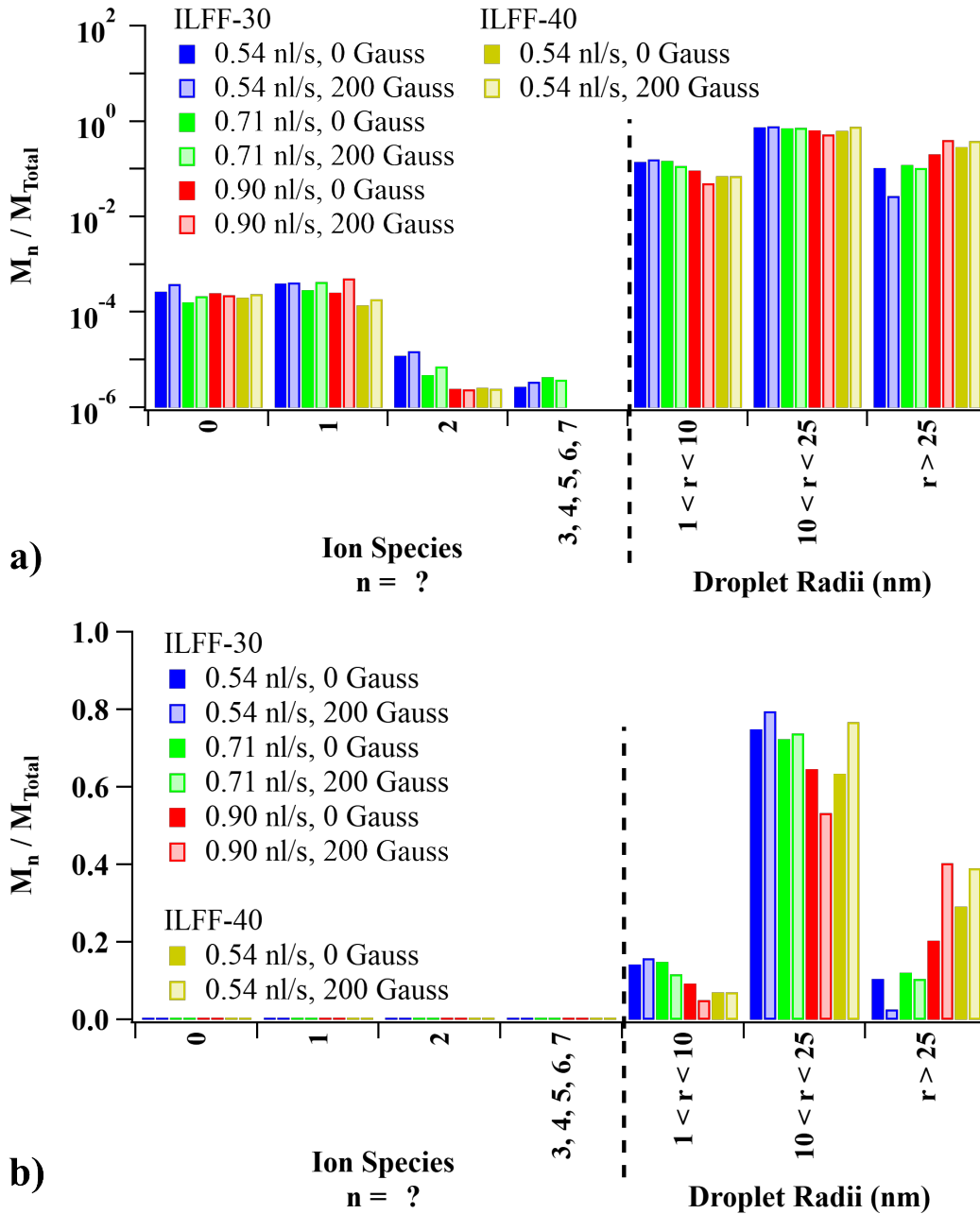
Figure 6.11. Mass fractions of all electrosprays running at a nominal 0.5 nl/s. The left axis is on a log scale to better illustrate the magnitude of the mass fraction for the ion species.

6.4.6. Other Observations on Ionic Liquid Ferrofluid Capillary Electrospray Mass Spectra

Apart from the conclusions on the composition of the electrospray, the influence, or lack thereof, on the composition due to the magnetic field, and the absence of NP artifacts in the summed mass spectra, there were several observations on the masses within the summed TOF mass spectra that warrant some discussion.

6.4.6.a. Appearance of Low Mass-to-Charge Products (Ions)

The number of sequential cation species that existed in the summed mass spectra, N^+, was fewer for propellants with higher weight-percent nanoparticles, Table 6.2. The largest measured ion species in each spectrum was N^+ minus 1, *i.e.* for neat IL operating at a nominal 0.5 nl/s, $N^+ = 13$ which meant the largest ion species was n = 12.

Table 6.2. Tabulation of the number of cation species present in summed time-of-flight mass spectra for five propellants.

		Neat IL	ILFF-10	ILFF-20	ILFF-30	ILFF-40
		Number of Cation Species (N^+)				
Nominal Flowrate (nl/s)	0.5	13	8	5	5	3
	0.75		7	6	5	
	1	12	7	5	3	

The extinction of ion species between neat IL and ILFF-40 electrosprays suggests that the NPs enacted a change in the electrospray emission process, which could have reduced the ability for the CES to produce heavier ion species. In literature, species present in IL electrosprays appear to be a function of flowrate, extraction field, and/or thermal energy of the emitted species.[58, 134] The dependence on flowrate could be a factor in the observed ion species; the minimum operable flowrates for ILFFs was tied to their wt% of NPs. For

ILFF-30 the minimum flowrate was much nearly double that of neat IL. In the examination of summed mass spectra collected at minimum flowrates of neat IL and ILFF-30 of Appendix G., the five lightest cation species were observed in spectra for both propellants.

In an molecular dynamics study that energy of the ion species was shown to be directly related to the survival time for heavier ions species (*i.e.* time prior to dissociation into lighter ions species);[135] this would mean that heavier ions may not have been included summed TOF mass spectra in this study, where the cutoff of minimum ion energy was 550eV (Appendix I). Results from the beam energy study on ILFF-30 and ILFF-40 (Section 5.3.5.) showed that a fraction of the electrospray had an energy less than 50 percent of the extraction potential, which complements this theory. However, an angular-resolved mass spectrum of ILFF electrosprays, which included summed spectra for the entire range of energy defects (0 eV to 900 eV) would be necessary to completely determine the driving factor(s) for the absence of ion species in ILFF electrosprays that exist in neat IL electrosprays.

6.4.6.b. Magnetic Influence on Ion Peak Intensity

Another observation came when comparing the summed mass spectra of magnetic-field-free to magnetically-stressed electrosprays, specifically those using ILFF-30 and ILFF-40 propellants. The application of a magnetic stress enacted a change in the magnitude of the intensity peaks for three lightest ions species, Figure 6.12. In the figure, the intensity axis is a $\log_{10}$ scale for clarity. The plots show that only electrosprays operating with higher flowrates of ILFF-30 were influenced by the magnetic stress, which increased in the peak intensities of all three of the $n = 1$ and $n = 2$ ion species. Similarly,

the magnetic stress also increased the n = 1 ion peak intensity of the ILFF-40 summed TOF mass spectrum, Figure 6.12.d). While the observation was interesting as it showed further influence of the magnetic field on an operating ILFF electrospray, the effect was only significant for a few combinations of propellant/operating conditions, and therefore was not considered an overall trend of the magnetic influence on an ILFF electrospray.
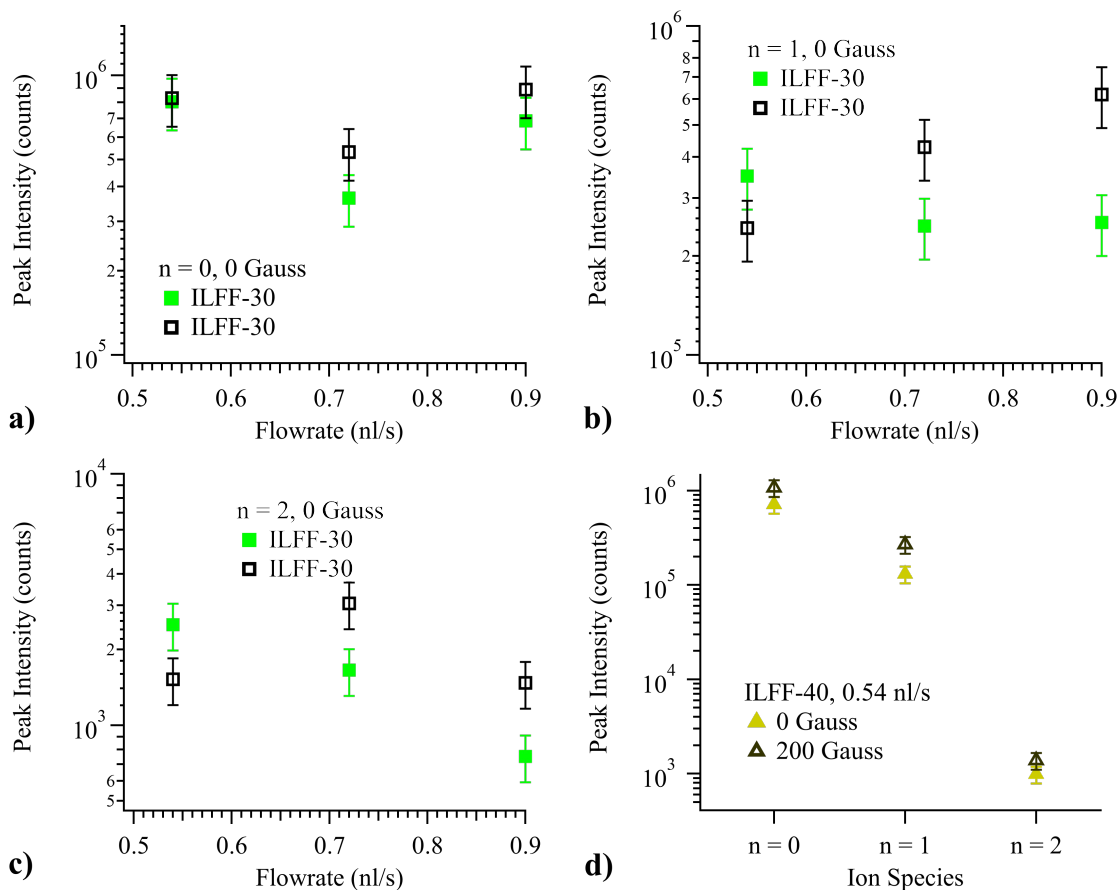
Figure 6.12. Peak intensity of cation species a) n = 0, b) n = 1, c) n = 2. d) the current fraction of the summed TOF mass spectra for the four ILFF propellants.

6.4.6.c. Distributions in High Mass-to-Charge Range (Droplets)

There were a couple observations made during the analysis of the high m/q range of the summed TOF mass spectra that warrant discussion. One was during the examination of

179

the energy dependence of distributions in the large m/q range. An inspection of individual spectra collected at different energy defects used to create summed TOF mass spectrum was done graphically, Figure 6.13. The large m/q range of summed mass spectra from neat IL and ILFF-10 electrosprays are shown in Figure 6.13.a).
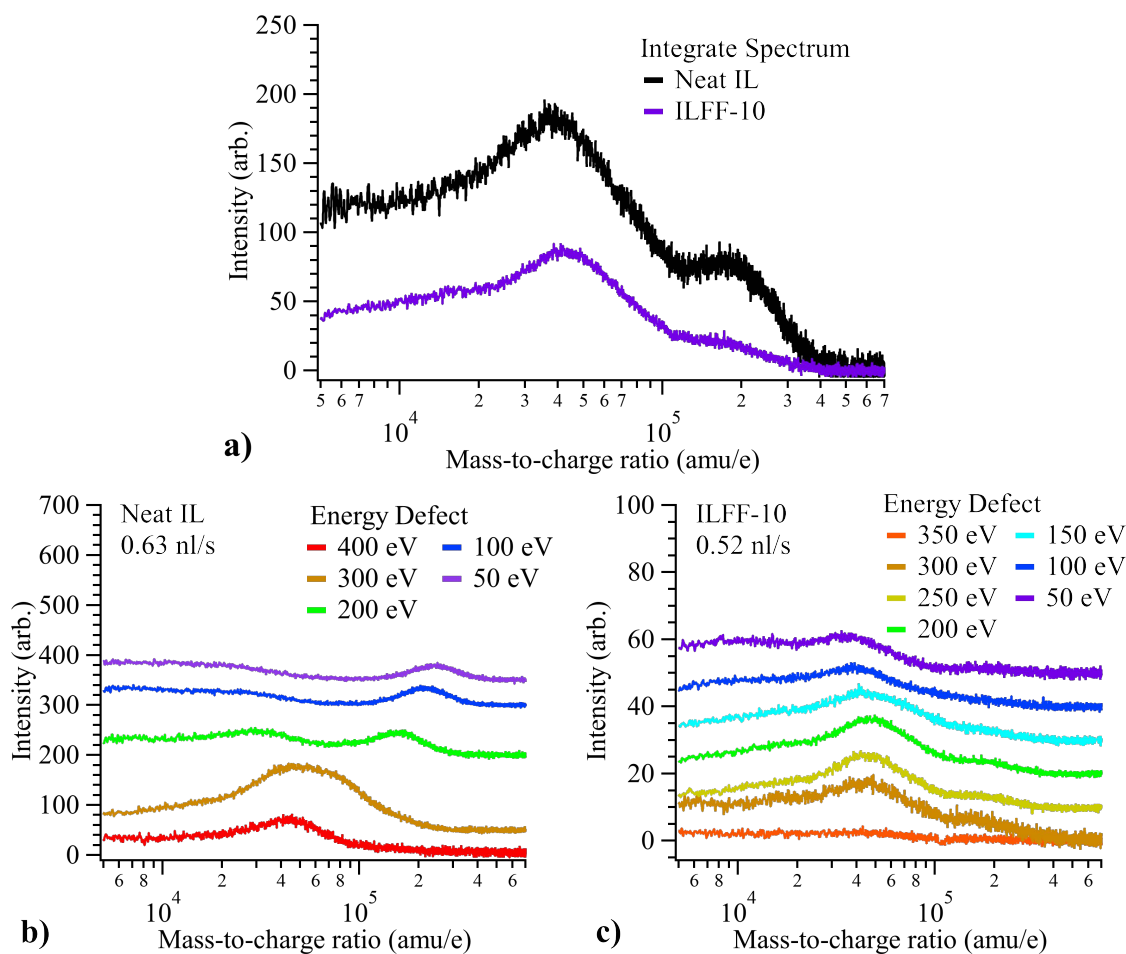
Figure 6.13. a) Summed TOF mass spectra from CES running on neat IL and ILFF-20 at $Q = 0.63$ nl/s and 0.52 nl/s, respectively. b) Individual spectra at different energy defects which sum to the neat IL summed TOF mass spectra in a. c) Individual spectra which sum to the ILFF-10 summed TOF mass spectra in a. The intensity-axis was incrementally shifted by arbitrary amounts to provide better clarity between spectra.

Two distributions appeared in both curves and, while the intensity of the distributions was significant greater in the neat IL spectra than ILFF-10, both were at approximately the same locations (most probable m/q at ~40,000 amu/e and ~150,000 amu/e). This suggested

180

that the individual spectra at each energy defect would appear similar, albeit at different intensities. However, this was not the case as Figure 6.13.b) and c) illustrates. In the two plots, which present the individual spectra that comprised the summed TOF mass spectra of Figure 6.13.a), the data that formed the two distributions of the summed TOF mass spectra differed substantially. Specifically, the neat IL summed mass spectrum was comprised of a spectrum that had only a single distribution at an energy defect of 300 eV and 400-eV centered at 45,000 amu/e, but split into two distributions the lower energy defect spectra, which were centered at 20,000 amu/e and 240,000 amu/e in the 50-eV spectrum (a drop of 60-percent and an increase of 380-percent, respectively). This analysis aligned with observations by Miller *et al.* when spraying EMIM-NTf2 and BMIM-DCA propellants at flowrates between 0.09 and 2.35 nl/s.[58] They concluded that the observed shift of the distributions was a consequences of a single droplet species (same size and mass) having a range of charge that fall within 0 to 100% of the Rayleigh limit, (2.13), and that the droplet charge correlated to the droplet's birth location. Therefore, the shift in the m/q was a function of the energy defect of the droplet.

However, the spectra that comprised the ILFF-10 summed mass spectrum differed from the neat IL. All the individual spectra contained two distributions which were less dependent on the energy defect at which the spectrum was collected; *e.g.* between the spectrum collected for an energy defect of 300 eV and the spectrum for 50 eV the center m/q of the lighter distribution dropped 20-percent, while the center m/q of the heavier distribution increased in by 20-percent. The noticeable difference in the individual spectra of an ILFF-10 electrospray to those of a neat IL electrospray was unexpected given the relatively small amount of NPs (1.6 %v/v) in the propellant. The insensitivity of the

individual spectra to the energy defect of the electrospray also suggested that the estimated droplets populations were born at relatively the same emission location. Therefore, the NPs must influence the with the emission process of the IL droplet distributions, though the mechanism was not determined in this research.

A final observation on the high m/q range came when during the attempt to reconcile the individual distributions that existed in the summed TOF mass spectra. This was completed by creating a set of M-B distributions that fit the curve of the summed mass spectra for the m/q range of 10,000 to 750,000 amu/e; a similar process was conducted by Miller *et al* on summed mass spectra of EMIM-NTf2 and EMIM-DCA.[58] The summed mass spectrum from the CES running on neat IL at 0.705 nl/s will be used as an example, with the final result in Figure 6.14. (also shown previously in Figure 6.6.)

The fits were composed of arbitrarily scaled M-B distributions. This type of distribution was used due to the assumed statistical nature of the m/q of the emitted particles. Two distributions were chosen initially based on the two distributions observed in Figure 6.13.; additional distributions were added if necessary to fit the data while remaining physically possible (i.e. distributions below m/q of 10,000 amu/e were considered to be part of a plateau comprised of multiply charge ions or ions with varying energy).[58] In the case of the neat IL spectrum in Figure 6.14. a third distribution was necessary to fit the data. The M-B distributions were centered at m/q of 32,000, 59,000, and 172,000 amu/e.
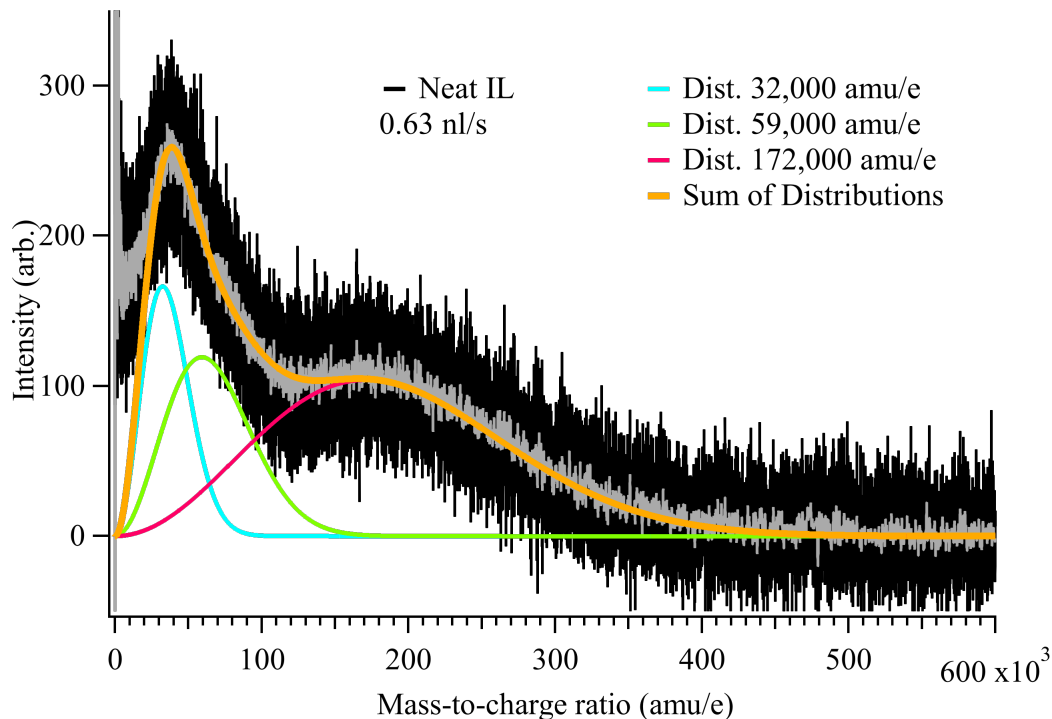
Figure 6.14. Maxwell-Boltzmann fits to the large m/q range of the CES running on neat IL at 0.63 nl/s. The M-B fits represent potential droplet distributions within the electrospray beam. The sum of all the M-B fits was determined as well (orange curve).

The interesting finding from the process of fitting M-B distributions to the neat IL summed TOF mass spectra was that only three distributions were needed to form a summed curve which fit the spectra from 20,000 to 700,000 amu/e (orange curve of Figure 6.14.). The analysis was repeated for spectra collected from electrosprays of ILFF-10, ILFF-20, ILFF-30, and ILFF-40 propellants all at a nominal flowrate of 0.5 nl/s to show that a similar set of M-B distributions also summed to a curve that expressed the data well; the graphical results are presented in Figure 6.15. Interestingly, the spectra from ILFF-40 electrospray required a fourth distribution to properly fit the data, which could either be another droplet population or the hypothetical NP distribution. However, as this fourth distribution was buried in the noise of the spectra, illustrated in Figure 6.15.d), there was no conclusive evidence that this distribution was real.

183
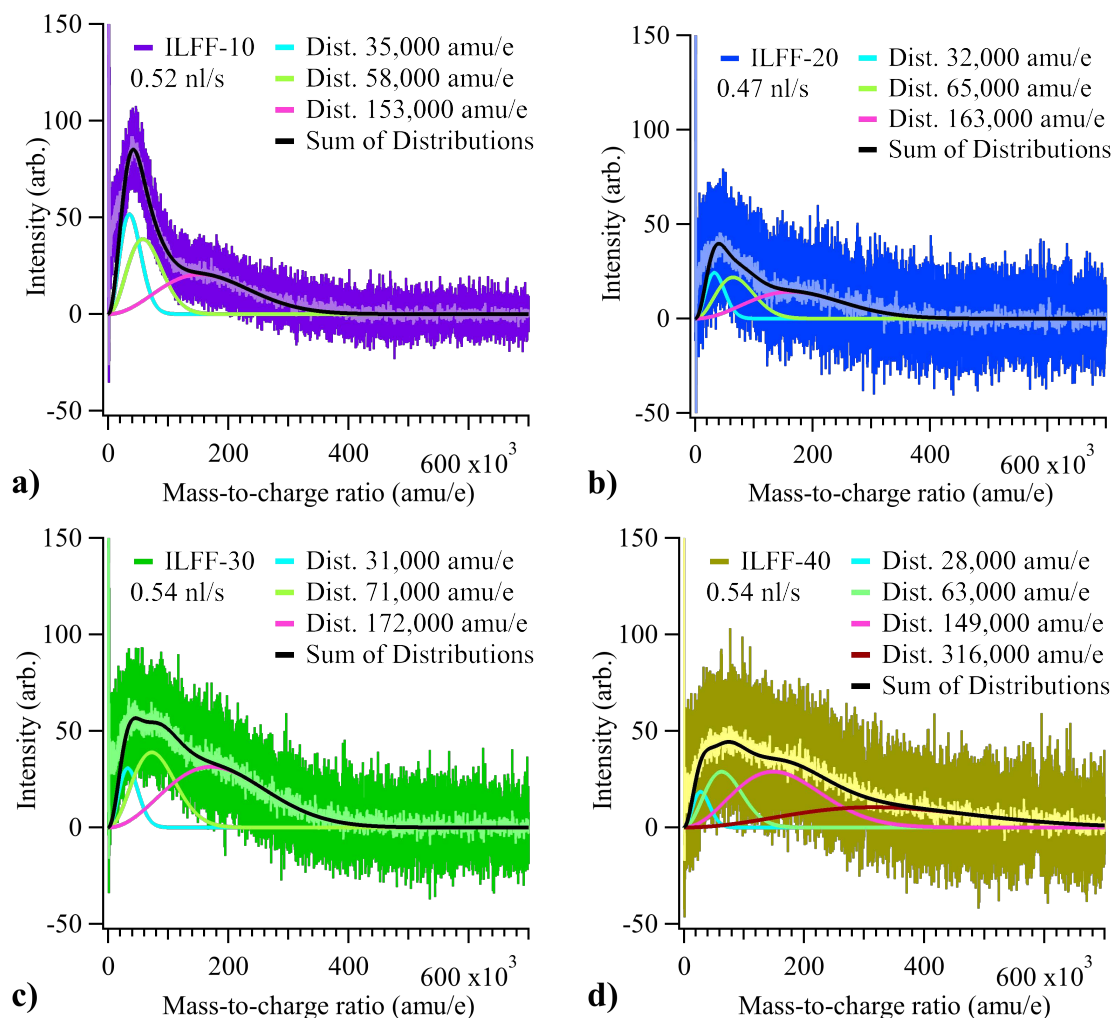
Figure 6.15. Maxwell-Boltzmann fits to the large m/q range of the CES running on a) ILFF-10 at Q = 0.52 nl/s, b) ILFF-20 at Q = 0.47 nl/s, c) ILFF-30 at Q = 0.54 nl/s and d) ILFF-40 at Q = 0.54. The M-B fits represent potential droplet distributions within the electrospray beam. The light-purple, light-blue, light-green and light-yellow curves of a, b, c, and d, respectively are the smoothed data.

The droplets distributions centered at approximately 32,000 and 172,000 amu/e that appear in summed mass spectra from all propellants were similar to those observed by Miller *et al.*[58] If the center m/q of each distribution was assigned a charge of 0.44 times its Rayleigh limit, $q_D^{0.44}$, the radius, R_D, can be found via (6.2). Here ρ and γ are the density and surface tension of EMIM-NTf2, respectively.

$$R_D = \left(\frac{m}{q_D^{0.44}} \frac{6*0.44(\varepsilon_0\gamma)^{1/2}}{\rho} \right)^{2/3} \tag{6.2}$$

The R_D for each of three droplet distributions fit to the neat IL summed mass spectra were determined as 4.8, 7.1, and 14.4 nm, which match well with Miller et al. findings using the same IL propellant. Furthermore, the jet diameter estimated via the definition $R_j = 0.2(Q\varepsilon\varepsilon_0/K)^{1/3}$ defined by the same group, was 8.4nm; or 1.71 times the largest R_D determined from the M-B fits, which also aligns with the $R_D = 1.69\,R_j$ from literature. (In the determination of jet radius, Q, ε, and K were 0.63 nl/s, 12, and 0.91 S/m respectively). The same approach was taken for each of the M-B fits to the ILFF spectra of Figure 6.15. and the results, combined with the estimated R_D of the neat IL, are in Table 6.3. The results show that despite the addition of NPs, the ILFF electrosprays still appear to have similar droplet distributions as an electrospray using their carrier propellant.

Table 6.3. Droplet radii of neat IL and ILFF electrosprays running at a nominal $Q = 0.5$ nl/s

	Droplet Distribution R_D (nm)			
Propellant	1	2	3	4
Neat IL	4.8	7.1	14.4	
ILFF-10	5.0	7.1	13.4	
ILFF-20	4.7	7.5	14.0	
ILFF-30	4.8	8.1	14.4	
ILFF-40	4.3	7.4	13.1	21.7

The above analysis showed a potential method to fit the m/q distributions of droplets in neat IL and ILFF electrosprays, and one to determine an estimated droplet size for the most probable m/q of the distributions; however, the physical reason for distribution width was not determined. Also, because the TOF-MS only differentiates based on m/q, this

width could have come from either varying size, varying charge, or a combination of the two, and cannot be separated. To postulate that a droplet in the distribution maintained a charge above 50 percent of the Rayleigh limit is unwarranted, as noted in literature; also noted in literature was the large range of size for satellite droplets (*i.e.* those not formed directly from jet breakup). Both support the conclusion (that this study also maintains) that the distribution width of electrosprays comes from varying charge and size of polydisperse droplets.

6.5. Conclusions: Mass Spectrometry of Ionic Liquid Ferrofluid Capillary Electrospray

The goals of this chapter were to measure the emitted species (ions and droplets) within the mass spectra of four ILFF propellants and compare it to the emitted species of the control neat IL electrospray, to observe and measure the magnetic NPs within the electrospray beam using TOF mass spectrometry, and to measure the influence of a magnetic field on the emitted species within the mass spectra of the ILFF propellants.

The CES running on all the propellants (neat IL and four ILFF) was shown to operate in a mixed ion/droplet mode. The mass fraction of each of the electrospray was heavily concentrated in droplets with estimated droplet radii between 10-25 nm. As such the NPs were concluded not to be a factor in the measured mass flowrate in the summed TOF mass spectra.

In fact, detection of the NP proved to be less intuitive than simply extending the collection range of the TOF mass spectrometer. The size of the NP emitted from the electrospray was hypothesized to be approximately 30 nm in radius, assuming a 15-nm

layer of IL coated the surface of the NP and provided the charge. The estimated center m/q of the NP distribution (most probable m/q) was determined through Rayleigh limit criterion as 585,000 amu/e; however, no distributions were observed in any of the ILFF propellants that fit this assumption. This may be attributed to the potentially low intensity of the distribution as NP was likely emitted only once for every ~100 droplets (based on % v/v of NPs in the propellant). Therefore, if future investigations wish to achieve this measurement they will need to determine a better approach to collect the low signal of the potential NP distribution and distinguish it from background noise.

Lastly, the magnetic field was less influential on the summed mass spectra of the ILFF electrosprays, and was only significant on the spectra collected from ILFF-30 and ILFF-40 electrosprays. Specifically, the spectra collected from the magnetically-stressed electrosprays had changed the relative intensity of the ion species. There didn't appear to be a trend correlated the change to flowrate or NPs, though all electrosprays (except the ILFF-30 electrospray operating at its lowest tested flowrate) increased the relative intensity of heavier ion species. Lastly, the large m/q distribution were negligibly influenced by the magnetic field. Overall the combined analyses of the summed mass spectra of magnetically-stressed electrosprays suggest that the magnetic field could potentially increase the average m/q of the center of the electrospray beam, however, this was only achievable for certain propellants and (Q, *Vext*) settings. As such, if a higher average m/q in an electrospray was desired, a more reasonable approach would be increase the NPs in the propellant or increase flowrate of the of the propellant to the source.

Chapter 7

Electrospray from a Single Peak Rosensweig

Instability

The development and testing of the Rosensweig peak electrospray source (RP-ES) was conducted to understand how removal of the backbone structure of traditional electrospray device affects the emission characteristics of an electrospray from a single emitter. The following chapter details the motivation and goal of the experiments using the RP-ES followed by a discussion of the results and comparison to two other electrospray sources: the CES and a solid-needle electrospray source (SN-ES).

7.1. Motivation and Goal

The driving motivation of the research of this dissertation revolved around the new ILFF propellant and its ability be both the backbone structure that resembled emitters used for electrospray ionization and the electrospraying fluid simply through the concurrent application of magnetic and electric fields. In the proceeding chapters, the unique properties of the ILFF propellant (NPs and magnetic susceptibility) were individually examined by electrospraying the propellant from a magnetically-stressed capillary source. However, the prospect of using the ILFF as both structure and propellant would answer a new set of research questions revolved around the concept of combined electric and magnetic field electrospraying. Specifically, the motivation of this research revolved

189

around the three questions: (1) How does an electrospray from an electrically stressed, magnetically-induced ILFF peak operate (*i.e.* emission current and extraction potential), and how does this differ from electrospray emitted from other types of sources (*e.g.* electrically stressed and induced pressure-driven capillary emitter and/or neat IL needle emitter)? (2) Does the composition of particles emitted from the magnetically-induced ILFF peak differ from those emitted from other types of sources? (3) Does variation in the magnetic field used to create an ILFF peak change the operational parameters or composition of the particles emitted from the, magnetically-induced ILFF peak?

This chapter attempts to answers these three questions through the completion of two experiments on the RP-ES, and one on a neat IL SN-ES. The SN-ES was built and tested in this study to provide a second electrospray source to which the RP-ES was compared. The SN-ES differs from the CES in several areas, but the primary focus of the study was to compare the emission products of the two sources to those from the RP-ES. In this regard, needle sources are known to emit lighter m/q products including only the lightest two or three ion species and usually no droplets; this contrasts with capillary sources which emit up to a dozen ion species and several droplet populations, as Chapter 6 established.

The goal of the experiments was three-fold, 1) to determine the operating emission current and extraction potential of the RP-ES while varying the magnetic field strength used induce the Rosensweig peak. 2) to determine the mass-to-charge composition of the emission products in the center of the electrospray beam emitted from the RP-ES and SN-ES, 3) compare RP-ES operating parameters and mass spectra to the operating

parameters and spectra from the CES and SN-ES to define the differences between the Rosensweig source and two prevailing electrospray sources.

7.2. Apparatus and Procedure

The apparatus and experimental procedures for the research based on the RP-ES are described below. Two sources were used for these experiments which are detailed first. The diagnostic and facilities and the experimental procedures used to characterize the RP-ES and measure the mass composition of both the RP-ES and the SN-ES follow.

7.2.1. Rosensweig Peak Electrospray Source

The RP-ES apparatus used to produce and measure electrospray from a single Rosensweig instability peak is shown in Figure 7.1. The apparatus is comprised of five main components; the extractor plate, the collector plate, the isolation block, the ILFF reservoir, and the neodymium magnets. The extractor plate is stainless-steel and has a 1-mm aperture. It was offset from the reservoir surface by 3 mm. The collector plate (not shown) was only used in the emission experiments in the UHV facility, and is a stainless-steel plate offset 10 mm from the extractor plate. The isolation block was machined from PTFE and provided isolation between the reservoir, which is biased during testing, and the magnets and the testing chamber.
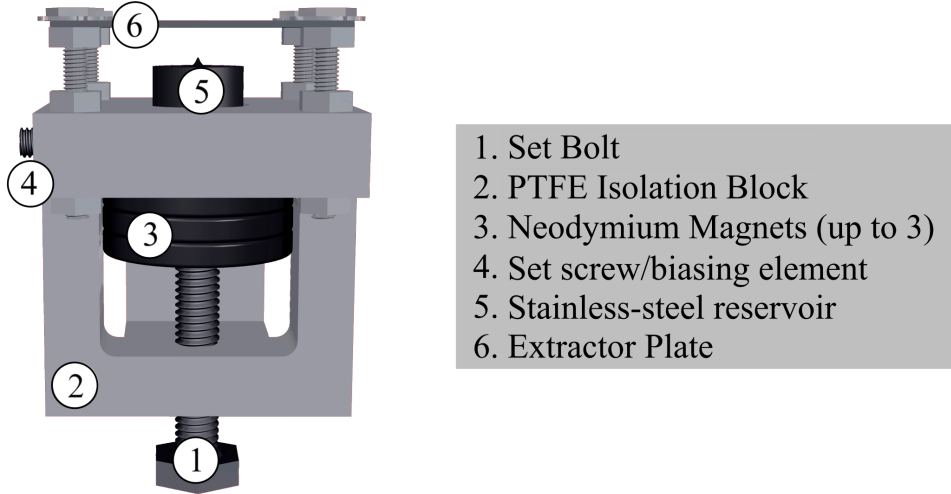
Figure 7.1. Rosensweig electrospray apparatus for TOF facility experiments with components denoted.

The reservoir is an important component of the RP-ES as required a geometry that would both hold the ILFF and limit the Rosensweig instability to one peak. To form a single peak of the ILFF in the reservoir must be less than critical wavelength of the Rosensweig instability. The critical wavelength, $\lambda_{c,FF}$, was defined as the wavelength beyond which one peak splits into two peaks. Here, $\lambda_{c,FF}$ was that determined by Rupp through his analysis of a scenario where the non-uniform magnetic field acting on a flat ferrofluid becomes the dominant body force (over gravity),[136] and was defined as (7.1). Meyer empirically confirmed this hypothesized capillary wavelength using EFH1 Ferrofluids.

$$\lambda_{c,FF} = 2\pi\sqrt{\frac{\gamma}{M\nabla B}} \approx 2\pi\sqrt{\frac{\gamma}{M\frac{d}{dz}(B)}} \tag{7.1}$$

The term in the denominator of the right-side of (7.1) was estimated through the measurement of magnetic field strength at two points, one directly at, and a second 1.54-mm above the surface of a magnetic fluid. M was found using the magnetization

curves for NJ397074 performed by the University of Sydney (Appendix L.). For the magnetic fields used in these experiments (333.9 Gauss to 690.4 Gauss), $\lambda_{c,FF}$ was 2.53 mm to 3.37 mm. As the reservoir needed to remain less than 2.53 mm, the diameter of the reservoir, d_{res}, was approximately $0.8\lambda_{c,FF}$, Figure 7.2.

The final design was a 2-mm-diameter, 4-mm-deep hole was machined into a stainless-steel cylinder to create the reservoir. The reservoir hole is also chamfered at the top face to reduce boundary effects on the Rosensweig peak. The RP-ES was subjected to varying magnetic field strengths to observe any resulting effects. One, two, and three 25.4-mm-diameter, N52-grade, neodymium permanent magnets were placed behind the ILFF reservoir to produce varying magnetic fields strengths at the reservoir surface (measured with no fluid in the reservoir) of 333.9, 520.5, and 690.4 Gauss, respectively.
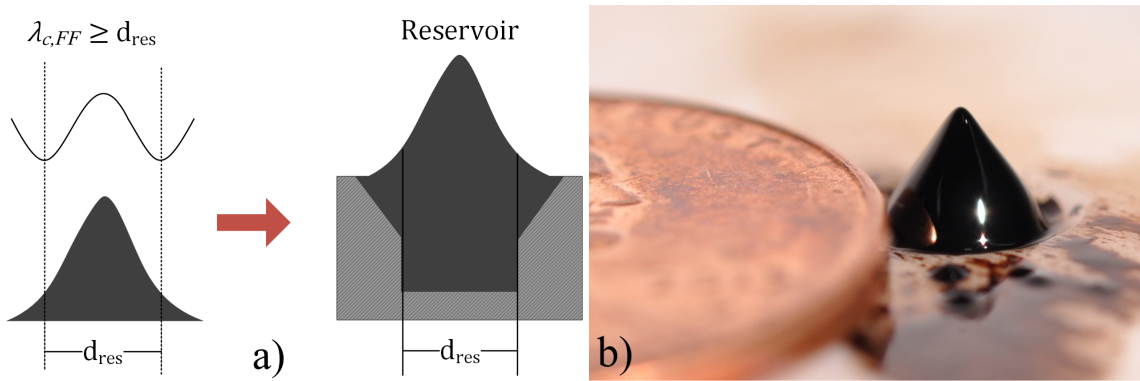
Figure 7.2. ILFF reservoir design for the RP-ES. a) Illustration on how the diameter of the reservoir was defined by the critical wavelength of the Rosensweig instability. b) Single Rosensweig peak formed in reservoir using 520.5-Gauss magnetic field.

7.2.2. Solid Needle Emitter Electrospray Source Apparatus

The SN-ES was built by the team at the AFRL and is shown in Figure 7.3. The source is comprised of a chemically etched tungsten needle with a tip radius of approximately 5

μm. A cross bar is welded onto the shaft of the needle to provide support for the liquid droplet. The needle is inserted into a notched copper cylinder and secured using a copper piece and screws. The source is fit into a rotatable stage that has a fixed extractor plate approximately 0.5 mm downstream from the needle apex. The rotatable stage allowed for collection of the electrospray beam from off-axis angles to acquire spatially resolved measurements of the beam.

1. Source Holder
2. Copper Cylinder Holder
3. Isolation Rods
4. Tungsten Needle
5. Ionic Liquid
6. Crossbar-needle Junction
7. Extraction Plate
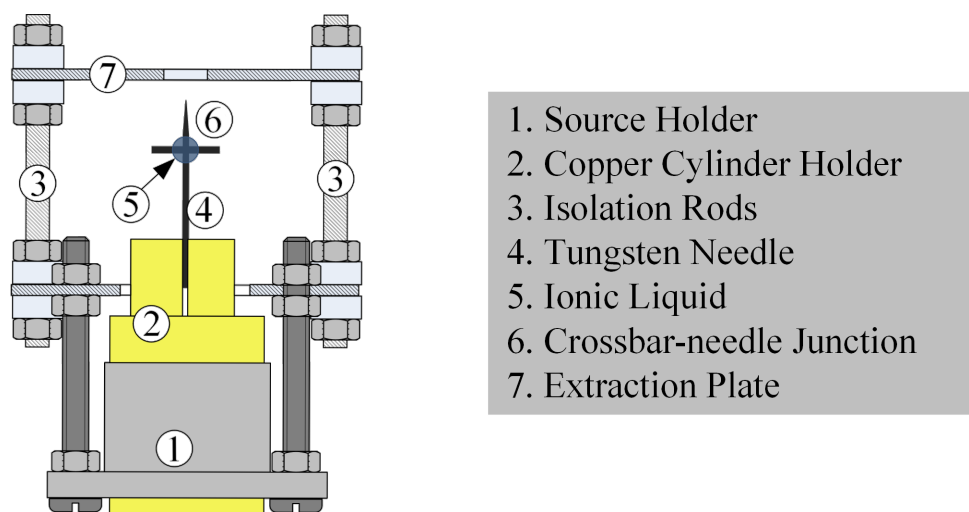
Figure 7.3. SN-ES apparatus with components denoted.

7.2.3. Experiments

The study present in this chapter had three experiments. One experiment was done to characterize the RP-ES emission current, extraction voltage and average mass-to-charge of the emitted beam. This was followed by another experiment that used the AFRL TOF-MS to collect mass spectra from the RP-ES. The final experiment also used the TOF-MS and was done to collect mass spectra from neat IL needle electrospray source. The procedures for each are presented below.

7.2.4. Procedure for Rosensweig Peak Electrospray Source Characterization

An experiment to measure the electrospray characteristics of emission current and mass flowrate of the RP-ES was conducted in the UHV facility at Michigan Tech, ERP-1, while an experiment to measure the mass-flowrate and current density was conducted in the TOF-MS at AFRL, ERP-2. The following outlines the procedures used to complete the experiments. The preparation procedure included cleaning all components via sonication in ethanol. After cleaning, the ILFF reservoir was secured in the PTFE block and one, two, or three permanent magnets were inserted into the block to produce the desired magnetic field strength. Next the ILFF was dispensed into the reservoir via a syringe pump. The volume of ILFF used in each test was held at a constant 20 μL. The extractor plate was placed at approximately 1.5 mm from the apex the Rosensweig instability peak prior to emission and the aperture was centered on the peak axis.

Once the source was assembled, it was either placed into the UHV facility as shown in Figure 7.4. (ERP-1), or it was attached to a lens stack and then placed into the TOF-MS source chamber (ERP-2). In ERP-1, the extractor plate was biased using a 0.5 Hz square wave overlaid on a two-minute ramp from ground to the maximum peak voltage and back to ground. The current on the collector plate was recorded during the entire ramp. In ERP-2, a 0.5-Hz square wave with constant amplitude of ±800 V was applied to the reservoir, and a second 0.5-Hz square wave with varying peak-to-peak amplitude was applied to the extractor plate. The two square waves were 180 degrees out of phase. The QCM was placed downstream of the source to acquire start-up mass measurements, after which the Faraday cup was moved into the downstream position to collect current.
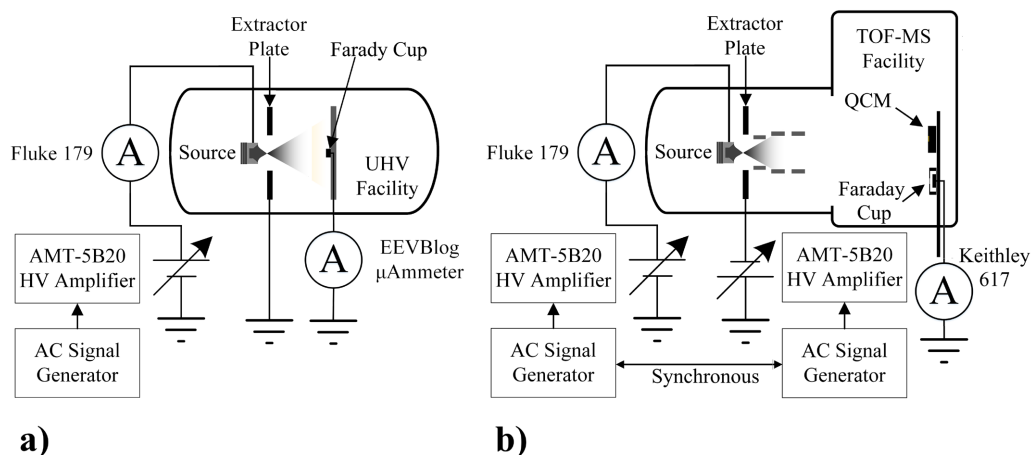
Figure 7.4. a) Setup for the RP-ES characterization experiment in the UHV Facility. b) Setup for the RP-ES and SN-ES experiments in the AFRL TOF-MS Facility

7.2.5. Procedure to collect TOF Mass Spectra from the Rosensweig Peak Electrospray Source

TOF spectra were collected for an electrospray from RP-ES using the following procedure. The preparation procedure was identical to ERP-1 and ERP-2 experiments described in 7.2.4 A 0.5-Hz square wave with constant amplitude of ±800 V was applied to the reservoir; a second 0.5-Hz square wave with varying peak-to-peak amplitude was applied to the extractor plate. The two square waves were 180 degrees out of phase. Typical starting voltages (difference between needle and extractor potentials) ranged from |2400 V| to |3000 V|, depending on the magnetic field strength applied to the ILFF. The reservoir bias with respect to ground provided the maximum mean kinetic energy of the cations and anions of +800 eV/q and -800 eV/q, respectively, although the kinetic energy has observed to be significantly.[43]

The orthogonal extraction used to send the emission products of the electrospray beam into the TOF flight tube was described in 3.6. For this experiment pulse width and magnitude were 2.5 µs and 240 V, respectively. After travelling through the flight tube,

196

cations were detected by an MCP with a first stage voltage of -2000 V (for anion detection a +3900 V was split between the stages of the MCP; see Section 7.3.2. for a detailed description). The MCP signal was directed into two amplification stages of a 300 MHz Stanford Research pre-amplifier and then read by a multichannel scaler or a TOF card to produce TOF spectra.

7.2.6. Procedure to collect TOF Mass Spectra from the Solid Needle Electrospray Source

The following steps were taken for the electrospray experiments using the SN-ES. First, the needle of the source was cleaned and inserted into the copper needle holder. Pure IL was applied using a syringe such that the needle was wetted to the apex and a drop was held in the crossbar-needle junction (see Figure 7.3.). The needle and copper holder were then placed in the rotatable stage, which was affixed to the lens stack, and positioned such that the apex of the needle was centered with the aperture of the extractor plate. The assembly was then placed into the TOF source chamber and the Faraday cup positioned downstream of the source. The needle source was run at the same operating parameters as the RP-ES. Typical starting voltages for the needle source were |1700 V|. Once a stable emission current of 1-2 nA was observed on the Faraday cup, a spectrum was collected via the procedure described in 7.2.5.

7.3. Results from Experiment

Results of the experiment include the both emission characteristics, cation and anion mass spectra, and QCM measurements for three different magnetic field strengths from the RP-ES, and cation and anion mass spectra from the SN-ES.

7.3.1. Characteristics of a Rosensweig Instability Peak Source

The RP-ES was observed to have four modes of electrospray emission; one that was transient (designated 'transient-emission' in later sections), which began at the start of each emission test (start refers to either the first run with new ILFF in reservoir or a change between DC and AC operation) and would last for approximately five minutes, and two at which an electrospray could be emitted continuously, (designated 'continuous-emission' in later sections). The transient-emission mode would operate with an emission current range of 20-30 µA until it transitioned to either of the two continuous-emission modes. The two continuous-emission modes are termed the low-current mode and high-current mode, based on their respective operating emission currents of 1-10 µA and 30-80 µA. To move between the two continuous-emission modes, 50-100 V was either applied or removed from the extraction voltage. A fourth, unstable, mode also existed if the RP-ES was operated at emission current greater than 100 µA, thus it was termed the very-high-current-mode. This mode was avoided during operation as it would lead to exceedingly long filamentary jets from the ILFF that bridged the gap between reservoir and extractor plate, shorting the emission. However, it did prove to be a mode in which high mass accumulation rates existed.

The continuous-emission modes were documented in the emission tests in the UHV facility. Figure 7.5 a) shows the I-V telemetry of the RP-ES during normal startup. The transition between the low-current and transient-current modes was seen in the collected current, Figure 7.5.b).
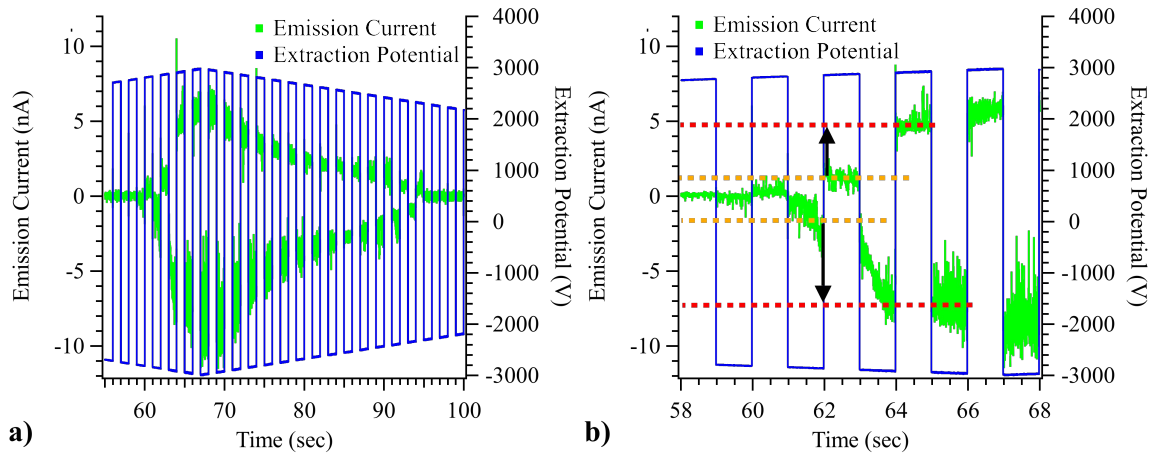
Figure 7.5. a) Telemetry of ILFF electrospray from Rosensweig instability source under 333.9 Gauss. The dashed lines show the transition of from low-current mode (orange lines at 1.2 nA and -1.3 nA) to transient-current mode (pink lines at 4.7 nA and -6.5 nA) through an increase of |50 V| in extraction voltage.

The arrows between the orange and pink dashed lines in Figure 7.5.b) represent the transition between the lower currents of low-current mode and the higher currents of transient-emission mode. Figure 7.6. illustrates that the transition in between low- and high-current modes is associated with a change in the general shape of the Rosensweig peak, as well as a change in the apex shape, illustrated by inset images of Figure 7.6.a) and b).
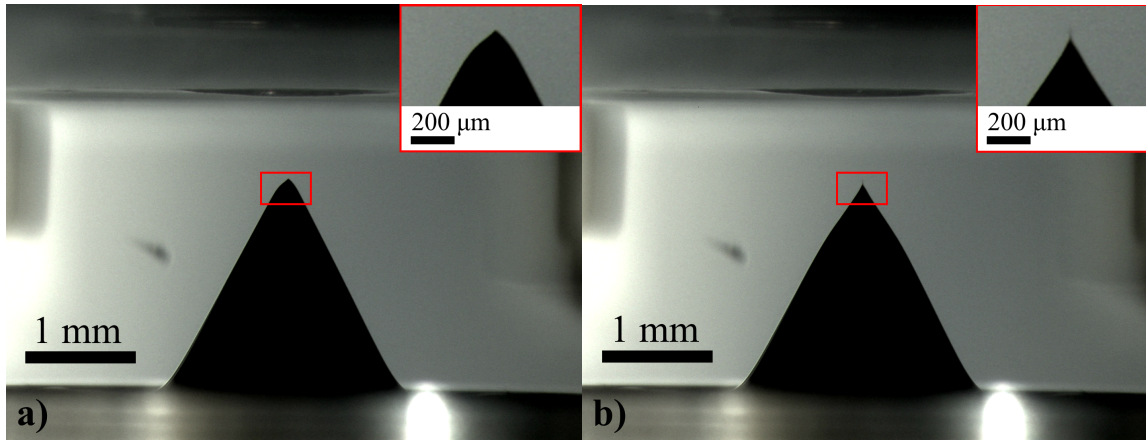
Figure 7.6. Images capturing the operation of an ILFF electrospray emitted from a RP-ES in a) low-current mode of operation, and b) high-current mode of operation.

Images captured during high-current continuous-emission of the RP-ES under four magnetic field strengths provides an illustration of the effect magnetic field has on the emission site. Specifically, Figure 7.7. captures progression of a single Rosensweig peak splitting into two peaks via the addition of permanent magnets. The critical wavelength, $\lambda_{c,FF}$, for the peak shown in Figure 7.7.d) as calculated by (7.1) was 2.36 mm while the ILFF reservoir is 2 mm in diameter.
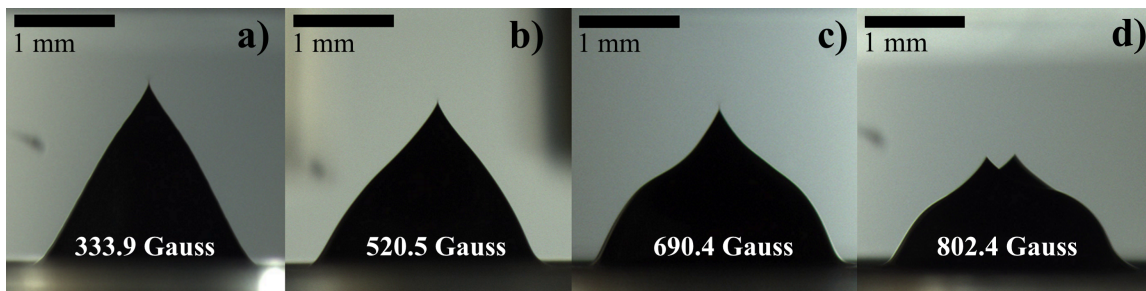
Figure 7.7. Tip shape under varying magnetic field strengths. The critical wavelength for peak splitting is a) 3.37 mm, b) 2.84 mm, c) 2.54 mm, d) 2.36 mm. In each image, the initial fluid volume in the reservoir was 20 µL.

This demonstrated that the use of the estimated $\lambda_{c,FF}$ in (7.1) was the correct approach in designing the RP-ES. Furthermore, the visual results in Figure 7.7.d) defined the maximum magnetic field for experiments using the RP-ES as 802.4 Gauss.

The mass flow of the RP-ES was also measured using the QCM throughout the characterization experiment. Downstream current density was also recorded using the Faraday cup with a front plate and aperture which limited the current collection area to one equal to the QCM crystal area. The results are included in Table 7.1.

Table 7.1. Mass accumulation rates and current measurements collected throughout testing.

Emission Mode		Emission Current Range (µA)	Magnetic Field Strength (Gauss)	Mean Mass Flowrate (ng/s)	Mean Current Density (µA/mm^2)
Transient-Emission		20 to 30	333.9	5.39	1.42
			520.5	6.42	2.12
			690.5	2.82	0.18
Continuous-Emission	Low-Current	1 to 10	333.9	0.01	0.06
			520.5	0.01	0.04
			690.5	0.06	0.10
	High-Current	30 to 80	333.9	0.52	0.90
			690.5	0.15	0.46
Very-High-Current		>100	690.5	5.65	1.86

The mass accumulation rates were highest during the transient-emission current mode and the unstable, very-high-current mode, and averaged 5 ng/s. In the transient-emission mode, this mass accumulation rate continued for the entire five-minute period, after which time it dropped several orders of magnitude (see Table 7.1). In very-high-current mode, however, the mass accumulation rate was only be maintained for approximately 30 seconds; longer emission periods in this mode induced the long filamentary jets that would bridge the extractor gap. A change between high- and low-current modes had only a small effect on the mass accumulation rate.

7.3.2. Rosensweig Peak Electrospray Source Cation TOF Spectrum

Unlike the spectra collected in experiments using the CES (Chapter 6), the cation TOF spectrum from the RP-ES was only collected for only one pulsing plate potential, 750 V. Therefore, the resulting TOF mass spectra contain only those ions with a kinetic energy within 50 eV of the emitter bias, as slower moving ions and droplets would be unable to overcome the +750 V potential barrier established by VA1 and VA2, and subsequently would not enter the extraction region. Spectra were collected while the RP-ES operated in low-current and high-current modes of operation and are shown in Figure 7.8.a) and b), respectively. As Figure 7.8. illustrated, ion species at an $m/q = 111$ amu/e and an $m/q = 502$ amu/e, which are the $EMIM^+$ species $n = 0$ and $n = 1$ respectively, existed in the spectra collected from the RP-ES operating in both low-current and high-current modes. Please note that the relative intensities between the three magnetic field cases may be caused by fluctuations in the emission current and should not be assumed to represent the average spectra for that case.
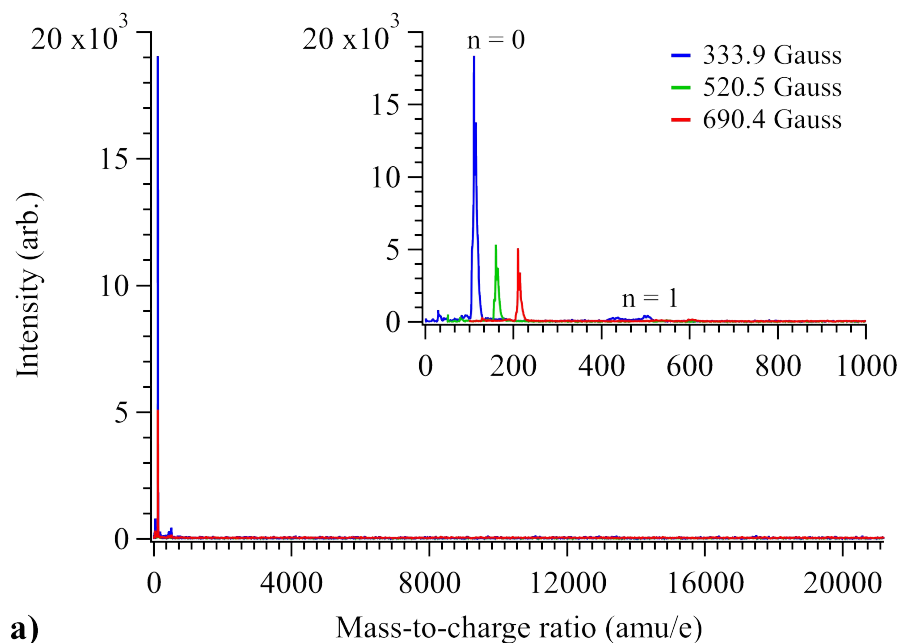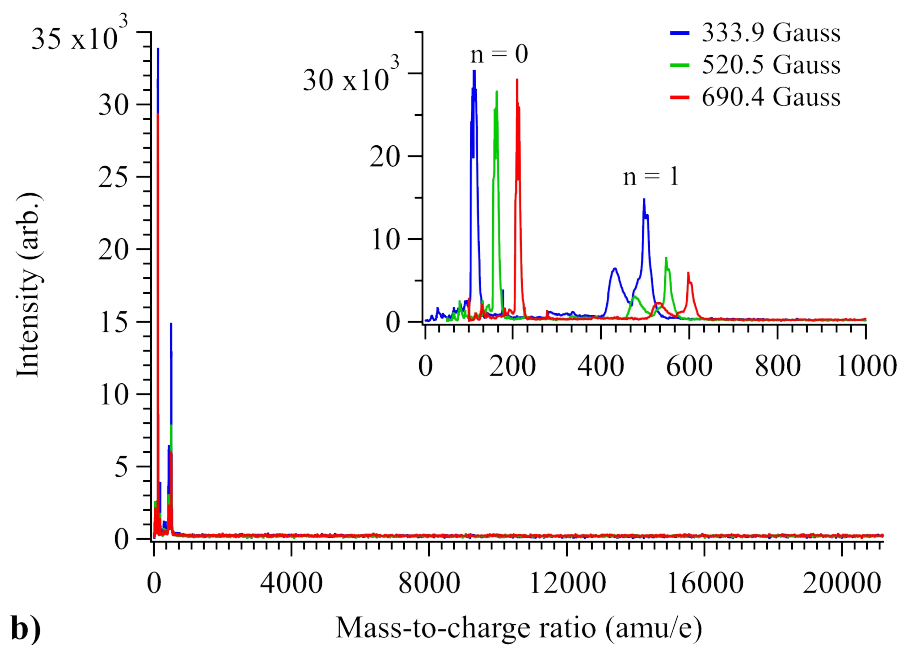
Figure 7.8. Cation TOF mass spectra of an ILFF electrospray beam emitted from the RP-ES in a) low-current mode for varying magnetic field strength and b) high-current mode for varying magnetic field strength. The spectra in the low mass plot have been incrementally shifted along the m/q axis for clarity by artificially adding 50 and 100 amu/e to green and red traces, respectively.

7.3.3. Rosensweig Peak Electrospray Source Anion Mass Spectrum

TOF mass spectra of the anion electrospray beam were also collected from the RP-ES under magnetic field strengths of 333.9, 520.5, and 690.4 Gauss at the reservoir surface. It should be noted that while both low- and high-current modes existed, collection of anions using an MCP is inherently more difficult. The MCP functions as an electron multiplier by accelerating an ion (or electron) towards an anode (or cathode) causing it to collide and produce an eruption of secondary electrons from the impact site. These secondary electrons then enter one channel of the MCP and impinge on the wall creating more secondary electrons. The secondary electrons impinge further down the channel wall and create a cascade of more secondary electrons, ultimately multiplying the signal by several orders of magnitude. The potential applied to the front anode during cation collection was approximately -1900 V. However, to accelerate the primary electron towards the channel, the front anode must be negative with respect to the channels and the cathode behind them. This means that, to collect anions, a much larger positive voltage of 3900 V must be used, and is split using a voltage divider to place a large positive potential on the front 'anode' yet still provide a negative potential relative to the MCP cathode to accelerate the primary electrons towards the channels. However, in applying a larger voltage the signal-to-noise ratio is reduced as other particles, including those that may be emitted at wide angles, will impact the detector in a random distribution. Therefore, only an electrospray with high signal could be measured by the MCP. Thus, the only anion spectrum collected for the ILFF electrospray beam was during the high-current mode of operation (Figure 7.9.). The TOF mass spectrum in Figure 7.9.b) shows three peaks, at m/q of 19, 280, and 315 amu/e.

The 19 and 280 amu/e peaks are known m/q representing the F^- anion fragment and NTF_2^- (n = 0) anion species, respectively. The 315 amu/e peak is unknown and could represent a fragment of the copolymer attached to an n = 0 anion. Once again note that the relative intensities between the three magnetic field cases may be caused by fluctuations in the emission current and should not be assumed to represent the average spectra for that case.
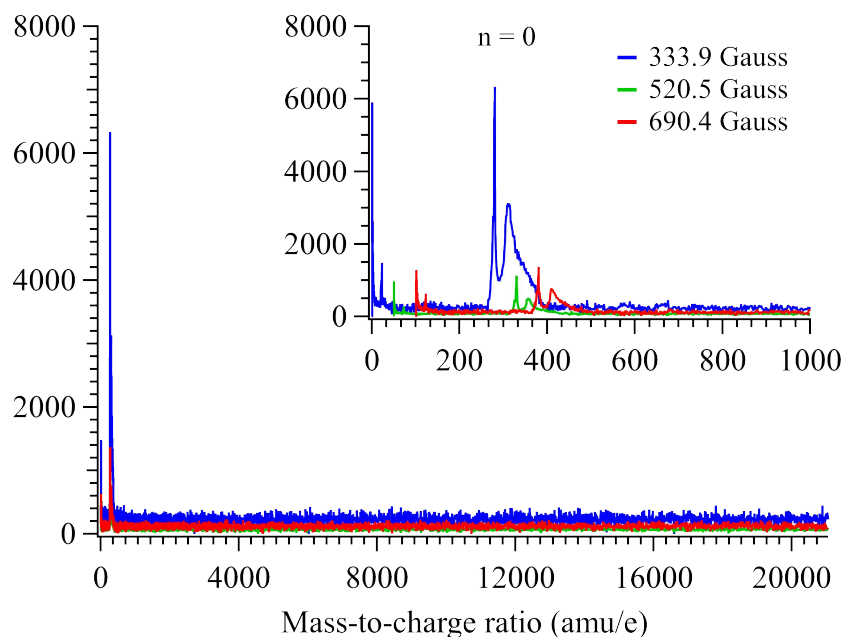
Figure 7.9. Anion TOF mass spectra of an ILFF electrospray beam emitted from a single Rosensweig peak during high-current mode and varying magnetic field strengths. The spectra in the low mass plot have been incrementally shifted along the m/q axis for clarity by artificially adding 50 and 100 amu/e to green and blue traces, respectively.

7.3.4. Solid-Needle Electrospray Mass Spectra using Neat Ionic Liquid

TOF mass spectra of neat IL emitted from the SN-ES allow direct comparison to the observed TOF spectra obtained using the RP-ES under varying magnetic field strengths and emission conditions. Cation and anion TOF mass spectra of an EMIM-NTF_2 electrospray beam are provided in Figure 7.10. and Figure 7.11. In Figure 7.10. the inset

plot, which magnifies the mass axis for clarity, shows peaks corresponding to known n = 0 and n = 1 cation species. In Figure 7.11. the inset plot, which magnifies the mass axis for clarity, shows peaks corresponding to known anion species at 280 amu/e for the n = 0 species and 671 amu/e for the [EMIM][NTf2] NTf2- (n = 1) species. Peaks at m/q less than 100 amu/e in the cation spectrum are associated with the known EMIM+ fragments described in Section 7.4.2. Peaks were also recorded in the anion mass spectrum at m/q of 19 and 350 amu/e; the peak at an m/q of 19 amu/e was associated with the F- anion fragment, while the peak at 350 amu/e was unknown.
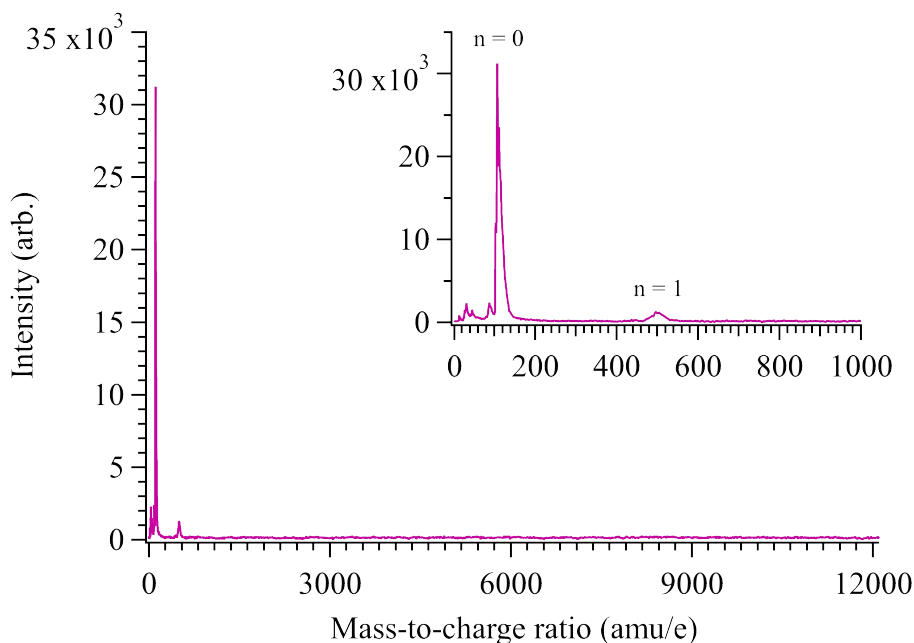
Figure 7.10. Cation TOF mass spectrum of a pure EMIM-NTF2 electrospray beam emitted from the SN-ES. Inset plot presents the low mass range for clarity of ion species.
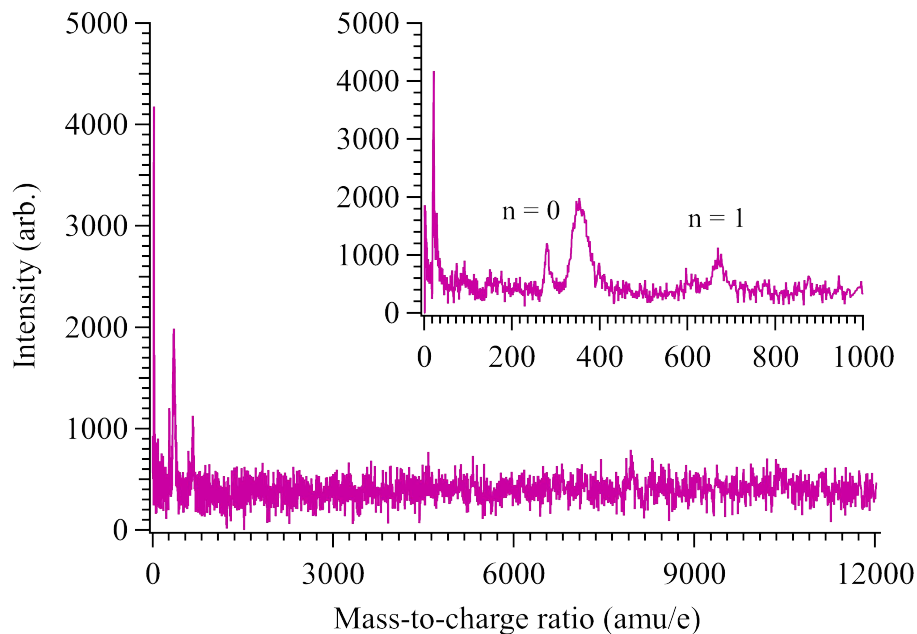
Figure 7.11. Anion TOF mass spectrum of a pure EMIM-NTF$_2$ electrospray beam emitted from the SN-ES. Inset plot presents the low mass range for clarity of ion species.

7.4. Analysis and Discussion

The results in Section 7.3. document the mass spectra of an ILFF electrospray beam from a RP-ES and SN-ES. There are several observations of the spectra and the operation of the ILFF electrospray that will be discussed in the following Sections 7.4.1. through 7.4.5.

7.4.1. Mass Flow Rate Variability

The research group at Michigan Tech noted visual evidence of dark residue on the collector plate after ILFF electrospray emission from a Rosensweig instability peak, which is indicative of nanoparticles.[46, 137] This residue accumulation could only arise from very high mass flow rates that include emission of nanoparticles. Literature reports that the

existence of droplets in the electrospray beam was a consequence of relatively high mass flow rates (7.5 ng/s) and large average m/q (24,200 amu/e) values.[3] It was assumed that the main fraction of the mass flow in this study resulted from large charged-droplets. In the case of mixed ion-droplet operational mode, the average m/q value as measured by a current sensor and a mass sensor will necessarily be a weighted average between the m/q of the small ions and the true m/q value of the large droplets. In Section 6.3., which presents measurement of droplets emitted from the CES operating on neat IL, the mass flowrate and average m/q of electrospray during TOF spectra collection at 0.63 nl/s was 1.81 ng/s and 28,200 amu/e, respectively. These magnitudes were calculated as the sum of QCM mass flowrate and Faraday current of the center axis of the beam measured downstream of the TOF extraction region.

For the parent ILFF, the mass of a 30-nm-diameter NP with associated copolymer and a 15-nm-thick layer of EMIM-NTf$_2$ (the hydrodynamic diameter of particles in similar ILFFs is approximately 60 nm[12]) would be 370-million amu. Therefore, a droplet involving the nanoparticle and copolymer emitted from the RP-ES would be in the m/q range of 23,400 to 370-million amu/e (the lower limit is the Rayleigh limit of a 60-nm diameter IL and the upper limit is assuming the droplet is singly-charged). The average m/q calculated from the data presented in Table 7.1. indicates a larger fraction of the beam emitted from the RP-ES during very-high-current and transient-emission modes was from relatively large masses. However, since small ionic species were also observed in the TOF mass spectrum in these operational modes, the average m/q is weighted by some factor towards a smaller m/q value. Unfortunately, droplets could not be definitively identified in the TOF mass spectrum which may have been the result of collecting only spectra for one

energy defect and at relatively small m/q range of 24,000 amu/e. If the same range of 0-24,000 amu/e is examined for the 50-eV energy defect spectrum of the CES operating on neat IL at 0.63 nl/s, Figure 7.12., no droplet population can be discerned. However, if the range is extended to 600,000 amu/e for the same energy defect spectrum, a droplet population is easily discerned at a center m/q of 240,000 amu/e. Furthermore, as Figure 6.4. shows, the intensity and location of droplet populations in the summed mass spectrum is much different, revealing the potentially three droplet distributions described in Section 6.4.3. As such, whether droplets were observed or not in the spectra from the RP-ES may not be due to the absence of droplets, but the extent to which the beam was measured.
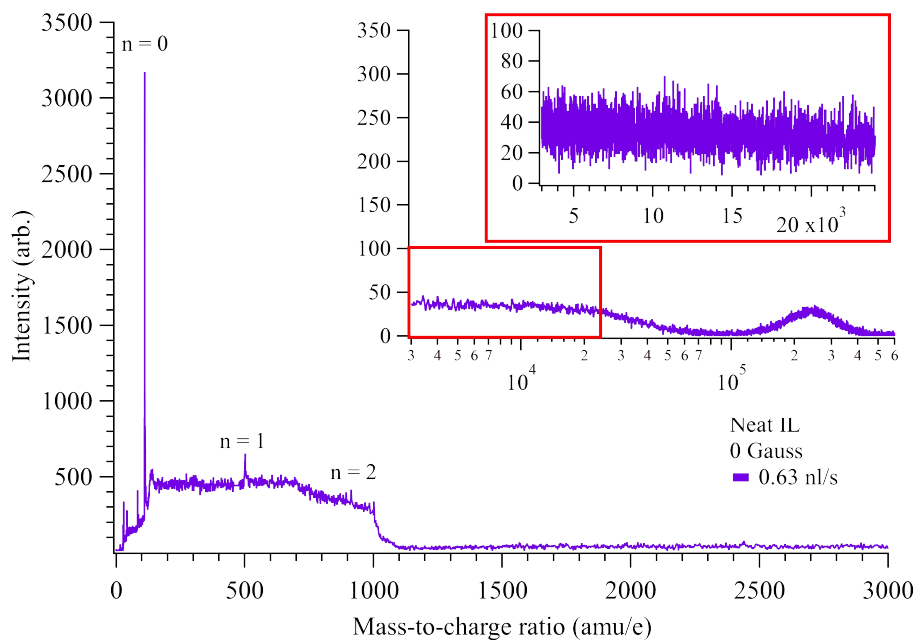
Figure 7.12. TOF mass spectrum of CES operating on neat IL at 0.63 nl/s under extraction conditions described in Section 6.3.2. The spectrum was collected for an energy defect of 50 eV. Inset plots illustrate two m/q ranges of 3000-600,000 amu/e and 3000-24,000 amu/e.

Returning to the examination of the variable mass flow and emission current of the RP-ES, the transient-emission and very-high-current modes of operation were calculated to have an average m/q, as measured by the Faraday cup and QCM, ranged from 100,000

209

to 130,000 amu/e. Over a period of approximately five minutes operating in transient-emission or very-high-current modes, the average m/q fell to a value near 15,000 amu/e. This transition to smaller masses indicates that droplet emission ceased, ion production greatly increased, or some lesser combination of the two. Time-of-flight mass spectra taken at early operational times qualitatively reproduced those taken at low m/q value periods in terms of species identities and relative intensities. Qualitatively, this observation suggests that small ion production did not greatly increase and instead droplet formation decreased. Furthermore, it suggests that a future examination of the TOF mass spectra from the RP-ES is warranted so long as the mass range is extended to 500,000 amu/e or more.

7.4.2. Varying Emission Current

A difference in the TOF mass spectrum collected from the RP-ES emitting in low- or high-current mode is made apparent when overlaying the two spectra, Figure 7.13. The correlation between changes in species within the spectra and emission current mode of operation was likely attributed to both variations in the electric field inducing electrospray from the Rosensweig instability peak, and the mass flowrate of propellant emitted from the peak. The apex and foundation of the Rosensweig instability were observed to have noticeably different geometry when emitting in the low-current mode than when in the high-current mode (Figure 7.6.). The change in geometry would affect the electric field used to extract the electrospray beam via geometric enhancement. The magnitude of the extraction field can be highly influential on electrospray emission. In externally wetted needles, the electric field defines the flowrate and, consequently, emission current of the

source.[18, 33, 34, 104] The electric field also influenced the ion species present in the beam; however, the correlation between the two variables as reported in literature is not proportional nor linear as some researchers reported an increase in heavier ion species,[34, 138] while others observed or predicted the opposite.[34, 134] However, the higher mass flowrates associated with the high-current mode (Table 7.1) were on the same order as flowrates used in capillary electrospray from the CES (Section 6.4.3. and studies by Miller *et al.*,[43, 58] and Chiu *et al.*[3] all showed that higher flowrates correlated to the production of heavier ion species, *i.e.* n = 1, 2, 3, 4…). Therefore, a change mass flowrate due to higher electric fields, plus the change in peak geometry (electric field) corresponding to the transition between low- and high-current modes likely accounted for the increase in peaks at higher m/q (including the n = 1 cation species) with respect to n = 0 cation species at higher emission currents, (Figure 7.13.).
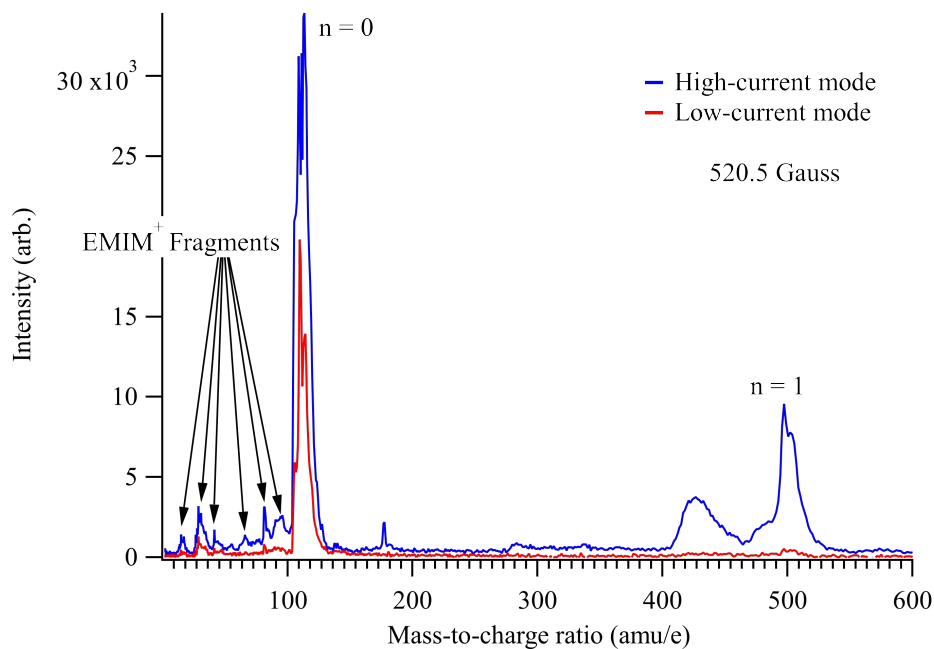
Figure 7.13. Cation TOF mass spectra of an electrospray from the RP-ES during the low- and high-current modes of operation.

211

Also identified in the TOF mass spectrum in Figure 7.13. were peaks at masses below 100 amu/e, which were present in both low- and high-current emission modes. The peak locations for these lighter masses were at m/q values of 15, 29, 42, 56, 85, and 96 amu/e. These lighter peaks have been examined in proceedings published by Terhune *et al*.,[139] in which they found that the widths of the peaks themselves are a consequence of how the specific particles in the TOF extraction region were preferentially selected based on their location.

There was also evidence of unusual ionic species that were observed in the cation TOF spectra taken at the various magnetic field strengths beginning near 280 amu/e and continuing to about 390 amu/e. An intense, broad feature beginning around 410 amu/e continues until just after the apparent n = 1 cation peak at 502 amu/e. Figure 7.14.a) examines the 400-520 amu/e range and overlays and offsets the low mass species by 396 amu/e. The strong correlation between the position and relative intensity of the fragments plus the 396-amu/e offset with the unidentified band in this region gives some degree of confidence that species in this region are ultimately the small mass ions (Figure 7.13.), which are carrying some component with mass 396 amu.
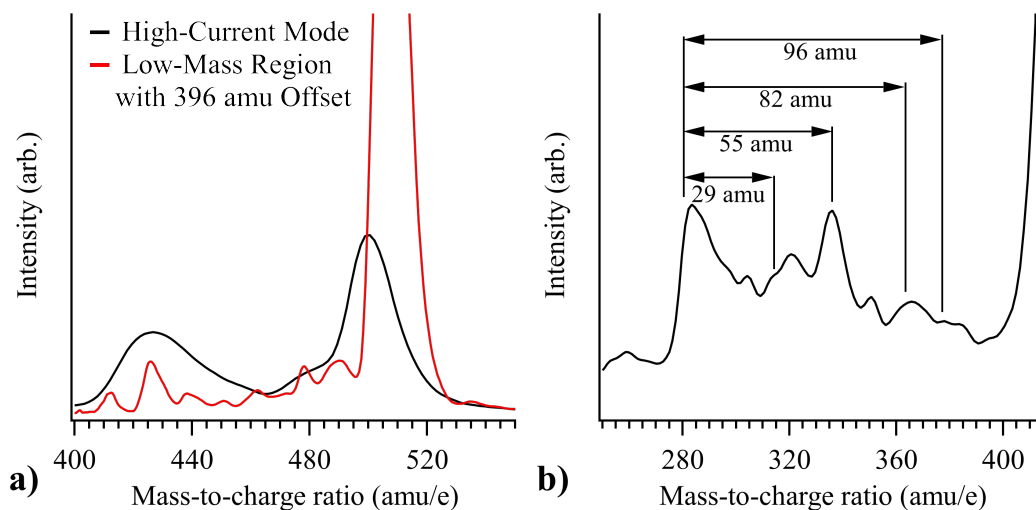
Figure 7.14. (a) TOF mass spectra of ILFF electrospray in high-current identifying the 400-550 amu/e region of the TOF mass spectrum with the low mass range offset by four PDA blocks. (b) The TOF mass spectra of ILFF electrospray in high-current offset by one EMIM$^+$ cation plus one PDA block to identify the four-particle species, each of which had one of four EMIM fragments attached to an EMIM$^+$ plus one PDA.

The ILFF copolymer contained a long backbone of two fundamental building blocks, a PMP block and PDA block. At the end of these chains are two end groups, $CH_3CHCOOH$ for the 60 PDA blocks of the copolymer, and $CS_3C_4H_9$ for the 10 PMP blocks of the copolymer. A mass of 396 amu is reached if a neutral component consisting of four of the PDA blocks is considered with the charge coming from the various EMIM$^+$ low mass fragments terminating with a contribution from the EMIM$^+$ cation at m/q of 507 amu/e. If the EMIM$^+$ $n = 0$ cation significantly contributes to the signal in the 502-amu/e region, the relative intensity of the $n = 1$ EMIM$^+$-[EMIM$^+$-NTf$_2^-$] ion to the $n = 0$ becomes difficult to disentangle without higher resolution investigation.

The mass region from 280-400amu/e is explored in a similar fashion to the 400-520 amu/e region in Figure 7.14.b). Like the progression observed above, key mass spectral features are separated by known fragment masses of EMIM$^+$. The initial sequence begins at 283 amu, tentatively assigned to the EMIM$^+$ cation paired with a single PDA block and

213

the associated CH₃CHCOOH end group. A single PDA block with the end group has a

mass value of 172 amu and, when coupled to the EMIM$^+$ cation, results in an m/q value of

283 amu/e with a net +1 charge. Each subsequent step at higher masses (+29 amu, +55

amu, etc.) is the inclusion of neutral (C_2H_5, MIM, etc.) fragments resulting from EMIM$^+$

fragmentation. The best example of a pairing with a neutral fragment in EMIM-NTf₂ is the

species that occurs at 140 amu/e and is assigned to EMIM$^+$ with a C_2H_5 neutral fragment.

In contrast to the progression in Figure 7.14.a), there is no significant intensity at the next

step in the sequence (+111 amu) since, under this hypothesized assignment, this would

result in a doubly charged species. Unfortunately, the species that would appear at m/q =

455 amu/e, and would be assigned to two PDA blocks with end group and an EMIM$^+$

cation, appears at mass values encompassed in the four PDA blocks + fragment ion

sequence highlighted in Figure 7.14.a). Similarly, the three PDA blocks + fragment ion

sequence should begin at m/q = 299 amu/e, which lies in the middle of the Figure 7.14.b)

sequence. No evidence of other multiples of PDA blocks, with or without the end group,

was observed in the mass spectrum.

7.4.3. Varying Magnetic Field Strength

Another observation made during the experiments was the mass spectra dependence on

the change in magnetic field strength. A correlation existed between the magnetic field

strength and the ratio of n = 0 cations to n = 1 cations, as observed in Figure 7.8. A similar

trend was also seen in Figure 7.9. between magnetic field strength and the ratio of the

relative intensity of n = 0 to the relative intensity of the peak at 430 amu/e. Qualitatively,

this suggests that a higher magnetic field actively induced the emission of the lighter, and

thus faster, particles in the center of the electrospray beam. The physical mechanism behind the shift to lighter-mass emission is likely a change in general shape of the peak formed by the Rosensweig instability (Figure 7.6.). The tip radius of the Rosensweig peak appeared to decrease with an increase in magnetic field strength. This would further enhance the electric field to the critical field required to dissociate heavier ion species into lighter ions and fragments. Therefore, a Rosensweig peak subjected to higher magnetic fields would emit higher quantities of lighter ion species. Potentially, the correlation could have been the result of the magnetic field acting on the focusing and TOF optics of the facility. This could lead to instrument-throughput preferentially increasing or decreasing the intensity of some peaks.

Any correlation between ion intensity peaks and the magnetic field strength in the anion TOF mass spectra of the ILFF electrospray beam could not be measured, Figure 7.9. This was because anion spectra had only one ion species, and the method used to determine magnetic field effect required comparison between the peak intensities of multiple ion species.

7.4.4. Comparison between Rosensweig Peak Electrospray Source and Solid Needle Electrospray Source

A comparison between the TOF mass spectra of the ILFF electrospray from a RP-ES and a neat IL electrospray from the SN-ES was useful to reference the Rosensweig peak electrospray technique against an established device. Figure 7.15. shows the mass spectra of electrosprays from both the SN-ES and RP-ES.

The cation spectrum of the SN-ES matched closely to the cation spectrum of the RP-ES in low-current mode (pink and light green traces Figure 7.15.a)), suggesting that the RP-ES operates like a needle when in the low-current mode. When in high-current mode, though, the RP-ES emitted several peaks that are not seen in the needle spectrum. These peaks, as mentioned previously, are believed to be associated with components of the copolymer used for steric stabilization. Furthermore, the intensity of the $n = 1$ cation species relative to the $n = 0$ cation species was much greater in high-current mode compared to the SN-ES or low-current mode of the RP-ES, owing to higher flowrate, providing further evidence that the RP-ES is to needle-like when in low-current mode.

Comparing the anion spectra of the RP-ES and the SN-ES, a peak in the ILFF spectrum that is not associated with fragments or neutrals of the IL appears at 310 amu/e. Therefore, it is believed that these peaks are associated with other components of the ILFF. The peak at 19 amu/e in the needle anion spectrum appeared in the RP-ES anion was associated with the F⁻ anion fragment. The unknown peak at 350 amu/e that was measured in the IL spectrum also appeared in the RP-ES spectrum, though it was combined with the unknown peak at 315 amu/e, attributing to its peak broadness. The assignment of this peak is unknown and would require further testing of both the IL and ILFF electrosprays from the SN-ES and RP-ES, respectively.

Figure 7.15. a) Cation and b) anion TOF mass spectra of an electrospray beam from the RP-ES and the SN-ES. In the main plot of a) the spectra are shifted by artificially adding 50 and 100 amu/e to the light-blue and red traces. In the inset plot of a) and in b) the baselines of the intensity axis are intentionally shifted by arbitrary amounts. The shifts in the spectra were done for clarity. The magnetic field strength for the RP-ES was 333.9 Gauss.

Comparing the anion spectra of the RP-ES and the SN-ES, a peak in the ILFF spectrum

that is not associated with fragments or neutrals of the IL appears at 310 amu/e. Therefore,

it is believed that these peaks are associated with other components of the ILFF. The peak at 19 amu/e in the needle anion spectrum appeared in the RP-ES anion was associated with the F⁻ anion fragment. The unknown peak at 350 amu/e that was measured in the IL spectrum also appeared in the RP-ES spectrum, though it was combined with the unknown peak at 315 amu/e, attributing to its peak broadness. The assignment of this peak is unknown and would require further testing of both the IL and ILFF electrosprays from the SN-ES and RP-ES, respectively.

The emission current of the two sources differed as well. The needle source operated stably at 1.75 ± 0.1 µA for the entire hour span of testing. The RP-ES had three emission modes, two of which, the low- and high-current modes, can be sustained continuously, however, not as stably with emission currents of 5 ± 4.5 µA and 50 ± 25 µA. The third transient-emission mode lasted only five minutes, though its emission current varied relatively less at 25 ± 4.5 µA.

I would like to note that the difference between the SN-ES and RP-ES boundary conditions (BCs) could influence the emission characteristics from each source. The SN-ES is comprised of a solid needle with a thin layer of liquid over the surface, whereas the RP-ES is only a continuous liquid peak. This means that the liquid velocity and thus charge conduction/convection within the volume of the propellant on the surface of the SN-ES would be dependent on both a solid-liquid and liquid-gas interface, whereas the RP-ES liquid velocity and charge advection is only dependent on the liquid-gas interface. This could explain the difference in emission current magnitude, which was higher for the RP-ES, and the products within the electrospray beam.

7.4.5. Comparison between Rosensweig Peak Electrospray Source and Capillary Electrospray Source

A comparison between the TOF mass spectra of the ILFF electrospray from a RP-ES and a neat IL and ILFF electrospray from the CES was done to understand the Rosensweig peak electrospray technique against another established device. However, the summed mass spectra from the CES presented in Chapter 6 were each composed of a summation of mass spectra collected at a range energy defects. As spectra from the RP-ES were only collected at a single pulsing plate potential equivalent to an energy defect of 50 eV, the best comparison between the two sources requires only examining those spectra collected for pulsing-plate potentials of 50 V below the extraction potential. Figure 7.16. shows the 50-eV mass spectra of an electrospray from the CES operating on five propellants with 0-Gauss and 200-Gauss magnetic fields applied to the source; the propellant flowrate was 0.63, 0.52, 0.47, 0.54, 0.54 nl/s for neat IL, ILFF-10, ILFF -20, ILFF -30, ILFF -40, respectively. Also included in Figure 7.16. are the spectra from the RP-ES operating with a 520.5 Gauss magnetic field in low- and high-current modes. The intensity of the $n = 0$ peak of both RP-ES spectra were normalized to the intensity of the $n = 0$ peak of the ILFF-10 spectrum as the intensity between the two experiments is not comparable due to changes in settings and conditions of the TOF-MS. However, the comparison provided an idea of the relative species emitted in the low-mass range for each source. Also note that the plateau observed in the CES spectra between 100 and 700 amu/e is the result of a longer pulse width used during mass spectra collection than for RP-ES mass spectra collection (100 μs compared to 2.5 μs), and was observed in all CES spectra. The plateau was

attributed to species in the electrospray beam that were allowed into the TOF flight tube with uncertain flight paths or starting energies.
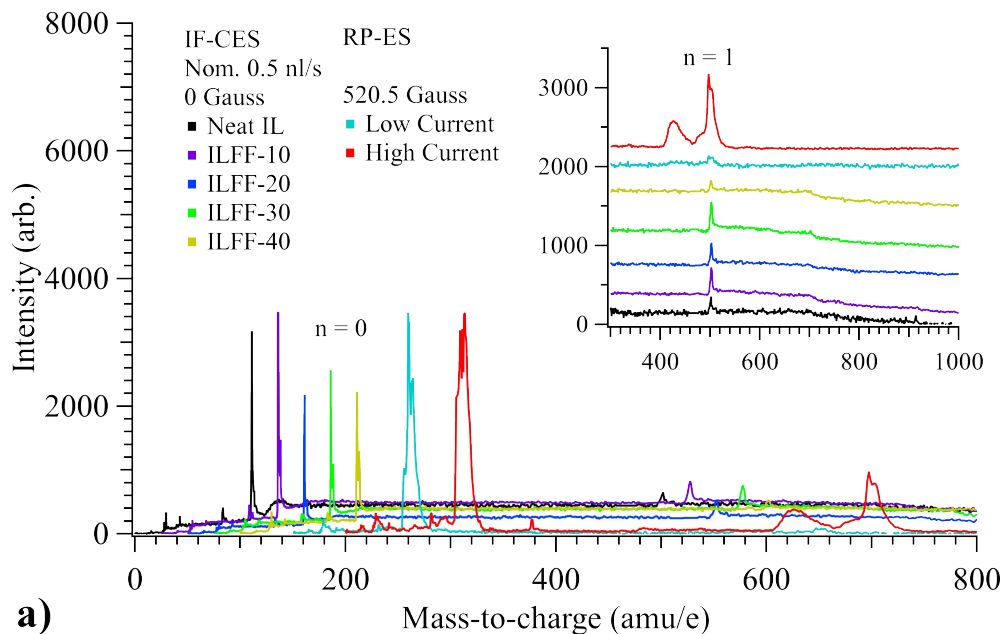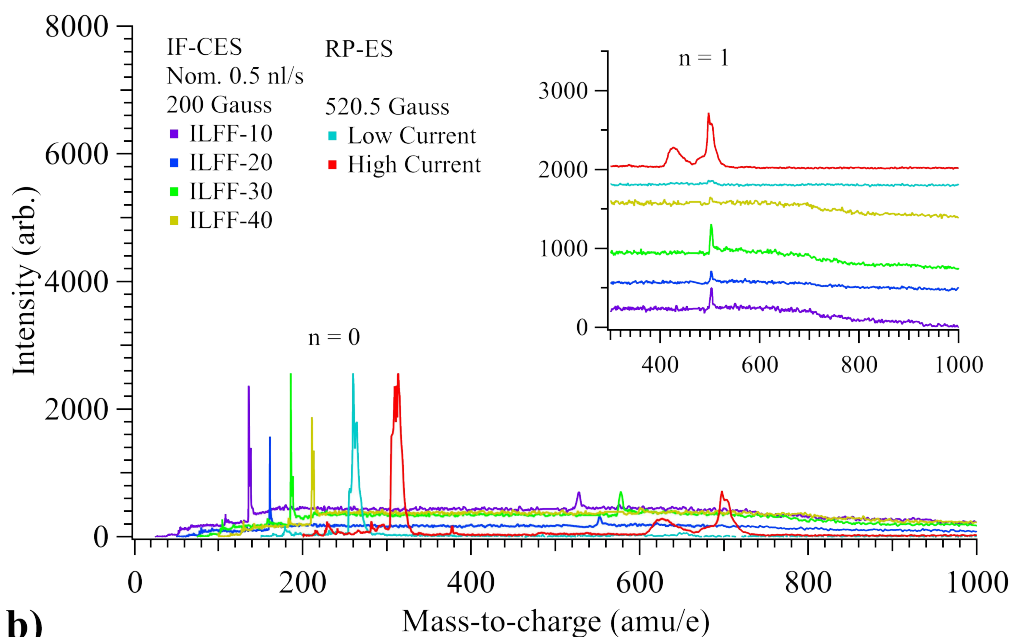
Figure 7.16. Cation TOF mass spectra from the CES and RPES collected at an energy defect of 50 eV. The magnetic field applied to the CES was a) a 0-Gauss and b) a 200-Gauss, and 520.5 Gauss for the RP-ES. Curves in the main plots of a) and b) are artificially shifted by 25, 50, 75, 100, 150 and 200 amu/e for the purple, blue, green, yellow, light-blue and red curves, respectively; the inset plots of a)and b) are arbitrarily shifted on the intensity axis.

Comparing the spectra from the CES to spectra from the RP-ES, Figure 7.16., revealed that the RP-ES operating in high-current mode produced similar species to a capillary emitter. Interestingly, the peak observed in the RP-ES spectra at 430 amu/e is not apparent in CES spectra, even for ILFF propellants with 14.15 weight-percent NPs (compared to 26-wt% NPs in ILFF used in the RP-ES). Comparing the average m/q of the ILFF-50 CES electrospray at minimum flowrate of 0.45 nl/s to the RP-ES in high-current mode, the average m/q in the center of the beam was more than ten-times greater in the CES, (179,000 amu/e), than in the RP-ES, maximum of (16,500 amu/e). This may suggest a stark difference in how the RP-ES operates and emits, including lighter droplet populations. As mentioned previously, spectra from RP-ES were not collected for the mass range necessary to observed droplets in the CES, nor was the collection of spectra from off-axis electrospray emission completed. Therefore, droplets very well could exist in the RP-ES electrospray beam.

Lastly, like the BCs between the RP-ES and the SN-ES, the BCs differed between the RP-ES and the CES. Specifically, both sources have a BC related to the liquid-gas interface, while the CES inherently has another BC from the solid-liquid interface between the capillary needle surface and the propellant. This would potentially lead to differences in the liquid velocity and thus charge conduction/convection within the volume of the propellant. However, the differences in BCs are less influential to liquid and charge motion in the emission sites of the two sources than the differences in the propellant feed method in each source. *I.e.* the CES has a propellant flowrate that is pressure-driven, whereas the

RP-ES flowrate is defined by the extraction potential.[81] The difference in propellant feed means the required flowrate for emission differed significantly resulting in different emission products; *e.g.* the CES requires higher flowrates and produces many ion and droplet species,[58] whereas the flowrate of a the RP-Es is likely similar to a needle emitter like the SN-ES is orders of magnitude less than that of a capillary, and only produces two or three ion species.[3, 104] Therefore, the differences in propellant feed, and subsequent differences in flowrate are likely the driving factors in the liquid velocity and charge advection at the emission site of both sources.

7.5. Conclusions: Rosensweig Peak Electrospray Source

This chapter presented the results from an apparatus which was built to use an ILFF propellant and the Rosensweig instability to produce electrospray. The emission current and the beam composition of the Rosensweig peak electrospray source (RP-ES) were measured using a Faraday plate/cup, a QCM, and a TOF mass spectrometer. The ILFF used was the NJ397074 batch, which comprised of 26.3-wt% iron-oxide nanoparticles, 3.9 wt% copolymer, and 69.8 wt% EMIM-NTf$_2$. The apparatus used one, two, or three permanent magnets to instigate the Rosensweig instability which produced magnetic field strengths that ranged from 333.9 Gauss to 690.5 Gauss.

During emission of the ILFF four modes of operation were observed. Three were easily attainable, a transient mode at the start of testing which emitted at 20-30 μA, a second at low currents of 1-10 μA, and a third at higher currents of 30-80 μA, which were called transient-emission, low-current, and high-current modes, respectively. The fourth mode

occurred when the extraction potential was increased beyond the high-current mode and emission in the mode would potentially bridge the gap between the ILFF peak and the extraction plate. The RP-ES was observed to emit with a high mass flow rate, up to 6 ng/s, in the first minutes of emission, after which the its flow rate dropped several orders of magnitude during sustained operation.

The cation and anion spectra from the RP-ES and SN-ES were collected at only a single pulsing plate potential which captured particles with energies greater than 90 percent of the extraction potential. Analyzing the collected TOF mass spectra revealed that electrospray beams from the RP-ES and SN-ES emitted only two cation and anion species, $n = 0$ and $n = 1$. The low- and high-current emission modes of the RP-ES differed in the ratio of $n = 0$ to $n = 1$ emitted; specifically, the spectra displayed a correlation between emission current and the relative intensity fraction of the $n = 1$ ion species. Furthermore, the electrospray beams from the high-current mode were shown to be partially-comprised of fragments of the respectively anion or cation. This correlation is believed to be a consequence of change in shape of the Rosensweig peak during adjustments in extraction voltage.

An adjustment in the magnetic field strength was shown to change the shape of the Rosensweig peak. However, there appeared to be no correlation between the H-field and the cation or anion spectra.

Comparing mass spectra, the RP-ES and SN-ES revealed that the ILFF electrospray produced from the RP-ES in low-current mode resembled that of a neat IL electrospray emitted from a needle. In high-current mode the relative production of the $n = 1$ ion species increased significantly. This could be the result of higher electric field as observed in

similar needle studies. The primary similarity between the sources was the limited number of ion species produced (n = 0 and n = 1).

Other masses existed in the mass spectra from the RP-ES that were not associated with a specific ion species. Peaks in the cation spectrum were believed to be associated with different combinations of the fragmented n = 0 cation, with a single peak identified as a combination of one fragment group of the copolymer and the n = 0 cation. The peaks in the anion spectrum were believed to be associated with fragments of the n = 0 anion, with two peaks associated with fragments of the copolymer paired with the n = 0 anion, and a fragment of the n = 0 anion.

However, in the ILFF spectra from the CES such artifacts were absent; this led to the conclusion that the products were a result the differing emission process between the two sources. Other differences between the sources include the absence of heavier ion species and droplets in the TOF mass spectra of the RP-ES. However, this was a consequence a relatively small m/q acquisition range during mass spectra collection from the RP-ES. This motivates future studies using the extended range of the mass spectra collected from the CES.

Chapter 8

Conclusions

8.1. Introduction

To reiterate, the goals of this research were fivefold: (1) separate the effects of magnetic nanoparticles from the effects magnetic stress on the electrospray emission of the CES, (2) separate the effects of magnetic nanoparticles from the effects magnetic stress on the electrospray beam structure of the CES, (3) separate the effects of magnetic nanoparticles from the effects magnetic stress on the mass-to-charge of masses emitted from the CES, (4) characterize the emission current from a solid-structure-free Rosensweig peak electrospray source (RP-ES), (5) measure the mass-to-charge of masses emitted from the RP-ES. This chapter revisits the results and conclusions drawn from Chapters 4 – 7 to ascertain how well each of these goals were met, beginning with a summary of the experiments, and continuing into conclusions pertaining to each of the research goals. The chapter ends with a discussion on potential avenues one can take to expand and/or improve the work presented in this dissertation.

8.2. Summary of Experiments and Findings

A capillary electrospray source was manufactured to operate on EMIM-NTf2 ferrofluid propellants, and the lower bound of the stability island of the source was established for five propellants, with and without magnetic field. Onset potential was also measured for

the capillary source subjected to a magnetic field. Three beam diagnostics were performed on the CES running on neat IL and several ILFF propellants: beam divergence, beam energy and TOF mass spectrometry, both with and without magnetic field. Conclusions are presented in 8.2.1. and 8.2.2.

An electrospray source which facilitated the formation of a single EMIM-NTf2 ferrofluid peak using the Rosensweig instability was designed and manufactured. Diagnostics including measurement of emission current, mass flowrate and TOF mass spectrometry were performed on the source and compared to normal operation of the CES operating on neat IL and a solid needle electrospray source. Conclusions are detailed in 8.2.3.

8.2.1. Operation of a Magnetic-Stress-Free ILFF Electrospray Source

The wt% of NPs in the base neat IL of the propellants had a significant effect on the stability island of the source, specifically their increased concentration correlated to a proportional increase of both the necessary extraction field and volumetric flowrate. Furthermore, higher wt% of NPs correlated to higher emission currents of the source (for a given flowrate). However, a consequence of the higher NPs was an increase in the emission current fluctuation. The instability caused variation of the current equal to upwards of 25% the meant current of the source (ILFF-50 propellant) The conclusion was that the NPs affect the stability island as well as emission stability, with the former providing the necessary settings for the remainder of the research.

The divergence of the source electrospray beam was measured over three flowrates for neat IL, ILFF-20, ILFF-30, and ILFF-40 propellants and revealed that both the flowrate and the wt% NPs in the propellant were influential to half-angle of the beam; an increase in flowrate broadened the electrospray beam for all propellants, and the addition of NPs produced broader beams than neat IL. Furthermore, higher wt% NPs ILFF propellants were more greatly intercepted by the extractor plate, reducing the percentage of the permitted beam current by upwards of 73-percent. Also, the higher wt% NPs ILFF propellants had high current densities at large half-angles, relative to lower wt% NPs propellants. Both observations were indicative of broadening due to increased NPs in the propellant.

The electrosprays of using higher wt% NPs ILFF propellants had $\langle \epsilon_{ion} \rangle$ that were consistently lower, relative to the extraction potential, than those of the low wt% NPs propellants. Furthermore, electrosprays from higher wt% NPs propellants emitted with ion species that were in two energy populations, with the second energy population at 30 to 50 percent of the extraction potential. This was determined to coincidence with two ion emission sites on the Taylor cone-jet structure.

The specific mass species of electrosprays from the CES were measured using a TOF-MS. Spectra collected from the CES for neat IL, ILFF-10, ILFF-20, ILFF-30, and ILFF-40 at varying pulsing plate potentials, which were sum into a single summed mass spectrum per operational setting. This summed mass spectrum captured emitted particles with kinetic energies greater than 50 percent of the extraction potential. From the summed mass spectra, it was determined that the CES operated in a mixed ion/droplet regime invariant of the propellant. The highest number of cation species identified within the beam

was n = 0 through n = 13 for neat IL; fewer species were observed in the ILFF propellants proportional to the weight-percent NPs in the ILFF, *e.g.* only n = 0, 1, and 2 could be identified in the ILFF-40 spectrum. This could stem from ILFF electrosprays operating closer to their respective minimum flowrates. The mass fractions for the summed mass spectra were also determined for each of the propellants, which showed that the highest fraction of the mass flowrate of the source was transported by medium sized droplets (10 to 25 nm in radius). These droplets were hypothesized to be in three droplet distributions with center m/q ranging from 38,000 to 172,000 amu/e. The mechanism behind the distributions widths was not measured but is believed to be the product of varying size and charge of droplets within each distribution.

8.2.2. Operation of a Magnetically Stressed ILFF Electrospray Source

The magnetic stress applied to the CES provide by two Helmholtz coils had several effects on the operation of ILFF electrosprays. Subjecting the CES to a 200-Gauss magnetic field while operating on ILFF propellants reduced the emission current of the source and increased the range of stable flowrates of the CES operating on several of the ILFF propellants. Furthermore, subjecting the CES to a magnetic field in discrete steps, while operating on the parent ILFF revealed an inverse linearity between the magnetic field strength and the onset potential of the source. Magnetic stress also induced fluctuations in the emission current upwards of 25 percent of the time-resolved mean; the magnitude of the fluctuations was correlated to the weight-percent NPs in the ILFF.

Magnetic stress also increased the $\langle \epsilon_{ion} \rangle$ of the primary energy population of the emitted species from the CES operating on the ILFF propellants, and increased the $\langle \epsilon_{ion} \rangle$ of the secondary energy population if it appeared in the RPA traces. Electrosprays of ILFF-30 were most affected, increasing by more than 10 percent for multiple operating conditions.

The effect a magnetic stress on the beam divergence was less conclusive due to fluctuations in the emission current. When statistically significant though, the magnetic field either broadened or tightened the beam depending on the propellant, flowrate, and extraction potential. The most significant results were measured while running the ILFF-20 propellant at 0.47 nl/s and 1600 V, where the application of the magnetic field increased the fraction of the current in the center of the beam by approximately 25 percent.

Comparing the summed mass spectra collected from the CES subjected to a 200-Gauss magnetic field for neat IL, ILFF-10, ILFF-20, ILFF-30, and ILFF-40 generally showed that a magnetic stress had less of an effect on emitted mass species of neat IL. The CES was still shown to operate in the ion/droplet mode, and had the highest fraction of the mass flowrate transported by medium sized droplets. The fraction of the mass transported by droplets greater than an estimated 25-nm radius was increased. Owing to the uncertainty in the peak intensities, only results from the ILFF-30 and ILFF-40 showed any true magnetic effects, which revealed that the magnetic stress changed the relative intensity of the ion species; however, the change was in no particular direction (increase/decrease) and had no correlation to wt% NPs of the propellants, and therefore may have been the results of fluctuations in the emission current induced by the magnetic field.

Overall, a magnetically-stressed electrospray was observed have a potentially greater m/q in the center of the electrospray beam, however, this was only achievable for certain propellants and (Q, V_{ext}) settings. The mechanism behind the observed influence from the magnetic stress was theorized to be the changed the shape of the emission site structure, including the Taylor cone and jet, caused by the magnetic field, which, consequently, changed the specific emission products of the source as well as the energy of the emission products. While these conclusions were provoking, I would note that using the ILFF propellant as a magnetic-field free electrospray had several shortcomings, including beam broadening and emission fluctuations, which the magnetic field could not fully correct.

8.2.3. Conclusions on Rosensweig Peak Source Operation

Development of a source using a single peak of the Rosensweig instability in ILFF provided the next step in ILFF electrospray research, i.e. electrosprays that do not require solid emitter structures. The source was found to operate in four modes, each with different emission characteristics; the transient-emission mode (startup, 20-30 µA), low-current mode (stable operation, 1-10 µA), and high-current mode (stable operation, 30-80 µA) and very-high current mode (unstable, >100 µA). The Taylor cone structure was expectedly susceptible to changes in magnetic field strength however, the effects on stable emission were inconclusive.

The individual mass species of both a positive and negative electrospray from the RP-ES and SN-ES were measured using a TOF-MS. The spectra from the RP-ES show only two ion species, n = 0 and n = 1, existed in both positive and negative electrospray beams. Switching from low-current to high-current emission of the RP-ES increased the

production of the $n = 1$ ion species with respect to $n = 0$, while also introducing fragments and small distributions not associated with any ion species. However, a change in magnetic field strength had no significant effect on the emission current from the RP-ES.

While the spectra for the RP-ES and SN-ES were not identical, it was surmised that an electrospray from a Rosensweig peak emitted with a similar composition to that of a needle electrospray. However, the emission current of the RP-ES was up to 25 times as high as the SN-ES, leading to the conclusion that the source produced relatively higher amounts of ions, but at either lower energies or higher half angles which could not be collected by the TOF mass spectrometer.

Comparison of the RP-ES to the CES revealed that the two sources operated quite differently, both in emission current (RP-ES had higher emission currents), average mass-to-charge ratio (CES had higher average m/q). Comparing the individual m/q spectra of the two sources revealed that the CES produced a beam with more cation species and large droplet distributions, but no small m/q distribution, leading to the conclusion that the RP-ES produced a more efficient beam with respect to mass consumption. However, the lack of mass spectra collected from the RP-ES at different pulsing plate potentials and at larger ranges of m/q may have omitted potential emission products, including droplets and nanoparticles, which may reverse this conclusion.

Overall, the study of a Rosensweig peak as an emission structure for electrospray emission revealed that it emits a central electrospray beam with a high fraction of light ions and could be a useful alternative to a needle electrospray emitter. However, further studies

are required to confirm whether other particles/droplets exist at lower energies or higher m/q, and what the electrospray beam look like at higher beam half-angles.

8.3. Achievement of Research Goals

When I entered this research, little information existed on the use of ILFFs as electrospray propellants, and as such my primary goal was to understand how these fluids worked in electrospray devices. To that end, this dissertation adds significant findings to this field of electrospray. Specifically, I have (1) obtain the lower boundaries of the operational stability island, including emission current and onset potential, for a capillary electrospray operating on several of the new ILFF fluids, (2) measured two characteristics of electrospray beams using the ILFF fluids, (3) determined the composition along the beam axis of an electrospray emitted from the capillary source operating the ILFF fluids, (4) measured the influence of an applied and/or varied magnetic field on each all of these measurements/characteristics of ILFF electrospray from a capillary source, and lastly (5) designed, built and measured the emission current and beam composition of a ILFF electrospray source formed from a single fluid peak of the Rosensweig instability.

With respect to the goals I set out to achieve, using the capillary source and Helmholtz coil I separated the effects of the magnetic field and nanoparticles on the onset potential, stability island, beam divergence, beam energy, TOF mass spectra of an ILFF capillary electrospray source. In each case, the nanoparticles appeared to be the driving factor for any changes observed between the neat IL and ILFF electrosprays. In some of the experiments, the techniques/instruments used did not facilitate the best collection of data;

232

as such some experiments on the structure of the beam (*i.e.* beam divergence), while noteworthy, need to be re-examined to make conclusive statements on the specific effects of either nanoparticle or magnetic field. This is discussed some in the next section. The final two goals were also achieved using the Rosensweig peak electrospray source (RP-ES) and provided useful results to continue the research on electrosprays from the ILFF instability.

8.4. Future Work

As noted throughout this dissertation, the research presented only attempted to answer several questions about the new ILFF propellants and source within which they are used. As such, there are several ways in which the results from this research can be strengthened, and several ways in which research using ILFF propellants and sources can be expanded.

This extent of the stability island of the CES determined in this research is not complete. It provided a sample of extraction potentials and flowrates from which several conclusions about the general effect nanoparticles and magnetic field were made. However, future work should expand on the range, including higher flowrates and extraction potentials to determine the upper limit of stability. Furthermore, the examination should involve extraction potentials in both polarities.

The beam diagnostics on the CES could be expanded and perfected. For example, a rotatable source would allow for the measurement beam energy over the entire electrospray beam. Also, a larger and collection disk with smaller incremented Faraday plates would provide a better resolved picture of the source's beam divergence. Using a rotatable

Faraday probe for this could also be possible, but a new experimental setup would be necessary as the Helmholtz coil currently inhibits such a device due to the small inner diameter.

While the summed mass spectra of the CES collected in this study provided a base for comparison between the new propellants and traditional IL, they did not capture the entire electrospray beam. As such, a future project should examine the spectra of the CES for pulsing plates potentials from 0 V to maximum extraction potential, as well as smaller increments in pulsing plate potential (20 V). This well ensure that emission products from the entire electrospray beam are captured. Also, an extension of the m/q range may provide the evidence of nanoparticles emitted in the electrospray beam.

A study on the ion and particle mobility of a ILFF Taylor cone is also suggested, and should examine if/how the magnetic field or colloidal particles influences the charge and mass mobility at the emission site. This could potentially explain the relative change in emission current of ILFF electrosprays while magnetically stressed.

Lastly, with regards to the RP-ES, the extent of studies on the source in this research were limited, and the potential for a complete characterization of the source is possible if similar diagnostics completed on the CES are done using the RP-ES. The most beneficial test to help define the electrospray from a Rosensweig peak would be collecting summed mass spectra for the source with a m/q range from 0-1,000,000 amu/e). This would provide a measured of the difference between the RP-ES and CES electrospray beam composition.

References

1. Lozano, P.C., *Studies on the Ion-Droplet Mixed Regime in Colloid Thrusters.* Department of Aeronautics and Astronautics, 2003, Doctoral Dissertation, Massachusetts Institute of Technology, Cambridge.
2. Courtney, D.G., Q.L. Hanqing, and L. Paulo, *Emission measurements from planar arrays of porous ionic liquid ion sources.* Journal of Physics D: Applied Physics, 2012. **45**(48): p. 485203.
3. Chiu, Y.H., et al., *Vacuum electrospray ionization study of the ionic liquid, [Emim][Im].* International Journal of Mass Spectrometry, 2007. **265**(2–3): p. 146-158.
4. Gassend, B.L.P., *A Fully Microfabricated Two-Dimensional Electrospray Array with Applications to Space Propulsion.* Department of Electrical Engineering and Computer Science, 2007, Massachusetts Institute of Technology, Cambridge.
5. Terhune, K.J., Lyon B. King. *Ion and Droplet Mass Measurements of an Electrospray Emitter using an ExB Filter.* in *32nd International Electric Propulsion Conference.* 2011. Wiesbaden, Germany.
6. Courtney, D.G., *Ionic Liquid Ion Source Emitter Arrays Fabricated on Bulk Porous Substrated for Spacecraft Propulsion.* Department of Aeronautics and Astronautics, 2011, Massachusetts Institute of Technology, Cambridge.
7. Gassend, B., et al., *A Microfabricated Planar Electrospray Array Ionic Liquid Ion Source With Integrated Extractor.* Microelectromechanical Systems, Journal of, 2009. **18**(3): p. 679-694.
8. Makela, J.M., R.L. Washeleski, and L.B. King, *Regenerable Field Emission Cathodes: Surface Morphology and Performance.* Journal of Propulsion and Power, 2011. **27**(5): p. 1097-1107.
9. Brikner, N., *On the Identification and Mitigation of Life-limiting Mechanims of Ionic Liquid Ion Sources Envisaged for Propulsion of Microspacecraft.* Department of Aeronautics and Astronautics, 2015, Massachusetts Institute of Technology, Cambridge.
10. Lenguito, G., J. Fernandez De La Mora, and A. Gomez, *Scaling up the power of an electrospray microthruster.* Journal of Micromechanics and Microengineering, 2014. **24**(5): p. 055003.
11. Rosensweig, R.E., *Ferrohydrodynamics* 1985, Mineola: Dover Publications, Inc.
12. Jain, N., et al., *Stable and Water-Tolerant Ionic Liquid Ferrofluids.* ACS Applied Materials & Interfaces, 2011. **3**(3): p. 662-667.
13. King, L.B., et al., *Self-Assembling Array of Magnetoelectrostatic Jets from the Surface of a Superparamagnetic Ionic Liquid.* Langmuir, 2014. **30**(47): p. 14143-14150.
14. Zeleny, J., *The electrical discharge from liquid points, and a hydrostatic method of measuring the electric intensity at their surfaces.* Physical Review, 1914. **3**(2): p. 69.
15. Krohn, V.E., *Liquid Metal Droplets for Heavy Particle Propulsion*, in *Electrostatic Propulsion* 1961, American Institute of Aeronautics and Astronautics. p. 73-80.

16. Krohn, V.E., *Glycerol Droplets for Electrostatic Propulsion*, in *Electric Propulsion Development*1963, American Institute of Aeronautics and Astronautics. p. 435-440.

17. Perel, J., et al. *Research on a charged particle bipolar thrustor*. in *6th Electric Propulsion and Plasmadynamics Conference*. 1967. Colorado Springs, CO, U.S.A.: American Institute of Aeronautics and Astronautics.

18. Gamero-Castaño, M. and V. Hruby, *Electrospray as a Source of Nanoparticles for Efficient Colloid Thrusters.* Journal of Propulsion and Power, 2001. **17**(5): p. 977-987.

19. Chiu, Y.-H., et al., *Mass Spectrometric Analysis of Ion Emission for Selected Colloid Thruster Fuels*, in *39th AIAA/ASME/SAE/ASEE Joint Propulsion Conference and Exhibit*2003, American Institute of Aeronautics and Astronautics: Huntsville, Alabama.

20. Earle, M.J. and K.R. Seddon, *Ionic liquids. Green solvents for the future*, in *Pure and Applied Chemistry*2000. p. 1391.

21. Taylor, G.I., *The stability of a horizontal fluid interface in a vertical electric field.* Journal of Fluid Mechanics, 1965. **2**: p. 1-15.

22. Taylor, G.I., *Conical free surfaces and fluid interfaces*, in *Applied Mechanics*, H. Görtler, Editor 1966, Springer Berlin Heidelberg. p. 790-796.

23. Taylor, G.I., *Instability of jets, threads, and sheets of viscous fluid*, in *Applied Mechanics*, M. Hetényi and W. Vincenti, Editors. 1969, Springer Berlin Heidelberg. p. 382-388.

24. Prewett, P.D. and G.L.R. Mair, *Focused ion beams from liquid metal ion sources*1991: Research Studies Press.

25. Krpoun, R. and H.R. Shea, *A method to determine the onset voltage of single and arrays of electrospray emitters.* Journal of Applied Physics, 2008. **104**(6): p. 064511.

26. Fernández de la Mora, J. and I.G. Loscertales, *The current emitted by highly conducting Taylor cones.* Journal of Fluid Mechanics, 1994. **260**: p. 155-184.

27. Gañán-Calvo, A.M., J. Dávila, and A. Barrero, *Current and droplet size in the electrospraying of liquids. Scaling laws.* Journal of Aerosol Science, 1997. **28**(2): p. 249-275.

28. Chen, D.-R. and D.Y.H. Pui, *Experimental Investigation of Scaling Laws for Electrospraying: Dielectric Constant Effect.* Aerosol Science and Technology, 1997. **27**(3): p. 367-380.

29. Rayleigh, L., *XX. On the equilibrium of liquid conducting masses charged with electricity.* Philosophical Magazine Series 5, 1882. **14**(87): p. 184-186.

30. Lozano, P. and M. Martínez-Sánchez, *Ionic liquid ion sources: suppression of electrochemical reactions using voltage alternation.* Journal of Colloid and Interface Science, 2004. **280**(1): p. 149-154.

31. Ziemer, J.K., *Performance of Electrospray Thrusters*, in *31st International Electric Propulsion Conference*2009: Ann Arbor, Michigan.

32. Martel, F., L. Perna, and P. Lozano, *Miniature Ion Electrospray Thrusters and Performance Tests on Cubesats*, in *Proceedings of the AIAA/USU Conference on Small Satellites*2012.

33.	Chiu, Y.-H., et al., *Mass Spectrometric Analysis of Colloid Thruster Ion Emission from Selected Propellants.* Journal of Propulsion and Power, 2005. **21**(3): p. 416-423.

34.	Romero-Sanz, I., et al., *Source of heavy molecular ions based on Taylor cones of ionic liquids operating in the pure ion evaporation regime.* Journal of Applied Physics, 2003. **94**(5): p. 3599-3605.

35.	Courtney, D.G. and P. Lozano, *Characterization of Conical Ionic Liquid Ion Sources for 2-D Electrospray Thruster Arrays on Porous Substrates.* TRANSACTIONS OF THE JAPAN SOCIETY FOR AERONAUTICAL AND SPACE SCIENCES, AEROSPACE TECHNOLOGY JAPAN, 2010. **8**(ists27): p. Pb_73-Pb_78.

36.	Legge, R.S. and P.C. Lozano, *Electrospray Propulsion Based on Emitters Microfabricated in Porous Metals.* Journal of Propulsion and Power, 2011. **27**(2): p. 485-495.

37.	Courtney, D.G., H. Li, and P.C. Lozano, *Electrochemical Micromachining on Porous Nickel for Arrays of Electrospray Ion Emitters.* Journal of Microelectromechanical Systems, 2013. **22**(2): p. 471-482.

38.	Miller, C.E., et al. *Characterization of EMI-(HF)2.3F Using Carbon Xerogel Electrospray Thrusters*. in *35th International Electric Propulsion Conference*. 2017. Atlanta, Georgia, USA.

39.	Brikner, N. and P.C. Lozano, *The role of upstream distal electrodes in mitigating electrochemical degradation of ionic liquid ion sources.* Applied Physics Letters, 2012. **101**(19): p. -.

40.	Krpoun, R., *Micromachined Electrospray Thrusters for Spacecraft Propulsion.* Institute of Microengineering, 2009, Swiss Federal Institute of Technology in Lausanne, Lausanne.

41.	Krejci, D., et al., *Emission Characteristics of Passively Fed Electrospray Microthrusters with Propellant Reservoirs.* Journal of Spacecraft and Rockets, 2017. **54**(2): p. 447-458.

42.	Goebel, D.M. and I. Katz, *Fundamentals of electric propulsion: ion and Hall thrusters*. Vol. 1. 2008: John Wiley & Sons.

43.	Miller, S.W., et al., *Electrospray of 1-Butyl-3-Methylimidazolium Dicyanamide Under Variable Flow Rate Operations.* Journal of Propulsion and Power, 2014: p. 1-10.

44.	Miller, C.E. and P.C. Lozano, *Measurement of the Fragmentation Rates of Solvated Ions in Ion Electrospray Thrusters*, in *52nd AIAA/SAE/ASEE Joint Propulsion Conference*2016: Salt Lake City, UT.

45.	Rosensweig, R.E., *Magnetic Fluids.* Annual Review of Fluid Mechanics, 1987. **19**: p. 437-461.

46.	Meyer IV, E.J., *Development of an Ionic Liquid Ferrofluid Electrospray Source and Mode Shape Studies of a Ferrofluid in a Non-uniform Magnetic Field.* Mechanical Engineering - Engineering Mechanics, 2014, Doctoral Dissertation, Michigan Technological University, Houghton, MI.

47.   Ghatee, M.H. and A.R. Zolghadr, *Surface tension measurements of imidazolium-based ionic liquids at liquid–vapor equilibrium.* Fluid Phase Equilibria, 2008. **263**(2): p. 168-175.

48.   MacFarlane, D.R., et al., *Ionic liquids based on imidazolium, ammonium and pyrrolidinium salts of the dicyanamide anion.* Green Chemistry, 2002. **4**(5): p. 444-448.

49.   Bini R Fau - Bortolini, O., et al., *Development of cation/anion "interaction" scales for ionic liquids through ESI-MS measurements.* Journal of Physical Chemistry B, 2007(1520-6106 (Print)).

50.   Stalcup, A.M. and B. Cabovska, *Ionic Liquids in Chromatography and Capillary Electrophoresis.* Journal of Liquid Chromatography & Related Technologies, 2005. **27**(7-9): p. 1443-1459.

51.   Zheng, J. and Z. Row, *Effects of Ionic Liquid on the Separation of 2-Chlorophenol and 2,4,6-Trichlorophenol in RP-HPLC.* Journal of Chromatographic Science, 2009. **47**(5): p. 392-395.

52.   Garoz, D., et al., *Taylor cones of ionic liquids from capillary tubes as sources of pure ions: The role of surface tension and electrical conductivity.* Journal of Applied Physics, 2007. **102**(6): p. 064913-10.

53.   Alexander, M.S., et al., *Electrospray Performance of Microfabricated Colloid Thruster Arrays.* Journal of Propulsion and Power, 2006. **22**(3): p. 620-627.

54.   Grustan-Gutierrez, E., S. Jhuree, and J.P.W. Stark. *Modelling of Colloid Thrusters for Mission Analysis*. in *35th International Electric Propulsion Conference*. 2017. Atlanta, Georgia, USA.

55.   Lozano, P.C., *Energy properties of an EMI-Im ionic liquid ion source.* Journal of Physics D: Applied Physics, 2006. **39**(1): p. 126.

56.   Gamero-Castaño, M., *Characterization of the electrosprays of 1-ethyl-3-methylimidazolium bis(trifluoromethylsulfonyl) imide in vacuum.* Physics of Fluids, 2008. **20**(3): p. 032103.

57.   Prince, B.D., *Droplet Measurements in TOF-MS,* 11 December 2014, *Personal Communication*.

58.   Miller, S.W., et al., *Mass Spectrometry of Selected Ionic Liquids in Capillary Electrospray at Nanoliter Volumetric Flow Rates*, in *52nd AIAA/SAE/ASEE Joint Propulsion Conference*2016: Salt Lake City, UT.

59.   Papell, S.S., *Low viscosity magnetic fluid obtained by the colloidal suspension of magnetic particles*, 1965, USA, 3,215,572.

60.   Odenbach, S., *Ferrofluids—magnetically controlled suspensions.* Colloids and Surfaces A: Physicochemical and Engineering Aspects, 2003. **217**(1–3): p. 171-178.

61.   Raj, K., B. Moskowitz, and R. Casciari, *Advances in ferrofluid technology.* Journal of Magnetism and Magnetic Materials, 1995. **149**(1–2): p. 174-180.

62.   Laurent, S., et al., *Magnetic iron oxide nanoparticles: synthesis, stabilization, vectorization, physicochemical characterizations, and biological applications.* Chemical reviews, 2008. **108**(6): p. 2064-2110.

63.   Halbreich, A., et al., *Biomedical applications of maghemite ferrofluid.* Biochimie, 1998. **80**(5–6): p. 379-390.

64.   Rudolf, H., et al., *Magnetic particle hyperthermia: nanoparticle magnetism and materials development for cancer therapy.* Journal of Physics: Condensed Matter, 2006. **18**(38): p. S2919.

65.   Rosensweig, R.E., J.W. Nestor, and R.S. Timmins, *Ferrohydrodynamics fluids for direct conversion of heat energy*1965, United Kingdom: Institution of Chemical Engineers.

66.   Rosensweig, R.E. and R. Kaiser, *Study of Ferromagnetic Liquid, Phase I*, 1967, NASA Office of Advanced Research and Technology: Washington, D.C.

67.   Boudouvis, A.G., et al., *Normal field instability and patterns in pools of ferrofluid.* Journal of Magnetism and Magnetic Materials, 1987. **65**(2–3): p. 307-310.

68.   Berger, P., et al., *Preparation and Properties of an Aqueous Ferrofluid.* Journal of Chemical Education, 1999. **76**(7): p. 943.

69.   Auzans, E., et al., *Synthesis and properties of Mn-Zn ferrite ferrofluids.* Journal of Materials Science, 1999. **34**(6): p. 1253-1260.

70.   Jain, N., et al., *Optimized steric stabilization of aqueous ferrofluids and magnetic nanoparticles.* Langmuir, 2009(1520-5827 (Electronic)).

71.   Mestrom, L., et al., *Stable ferrofluids of magnetite nanoparticles in hydrophobic ionic liquids.* Nanotechnology, 2015. **26**(28): p. 285602.

72.   Rodríguez-Arco, L., et al., *Steric repulsion as a way to achieve the required stability for the preparation of ionic liquid-based ferrofluids.* Journal of Colloid and Interface Science, 2011. **357**(1): p. 252-254.

73.   Huang, W. and X. Wang, *Study on the properties and stability of ionic liquid-based ferrofluids.* Colloid and Polymer Science, 2012. **290**(16): p. 1695-1702.

74.   Zakinyan, A., E. Tkacheva, and Y. Dikansky, *Dynamics of a dielectric droplet suspended in a magnetic fluid in electric and magnetic fields.* Journal of Electrostatics, 2012. **70**(2): p. 225-232.

75.   Dikanskii, Y.I., O.A. Nechaeva, and A.R. Zakinyan, *Deformation of magnetosensitive emulsion microdroplets in magnetic and electric fields.* Colloid Journal, 2006. **68**(2): p. 137-141.

76.   Tyatyushkin, A.N. and M.G. Velarde, *On the Interfacial Deformation of a Magnetic Liquid Drop under the Simultaneous Action of Electric and Magnetic Fields.* Journal of Colloid and Interface Science, 2001. **235**(1): p. 46-58.

77.   Mkrtchyan, L., A. Zakinyan, and Y. Dikansky, *Electrocapillary Instability of Magnetic Fluid Peak.* Langmuir, 2013. **29**(29): p. 9098-9103.

78.   Dikansky, Y.I. and O.A. Nechaeva, *Electrohydrodynamical instability of microdrops shapes in a magnetic fluid.* Journal of Magnetism and Magnetic Materials, 2005. **289**: p. 90-92.

79.   Lozano, P.C., et al., *Nanoengineered thrusters for the next giant leap in space exploration.* MRS Bulletin, 2015. **40**(10): p. 842-849.

80.   Li, H.Q., et al. *Fabrication and testing of an ionic electrospray propulsion system with a porous metal tip array*. in *2011 16th International Solid-State Sensors, Actuators and Microsystems Conference*. 2011.

81.   King, L.B., *Ferroelectrohydrodynamics of ionic liquid ferrofluid surface instabilities and jets*, in *50th AIAA/ASME/SAE/ASEE Joint Propulsion Conference & Exhibit*2014: Cleveland, OH.

82. Fröba, A.P., H. Kremer, and A. Leipertz, *Density, Refractive Index, Interfacial Tension, and Viscosity of Ionic Liquids [EMIM][EtSO4], [EMIM][NTf2], [EMIM][N(CN)2], and [OMA][NTf2] in Dependence on Temperature at Atmospheric Pressure.* The Journal of Physical Chemistry B, 2008. **112**(39): p. 12420-12430.

83. Kim, S.J., et al., *Surface wettability change during pool boiling of nanofluids and its effect on critical heat flux.* International Journal of Heat and Mass Transfer, 2007. **50**(19): p. 4105-4116.

84. Tanvir, S. and L. Qiao, *Surface tension of Nanofluid-type fuels containing suspended nanomaterials.* Nanoscale Research Letters, 2012. **7**(1): p. 226.

85. Bao Jie Zhu, W.L.Z., Jin Kai Li, Yan Xiang Guan, Dong Dong Li, *Thermophysical Properties of Al₂O₃-Water Nanofluids.* Materials Science Forum, 2011. **688**: p. 266-271.

86. Bhuiyan, M.H.U., et al., *Effect of Nanoparticles Concentration and Their Sizes on Surface Tension of Nanofluids.* Procedia Engineering, 2015. **105**(Supplement C): p. 431-437.

87. Radiom, M., C. Yang, and W.K. Chan. *Characterization of surface tension and contact angle of nanofluids*. in *Fourth International Conference on Experimental Mechanics*. 2010. International Society for Optics and Photonics.

88. Saeid, V., et al., *The effect of nanoparticles on the liquid–gas surface tension of Bi 2 Te 3 nanofluids.* Nanotechnology, 2009. **20**(18): p. 185702.

89. Miller, S.W., B.D. Prince, and J.L. Rovey. *Capillary Extraction of the Ionic Liquid [Bmim][DCA] for Variable Flow Rate Operations*. in *48th AIAA/ASME/SAE/ASEE Joint Propulsion Conference & Exhibit*. 2012. Atlanta, Georgia: AIAA.

90. Cloupeau, M. and B. Prunet-Foch, *Electrostatic spraying of liquids in cone-jet mode.* Journal of Electrostatics, 1989. **22**(2): p. 135-159.

91. Jaworek, A. and A. Krupa, *CLASSIFICATION OF THE MODES OF EHD SPRAYING.* Journal of Aerosol Science, 1999. **30**(7): p. 873-893.

92. Jaworek, A. and A. Krupa, *Jet and drops formation in electrohydrodynamic spraying of liquids. A systematic approach.* Experiments in Fluids, 1999. **27**(1): p. 43-52.

93. Makela, J.M., *Re-generable Field Emission Cathodes for Electric Propulsion.* Mechanical Engineering – Engineering Mechanics, 2010, Michigan Technological University, Houghton, MI.

94. Jackson, B.A., K.J. Terhune, and L.B. King, *Ionic liquid ferrofluid interface deformation and spray onset under electric and magnetic stresses.* Physics of Fluids, 2017. **29**(6): p. 064105.

95. Miller, S.W., *ANALYSIS OF ION EMITTING JET STRUCTURES DURING IONIC LIQUID ELECTROSPRAYING.* AEROSPACE ENGINEERING, 2015, Doctoral, MISSOURI UNIVERSITY OF SCIENCE AND TECHNOLOGY, Rolla, MO.

96. Kaiser, R., et al., *Study of ferromagnetic liquid*1969, [Washington]: [National Aeronautics and Space Administration]; for sale by the Clearinghouse for Federal Scientific and Technical Information, Springfield, Va.

97. Grosse, C. and A.V. Delgado, *Dielectric dispersion in aqueous colloidal systems.* Current Opinion in Colloid & Interface Science, 2010. **15**(3): p. 145-159.

98. Jayasinghe, S.N. and M.J. Edirisinghe, *Electrostatic atomisation of a ceramic suspension.* Journal of the European Ceramic Society, 2004. **24**(8): p. 2203-2213.

99. Suh, J., et al., *Highly charging of nanoparticles through electrospray of nanoparticle suspension.* Journal of Colloid and Interface Science, 2005. **287**(1): p. 135-140.

100. Zhu, T., et al., *Electrospray Dense Suspensions of TiO2 Nanoparticles for Dye Sensitized Solar Cells.* Aerosol Science and Technology, 2013. **47**(12): p. 1302-1309.

101. Halimi, S.U., et al., *Electrospray deposition of titanium dioxide (TiO2) nanoparticles.* AIP Conference Proceedings, 2014. **1586**(1): p. 57-62.

102. Fernández de la Mora, J., *The Fluid Dynamics of Taylor Cones.* Annual Review of Fluid Mechanics, 2006. **39**(1): p. 217-243.

103. Higuera, F.J., *Flow rate and electric current emitted by a Taylor cone.* Journal of Fluid Mechanics, 2003. **484**: p. 303-327.

104. Gamero-Castaño, M. and J. Fernández de la Mora, *Direct measurement of ion evaporation kinetics from electrified liquid surfaces.* The Journal of Chemical Physics, 2000. **113**(2): p. 815-832.

105. Gañán-Calvo, A.M., *On the theory of electrohydrodynamically driven capillary jets.* Journal of Fluid Mechanics, 1997. **335**: p. 165-188.

106. Legge, R.S., Jr., *Fabrication and Characterization of Porous Metal Emitters for Electrospray Applications.* Department of Aeronautics and Astronautics, 2008, Massachusetts Institute of Technology, Cambridge.

107. Madden, A., et al., *Effect of a homogeneous magnetic field on the electrospraying characteristics of sulfolane ferrofluids*, 2016, Yale University.

108. Driesel, W., C. Dietzsch, and M. Moser, *In-situ HV TEM observation of the tip shape of lead liquid metal ion sources.* J. Phys. D: Appl. Phys, 1996. **29**: p. 2492-2500.

109. De La Mora, J.F., *The effect of charge emission from electrified liquid cones.* Journal of Fluid Mechanics, 1992. **243**: p. 561-574.

110. Jackson, B.A., *Characterization of an Ionic Liquid Ferrofluid Electrospray Emission Pattern*, in *50th AIAA/ASME/SAE/ASEE Joint Propulsion Conference & Exhibit* 2014: Cleveland, OH.

111. Cui, Y., et al., *Design and operation of a retarding field energy analyzer with variable focusing for space-charge-dominated electron beams.* Review of Scientific Instruments, 2004. **75**(8): p. 2736-2745.

112. Enloe, C.L. and J.R. Shell, *Optimizing the energy resolution of planar retarding potential analyzers.* Review of Scientific Instruments, 1992. **63**(2): p. 1788-1791.

113. Partridge, J.M., *DEVELOPMENT OF A MICRO-RETARDING POTENTIAL ANALYZER FOR HIGH-DENSITY FLOWING PLASMAS* Mechanical Engineering, 2005, Masters Thesis, WORCESTER POLYTECHNIC INSTITUTE, Worcester.

114. Satir, M., et al., *Design of the retarding potential analyzer to be used with BURFIT-80 Ion thruster and validation using PIC-DSMC code*, in *2015 7th International Conference on Recent Advances in Space Technologies (RAST)* 2015. p. 577-582.

115. Hutchinson, I.H., *Principles of Plasma Diagnostics*. 2 ed2002, Cambridge: Cambridge University Press.

116. Berg, S.P., *Design and development of ionic liquid dual-mode spacecraft propellants.* Aerospace Engineering, 2012, Masters Thesis, Missouri University of Science and Technology, Rolla.

117. Gamero-Castaño, M., *The Expansion of Colloid Thruster Beams and its Dependence on Emission Temperature*, in *49th AIAA/ASME/SAE/ASEE Joint Propulsion Conference*2013, American Institute of Aeronautics and Astronautics.

118. !!! INVALID CITATION !!!

119. Morad, M.R., et al., *A Very Stable High Throughput Taylor Cone-jet in Electrohydrodynamics.* 2016. **6**: p. 38509.

120. Jackson, B.A. and L.B. King. *Time Resolved Divergence Mapping and Long Duration Emission Studies of an Ionic Liquid Ferrofluid Electrospray Source*. in *35th International Electric Propulsion Conference*. 2017. Atlanta, Georgia, USA.

121. Jackson, G.P. and D.C. Duckworth, *Electrospray mass spectrometry of undiluted ionic liquids.* Chemical Communications, 2004. **0**(5): p. 522-523.

122. Dyson, P.J., et al., *Direct probe electrospray (and nanospray) ionization mass spectrometry of neat ionic liquids.* Chemical Communications, 2004. **0**(19): p. 2204-2205.

123. Gamero-Castaño, M., *Electrosprayed Heavy Ion and Nanodrop Beams for Surface Engineering and Electrical Propulsion*, 2014, University of California, Irvine.

124. Nabity, J.A. and J.W. Daily, *Effect of Ionic Liquid Composition on Colloid Thruster Emission and Thrust Performance.* Journal of Propulsion and Power, 2017: p. 0-0.

125. Chowdhury, S.K., V. Katta, and B.T. Chait, *An electrospray-ionization mass spectrometer with new features.* Rapid Communications in Mass Spectrometry, 1990. **4**(3): p. 81-87.

126. Hofstadler, S.A. and D.A. Laude, *Trapping and detection of ions generated in a high magnetic field electrospray ionization Fourier transform ion cyclotron resonance mass spectrometer.* Journal of the American Society for Mass Spectrometry, 1992. **3**(6): p. 615-623.

127. Wu, Q., et al., *A high performance low magnetic field internal electrospray ionization-fourier transform ion cyclotron resonance mass spectrometer.* Journal of the American Society for Mass Spectrometry, 1996. **7**(9): p. 915-922.

128. Hofstadler, S.A. and D.A. Laude, *Electrospray ionization in the strong magnetic field of a Fourier transform ion cyclotron resonance mass spectrometer.* Analytical Chemistry, 1992. **64**(5): p. 569-572.

129. Balachandran, W., P. Miao, and P. Xiao, *Electrospray of fine droplets of ceramic suspensions for thin-film preparation.* Journal of Electrostatics, 2001. **50**(4): p. 249-263.

130. Böttger, P.H.M., et al., *Electrospraying of colloidal nanoparticles for seeding of nanostructure growth.* Nanotechnology, 2007. **18**(10): p. 105304.

131. Meyer, E.J., Lyon B. King. *Electrospray from an Ionic Liquid Ferrofluid utilizing the Rosensweig Instability* in *49th AIAA/ASME/SAE/ASEE Joint Propulsion Conference & Exhibit*. 2013. San Jose, CA.

242

132.   Fernández de la Mora, J., *On the Outcome of the Coulombic Fission of a Charged Isolated Drop.* Journal of Colloid and Interface Science, 1996. **178**(1): p. 209-218.

133.   Krpoun, R. and H.R. Shea, *Integrated out-of-plane nanoelectrospray thruster arrays for spacecraft propulsion.* Journal of Micromechanics and Microengineering, 2009. **19**(4): p. 045019.

134.   Prince, B.D., et al., *Molecular Dynamics Simulations of 1-Ethyl-3-methylimidazolium Bis[(trifluoromethyl)sulfonyl]imide Clusters and Nanodrops.* The Journal of Physical Chemistry A, 2015. **119**(2): p. 352-368.

135.   Prince, B.D., et al. *A Combined Experimental and Theoretical Treatment of Ionic Liquid Thermal Dissociation*. in *53rd AIAA/SAE/ASEE Joint Propulsion Conference*. 2017. American Institute of Aeronautics and Astronautics.

136.   Rupp, P., *Spatio-temporal phenomena in a ring of ferrofluid spines.* Physics, 2003, Doctoral thesis, University of Bayreuth,

137.   Meyer, E.J., Lyon B. King, Nirmesh Jain, and Brian S. Hawkett. *Ionic liquid ferrofluid electrospray with EMIM-NTf2 and ferrofluid mode studies with FerroTec EFH-1 in a non-uniform magnetic field* in *33rd International Electric Propulsion Conference* 2013. The George Washington University, USA.

138.   Ticknor, B., S.W. Miller, and Y.-H. Chiu. *Mass Spectrometric Analysis of the Electrospray Plume from an Externally Wetted Tungsten Ribbon Emitter*. in *46th AIAA/ASME/ASEE Joint Propulsion Conference and Exhibit*. 2009. Denver, Colorado.

139.   Terhune, K.J., Lyon B. King, Michael L. Hause, Benjamin D. Prince, Nirmesh Jain, Brian S. Hawkett. *Species measurements in the beam of an ionic liquid ferrofluid electrospray source*. in *50th AIAA/ASME/SAE/ASEE Joint Propulsion Conference & Exhibit*. 2014. Cleveland, OH.

140.   Dahl, D.A., *SIMION for the personal computer in reflection.* International Journal of Mass Spectrometry, 2000. **200**(3).

Appendix A.

µAmmeter Calibration Tables

Table A.1. Calibration for uA1 and uA2 microammeters

µA1		µA2	
Current (mA)	µA Voltage (V)	Current (mA)	µA Voltage (V)
0	3.5241	0	3.4
0.01	3.5245	0.01	3.4017
0.02	3.5248	0.02	3.4045
0.03	3.5254	0.03	3.4067
0.04	3.5257	0.04	3.4083
0.05	3.526	0.05	3.4115
0.06	3.5261	0.06	3.4133
0.07	3.5263	0.07	3.4146
0.08	3.527	0.08	3.4161
0.09	3.5275	0.09	3.4174
0.1	3.528	0.1	3.4184
0.11	3.5283	0.11	3.4196
0.12	3.5281	0.12	3.4204
0.13	3.5284	0.13	3.4222
0.14	3.5288	0.14	3.4235
0.15	3.5291	0.15	3.4254
0.16	3.5292	0.16	3.4271
0.17	3.5296	0.17	3.429
0.18	3.5301	0.18	3.431
0.19	3.5305	0.19	3.4308
0.2	3.5306	0.2	3.4322
0.21	3.5309	0.25	3.4386
0.22	3.531	0.3	3.4463
0.23	3.5315	0.35	3.4539
0.24	3.5322	0.4	3.4616
0.25	3.5325	0.45	3.4654
0.26	3.5331	0.5	3.4736
0.27	3.5334	0.55	3.4811
0.28	3.5334	0.6	3.4881
0.29	3.5341	0.65	3.4956
0.3	3.5343	0.7	3.5034
0.35	3.5361	0.75	3.5103
0.4	3.5383	0.8	3.5192
0.45	3.5402	0.85	3.5261

0.5	3.5422	0.9	3.5325
0.55	3.5436	0.95	3.5392
0.6	3.5452	1	3.5463
0.65	3.5463		
0.7	3.5483		
0.75	3.5504		
0.8	3.5522		
0.85	3.5543		
0.9	3.5558		
0.95	3.5571		
1	3.5587		
0	3.5233		

Table A.2. Calibration curves for uA2 microammeter

µA2								
	Run 2	Run 3	Run 4	Run 5	Run 6	Run 7	Run 8	Run 9
Current (µA)	µA Voltage (V)							
0	3.693	4.249	4.238	4.234	4.044	4.2165	4.238	4.226
100	3.712	4.259	4.257	4.253	4.054	4.234	4.255	4.243
300	3.7485	4.294	4.291	4.288	4.089	4.272	4.29	4.278
500	3.7885	4.331	4.325	4.324	4.126	4.308	4.327	4.314
700	3.8215	4.368	4.363	4.359	4.163	4.344	4.364	4.35
1000	3.8755	4.418	4.416	4.413	4.213	4.398	4.419	4.404
1200								4.44
1500								4.495
1800								4.545
2000								4.582

Appendix B.

Emission Frequency in Electrospray Onset Experiments

The onset potential experiment was also completed at vacuum pressure following the same procedure. The test yielded inconsistent emission even after the onset potential was reached and maintained. Note that with the application of the magnetic field, the frequency of emission onset and cessation was appreciably reduced, Figure B.1.

As noted previously, the onset potential of an electrospray source is higher than the extraction potential necessary to maintain emission. Normally when the onset potential was reached, the source continued to emit so long as it was sufficiently fed with propellant or the extraction potential applied to remained above a critical limit. The periodic emission onset and cessation observed in Figure B.1. occurred during an increase in extraction potential. This suggests that a lack of propellant (*i.e.* insufficient vial pressure) caused the phenomenon and that the measurement of the onset potential would not be for stable cone-jet emission, which is outside the scope of this research. While the experiment at vacuum was not successful in accurately measuring onset potential, it did show that the magnetic field affects other emission characteristics from a capillary source, specifically, it reduces the frequency of fluctuations in emission current. Similar results have been observed in my past experiments, wherein fluctuations in the emission current of an ILFF electrospray during operation were significantly reduced through the addition of a 200-Gauss magnetic field.
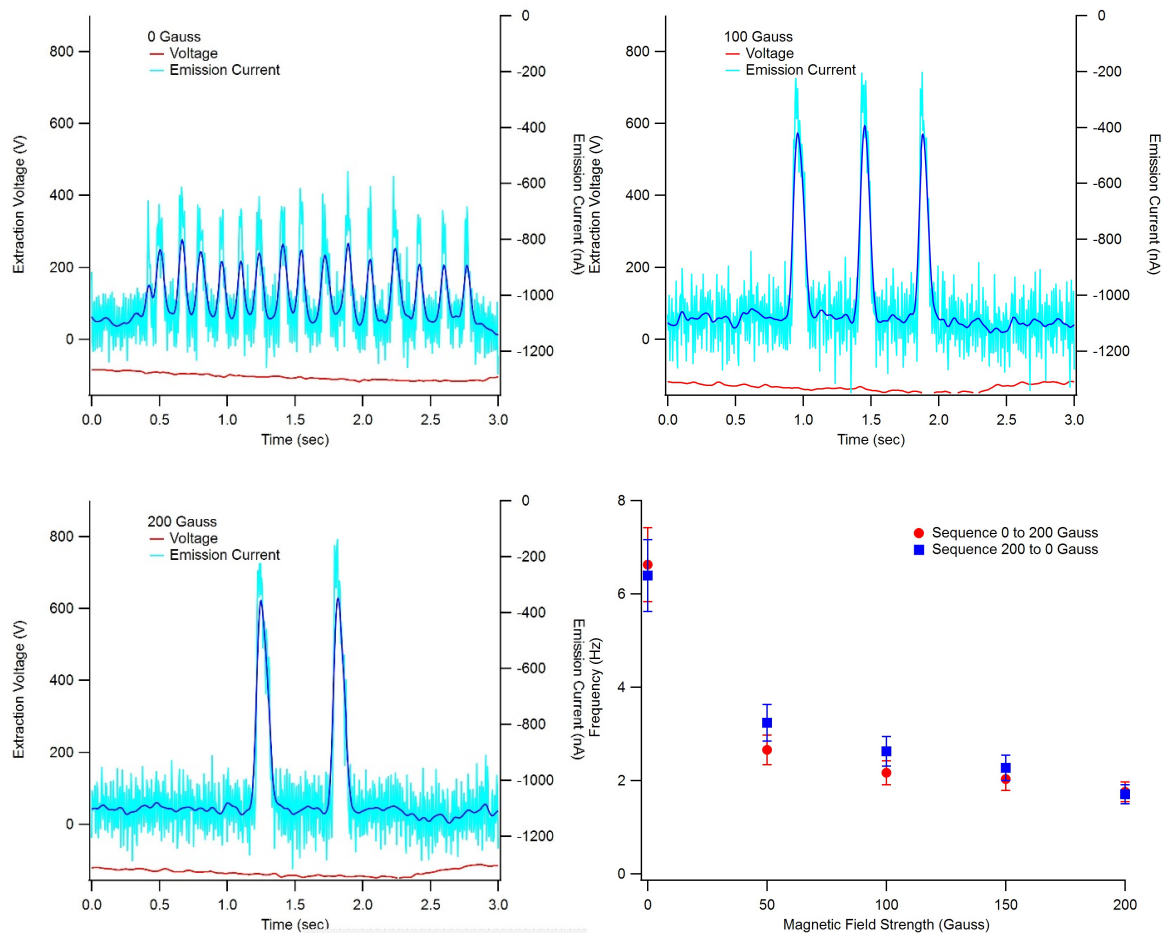
Figure B.1. Frequency in the emission current caused by zero-flow to needle apex while electrospray was subjected to a) zero magnetic field, b) a 100 Gauss magnetic field, and c) a 200 Gauss magnetic field. d) The frequency observed in the emission current plotted against the magnetic field strength subjected to the electrospray.

248

Appendix C.

Current Density Plots from Beam Divergence Experiment

Plots for the current densities as a function of beam half-angle for all operating conditions of the CES (including several presented in Sections 5.3.2. and 5.3.3.) are provided below. Those from Neat IL ILFF-20, ILFF30, and ILFF-40 electrosprays are in Figure C.1. and Figure C.2., Figure C.3. and Figure C.4., Figure C.5. and Figure C.6., and Figure C.7. and Figure C.8., respectively.
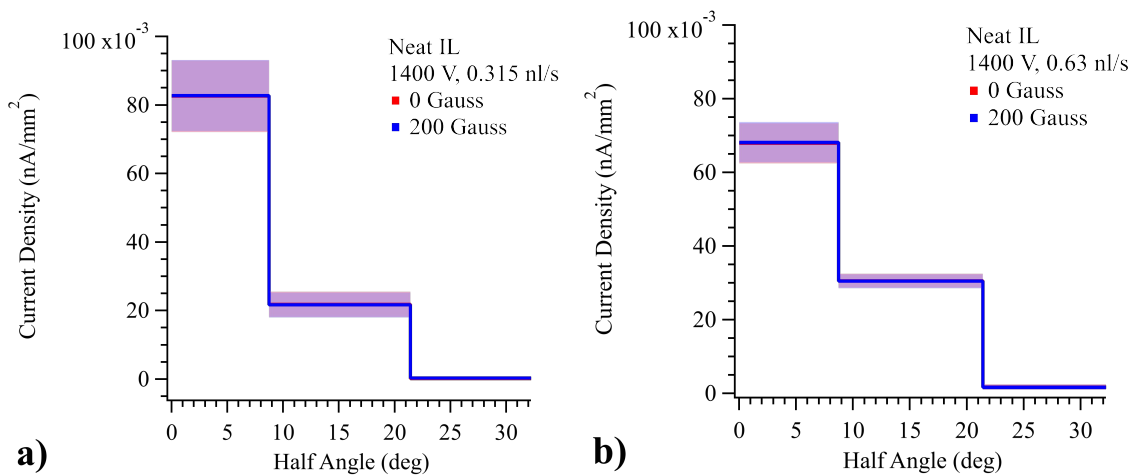
Figure C.1. Current density plots for neat IL electrospray from CES with and without B-field. Settings for Q and V_{ext} were a) 0.315 nl/s and 1400 V and b) 0.63 nl/s and 1400 V. Error shading is one standard deviation of mean current density.
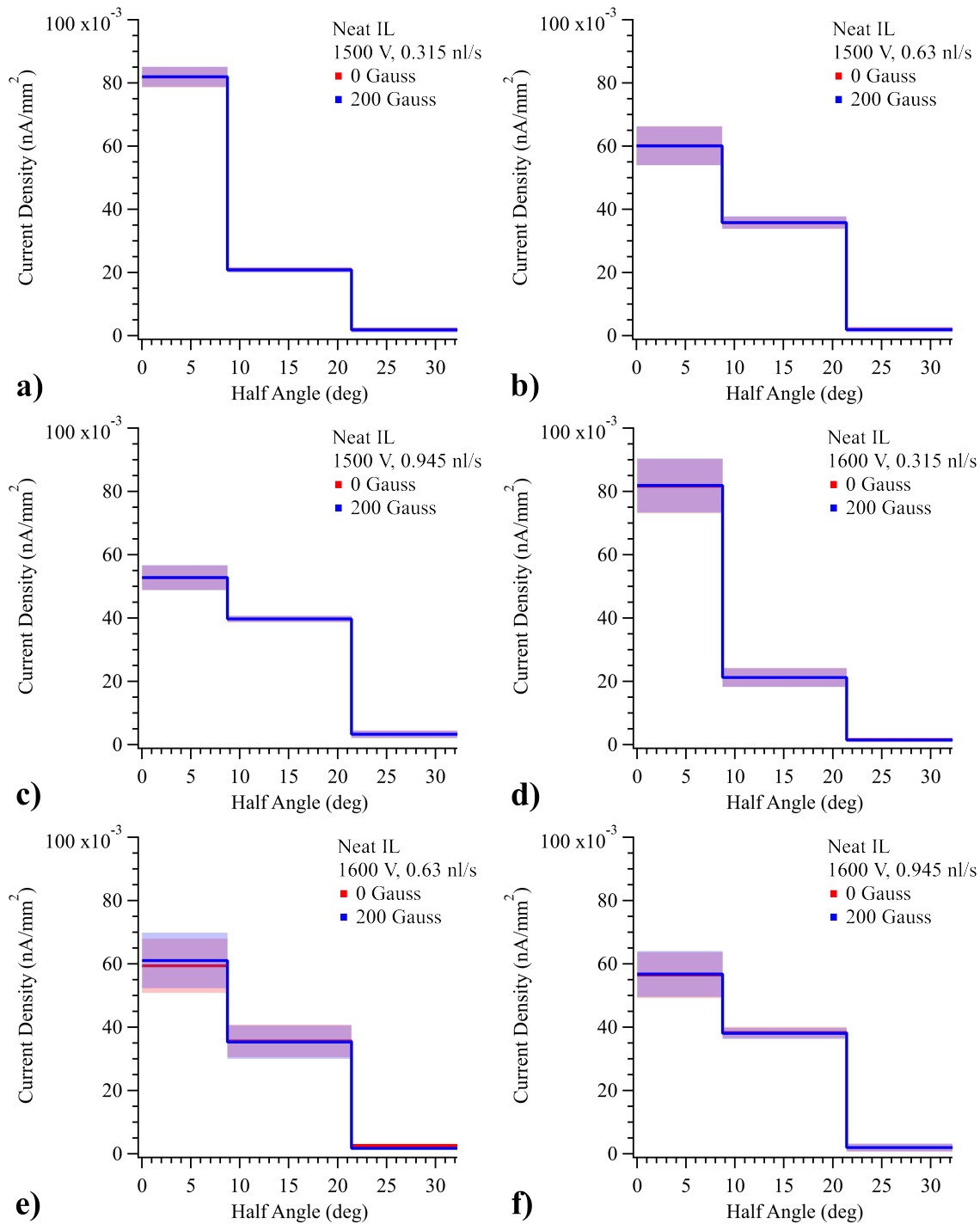
Figure C.2. Current density plots for neat IL electrospray from CES with and without B-field. Settings for *Q* and *V_{ext}* were a) 0.315 nl/s and 1500 V, b) 0.63 nl/s and 1500 V, c) 0.945 nl/s and 1500 V, d) 0.315 nl/s and 1600 V, e) 0.63 nl/s and 1600 V, and f) 0.945 nl/s and 1600 V. Error shading is one standard deviation of mean current density.

250
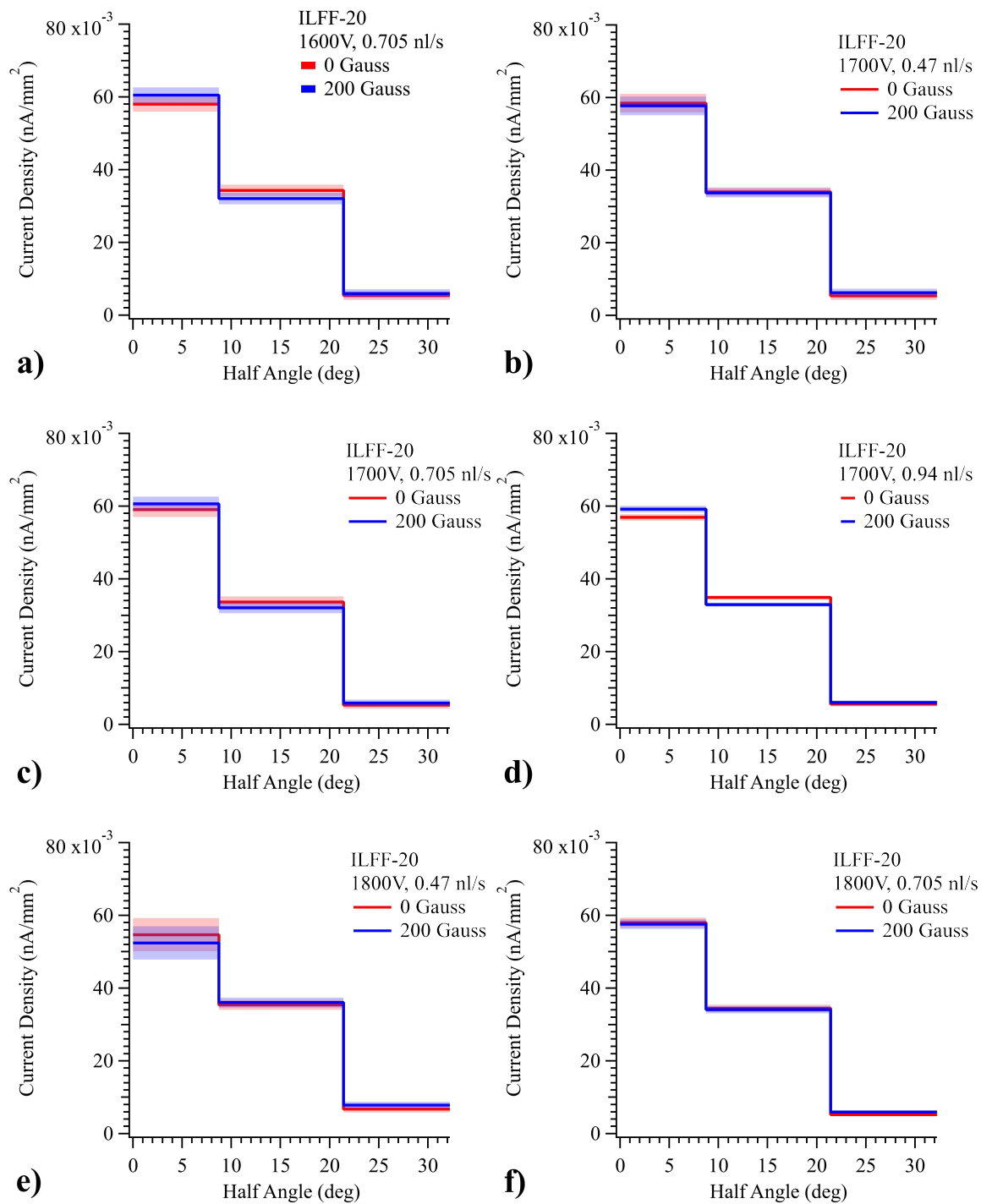
Figure C.3. Current density plots for ILFF-20 electrospray from CES with and without B-field. Settings for Q and V_{ext} were a) 0.705 nl/s and 1600 V, b) 0.47 nl/s and 1700 V, c) 0.705 nl/s and 1700 V, d) 0.94 nl/s and 1700 V, e) 0.47 nl/s and 1800 V, and f) 0.705 nl/s and 1800 V. Error shading is one standard deviation of mean current density.

251
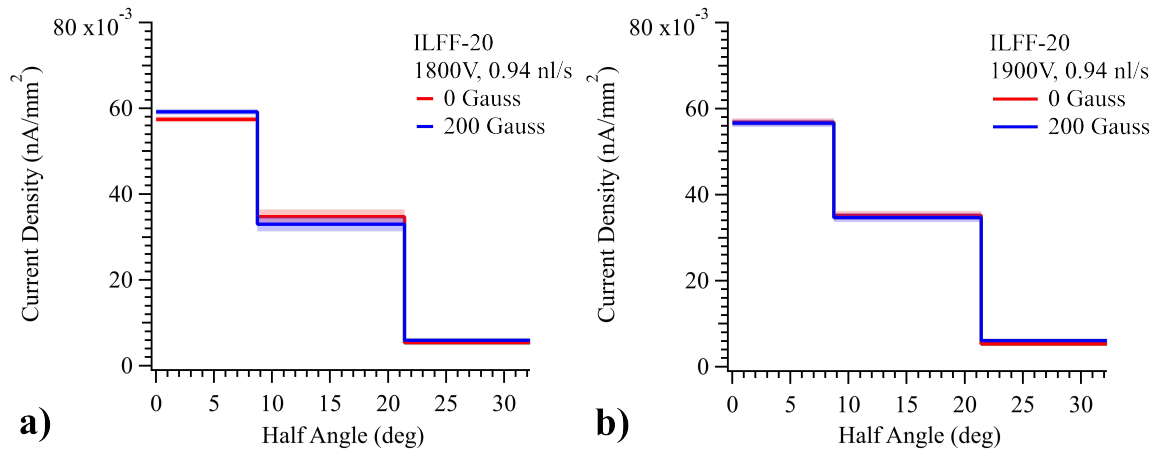
Figure C.4. Current density plots for ILFF-20 electrospray from CES with and without B-field. Settings for Q and V_ext are a)0.94 nl/s and 1800 V, and d) 0.94 nl/s and 1900 V. Error shading is one standard deviation of mean current density.
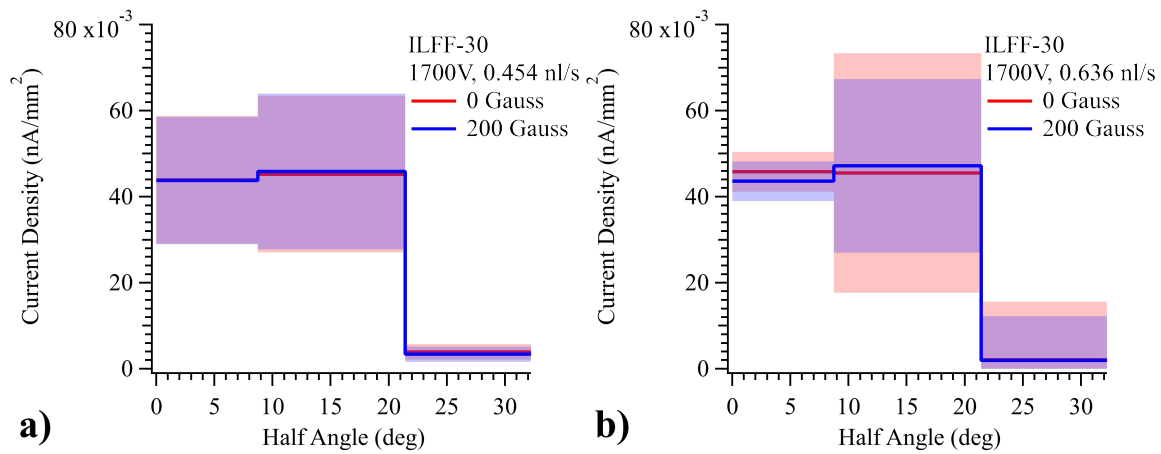
Figure C.5. Current density plots for ILFF-30 electrospray from CES with and without B-field. Settings for *Q* and *V_ext* were a) 0.454 nl/s and 1700 V and b) 0.636 nl/s and 1700 V. Error shading is one standard deviation of mean current density.
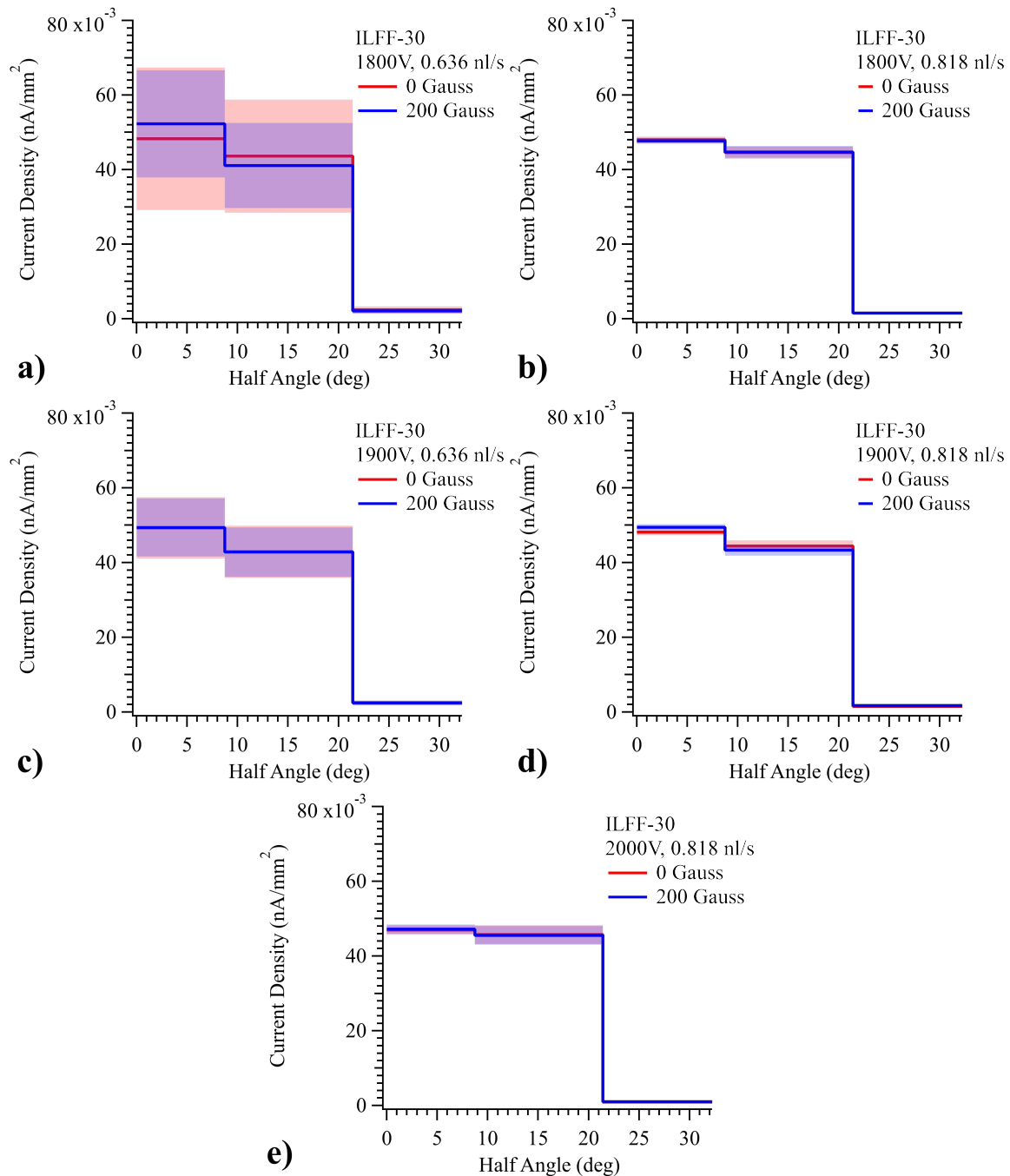
Figure C.6. Current density plots for ILFF-30 electrospray from CES with and without B-field. Settings for Q and V_{ext} were a) 0.636 nl/s and 1800 V, b) 0.818 nl/s and 1800 V, c) 0.636 nl/s and 1900 V, d) 0.818 nl/s and 1900 V, and e) 0.818 nl/s and 2000 V. Error shading is one standard deviation of mean current density.

253
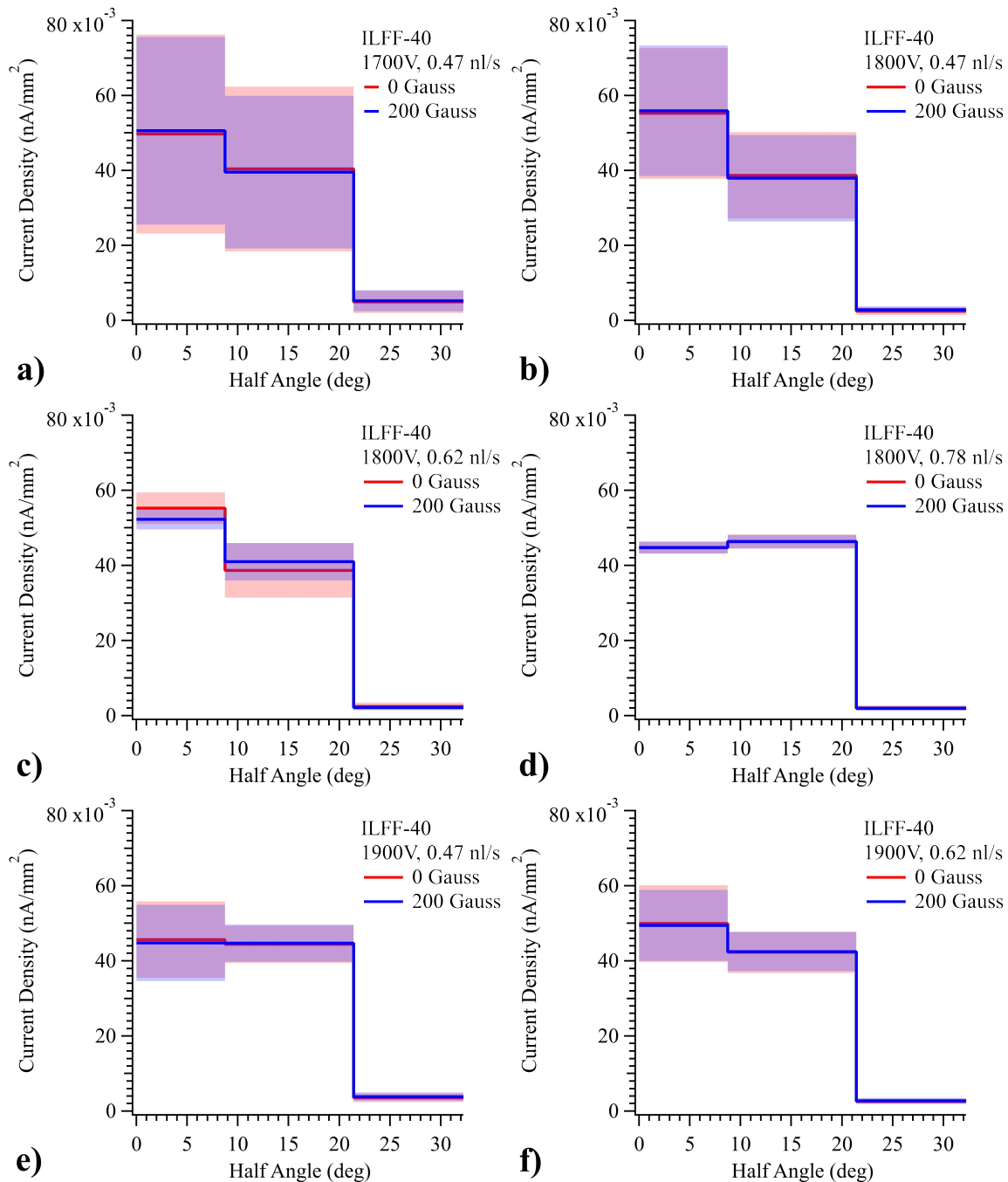
Figure C.7. Current density plots for ILFF-40 electrospray from CES with and without B-field. Settings for *Q* and *V*_{ext} were a) 0.47 nl/s and 1700 V, b) 0.47 nl/s and 1800 V, c) 0.62 nl/s and 1800 V, d) 0.78 nl/s and 1800 V, d) 0.47 nl/s and 1900 V, and f) 0.62 nl/s and 1900 V. Error shading is one standard deviation of mean current density.
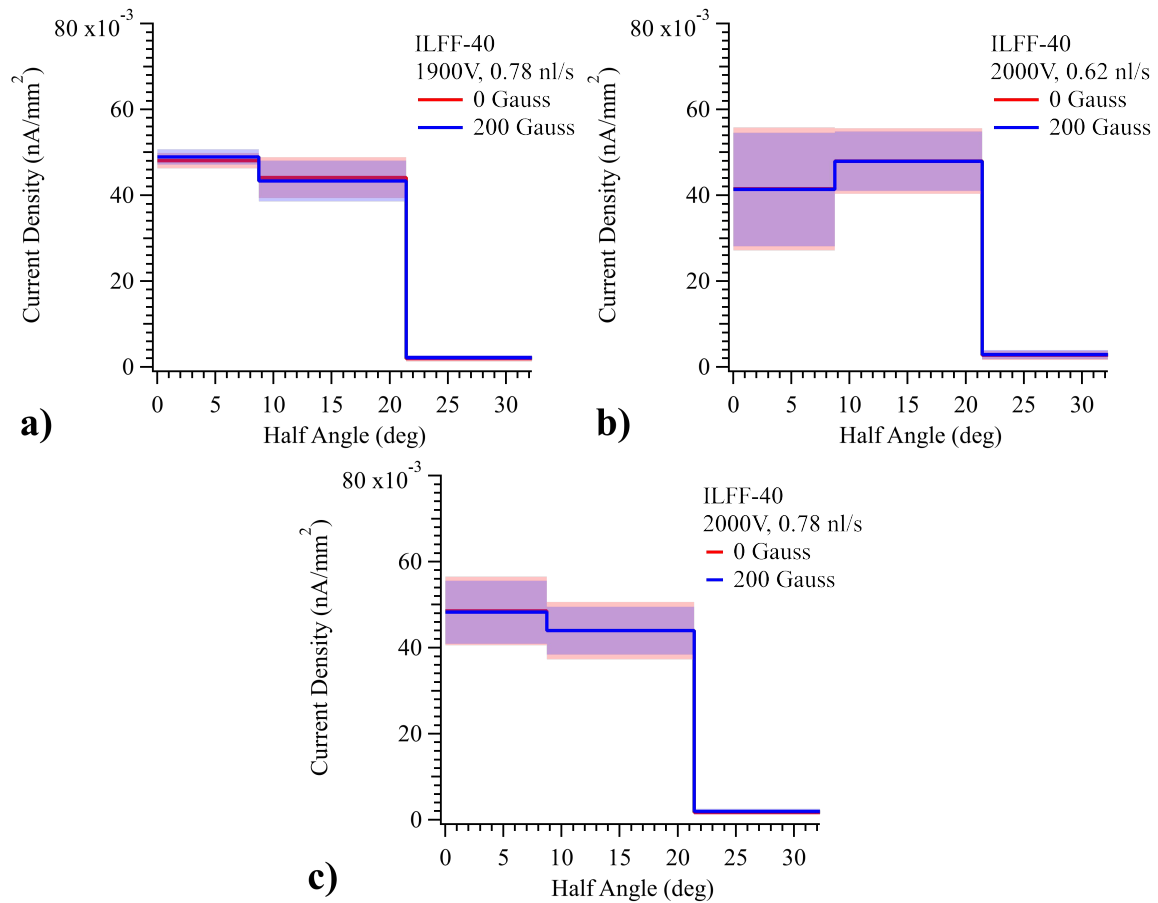
Figure C.8. Current density plots for ILFF-40 electrospray from CES with and without B-field. Settings for Q and V_{ext} were a) 0.78 nl/s and 1900 V, b) 0.62 nl/s and 2000 V, and c) 0.78 nl/s and 2000 V. Error shading is one standard deviation of mean current density.

Appendix D.

Motivation of Beam Energy Experiments

A motivating factor for the beam energy experiments was the measurement of beam energy using TOF mass spectrum data for magnetic-field-free and magnetically-stress ILFF electrosprays. The pulsing plates of the TOF-MS can act as an RPA by systematically increasing their bias potential until it equals that of the maximum particle potential, while measuring the current that enters the extraction region via a Faraday cup and the TOF MCP. Figure D.1. illustrates an example of how the pulsing plates were used as an RPA; in doing so it shows a correlation exists between the magnetic field strength and the kinetic energy of the ions emitted from the electrospray sources. In the figure, ψ_{peak} of the spectra is greater than 1 for energies between 600-700 eV, indicating a higher intensity of the $n = 0$ and $n = 1$ peaks of spectra collected from the source under a 200-Gauss magnetic field. This translates to an electrospray beam comprised of $n = 0$ and $n = 1$ ions with energies 100 eV greater than the most energetic ions within the electrospray beam under a 0-Gauss magnetic field. The results of Chapter 5 aligned with these results from the TOF-RPA experiment, and confirmed the necessity to gather TOF spectra at as many possible energies to ensure that the emission products of an electrospray are completely captured.
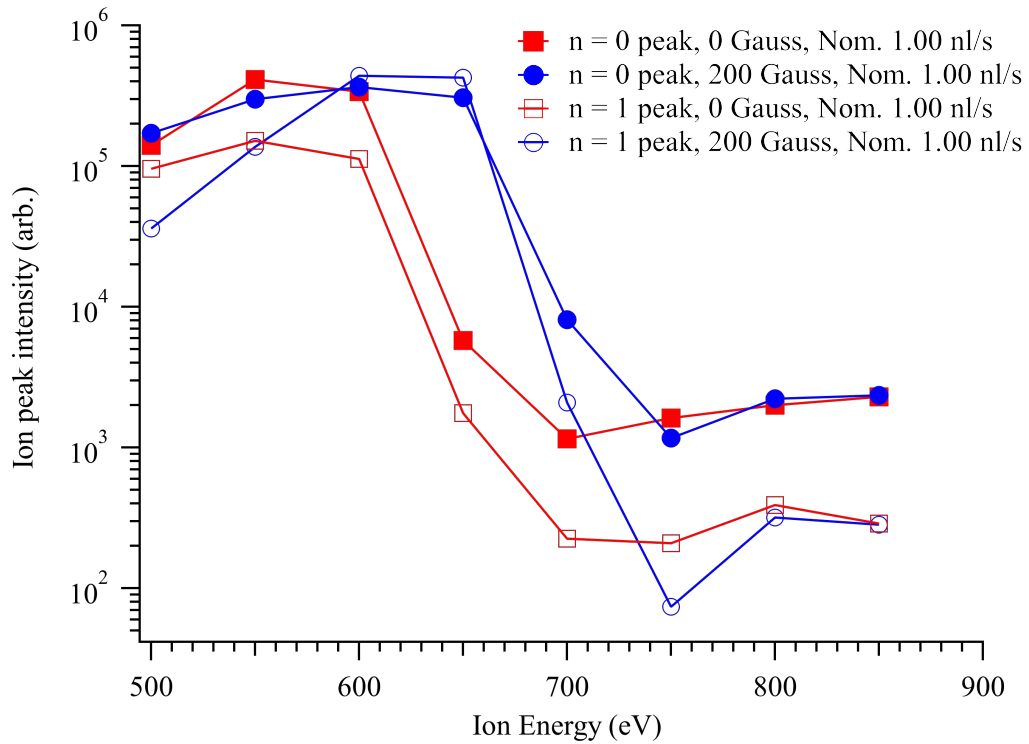
Figure D.1. Ion peak intensity as a function of ion energy illustrating use of pulsing plates as an energy analyzer. The magnetic effect on ion energy can be measured through a comparison of the red (0 Gauss) and blue (200 Gauss) curves.

Appendix E.

Magnetic Lorentz Force on Charged Particles in CES Electrospray Beam

The magnetic Lorentz force acting on different species of particles and droplets was calculated to determine whether it influence beam tightening or expansion. The full Lorentz force is defined as,

$$\mathbf{F}_{Lorentz} = q(\mathbf{E} + \mathbf{v} \times \mathbf{B}).$$ (E.1)

The region after the extractor plate of the CES is free of electric field influence, therefore the electric field term, $\mathbf{E}$, in (E.1) is zero; as such velocity, $\mathbf{v}$, and magnetic field strength, $\mathbf{B}$, are the only factors in calculating the Lorentz force. $\mathbf{B}$ is assumed to be a uniform to 200 Gauss field with a direction in line with the center axis of the electrospray beam. The velocity, $\mathbf{v}$, of each particle species was calculated based on the kinetic energy imparted on a particle by travelling through the electric field, $mv^2/2 = qE$. Rearranging the kinetic energy equation to solve for v produces the relationship,

$$v = \sqrt{2\frac{q}{m}V_{ext}},$$ (E.2)

where V_{ext} is the extraction potential; the direction of the velocity vector is the beam half angle. As the magnetic component of Lorentz force only acts particles travelling orthogonal to the magnetic field, only the radial component of velocity determined by (E.2) is used in its calculation.

The solution of Lorentz force in this experiment in time-variant; a particle's velocity vector is dependent on the amount of time the Lorentz force acts upon it, which consequently changes the magnitude of the Lorentz force. Thus, the Lorentz force acting a particle was calculated as a function of half-angle and its corresponding radial component of particle velocity. The starting velocity magnitude was assumed; this is an overestimate, as the velocity magnitude of an off-axis particle would be reduced by the Lorentz force as is progressed downstream. The magnitude of the Lorentz force was divided by the mass of the particle species to derive the acceleration, the second derivative of which provided the magnitude of orthogonal distance the particle shifted along its flight, Figure E.1.a). Simple trigonometry then produces the angular shift in in the velocity vector, Figure E.1.b).
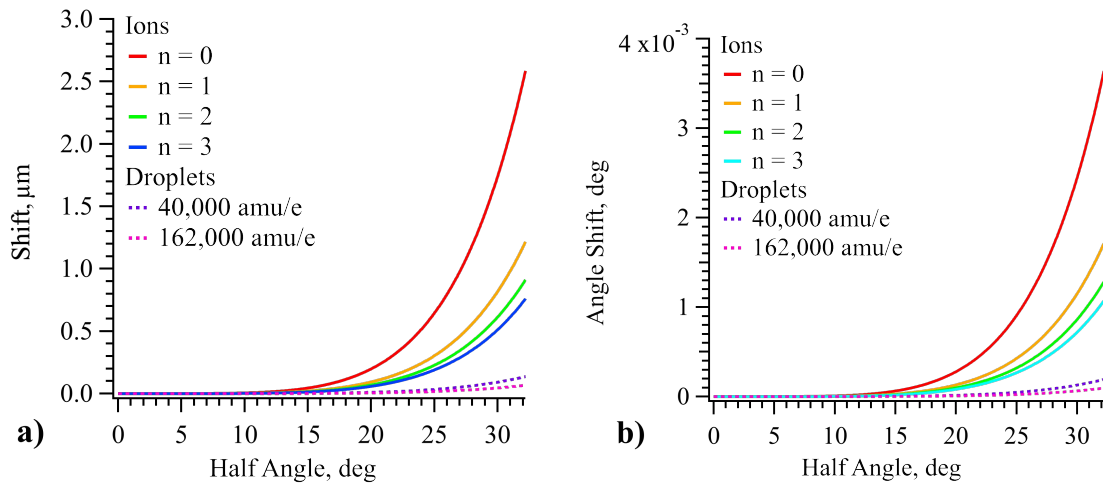
Figure E.1. a) Shift in particle location along the axis orthogonal to the electrospray beam axis after 41.75-mm of travel as a function of the half angle of the particle's starting velocity vector. b) Angular shift of the velocity vector of a particle after 41.75-mm of travel as a function of the half angle of the particle's starting velocity vector. The plotted particles are the primary species of ions and droplets in CES running on ILFF-30 propellant.

Figure E.1. proves that the Lorentz force will have negligible effect on particles or droplets emitted from the CES as it pertains to the collection of beam current on the Faraday

stack of the beam divergence experiment. Given that the velocity magnitude used in the derivation was an over-estimate only provides further proof of this conclusion.

Another way to interpret the effect of Lorentz force is examining the Larmor radius of some of the particles that would be within the electrospray beam. The Larmor radius, r_{larmor}, also known as the gyroradius, is the radius of the circular motion that a charged particle takes when it is in the presence of a magnetic field, and is found by equating Lorentz force to the centripetal force. The result is the expression shown in (E.3).

$$r_{larmor} = \frac{mv_{\perp}}{|q|B} \tag{E.3}$$

Here, $v_{\perp}$, is the perpendicular velocity of a particle.

The Larmor radius was calculated for ion species between n = 0 and n = 11, the two IL droplet species, and estimated IL coated NP all accelerated using a 2000-V extraction potential. $v_{\perp}$ of the particles differed depending on the half-angle of their initial velocity vector. The results are presented in Figure E.2. The results show that the Larmor radius is greater than the distance between the extractor plate of the CES and the SRP of the Faraday stack (Chapter 5) unless the initial particle velocity has a half angle less than 0.75 degrees. This means that within the Faraday Plate diagnostic the particles are not attached to the magnetic field lines unless they are within the center 1.5 degrees of the electrospray beam. This also explains why the potential shift in particle trajectory shown in Figure E.1. is relatively small compared to the length of the Faraday stack; *i.e.* the Larmor radius for particles at high angles is orders of magnitude greater than the length of the Faraday stack or the length of the Helmholtz coil (10 cm), and, therefore, the particles would move

relatively little in the radial direction over the course of traveling through the Faraday

Stack.
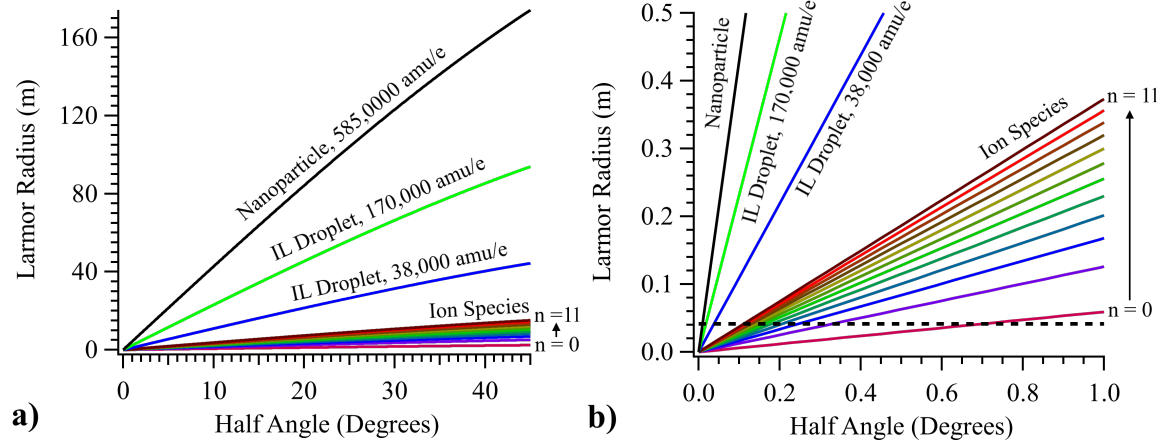
Figure E.2. a) Larmor radius of ion species, droplet species and the estimated NP species as a function of the half angle of the particle's initial velocity vector. b) Low-half-angle SRP Faraday plate in the Faraday stack (black dashed line at 41.75-mm) when the half-angle of the particles initial velocity vector is less than 1-degree.

Appendix F.

Beam Energy plots from RPA Experiment

This appendix provides the usable beam energy plots using all tested electrospray propellants, extraction potentials, and flowrates. Some of the RPA traces for certain flowrates were too noisy and consequently unmeaningful, and were therefore omitted for this appendix.
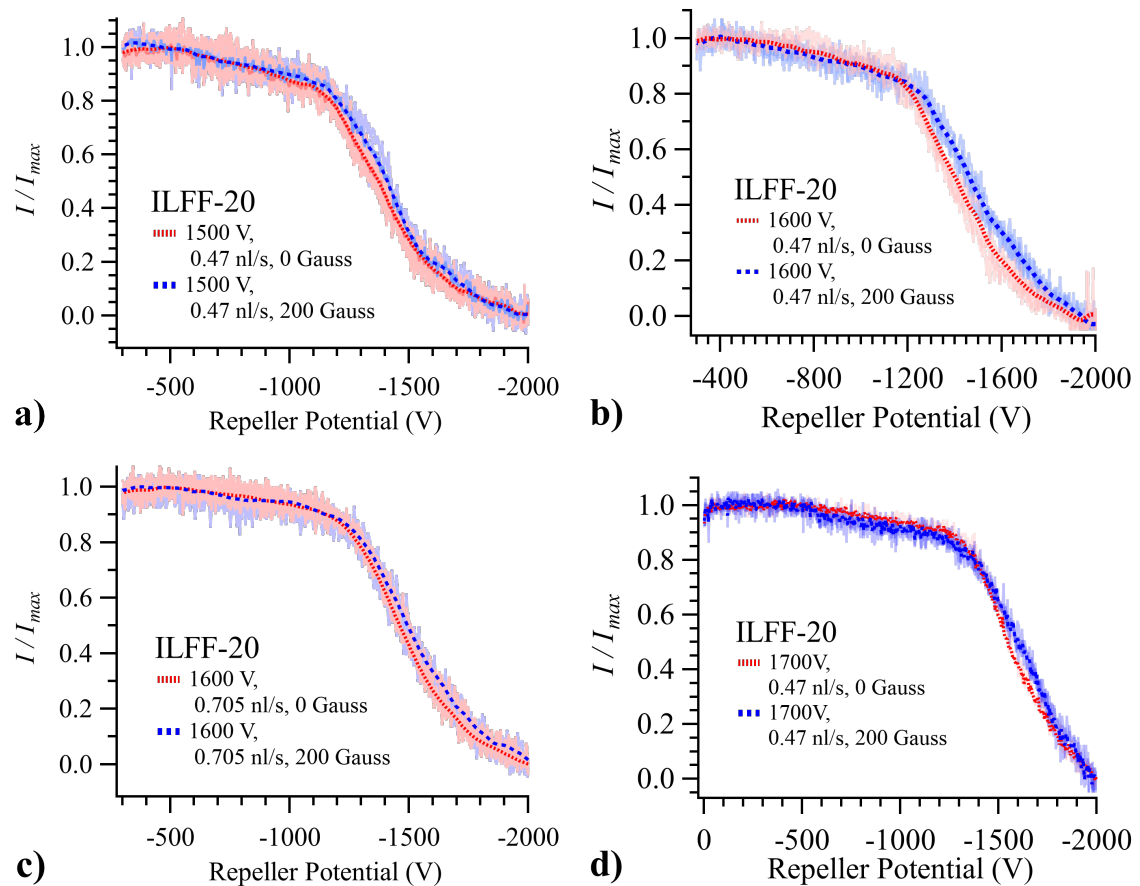
Figure F.1. Beam energy plots for the ILFF-20 electrosprays at various (Q, V_{ext}) settings
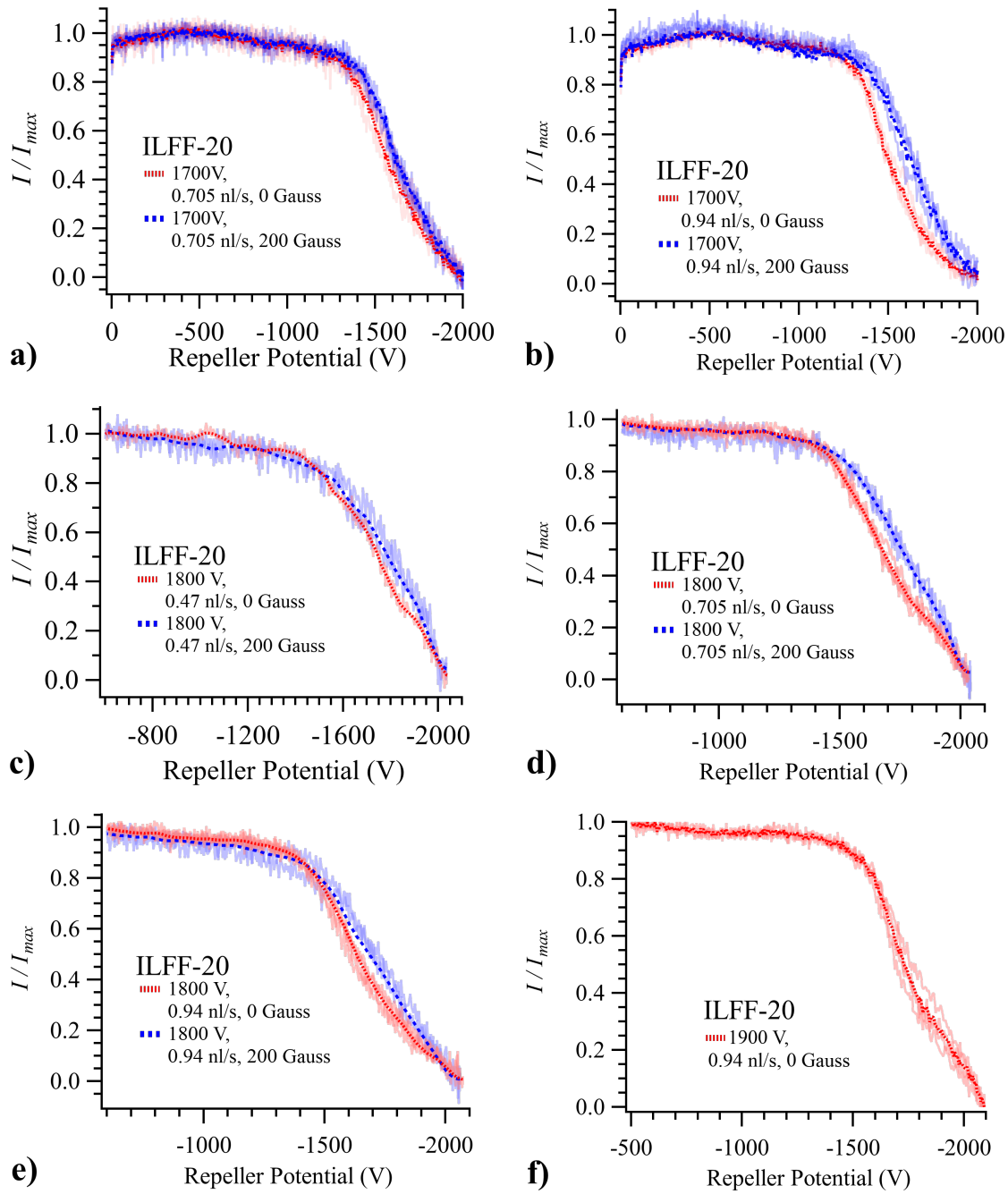
Figure F.2. Beam energy plots for the ILFF-20 electrosprays at various (*Q*, *V*$_{ext}$) settings

264
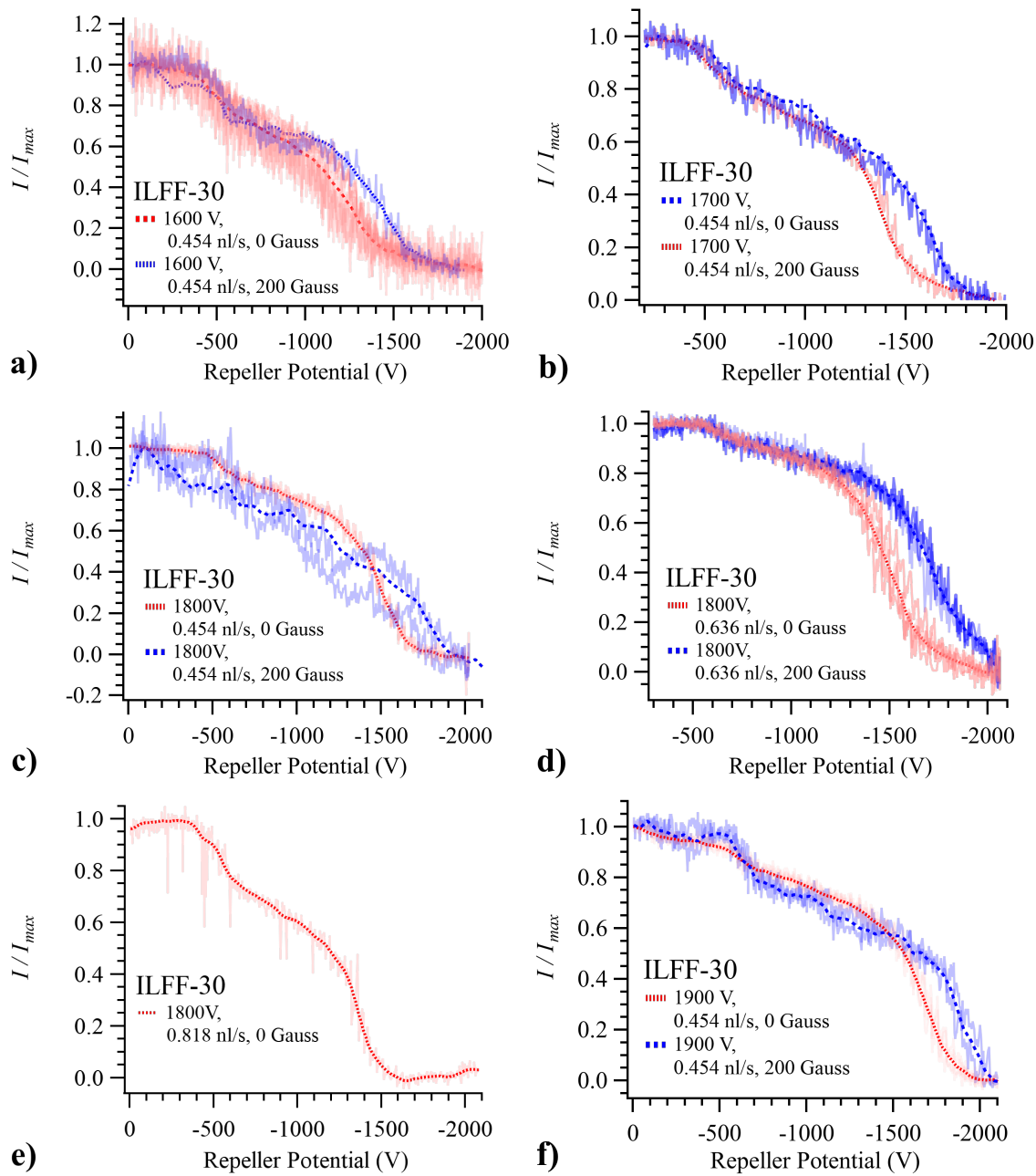
Figure F.3. Beam energy plots for the ILFF-30 electrosprays at various (Q, V_{ext}) settings
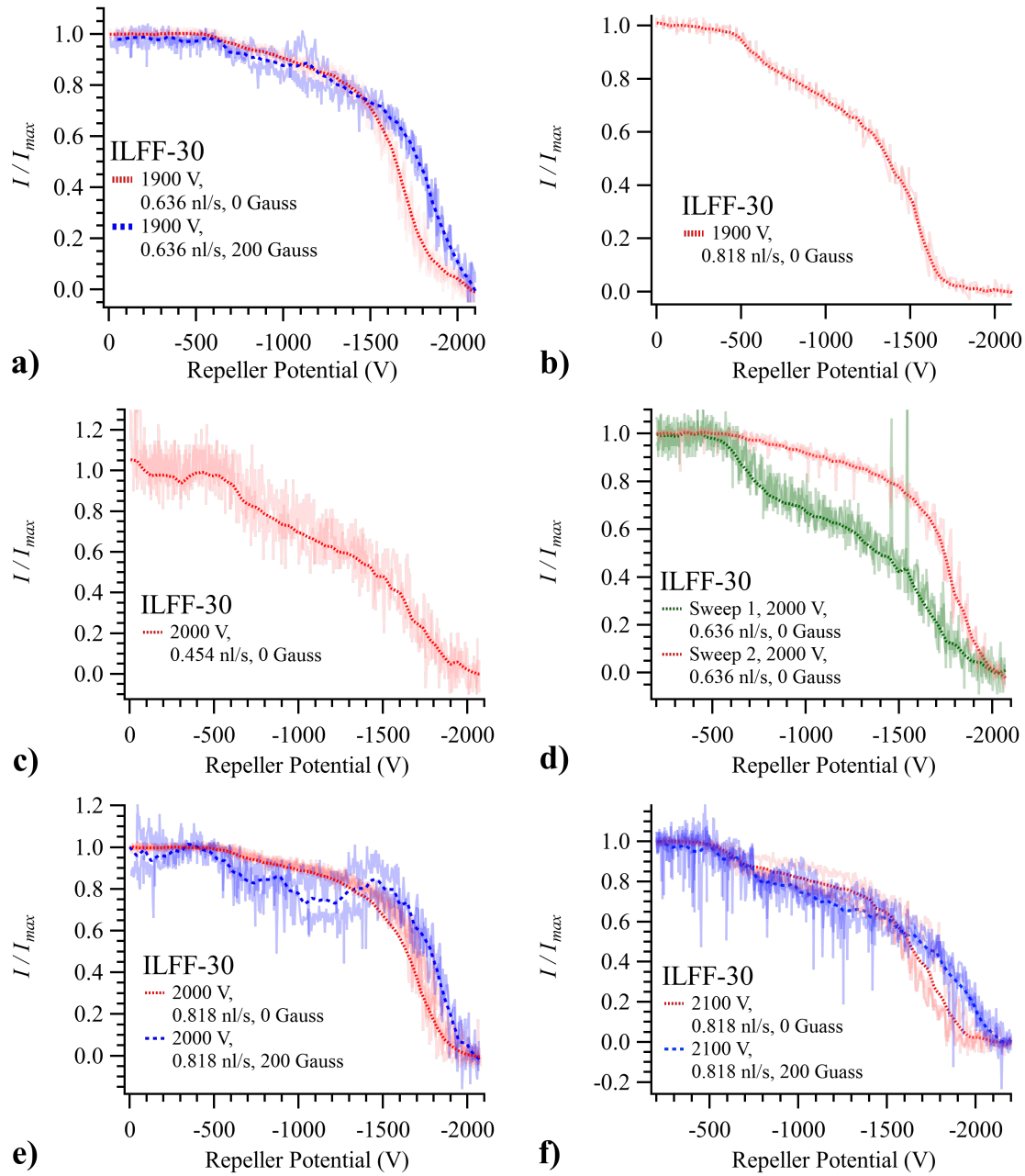
Figure F.4. Beam energy plots for the ILFF-30 electrosprays at various (Q, V_{ext}) settings

266
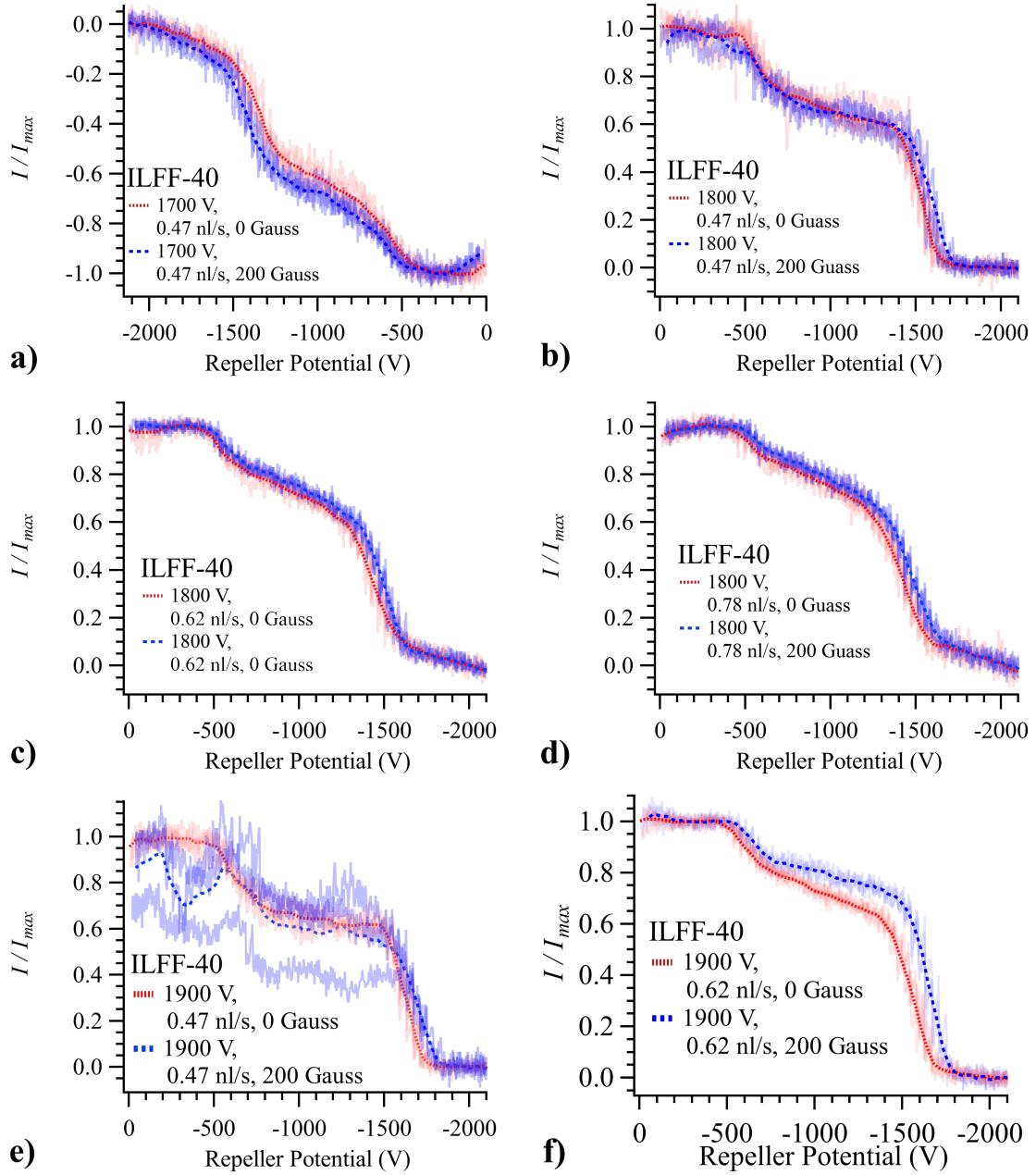
Figure F.5. Beam energy plots for the ILFF-40 electrosprays at various (Q, V_{ext}) settings

c)

d)
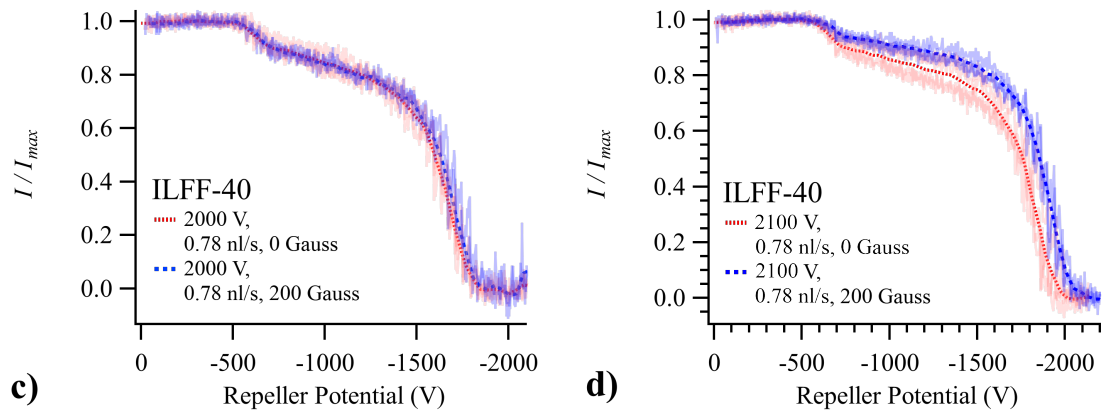
Figure F.6. Beam energy plots for the ILFF-40 electrosprays at various (Q, V_{ext}) settings

Appendix G.

Mass Spectra of ILFF Electrospray at Minimum Flowrate Operation

Mass spectra were also collected for electrosprays running at the minimum flowrates of the original source, as specified in 4.3.2.c. The process of collecting and integrating the mass spectra for each flowrate is described by 6.3.1. and Appendix I. The summed mass spectra of the neat IL electrospray operating at the minimum flowrate, with and without an applied magnetic field, is show in Figure G.1., while the summed mass spectra for ILFF-10 and ILFF-30, with and without an applied magnetic field are provided in Figure G.2. In both figures, the lower range of masses are shown in the main plot. The inset plot shows the larger m/q range illustrating the larger mass distributions of the electrospray beam. Cations species within the spectra are denoted as $n = 0$, $n = 1$, and $n = 2$ for $EMIM^+$, [EMIM-NTf2] $EMIM^+$, and [EMIM-NTf2]$_2$ $EMIM^+$, respectively. Note that the magnetic field had no significant effect on the neat IL minimum flowrate. Mass fractions for the three propellants, under both magnetic field conditions, were also calculated using the method outline in Section 6.4.3 and are provided in Figure G.3.

The conclusion of the experiment was that by applying a magnetic field to the CES and reducing its minimum operable flowrate the magnitude of the ion peak present change, as seen in Figure G.2. The ratio of $n = 1$ to $n = 0$ is reduced by 33- to 50-percent depending on the solution, which is significant even with a 20-percent uncertainty in intensity axis (see Section 6.4.1. for description regarding spectra comparison and repeatability). This is

interpreted as a shift in the average m/q from heavier to lighter mass species, or specifically the mass fraction transported by the ions was increased by the application of a magnetic field, Figure G.3. The cause of the change in ion peak intensities was most likely the act of operating the CES at lower flowrates, and not a direct influence of the applied magnetic field as literature shows a similar correlation between emitted ions species/intensity and flowrate. Also, despite the dramatic change in ion peak intensity, the mass fraction on the ions relative to that of the droplet population was still insignificant; however, the current transported by the ion species would be significantly higher (as illustrated by the summed TOF mass spectra of Figure G.1. and Figure G.2.). The combined observations illustrate that the CES still operated in a mixed ion/droplet mode even at the minimum operable flowrate.
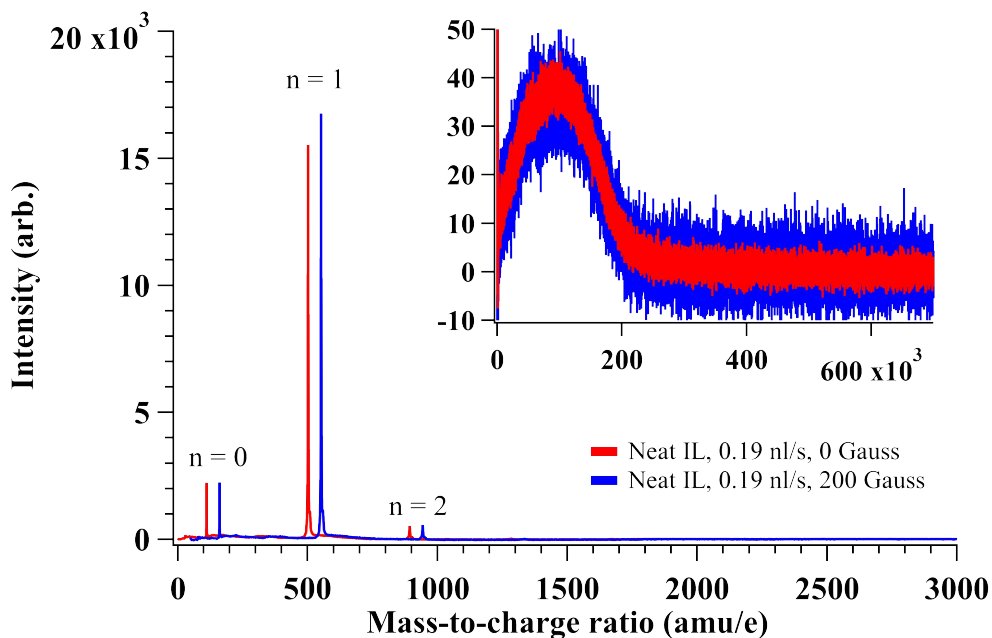
Figure G.1. Mass spectra neat IL emitted from the CES at its minimum flowrate under zero and 200-Gauss applied magnetic fields. The spectra in the low-mass plot (0-3000 amu/e) have been shifted on the m/q axis by arbitrarily adding 50 amu/e to the blue curve to ease comparison.

270
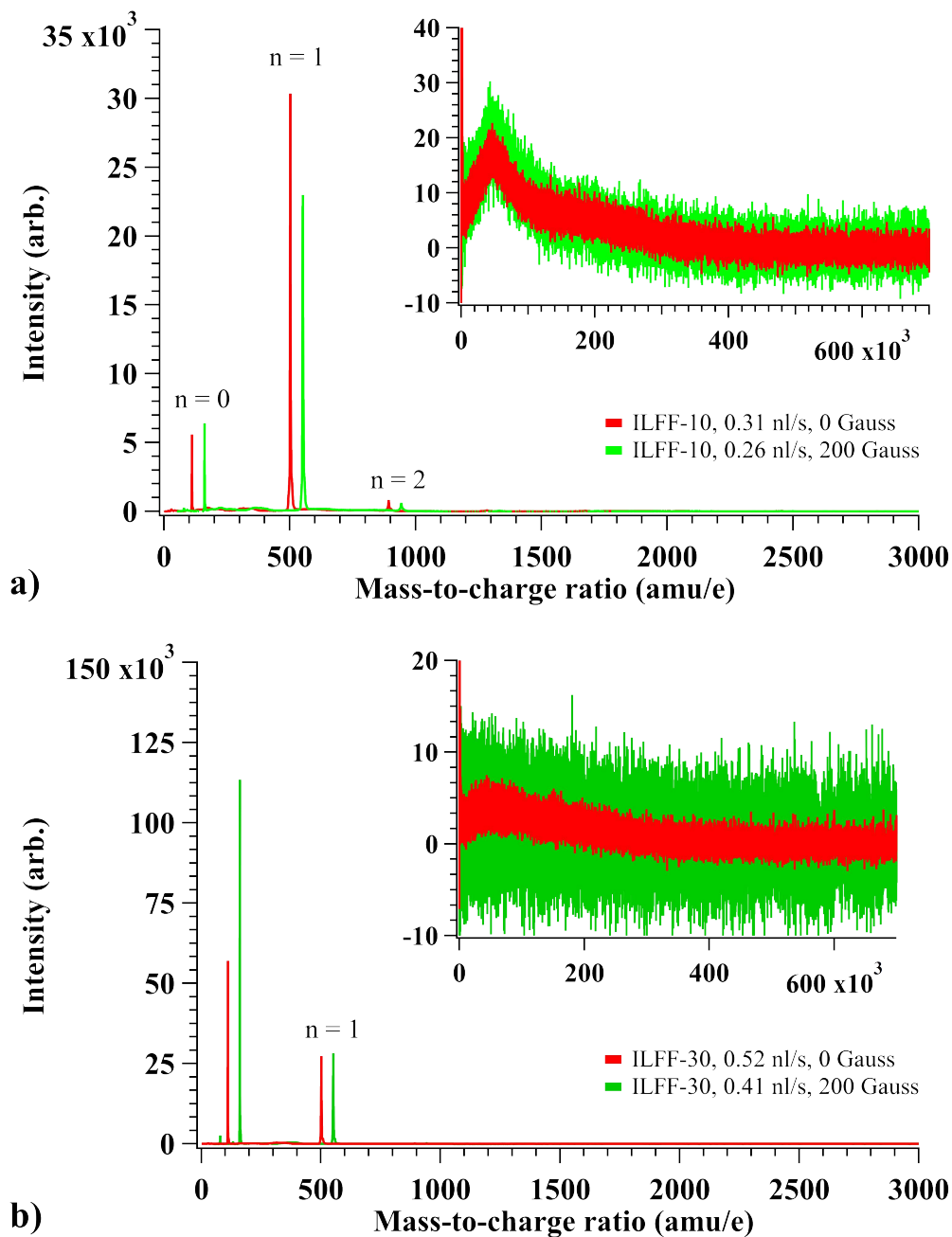
Figure G.2. (a) Mass spectra of ILFF-10 propellant emitted from the CES at its minimum flowrate under zero and 200-Gauss applied magnetic fields. (b) Mass spectra of ILFF-30 propellant emitted from the CES at its minimum flowrate under zero and 200-Gauss applied magnetic fields. The spectra in the low-mass plot (0-3000 amu/e) have been shifted on the m/q axis by arbitrarily adding 50 amu/e to the green curves to ease comparison.
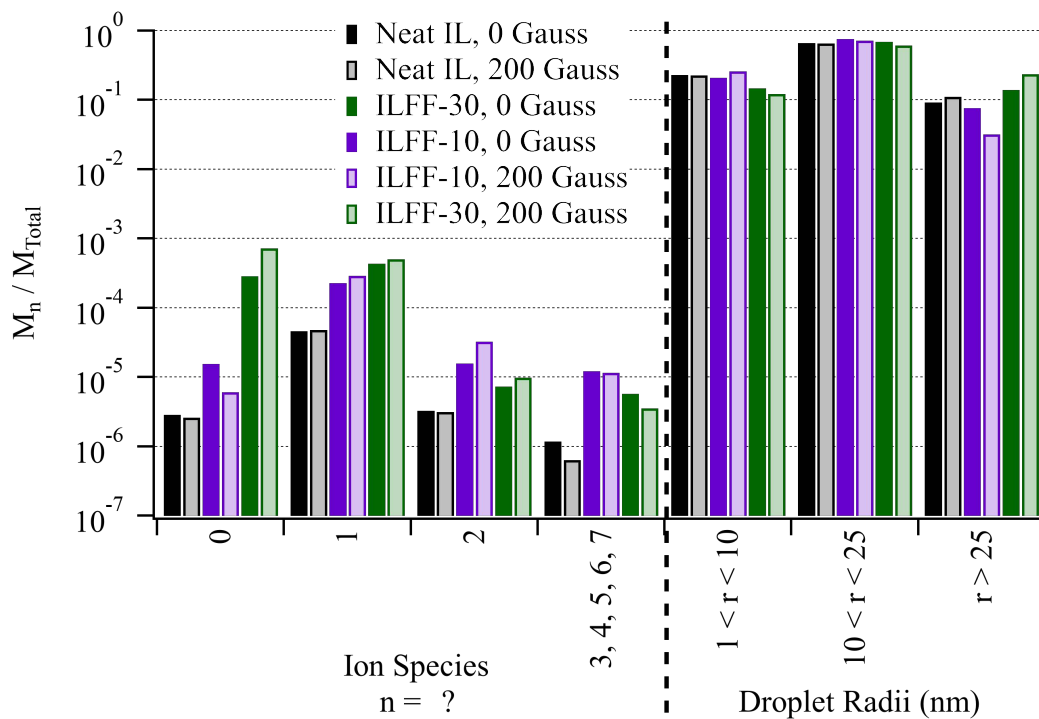
Figure G.3. Mass fractions of all the neat IL, ILFF-10, and ILFF-30 electrosprays running at their respective minimum *Q*, with zero and 200-Gauss magnetic fields applied to the source. The left axis is on a log scale to better illustrate the magnitude of the mass fraction for the ion species.

Appendix H.

SIMION Simulations of TOF-MS Extraction

Region

This analysis was performed by B.D. Prince as part of a manuscript submitted to the 50th AIAA/ASME/SAE/ASEE Joint Propulsion Conference & Exhibit which also included data from Chapter 7.[139] An email providing me permission to reprint this analysis is shown in Figure H.1.

PRINCE, BENJAMIN D DR-02 USAF AFMC AFRL/RVBXB <benjamin.prince.2@us.af.mil>   Thu, Nov 9, 2017 at 11:14 AM
To: Kurt Terhune <kjterhun@mtu.edu>

Hi Kurt,

This is fine with me. Hope your writing is going well! Let me know if you need anything else.

Ben

-----Original Message-----
From: Kurt Terhune [mailto:kjterhun@mtu.edu]
Sent: Wednesday, November 8, 2017 5:53 PM
To: PRINCE, BENJAMIN D DR-02 USAF AFMC AFRL/RVBXB <benjamin.prince.2@us.af.mil>
Subject: [Non-DoD Source] Using Section from JPC14 Paper

Hi Ben,

I was hoping to use a section that you wrote for the JPC 2014 paper detailing the potential masses observed in the Rosensweig ILFF emitter as an Appendix in my dissertation. The section is part of V.A.i if you wanted a refresher (see link below).

http://aerospace.mtu.edu/__reports/Conference_Proceedings/2014_Terhune.pdf

Please let me know if this is fine. Otherwise, I will just reference the conference proceedings in the text of my dissertation.

Thanks!

-Kurt

Figure H.1. Email from Benjamin D. Prince giving permission to reprint the SIMION analysis.

Two-dimensional SIMION simulations were performed with a set of electrodes generated to reproduce the extraction region of the TOF mass spectrometer as shown in 3.6.[140] This region consisted of two 76.2-mm-long plates with an aperture of 6 mm located in the center of VA2. The two plates were separated from one another by 76.2 mm.

273

VA1 was held at +978 V while VA2 was assigned +750 V. A plate perpendicular to the beam-axis direction was placed after the repeller plates and held at the VA1 potential. Along the flight tube axis (orthogonal to beam axis), the extracted ions encounter an Einzel lens and deflector before entering a 1-m-long grounded tube acting as the TOF chamber. Ion distributions were placed at three locations along the beam axis: 0 mm, 20 mm, and 43 mm from the entrance to the extraction region. At these three positions, multiple distances, ranging from 2 to 72 mm, from VA1 were examined. 2500 ions were flown at each condition. For each 2500-ion simulation at a given initial position, a single mass was assigned a single positive charge with a uniform kinetic energy distribution ranging from 0.03 to 50 eV (i.e. ~750eV –800 eV) along the beam-axis direction. The simulated ions had a cone distributed with a half angle of 30 degrees. This cone distribution simulates a small amount of transverse velocity that would be expected in the generally-broad, ion plume of electrospray thrusters. An annotated schematic of the SIMION potential array is provided in Figure H.2.
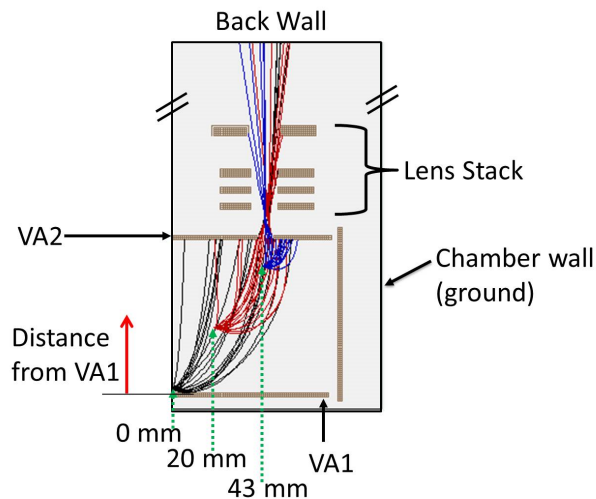
Figure H.2. SIMION potential array with the three locations at which the 25000-ion cone distributions with m/q of 502 amu/e were generated.

The flight time, kinetic energy, and number of ions reaching the back wall located 1 m along the TOF axis were recorded for masses at 15, 111, 502, and 50,000 amu. The key findings are presented in Figure H.3. In Figure H.3.a), the results from the $m/q = 502$ amu/e simulations are presented at two locations along the beam axis, at the entrance to the extraction region (0 mm) and at the center of the extraction region (43 mm). The x-axis encompasses points along the TOF axis measured relative to the VA1 position. In the top trace, the percentage of ions detected at the back wall to ions flown is presented. At 0 mm, ions could only be detected if they were within 40 mm (approximately halfway between VA1 and VA2) whereas the ions are detected at all distances when the ions are pulsed while in the center of the beam-axis within the extraction region. However, at distances where ions are detected, the percentage of ions reaching the back wall of the TOF chamber is essentially similar at both positions along the beam axis. Nearly identical kinetic energies are observed for fixed distance from VA1 regardless of the position along the beam axis. Notably, the kinetic energy (KE) of the ions measured as they impact the wall ranges from 1010 eV to 761 eV over the entire distance from VA1 where ions have successfully transmitted along the TOF axis. The bottom trace of Figure H.3.a) presents the average flight time of the ions beginning at these locations. The standard deviation of the flight time taken from the 43-mm data is also presented. In contrast to the significant standard deviations observed in the flight time, the standard deviation of the average kinetic energy (not shown) was found to be typically 4-9 eV. The difference in flight time over 1 m for a 502 amu mass at 1000 eV and 800 eV is approximately 6 μs yet the average value found at near and far distances from VA1 appears to be contrary to what is expected from their respective kinetic energies. This discrepancy results from the different trajectories taken

275

by the species that make it through the VA2 aperture. At distances close to VA1 (*i.e.* 2-22 mm), successfully extracted trajectories typically first move towards VA2 and then are repelled, whereas the ions at higher distance (greater than 22 mm from VA1) simply curve through the aperture, shortening their time spent in the pulsing acceleration region. In Figure H.3.b) the percent ion count and average kinetic energy as a function of the distance from VA1 are presented. The kinetic energy still exhibits a distance effect, as expected, and is independent of mass. The percentage of ions that reach the back wall is also found to be invariant of mass.
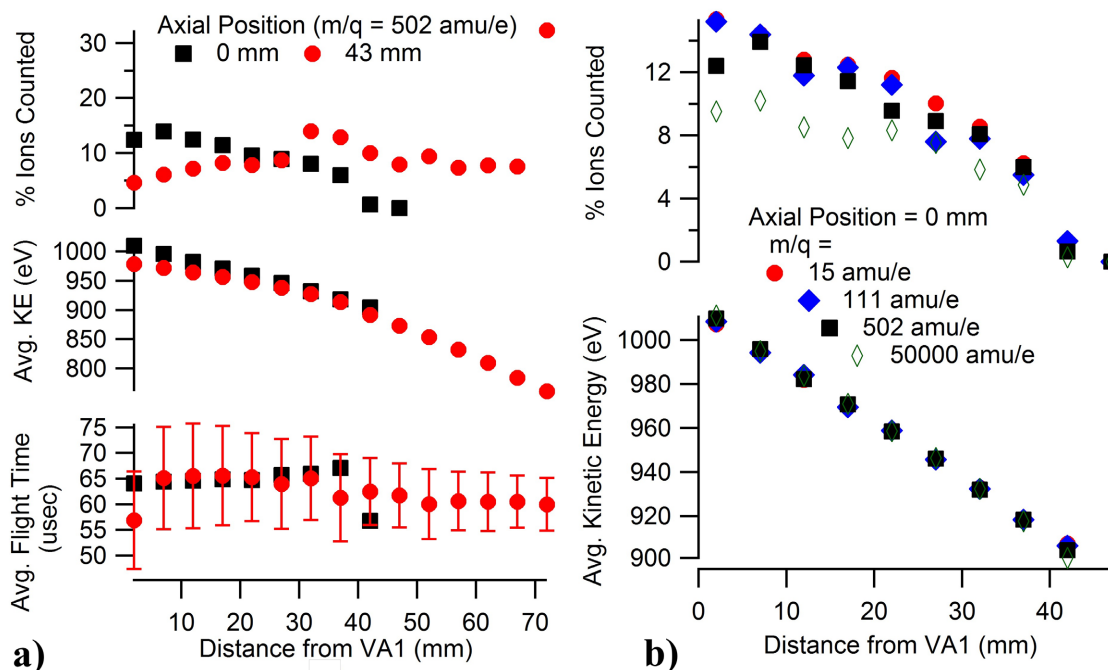
Figure H.3. Results from SIMION simulation of the TOF extraction region illustrating the percentage-of-ions that enter the flight chamber and average kinetic energy of ions versus a) position in extraction region and b) m/q of the ions. Also in (a) average flight time of ions versus position in extraction region (bottom).

Using the specific m/q values from the high-resolution data, their respective intensity ratios and the findings from the SIMION simulations, the needle TOF mass spectrum is

simulated in the flight time domain and then converted to the mass domain. All masses below 83 amu were modeled with kinetic energy line-widths equal to the pulsing potential (+240 eV) and centered at the VA1 voltage suggesting these species are detected at all positions in the extraction region. As the mass increases the required kinetic energy line-width necessary to generate the proper mass and flight time line-widths becomes smaller and smaller, although the average kinetic energy appears to still be close to the value of VA1. The product of this simulation is a qualitatively accurate intensity versus time-of-flight mass spectrum.

Appendix I.

Discussion on Summed Mass Spectrum

The summed mass TOF mass spectra were the primary data sets of Chapter 6. The determining factor on whether individual spectra were collected at each energy defect was based on the number of ion peaks that could be observed in a specific energy-defect spectrum. Without two or more peaks, the m/q mass axis could not be determined. As such the number of spectra that should be used to create a single summed TOF mass spectrum differed depending on the propellant, and the propellant flowrate. However, to provide a better comparison between all propellants and flowrates only a set number of energy-defect spectra was summed to create a single summed mass spectrum. This appendix will go through the process of creating one of these summed mass spectra and illustrate the impact of omitting energy-defect spectra.

Section 6.3.1. described the procedure to collect individual spectra at each energy-defect of a specific electrospray. Figure I.1. presents an example of the spectra from an ILFF-40 electrospray collected at energy-defects of 50 eV to 450 eV. Ion species peak intensities varied across the spectra collected at each energy defect, and in some case the peaks did not appear. The distributions that existed in the large m/q range of the individual spectra also differed in intensity and $\left\langle \frac{m}{q} \right\rangle$ (due to the variation in charge, as described in Section 6.4.2.) depending on the energy-defect of the particles collected in the spectrum.
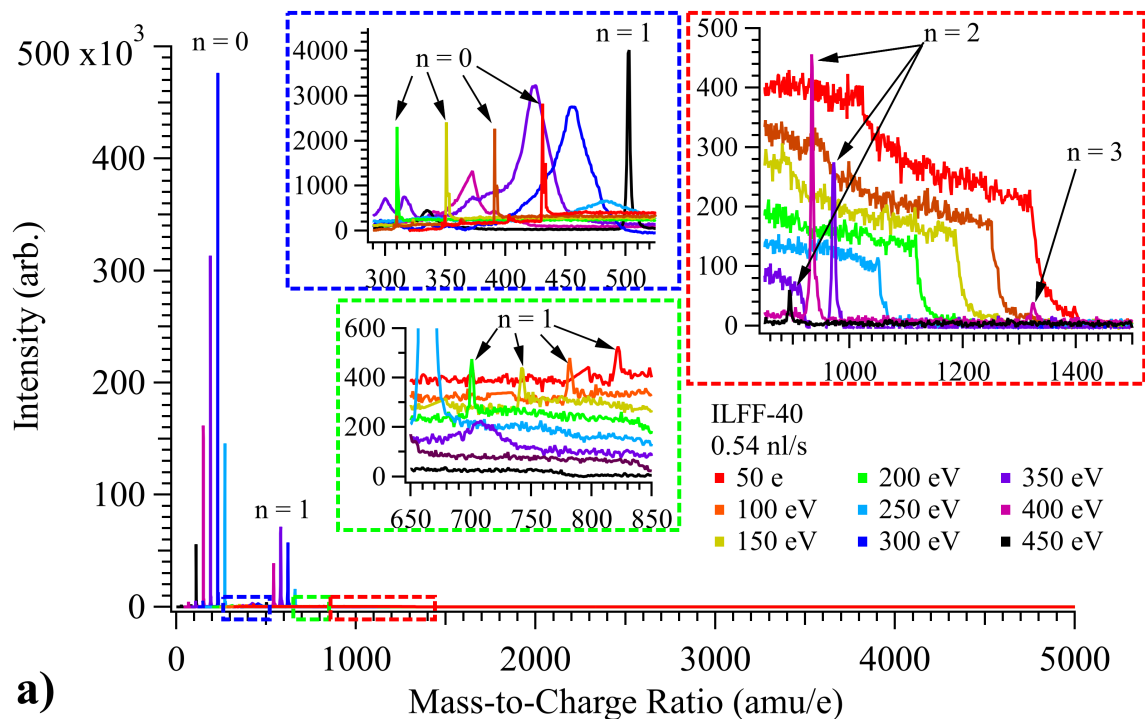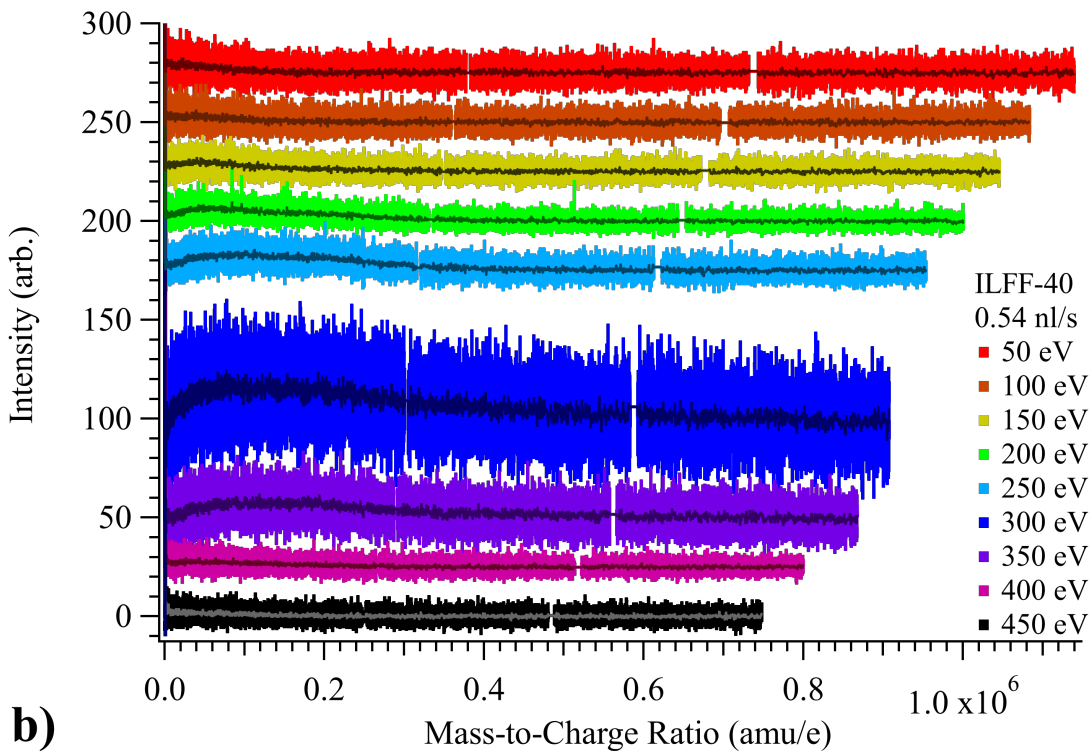
Figure I.1 a) low m/q range and b) high m/q range of the individual energy-defect spectra that comprise a single summed mass spectrum. Inset plots of a) magnify specific ranges of the m/q scale to present heavier ion species. The spectra of b) have been shifted on the intensity axis by artificially adding arbitrary dc-offsets to all but the 850-eV curve. Note for the summed mass spectra examined in this research the 400- and 450-eV spectra are omitted.

280

A summed mass spectrum was created by first truncating each individual spectrum such that the m/q range of all spectra were equal in length. The spectra were then summed to produce the summed mass spectrum. The summed mass spectra used analyzed in Chapter 6 used seven spectra to produce each, and therefore omitted data in two ways. First, the truncation removed data at m/q greater than 867700 amu/e; as Figure I.1. illustrates, this omitted data from a range of over 270,000 amu/e from the lowest energy-defect spectrum. Luckily, the individual spectra did not appear to measure any significant populations at this range. Second, data within the higher energy-defect spectra (those greater than 350 eV) was omitted. This was done for accurate comparison between summed mass spectra for all propellants and flowrates, *i.e.* only examining particles in the electrosprays that had maximum energy-defects of 350 eV. As Figure I.1. illustrates, multiple ion species existed in spectra that were collected for energy defects of 400- and 450-eV. This meant that it was possible that some of the summed mass spectra of Chapter 6 had higher relative intensities of ions if the entire energy range of the electrospray was collected. The lower energy of these particles would impact the efficiency of the electrospray, specifically lowering η_V. The comparison of the summed mass spectrum created using all the individual energy-defect spectra in Figure I.1. and the summed mass spectrum created after omitting the 400- and 450-eV spectra is presented in Figure I.2.
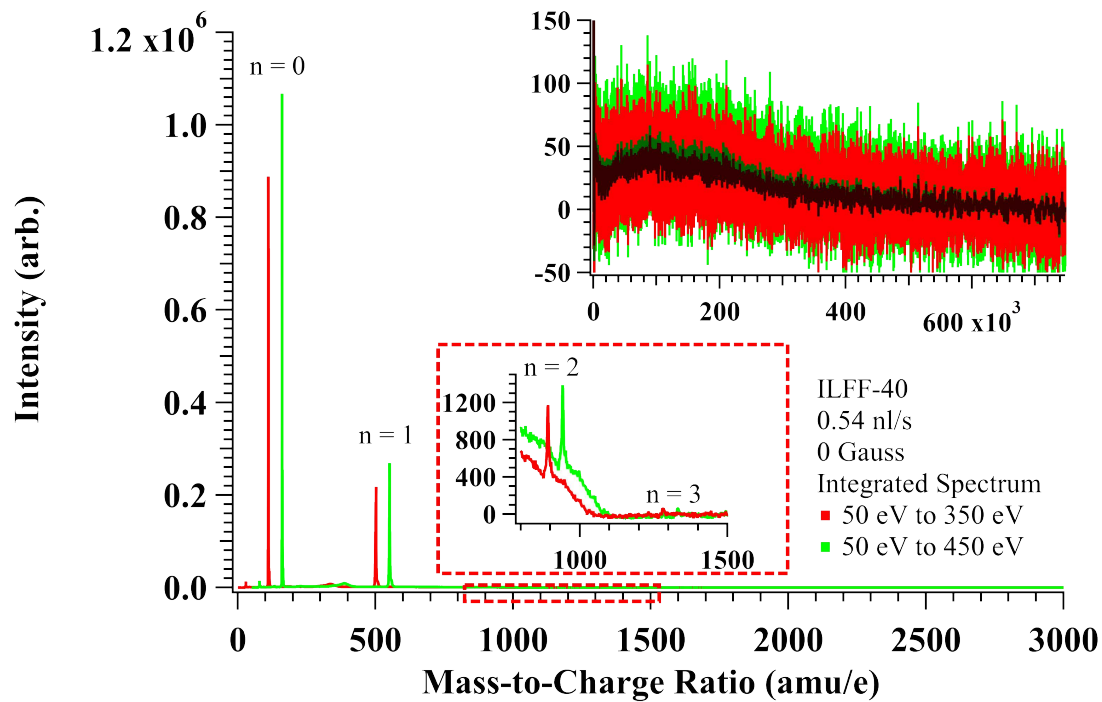
Figure I.2. Summed TOF mass spectra of an ILFF-40 electrospray operating at 0.54 nl/s. The red spectrum was created through the sum of 7 spectra collected at energy defects between 50 eV and 350 eV at 50 eV intervals. The green spectrum was created through the sum of 9 spectra collected at energy defects between 50 eV and 450 eV at 50 eV intervals. The red spectrum has been shifted along the m/q axis by artificially adding 50 m/q; this was done for clarity.

Appendix J.

Summed TOF Mass Spectra for ILFF propellants

This appendix presents summed TOF mass spectra from the mass spectrometer experiment. The summed mass spectra from magnetic-field-free ILFF-10, ILFF-20, and ILFF-30 electrosprays are given in Figure J.1., Figure J.2., and Figure J.3, respectively. The summed mass spectra from magnetically-stressed ILFF-10, ILFF-20, and ILFF-30 electrosprays are given in Figure J.4., Figure J.5., and Figure J.6., respectively. The summed mass spectra from magnetic-field-free and magnetically-stressed ILFF-40 electrosprays are given in Figure J.7. Some of the spectra are also included in figures of Chapter 6.
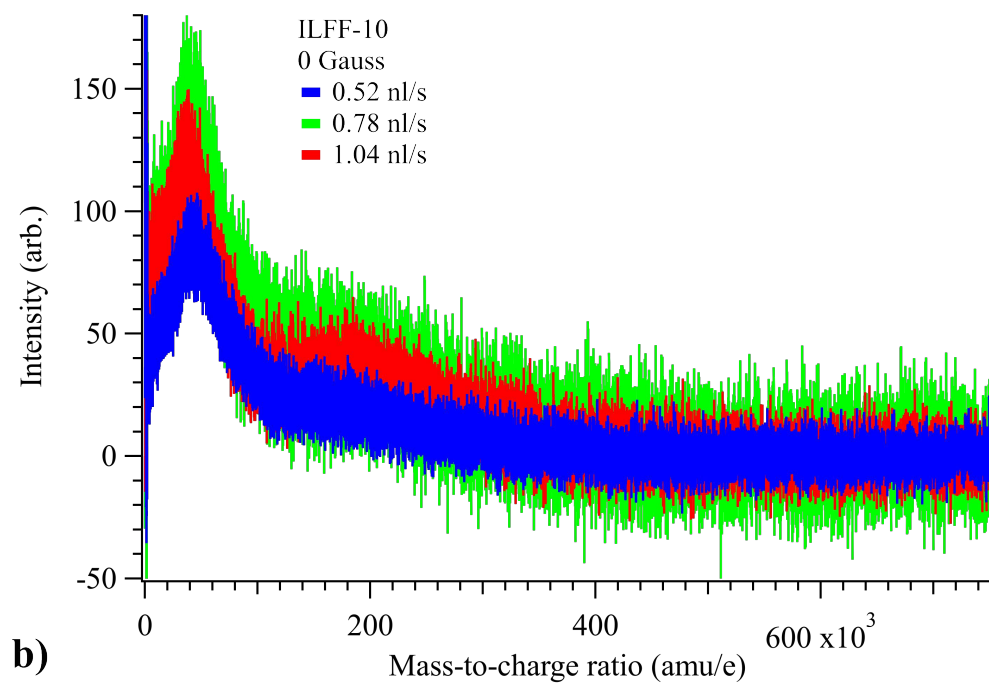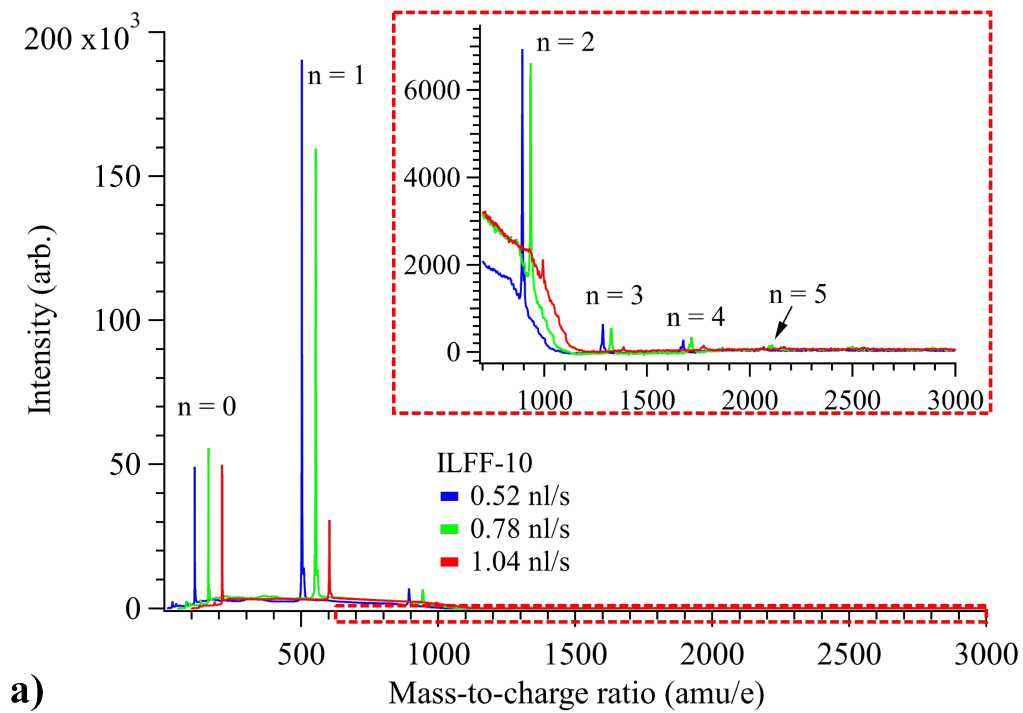
Figure J.1. Full range of summed TOF mass spectra for CES running the ILFF-10 propellant. a) Low m/q range (ions); b) High m/q range (droplets). No magnetic field applied to the source.
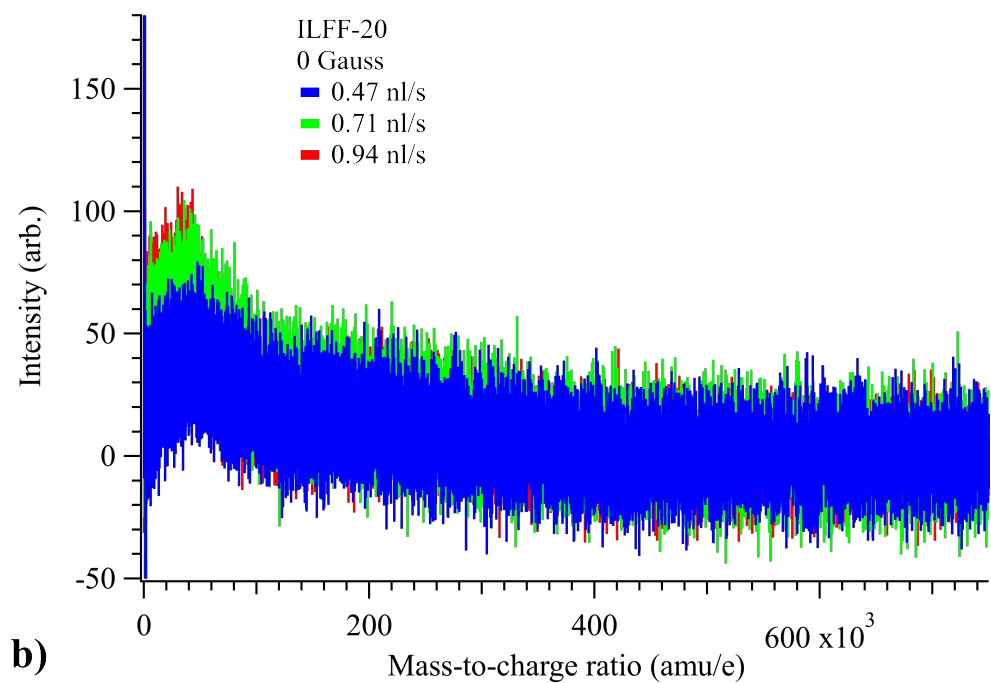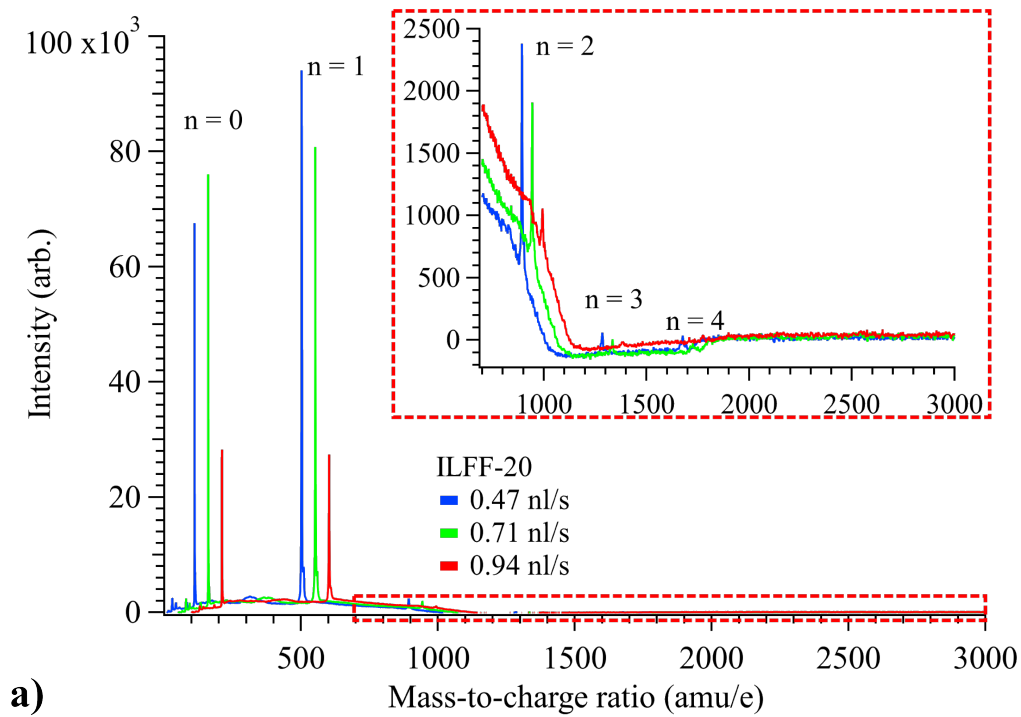
Figure J.2. Full range of summed TOF mass spectra for CES running the ILFF-20 propellant. a) Low m/q range (ions); b) High m/q range (droplets). No magnetic field applied to the source.

285
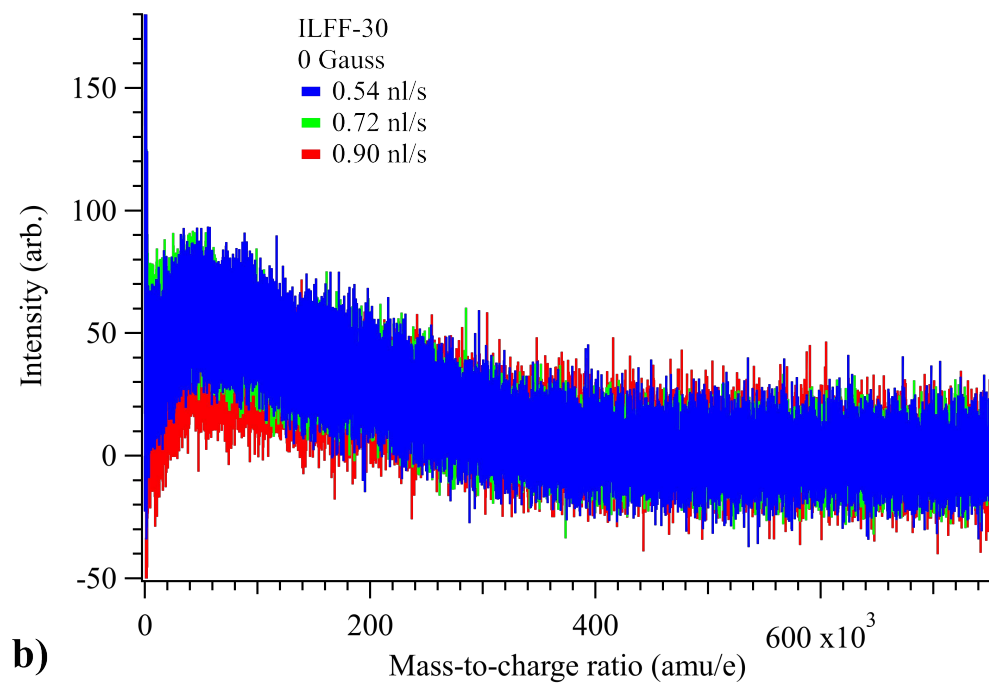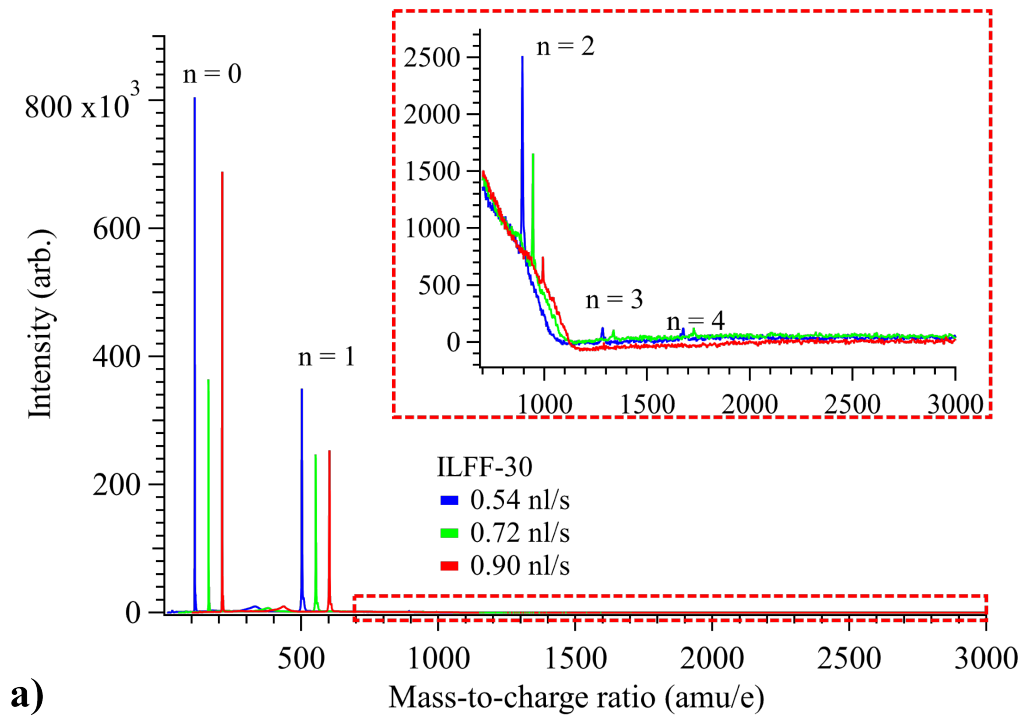
Figure J.3. Full range of summed TOF mass spectra for CES running the ILFF-30 propellant. a) Low m/q range (ions); b) High m/q range (droplets). No magnetic field applied to the source.
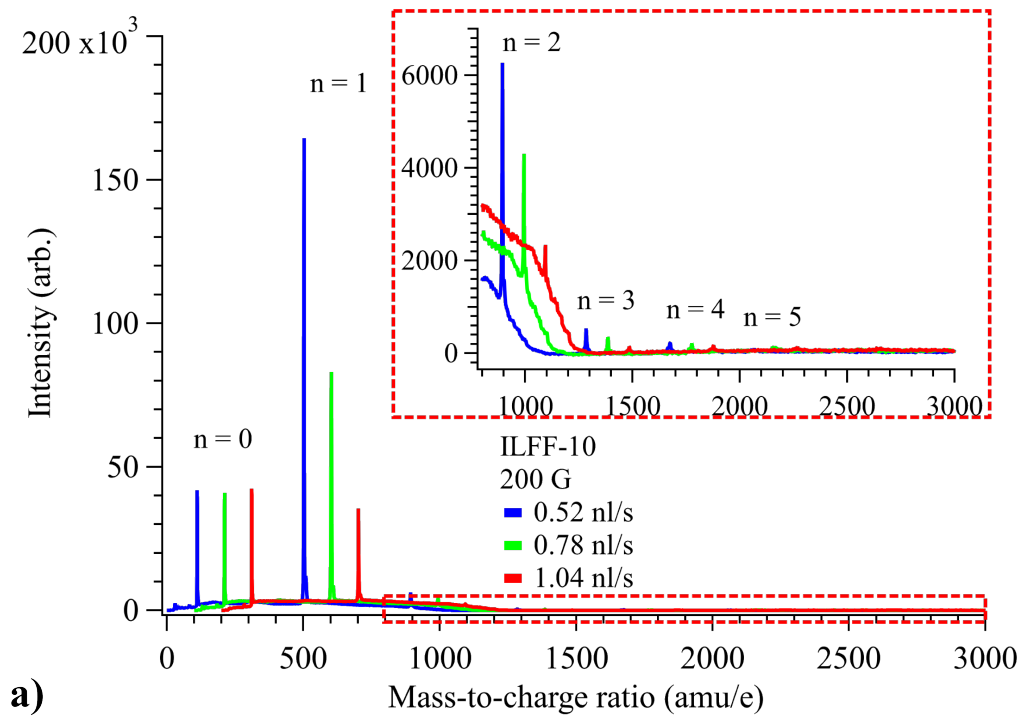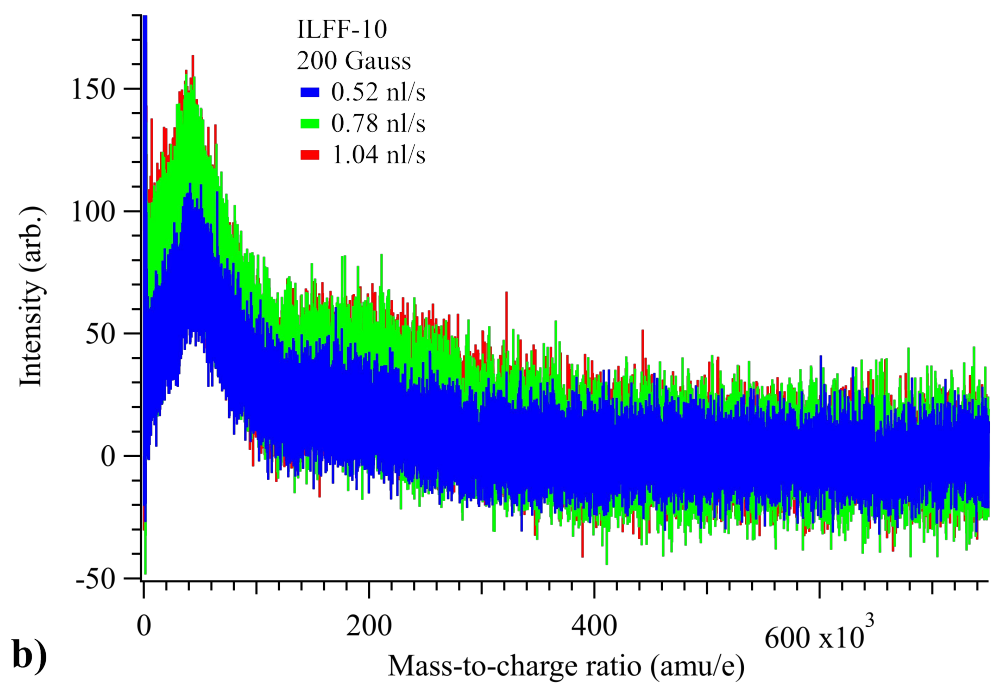
Figure J.4. Full range of summed TOF mass spectra for CES running the ILFF-10 propellant. a) Low m/q range (ions); b) High m/q range (droplets). 200-Gauss magnetic field applied to the source.

287
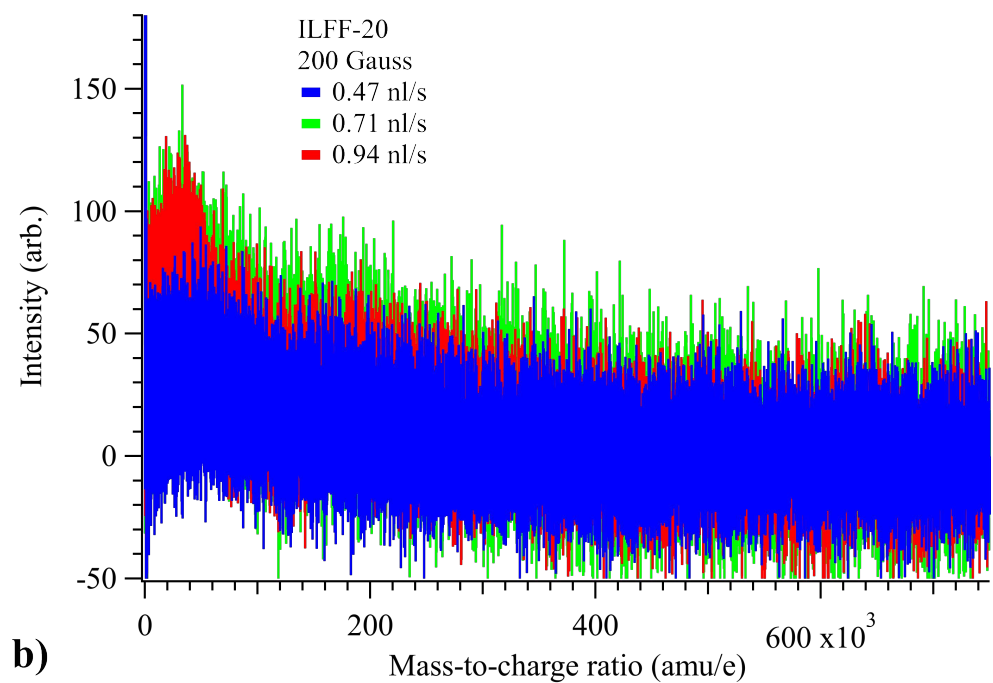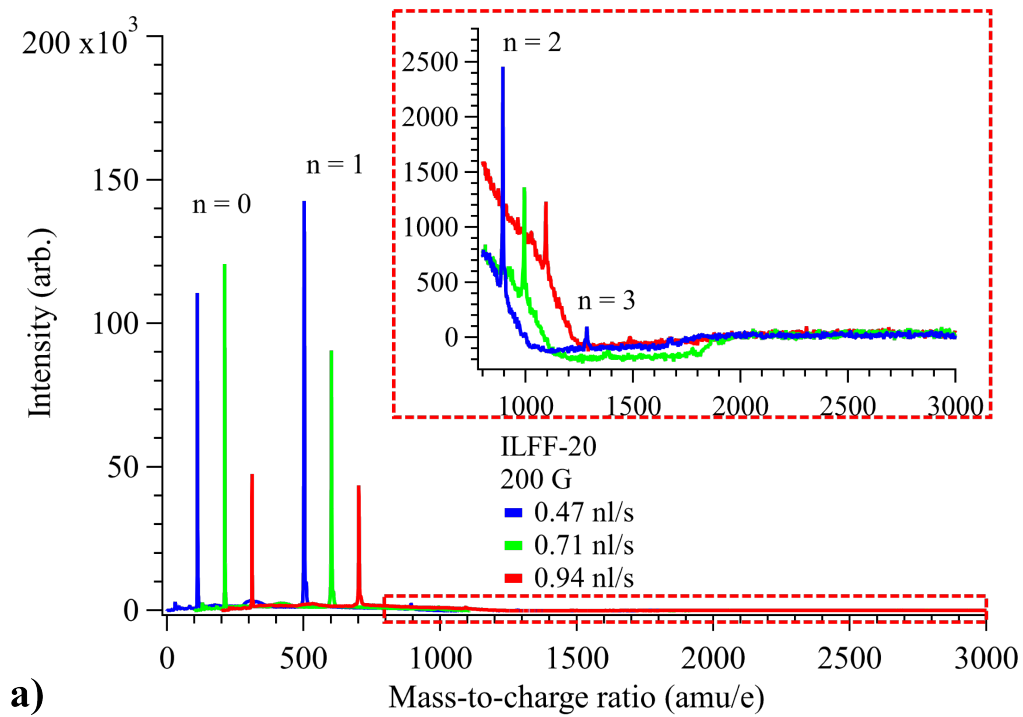
Figure J.5. Full range of summed TOF mass spectra for CES running the ILFF-20 propellant. a) Low m/q range (ions); b) High m/q range (droplets). 200-Gauss magnetic field applied to the source.

288
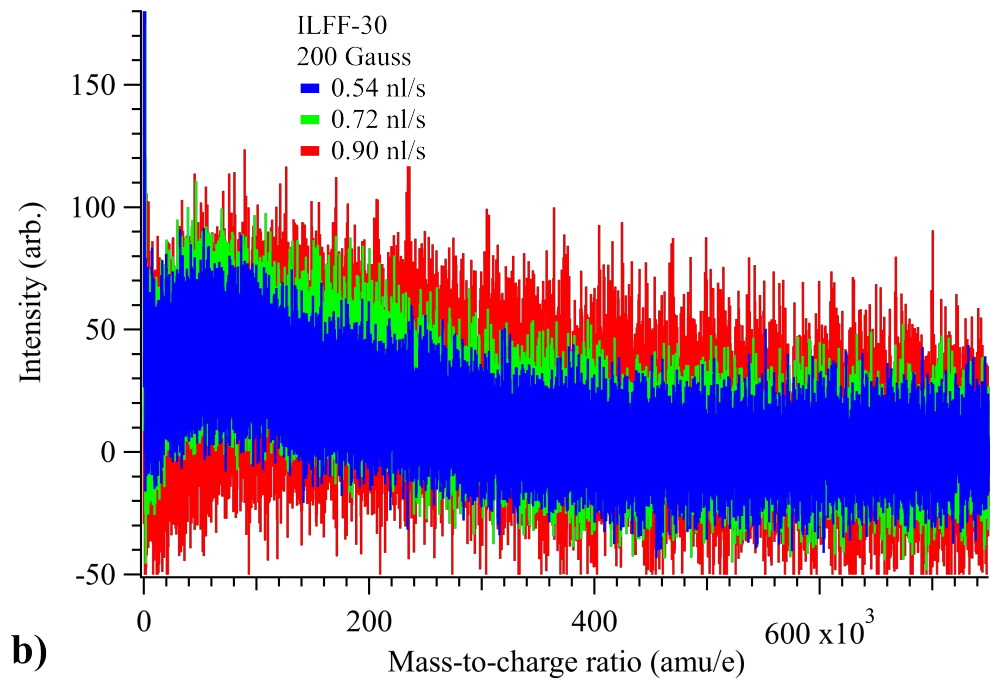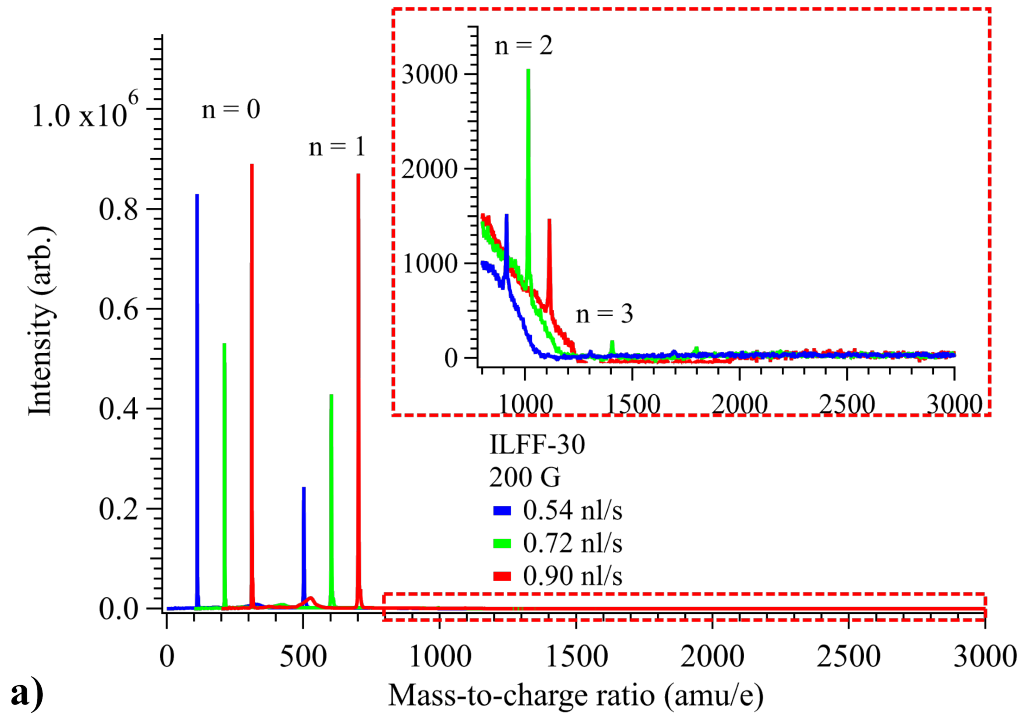
Figure J.6. Full range of summed TOF mass spectra for CES running the ILFF-30 propellant. a) Low m/q range (ions); b) High m/q range (droplets). 200-Gauss magnetic field applied to the source.

289
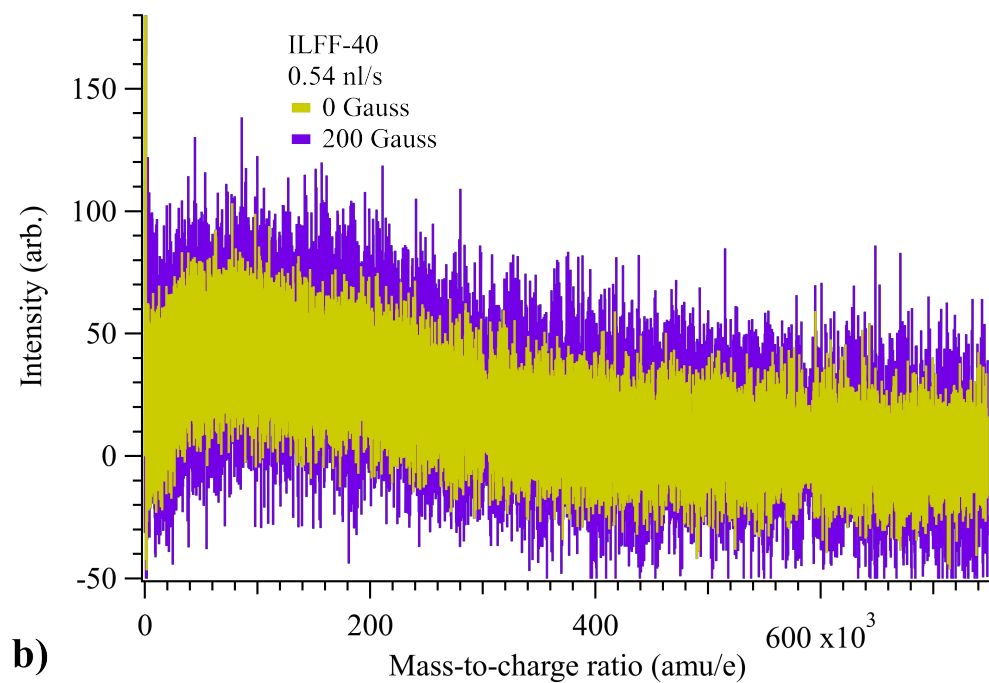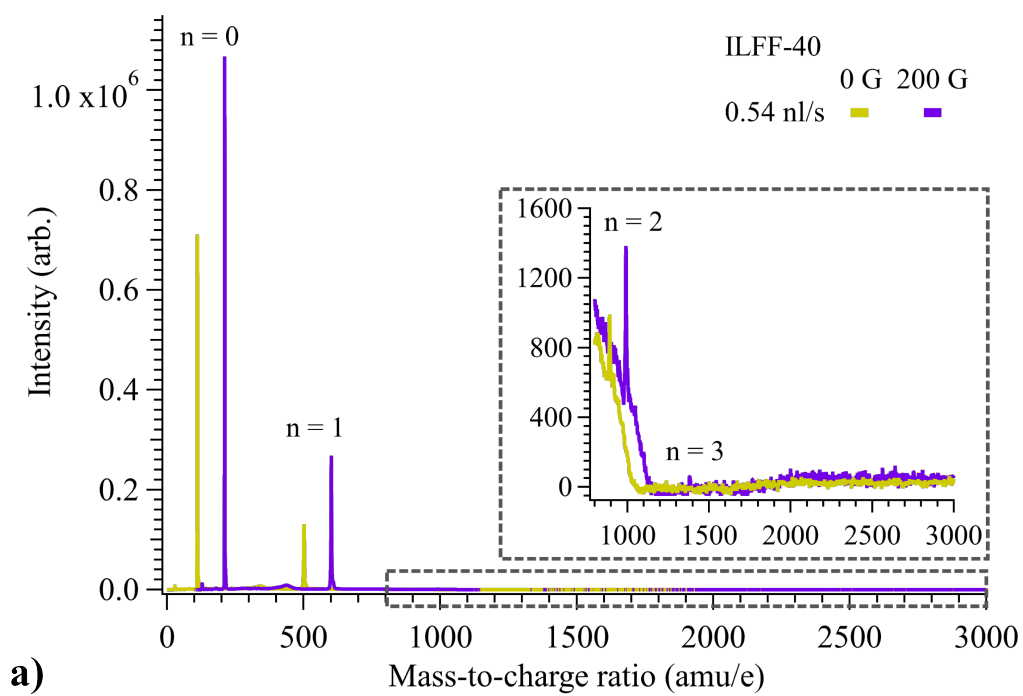
Figure J.7. Full range of summed TOF mass spectra for CES running the ILFF-40 propellant with and without a 200-Gauss magnetic field. a) Low m/q range (ions); b) High m/q range (droplets).

290

Appendix K.

VSM Data for NJ39074 ILFF

# magnets	B-field at face (Gauss)	M (emu/g)	B-field 1.54 mm from face (Gauss)	M at 1.54 mm (emu/g)	wavelength (m)	wavelength (mm)	
1	333.9	45.04543596	255.5	37.00034851	0.00236136	2.361360391	
2	520.5	52.82991092	426.4	49.98206436	0.001990265	1.990265211	
3	690.4	55.6177362	578.2	54.01219586	0.001776408	1.776407591	
4	802.4	56.67249148	675.4	55.44199124	0.001654084	1.65408449	
5	894.2	57.2937296	755.9	56.28281061	0.001576453	1.576453139	
6	967.5	57.68435489	820.7	56.8105557	0.001524943	1.524943155	

	H (A/m)	M (A/m)	H at 1.54mm (A/m)	M at 1.54mm (A/m)	wavelength (m)	wavelength (mm)	0.8*wavelength (nm)
1	26570.91775	220722.6362	20332.04398	181301.7077	0.003373372	3.373371987	3.036035
2	41420.07394	258866.5635	33931.83387	244912.1154	0.002843236	2.843236016	2.558912
3	54940.28636	272526.9074	46011.69405	264659.7597	0.002537725	2.53772513	2.03018
4	63852.96317	277695.2082	53746.62428	271665.7571	0.002362978	2.362977843	1.890382
5	71158.17506	280739.275	60152.61074	275785.772	0.002252076	2.252075913	1.801661
6	76991.20372	282653.3389	65309.2309	278371.7229	0.00217849	2.178490222	1.742792

NJ397074	Sample weight, g	Solids %	Pure Fe2O3	emu	emu/g		
	0.00831	20.6	0.00171186	0.10993	64.22		
Time Stamp (sec)	**Temperature (K)**	**Magnetic Field (Oe)**	**Moment (emu)**	**M. Std. Err. (emu)**	**emu/g**	**H (A/m)**	**M (A/m)**
523269.75	297.8821411	0.043	-0.013325745	3.90E-06	-1.60358	3.421831	-2910.5
523295.39	297.9080505	923.0855	0.054269902	1.18E-05	6.530674	73456.81	11853.17
523299.07	297.9125977	1753.9535	0.102262102	4.15E-05	12.30591	139575.2	22335.22
523299.705	297.9134979	1896.1785	0.103538864	3.19E-05	12.45955	150893.1	22614.08
523300.97	297.913971	2159.4795	0.103974556	3.45E-05	12.51198	171845.9	22709.24
523302.19	297.9151612	2413.976	0.104392877	2.95E-05	12.56232	192098.1	22800.61
523303.315	297.916092	2664.357	0.104755773	3.13E-05	12.60599	212022.8	22879.87
523304.485	297.917389	2917.7035	0.105063233	3.07E-05	12.64299	232183.5	22947.02
523305.505	297.9194489	3124.6295	0.105318013	2.67E-05	12.67365	248650.1	23002.67
523306.53	297.9208069	3311.456	0.105544702	2.79E-05	12.70093	263517.3	23052.18
523308.46	297.9216003	3692.576	0.105955814	2.48E-05	12.7504	293845.9	23141.97
523309.115	297.9226685	3821.785	0.106166896	2.20E-05	12.7758	304128	23188.08
523310.195	297.9237366	4043.5465	0.106313264	2.75E-05	12.79341	321775.2	23220.04
523311.19	297.9240418	4222.5245	0.10646425	2.67E-05	12.81158	336017.8	23253.02
523312.175	297.9249878	4401.216	0.106638154	2.21E-05	12.83251	350237.6	23291
523313.19	297.9256592	4595.4135	0.106733511	1.50E-05	12.84398	365691.4	23311.83
523314.315	297.9272766	4821.5775	0.106886056	1.99E-05	12.86234	383688.9	23345.15
523315.465	297.9292908	5053.293	0.10697149	1.73E-05	12.87262	402128.3	23363.81
523317.43	297.9310608	5412.3945	0.107189207	1.65E-05	12.89882	430704.7	23411.36
523318.095	297.9319153	5535.4795	0.107287021	1.61E-05	12.91059	440499.5	23432.72
523319.26	297.9331818	5748.1475	0.107388812	2.03E-05	12.92284	457423	23454.96
523320.29	297.9340821	5938.037	0.107465097	1.97E-05	12.93202	472534	23471.62
523322.215	297.9367981	6283.932	0.10755187	1.81E-05	12.94246	500059.4	23490.57
523323.795	297.938324	6596.0415	0.107723826	2.08E-05	12.96316	524896.3	23528.13
523324.32	297.9386444	6696.7275	0.10778408	1.97E-05	12.97041	532908.6	23541.29
523325.205	297.938797	6852.2555	0.107845867	2.05E-05	12.97784	545285.2	23554.78
523327.13	297.9407349	7215.0925	0.107883884	1.88E-05	12.98242	574158.8	23563.09
523327.765	297.9412995	7337.41	0.107952339	2.02E-05	12.99065	583892.5	23578.04

523328.83	297.9419403	7527.011	0.108056143	2.15E-05	13.00315	598980.5	23600.71
523329.93	297.9427338	7716.8025	0.108157099	1.85E-05	13.01529	614083.6	23622.76
523331.08	297.9441071	7939.519	0.10819501	1.80E-05	13.01986	631806.8	23631.04
523332.27	297.9454346	8167.883	0.108267266	1.81E-05	13.02855	649979.5	23646.82
523333.485	297.9466553	8390.694	0.108330968	1.83E-05	13.03622	667710.2	23660.73
523334.61	297.9477845	8597.331	0.108411864	1.76E-05	13.04595	684153.9	23678.4
523335.7	297.9487153	8804.5425	0.108424937	2.01E-05	13.04753	700643.2	23681.26
523337.845	297.949997	9216.285	0.108501344	1.54E-05	13.05672	733408.7	23697.95
523338.635	297.9508209	9356.116	0.108554647	1.87E-05	13.06313	744536.1	23709.59
523339.745	297.951767	9568.3055	0.108582942	2.09E-05	13.06654	761421.6	23715.77
523340.87	297.952591	9774.2725	0.108656772	2.00E-05	13.07542	777811.9	23731.89
523342.135	297.9540101	9997.178	0.108714389	1.98E-05	13.08236	795550.1	23744.48
523343.275	297.955246	10204.293	0.10871216	1.85E-05	13.08209	812031.8	23743.99
523344.385	297.9556885	10411.3125	0.10877195	2.19E-05	13.08928	828505.9	23757.05
523345.515	297.9561005	10623.307	0.108816052	1.74E-05	13.09459	845375.9	23766.68
523346.56	297.9575196	10830.1345	0.108841975	1.75E-05	13.09771	861834.7	23772.34
523347.695	297.958725	11036.963	0.108869847	1.79E-05	13.10106	878293.6	23778.43
523348.9	297.9593353	11265.613	0.108930706	1.94E-05	13.10839	896489	23791.72
523350.065	297.9600067	11489.0955	0.108960406	2.20E-05	13.11196	914273.2	23798.21
523351.19	297.9598541	11679.078	0.109013796	2.29E-05	13.11839	929391.5	23809.87
523352.36	297.9604187	11903.803	0.108983434	1.90E-05	13.11473	947274.5	23803.24
523353.43	297.9613953	12111.6845	0.109064562	1.82E-05	13.1245	963817.2	23820.96
523354.35	297.9620514	12284.2485	0.109093758	2.06E-05	13.12801	977549.4	23827.34
523355.39	297.9633331	12473.849	0.109131406	2.03E-05	13.13254	992637.4	23835.56
523356.445	297.9639587	12669.096	0.10915039	1.80E-05	13.13482	1008175	23839.71
523357.465	297.9645538	12875.922	0.109216085	2.34E-05	13.14273	1024633	23854.05
523358.575	297.9656372	13083.801	0.109172779	2.53E-05	13.13752	1041176	23844.6
523359.765	297.9660187	13291.2985	0.109197376	2.38E-05	13.14048	1057688	23849.97
523360.96	297.9660187	13498.0305	0.109268751	2.30E-05	13.14907	1074139	23865.56
523362.11	297.9661255	13710.026	0.109283818	2.12E-05	13.15088	1091009	23868.85
523363.215	297.9665528	13917.044	0.109331387	1.80E-05	13.1566	1107483	23879.24
523365.14	297.9678955	14297.396	0.10925557	1.88E-05	13.14748	1137751	23862.68
523365.855	297.9676819	14421.053	0.109392076	2.46E-05	13.16391	1147591	23892.49
523367.105	297.96875	14661.666	0.109456261	1.72E-05	13.17163	1166738	23906.51
523368.23	297.9696655	14868.493	0.10943374	1.78E-05	13.16892	1183197	23901.59
523370.175	297.9702148	15222.043	0.109435322	1.48E-05	13.16911	1211332	23901.94
523370.83	297.9707489	15356.992	0.109526671	1.32E-05	13.1801	1222071	23921.89
523372.025	297.9711762	15596.7425	0.109552079	1.21E-05	13.18316	1241149	23927.44
523373.135	297.9714203	15786.342	0.109511506	1.73E-05	13.17828	1256237	23918.58
523374.15	297.971405	15960.2445	0.109544106	2.01E-05	13.1822	1270076	23925.7
523375.305	297.9722443	16189.946	0.109573854	1.79E-05	13.18578	1288355	23932.2
523376.35	297.9729309	16396.6785	0.109591844	1.77E-05	13.18795	1304806	23936.12
523378.335	297.9734802	16777.8855	0.109628716	1.26E-05	13.19238	1335142	23944.18
523380.04	297.9740754	17057.261	0.109632239	1.41E-05	13.19281	1357374	23944.95
523380.785	297.9744873	17196.421	0.109693973	1.70E-05	13.20024	1368448	23958.43
523382.035	297.9751129	17437.2255	0.109701591	1.92E-05	13.20115	1387610	23960.09
523383.12	297.9752045	17644.531	0.109702268	2.16E-05	13.20124	1404107	23960.24
523384.205	297.9756012	17857.578	0.109760147	1.57E-05	13.2082	1421061	23972.88
523385.305	297.975769	18064.788	0.109774597	1.11E-05	13.20994	1437550	23976.04
523386.42	297.9757996	18271.998	0.109795986	4.78E-06	13.21251	1454039	23980.71
523387.685	297.9770508	18512.803	0.109793629	1.36E-05	13.21223	1473202	23980.2
523388.86	297.9773407	18737.1445	0.109840221	1.14E-05	13.21784	1491055	23990.37
523390.005	297.9775543	18949.33	0.109864389	1.13E-05	13.22074	1507940	23995.65
523391.26	297.9784088	19172.43	0.109873879	1.59E-05	13.22189	1525694	23997.72
523392.54	297.9786682	19413.83	0.109903222	8.85E-06	13.22542	1544904	24004.13
523393.705	297.9792938	19625.4745	0.109895998	8.60E-06	13.22455	1561746	24002.56
523394.85	297.9799652	19789.012	0.109921906	1.09E-05	13.22767	1574760	24008.21
523396.035	297.9803009	19889.921	0.109935704	1.18E-05	13.22933	1582790	24011.23
523397.085	297.9810333	19924.1115	0.109936637	1.35E-05	13.22944	1585510	24011.43
523398.11	297.9814148	19934.883	0.109922609	9.69E-06	13.22775	1586368	24008.37
523407.12	297.9842835	20000.2175	0.10993107	8.01E-06	13.22877	1591567	24010.22
523417.3	297.9882813	19872.2725	0.109920051	1.73E-05	13.22744	1581385	24007.81
523417.985	297.9888001	19716.3885	0.109915141	1.23E-05	13.22685	1568980	24006.74
523420.135	297.9898376	19211.3495	0.109900344	1.18E-05	13.22507	1528791	24003.5

523420.615	297.9901123	19088.173	0.10987496	1.32E-05	13.22202	1518989	23997.96
523421.56	297.990326	18890.246	0.109867095	9.77E-06	13.22107	1503238	23996.24
523422.695	297.9903717	18658.0575	0.109835394	1.10E-05	13.21726	1484761	23989.32
523423.835	297.9904022	18431.6135	0.1097829	8.94E-06	13.21094	1466741	23977.85
523425.015	297.9905396	18209.5695	0.109782532	6.69E-06	13.21089	1449071	23977.77
523426.205	297.9906006	17972.786	0.109747263	1.09E-05	13.20665	1430229	23970.07
523427.26	297.9905396	17751.317	0.109733456	1.51E-05	13.20499	1412605	23967.05
523429.21	297.9909668	17381.785	0.109704322	1.17E-05	13.20148	1383199	23960.69
523429.81	297.9911499	17273.0595	0.109694109	8.33E-06	13.20025	1374546	23958.46
523430.735	297.9913788	17095.2325	0.109704739	1.06E-05	13.20153	1360395	23960.78
523431.71	297.9917145	16900.5615	0.109640713	1.18E-05	13.19383	1344904	23946.8
523432.895	297.9923706	16667.129	0.109624734	1.16E-05	13.19191	1326328	23943.31
523434.115	297.9924927	16456.3775	0.109624223	9.80E-06	13.19184	1309557	23943.2
523435.265	297.9925385	16228.303	0.10959563	1.27E-05	13.1884	1291407	23936.95
523436.33	297.9932099	16012.0975	0.109572794	1.30E-05	13.18566	1274202	23931.96
523438.395	297.9933472	15630.4115	0.109531231	1.01E-05	13.18065	1243829	23922.89
523440.025	297.9942627	15328.545	0.109515207	9.21E-06	13.17873	1219807	23919.39
523441.685	297.9950256	15011.078	0.109464266	1.35E-05	13.1726	1194544	23908.26
523442.345	297.9949493	14885.5085	0.109454802	1.04E-05	13.17146	1184551	23906.19
523443.445	297.9949799	14657.913	0.109431876	1.21E-05	13.1687	1166440	23901.19
523444.585	297.9954529	14447.7405	0.109411129	9.36E-06	13.1662	1149715	23896.65
523446.605	297.9952087	14072.325	0.109357247	1.22E-05	13.15972	1119840	23884.89
523447.23	297.995285	13952.3045	0.10934342	1.20E-05	13.15805	1110289	23881.87
523448.27	297.9949951	13741.7445	0.109308379	1.09E-05	13.15384	1093533	23874.21
523449.41	297.9949188	13525.1545	0.109279993	9.57E-06	13.15042	1076298	23868.01
523450.525	297.9957123	13332.3955	0.109258657	6.04E-06	13.14785	1060958	23863.35
523451.5	297.9960632	13156.5775	0.109227181	9.56E-06	13.14407	1046967	23856.48
523453.61	297.9966125	12747.709	0.109175861	1.23E-05	13.13789	1014430	23845.27
523454.36	297.9970398	12610.8445	0.109156299	8.11E-06	13.13554	1003539	23841
523455.41	297.997467	12399.7095	0.109119602	1.10E-05	13.13112	986737.5	23832.98
523456.345	297.9971924	12223.6045	0.109093827	1.12E-05	13.12802	972723.5	23827.35
523457.57	297.9970856	11979.2595	0.109029604	8.91E-06	13.12029	953279.2	23813.33
523458.905	297.9972229	11728.6935	0.108996565	9.73E-06	13.11631	933339.8	23806.11
523461.005	297.9975586	11341.6455	0.108964638	1.14E-05	13.11247	902539.5	23799.14
523461.735	297.9974366	11199.325	0.108938126	1.07E-05	13.10928	891214	23793.35
523462.735	297.9976197	10988.2855	0.108868834	1.37E-05	13.10094	874420	23778.21
523463.84	297.9983978	10777.5335	0.10883869	9.97E-06	13.09732	857648.9	23771.63
523465.125	297.9985046	10566.687	0.108800967	1.02E-05	13.09278	840870.2	23763.39
523466.2	297.9983368	10350.2895	0.108750166	1.19E-05	13.08666	823649.9	23752.29
523467.18	297.9981843	10156.9565	0.108714976	1.26E-05	13.08243	808264.9	23744.61
523468.235	297.9980164	9963.1445	0.108693407	1.10E-05	13.07983	792841.8	23739.9
523469.445	297.9982453	9734.685	0.108645334	8.73E-06	13.07405	774661.6	23729.4
523470.61	297.998291	9524.5065	0.108589065	1.39E-05	13.06728	757936.1	23717.11
523472.72	297.9993286	9113.818	0.108517621	1.16E-05	13.05868	725254.6	23701.5
523474.315	297.9986267	8811.4735	0.108418319	1.07E-05	13.04673	701194.8	23679.81
523474.995	297.9998322	8675.0865	0.108375735	1.18E-05	13.0416	690341.4	23670.51
523476.095	298.000351	8464.333	0.108321778	1.39E-05	13.03511	673570.2	23658.73
523477.17	297.9995423	8264.5885	0.108263204	9.61E-06	13.02806	657675.1	23645.93
523478.215	297.9997254	8070.49	0.108214865	9.33E-06	13.02225	642229.2	23635.38
523479.125	298.0000763	7893.5225	0.10815835	1.08E-05	13.01545	628146.6	23623.03
523480.16	297.9998932	7699.5195	0.108101515	1.37E-05	13.00861	612708.3	23610.62
523481.415	298.0004578	7454.5975	0.107984794	1.30E-05	12.99456	593218	23585.13
523482.805	298.0016632	7169.095	0.107928505	8.96E-06	12.98779	570498.5	23572.83
523484.16	298.0022278	6922.9295	0.107853323	1.07E-05	12.97874	550909.2	23556.41
523485.34	298.0022431	6694.1845	0.107785834	1.33E-05	12.97062	532706.3	23541.67
523487.415	298.00177	6299.667	0.107625621	1.30E-05	12.95134	501311.6	23506.68
523488.09	298.0019531	6179.2635	0.107533853	1.35E-05	12.9403	491730.2	23486.64
523489.215	298.0021057	5967.7445	0.10746642	6.90E-06	12.93218	474898	23471.91
523490.345	298.0020905	5750.2925	0.107395723	1.21E-05	12.92367	457593.7	23456.47
523491.345	298.0022888	5554.7575	0.107286689	9.90E-06	12.91055	442033.6	23432.65
523492.325	298.0024719	5376.7365	0.107178681	1.35E-05	12.89755	427867.1	23409.06
523493.415	298.0024262	5181.6775	0.107074256	1.40E-05	12.88499	412344.8	23386.25
523494.42	298.0023804	4986.429	0.10697841	1.33E-05	12.87345	396807.4	23365.32
523495.54	298.0027314	4774.5275	0.106874733	1.05E-05	12.86098	379944.8	23342.68

523496.69	298.0027008	4544.6315	0.106742486	1.57E-05	12.84506	361650.3	23313.79
523497.735	298.0031891	4342.5875	0.106614077	1.86E-05	12.82961	345572.1	23285.75
523498.88	298.0041046	4129.3445	0.106325188	1.10E-05	12.79485	328602.8	23222.65
523500.015	298.0036621	3899.3525	0.106174929	1.49E-05	12.77677	310300.6	23189.83
523502.115	298.0036926	3467.3155	0.105818281	1.35E-05	12.73385	275920.2	23111.93
523502.885	298.0037995	3328.726	0.105622034	1.61E-05	12.71023	264891.6	23069.07
523504.135	298.0039521	3114.333	0.105402177	1.83E-05	12.68378	247830.7	23021.05
523505.22	298.0041962	2894.676	0.105149625	1.45E-05	12.65338	230351	22965.89
523506.16	298.0042267	2698.182	0.104890272	1.88E-05	12.62217	214714.5	22909.25
523507.175	298.003952	2517.6705	0.104587827	1.97E-05	12.58578	200349.9	22843.19
523508.235	298.0048065	2302.6085	0.104257345	2.19E-05	12.54601	183235.8	22771.01
523509.235	298.0057678	2105.1565	0.103888916	2.15E-05	12.50167	167523	22690.54
523510.29	298.0062714	1906.268	0.103453504	2.38E-05	12.44928	151696	22595.44
523511.21	298.006424	1725.183	0.102953278	2.80E-05	12.38908	137285.7	22486.19
523512.165	298.0056763	1543.906	0.102364076	2.90E-05	12.31818	122860.1	22357.5
523513.245	298.0058441	1326.4495	0.10164297	3.94E-05	12.2314	105555.5	22200
523514.22	298.0064087	1143.5465	0.100739679	4.69E-05	12.12271	91000.54	22002.71
523515.29	298.006546	925.037	0.099563846	6.34E-05	11.98121	73612.11	21745.89
523516.29	298.0066833	717.63	0.09793227	8.79E-05	11.78487	57107.18	21389.54
523517.235	298.0068665	550.6145	0.095435198	0.000144568	11.48438	43816.51	20844.15
523518.195	298.0074616	365.987	0.090831925	0.000301125	10.93044	29124.32	19838.74
523519.18	298.0076752	163.4605	0.077598916	0.001153762	9.338016	13007.77	16948.5
523520.21	298.0072022	-56.58	-0.002337748	0.007523463	-0.28132	-4502.49	-510.591
523524.345	298.0078125	-860.462	-0.054177294	6.32E-06	-6.51953	-68473.4	-11832.9
523527.95	298.0075989	-1561.356	-0.101502463	3.62E-05	-12.2145	-124249	-22169.3
523528.535	298.0077668	-1660.896	-0.102235198	2.85E-05	-12.3027	-132170	-22329.3
523529.48	298.0083466	-1814.704	-0.102803418	2.65E-05	-12.371	-144410	-22453.5
523530.305	298.0087585	-1967.3635	-0.103285717	2.21E-05	-12.4291	-156558	-22558.8
523531.155	298.0081482	-2134.2835	-0.103708756	1.73E-05	-12.48	-169841	-22651.2
523532.14	298.0075378	-2300.6285	-0.10408023	2.05E-05	-12.5247	-183078	-22732.3
523533.125	298.008255	-2465.539	-0.10438687	1.70E-05	-12.5616	-196201	-22799.3
523534.14	298.0083619	-2645.285	-0.104680408	1.32E-05	-12.5969	-210505	-22863.4
523535.14	298.0084992	-2823.3085	-0.104938861	1.72E-05	-12.628	-224672	-22919.9
523536.355	298.0090943	-3033.012	-0.105168044	1.35E-05	-12.6556	-241359	-22969.9
523537.3	298.0089417	-3196.9645	-0.10538589	1.28E-05	-12.6818	-254406	-23017.5
523538.05	298.008606	-3346.5605	-0.105606534	9.58E-06	-12.7084	-266311	-23065.7
523539	298.0089417	-3529.082	-0.105778584	1.42E-05	-12.7291	-280835	-23103.3
523539.975	298.009613	-3696.479	-0.105954507	1.71E-05	-12.7502	-294156	-23141.7
523541	298.009018	-3863.591	-0.106107919	1.79E-05	-12.7687	-307455	-23175.2
523543.195	298.0083618	-4272.1805	-0.106410165	1.84E-05	-12.8051	-339969	-23241.2
523543.94	298.008667	-4408.568	-0.106545783	1.58E-05	-12.8214	-350823	-23270.8
523545.135	298.008606	-4643.8225	-0.106661035	1.33E-05	-12.8353	-369544	-23296
523546.4	298.0083313	-4862.521	-0.106778963	1.08E-05	-12.8495	-386947	-23321.8
523547.41	298.0084992	-5049.3485	-0.106897289	1.35E-05	-12.8637	-401814	-23347.6
523548.305	298.0086975	-5220.3835	-0.10700502	6.92E-06	-12.8767	-415425	-23371.1
523549.445	298.0086823	-5408.3585	-0.107105338	1.21E-05	-12.8887	-430383	-23393
523550.41	298.0086823	-5579.2965	-0.107201224	8.66E-06	-12.9003	-443986	-23414
523551.36	298.0089722	-5771.292	-0.107285931	9.31E-06	-12.9105	-459265	-23432.5
523552.42	298.0088959	-5975.538	-0.10737415	1.32E-05	-12.9211	-475518	-23451.8
523553.5	298.0091706	-6164.469	-0.107457837	1.06E-05	-12.9311	-490553	-23470
523554.655	298.0093232	-6369.7665	-0.107536177	9.87E-06	-12.9406	-506890	-23487.1
523555.625	298.0095826	-6541.184	-0.107614259	9.98E-06	-12.95	-520531	-23504.2
523556.64	298.0105286	-6729.063	-0.107697506	9.05E-06	-12.96	-535482	-23522.4
523557.7	298.0104676	-6934.169	-0.10775494	6.86E-06	-12.9669	-551804	-23534.9
523558.655	298.0101624	-7106.3515	-0.107828936	1.49E-05	-12.9758	-565505	-23551.1
523559.625	298.010315	-7295.5695	-0.107869239	1.26E-05	-12.9807	-580563	-23559.9
523560.595	298.0101166	-7484.405	-0.107953758	7.45E-06	-12.9908	-595590	-23578.3
523561.635	298.0100098	-7673.337	-0.107983457	1.49E-05	-12.9944	-610625	-23584.8
523563.655	298.0101929	-8057.039	-0.10811062	1.18E-05	-13.0097	-641159	-23612.6
523565.31	298.0097961	-8352.3005	-0.108224755	6.76E-06	-13.0234	-664655	-23637.5
523565.975	298.0096436	-8468.9725	-0.108267379	1.02E-05	-13.0286	-673939	-23646.8
523566.975	298.0096131	-8658.095	-0.108322411	1.44E-05	-13.0352	-688989	-23658.9
523567.96	298.0103607	-8847.408	-0.108375385	1.43E-05	-13.0416	-704054	-23670.4
523568.97	298.0102539	-9036.53	-0.108408042	9.28E-06	-13.0455	-719104	-23677.6

523569.995	298.0092926	-9208.9985	-0.108452992	9.32E-06	-13.0509	-732829	-23687.4
523571.11	298.0092621	-9415.6365	-0.108495922	8.78E-06	-13.0561	-749273	-23696.8
523572.155	298.0093689	-9628.2065	-0.108532275	8.06E-06	-13.0604	-766188	-23704.7
523573.14	298.0092773	-9800.5795	-0.108577986	1.05E-05	-13.0659	-779905	-23714.7
523574.305	298.0090179	-10006.3565	-0.108614532	1.38E-05	-13.0703	-796281	-23722.7
523575.385	298.0089722	-10212.8015	-0.108656342	1.21E-05	-13.0754	-812709	-23731.8
523576.47	298.0086975	-10418.7675	-0.108687773	1.35E-05	-13.0792	-829099	-23738.7
523577.64	298.0084839	-10647.1295	-0.108765222	8.08E-06	-13.0885	-847272	-23755.6
523578.835	298.0086517	-10870.1325	-0.108795073	6.37E-06	-13.0921	-865018	-23762.1
523580.015	298.0087738	-11093.901	-0.108832969	8.59E-06	-13.0966	-882825	-23770.4
523581.17	298.0090027	-11306.375	-0.108855393	1.19E-05	-13.0993	-899733	-23775.3
523582.18	298.0090027	-11479.6085	-0.108898057	1.03E-05	-13.1045	-913518	-23784.6
523583.205	298.0084076	-11669.8795	-0.10893326	1.39E-05	-13.1087	-928660	-23792.3
523584.345	298.0082398	-11909.8225	-0.108957101	1.21E-05	-13.1116	-947754	-23797.5
523585.37	298.008667	-12100.3795	-0.108990683	1.29E-05	-13.1156	-962918	-23804.8
523586.425	298.0087433	-12273.4225	-0.109021198	1.16E-05	-13.1193	-976688	-23811.5
523587.37	298.0089264	-12462.6395	-0.109044712	1.47E-05	-13.1221	-991745	-23816.6
523589.285	298.0085449	-12814.469	-0.109097309	1.44E-06	-13.1284	-1019743	-23828.1
523589.985	298.0081787	-12948.843	-0.109119844	6.03E-06	-13.1311	-1030436	-23833
523591.1	298.0080719	-13156.1485	-0.109153814	6.55E-06	-13.1352	-1046933	-23840.5
523592.15	298.0078736	-13345.844	-0.10917984	8.95E-06	-13.1384	-1062029	-23846.1
523593.285	298.0080872	-13569.709	-0.109197613	3.95E-06	-13.1405	-1079843	-23850
523594.47	298.0089264	-13799.3175	-0.109221059	1.08E-05	-13.1433	-1098115	-23855.1
523595.67	298.0085907	-14005.5705	-0.109274994	1.24E-05	-13.1498	-1114528	-23866.9
523596.9	298.0081635	-14228.7645	-0.109290861	9.61E-06	-13.1517	-1132289	-23870.4
523598.01	298.0085907	-14441.431	-0.109313801	8.58E-06	-13.1545	-1149213	-23875.4
523598.99	298.0091401	-14615.2385	-0.109338469	8.27E-06	-13.1575	-1163044	-23880.8
523600.005	298.0092621	-14805.4115	-0.109360408	1.36E-05	-13.1601	-1178177	-23885.6
523601	298.009552	-14995.203	-0.109372301	1.09E-05	-13.1615	-1193280	-23888.2
523601.995	298.0091858	-15185.283	-0.109400774	5.41E-06	-13.165	-1208406	-23894.4
523603.2	298.0084687	-15431.6375	-0.109423088	1.09E-05	-13.1676	-1228011	-23899.3
523604.575	298.0084076	-15689.38	-0.109457489	7.09E-06	-13.1718	-1248521	-23906.8
523605.885	298.0082093	-15929.8965	-0.10948585	9.23E-06	-13.1752	-1267661	-23913
523606.99	298.0081482	-16137.2025	-0.109487591	1.28E-05	-13.1754	-1284158	-23913.4
523608.105	298.0085755	-16327.6635	-0.109511761	5.96E-06	-13.1783	-1299314	-23918.6
523609.185	298.0087586	-16523.293	-0.10953734	1.36E-05	-13.1814	-1314882	-23924.2
523610.165	298.0084839	-16712.702	-0.109550528	9.59E-06	-13.183	-1329955	-23927.1
523611.3	298.008667	-16936.7565	-0.10956792	1.04E-05	-13.1851	-1347784	-23930.9
523612.4	298.0088044	-17144.6365	-0.109591941	8.89E-06	-13.188	-1364327	-23936.1
523613.455	298.0085755	-17334.905	-0.109597657	3.43E-06	-13.1886	-1379468	-23937.4
523614.37	298.0084839	-17508.999	-0.109615042	7.47E-06	-13.1907	-1393322	-23941.2
523615.21	298.0081482	-17665.39	-0.10964332	6.54E-06	-13.1941	-1405767	-23947.4
523616.36	298.0075073	-17877.673	-0.109654824	5.41E-06	-13.1955	-1422660	-23949.9
523617.47	298.0072021	-18085.2645	-0.109668225	8.25E-06	-13.1971	-1439180	-23952.8
523618.39	298.0075378	-18259.2625	-0.109673658	1.04E-05	-13.1978	-1453026	-23954
523619.4	298.0073242	-18449.7225	-0.109713108	1.05E-05	-13.2025	-1468182	-23962.6
523620.335	298.0067749	-18623.0525	-0.109710032	1.15E-05	-13.2022	-1481975	-23961.9
523621.35	298.0069123	-18813.419	-0.109731366	9.60E-06	-13.2047	-1497124	-23966.6
523622.4	298.0070496	-19004.4555	-0.109742343	1.05E-05	-13.2061	-1512327	-23969
523623.335	298.0066376	-19178.458	-0.109766891	6.35E-06	-13.209	-1526173	-23974.4
523624.475	298.0063172	-19402.154	-0.109792521	1.20E-05	-13.2121	-1543974	-23980
523625.78	298.0056	-19640.6875	-0.109802426	1.06E-05	-13.2133	-1562956	-23982.1
523626.935	298.0051728	-19797.888	-0.109818032	1.04E-05	-13.2152	-1575466	-23985.5
523627.915	298.0054474	-19859.761	-0.109816814	1.16E-05	-13.215	-1580390	-23985.3
523628.955	298.0055237	-19889.157	-0.109825377	1.01E-05	-13.2161	-1582729	-23987.1
523629.96	298.0051728	-19900.862	-0.109832555	7.51E-06	-13.2169	-1583660	-23988.7
523638.94	298.0036774	-20000.519	-0.109836993	9.44E-06	-13.2174	-1591591	-23989.7
523648.765	298.0010681	-19901.469	-0.109808241	1.25E-05	-13.214	-1583709	-23983.4
523649.235	298.0014801	-19794.8535	-0.10982495	1.28E-05	-13.216	-1575224	-23987
523650.04	298.0020142	-19625.947	-0.109794759	1.07E-05	-13.2124	-1561783	-23980.4
523650.94	298.0016785	-19413.669	-0.109784294	1.05E-05	-13.2111	-1544891	-23978.2
523651.97	298.0015412	-19161.8625	-0.10976149	2.78E-06	-13.2084	-1524853	-23973.2
523652.96	298.0018616	-18942.5945	-0.109747071	7.04E-06	-13.2066	-1507404	-23970
523653.915	298.0019989	-18746.87	-0.109728599	7.37E-06	-13.2044	-1491829	-23966

295

523654.91	298.0019989	-18554.879	-0.109715391	9.27E-06	-13.2028	-1476550	-23963.1
523655.9	298.0014954	-18348.532	-0.10969586	1.36E-05	-13.2005	-1460130	-23958.8
523656.885	298.0012665	-18145.533	-0.109671861	6.50E-06	-13.1976	-1443976	-23953.6
523657.895	298.0010987	-17962.921	-0.109660528	1.02E-05	-13.1962	-1429444	-23951.1
523658.9	298.0010376	-17765.2845	-0.109648408	8.48E-06	-13.1948	-1413716	-23948.5
523659.9	298.0008392	-17568.891	-0.109617895	1.01E-05	-13.1911	-1398088	-23941.8
523660.9	298.000061	-17373.165	-0.109602754	8.60E-06	-13.1893	-1382513	-23938.5
523661.9	298.0007629	-17178.3015	-0.109582209	1.21E-05	-13.1868	-1367006	-23934
523662.9	298.0008698	-17000.571	-0.109563504	6.40E-06	-13.1845	-1352862	-23929.9
523663.915	297.9999085	-16806.952	-0.109545627	6.26E-06	-13.1824	-1337455	-23926
523664.94	297.9994812	-16590.746	-0.109526333	1.36E-05	-13.1801	-1320250	-23921.8
523665.915	297.9996338	-16397.1275	-0.109512333	1.11E-05	-13.1784	-1304842	-23918.8
523666.89	297.9999695	-16220.065	-0.109484717	9.92E-06	-13.1751	-1290752	-23912.7
523667.885	297.9998169	-16043.1935	-0.109468896	7.06E-06	-13.1732	-1276677	-23909.3
523668.9	298.0001221	-15850.1495	-0.109447077	9.31E-06	-13.1705	-1261315	-23904.5
523669.9	297.9997864	-15656.724	-0.109418569	9.08E-06	-13.1671	-1245923	-23898.3
523670.9	297.9991455	-15462.722	-0.109405966	7.37E-06	-13.1656	-1230484	-23895.5
523671.935	297.9992524	-15252.161	-0.109377444	7.53E-06	-13.1621	-1213728	-23889.3
523672.92	297.9994202	-15076.6315	-0.10935352	8.30E-06	-13.1593	-1199760	-23884.1
523673.885	297.9997101	-14900.624	-0.109342326	9.56E-06	-13.1579	-1185754	-23881.6
523674.88	298.0001831	-14707.102	-0.109317122	1.09E-05	-13.1549	-1170354	-23876.1
523675.88	297.9997101	-14530.998	-0.109285583	7.96E-06	-13.1511	-1156340	-23869.2
523676.88	297.9994507	-14337.9515	-0.109261448	6.91E-06	-13.1482	-1140978	-23864
523677.895	298.0001221	-14139.451	-0.109244154	8.99E-06	-13.1461	-1125182	-23860.2
523678.9	298.0001984	-13947.1725	-0.109221282	1.17E-05	-13.1434	-1109881	-23855.2
523679.9	297.9997711	-13753.8205	-0.109197371	7.32E-06	-13.1405	-1094494	-23850
523680.895	298.0001679	-13577.0265	-0.109177424	1.27E-05	-13.1381	-1080425	-23845.6
523681.925	298.0001221	-13383.8845	-0.109140389	7.72E-06	-13.1336	-1065056	-23837.5
523682.945	297.9997864	-13190.551	-0.109109374	1.05E-05	-13.1299	-1049671	-23830.7
523683.9	298.0001831	-13013.776	-0.1090861	5.26E-06	-13.1271	-1035603	-23825.7
523684.925	298.0002289	-12820.251	-0.109060498	1.35E-05	-13.124	-1020203	-23820.1
523685.94	298.0000458	-12627.2065	-0.109028727	1.09E-05	-13.1202	-1004841	-23813.1
523686.895	297.9994812	-12433.4915	-0.109004902	8.75E-06	-13.1173	-989426	-23807.9
523687.88	297.9998169	-12240.827	-0.108974083	9.09E-06	-13.1136	-974094	-23801.2
523688.885	298.0001679	-12065.2005	-0.108942186	9.12E-06	-13.1098	-960118	-23794.2
523689.9	298.0000306	-11871.5825	-0.108914122	1.11E-05	-13.1064	-944711	-23788.1
523690.895	298	-11672.125	-0.108883832	1.09E-05	-13.1027	-928838	-23781.5
523691.895	298.0004273	-11477.93	-0.108856929	5.72E-06	-13.0995	-913385	-23775.6
523692.91	298.0005646	-11284.0225	-0.10882294	1.31E-05	-13.0954	-897954	-23768.2
523693.885	298.0001068	-11107.4375	-0.10878089	9.23E-06	-13.0904	-883902	-23759
523694.885	297.999939	-10914.1045	-0.108746948	7.67E-06	-13.0863	-868517	-23751.6
523695.895	298.0005036	-10721.1545	-0.108713946	1.23E-05	-13.0823	-853162	-23744.4
523696.88	298.0005494	-10544.858	-0.108675176	1.12E-05	-13.0776	-839133	-23735.9
523697.88	298.0003357	-10350.57	-0.10863562	1.04E-05	-13.0729	-823672	-23727.3
523698.885	298.0003967	-10157.3315	-0.108602765	7.78E-06	-13.0689	-808295	-23720.1
523699.885	298.0000305	-9963.806	-0.10856218	1.04E-05	-13.064	-792894	-23711.2
523700.91	297.9997101	-9769.517	-0.108520135	9.99E-06	-13.059	-777433	-23702.1
523701.9	297.9994202	-9593.221	-0.108477867	1.00E-05	-13.0539	-763404	-23692.8
523702.87	297.9994507	-9399.6	-0.108436075	1.28E-05	-13.0489	-747996	-23683.7
523703.88	297.9996643	-9199.9495	-0.108392987	1.08E-05	-13.0437	-732109	-23674.3
523704.87	297.9993744	-9023.2705	-0.108343571	7.44E-06	-13.0377	-718049	-23663.5
523705.86	297.9991761	-8829.172	-0.108303693	9.20E-06	-13.0329	-702603	-23654.8
523706.87	297.9993134	-8635.553	-0.10825437	1.17E-05	-13.027	-687195	-23644
523707.87	297.9992371	-8459.352	-0.10820306	1.20E-05	-13.0208	-673174	-23632.8
523708.87	297.9987183	-8265.443	-0.108158951	8.94E-06	-13.0155	-657743	-23623.2
523709.885	297.9987488	-8070.8645	-0.1080908	1.04E-05	-13.0073	-642259	-23608.3
523710.865	297.9997711	-7893.2265	-0.108040237	7.12E-06	-13.0012	-628123	-23597.2
523711.875	297.9994202	-7699.8935	-0.1079791	1.13E-05	-12.9939	-612738	-23583.9
523712.885	297.9989777	-7506.369	-0.107919858	1.22E-05	-12.9867	-597338	-23570.9
523713.87	297.9990998	-7311.7915	-0.107856705	1.01E-05	-12.9791	-581854	-23557.2
523714.87	297.9986878	-7117.596	-0.107803383	1.07E-05	-12.9727	-566400	-23545.5
523715.85	297.9988251	-6940.245	-0.107727124	1.03E-05	-12.9636	-552287	-23528.8
523716.85	297.999054	-6740.117	-0.107662843	1.05E-05	-12.9558	-536361	-23514.8
523717.87	297.9989014	-6528.886	-0.107584299	8.37E-06	-12.9464	-519552	-23497.7

296

523718.88	297.9992981	-6334.4985	-0.107510147	7.76E-06	-12.9374	-504083	-23481.5
523719.87	297.9991303	-6157.147	-0.107428932	1.10E-05	-12.9277	-489970	-23463.7
523720.86	297.998642	-5979.701	-0.10734573	1.11E-05	-12.9177	-475849	-23445.5
523721.86	297.9987641	-5785.219	-0.107250055	4.79E-06	-12.9061	-460373	-23424.7
523722.87	297.9989472	-5590.2575	-0.10715195	8.99E-06	-12.8943	-444859	-23403.2
523723.86	297.9989014	-5395.4875	-0.107074495	6.19E-06	-12.885	-429359	-23386.3
523724.86	297.9986115	-5200.622	-0.106965932	1.18E-05	-12.872	-413852	-23362.6
523725.87	297.9987793	-5023.0795	-0.106860596	6.38E-06	-12.8593	-399724	-23339.6
523726.9	297.9989624	-4827.831	-0.106736594	1.13E-05	-12.8444	-384187	-23312.5
523727.9	297.9981385	-4632.4845	-0.106615306	1.24E-05	-12.8298	-368641	-23286
523728.86	297.9978791	-4438	-0.106484548	1.37E-05	-12.814	-353165	-23257.5
523729.875	297.9977417	-4236.435	-0.106344114	9.33E-06	-12.7971	-337125	-23226.8
523730.875	297.9974823	-4057.839	-0.106194839	8.94E-06	-12.7792	-322913	-23194.2
523731.845	297.9982758	-3879.4345	-0.106044663	1.03E-05	-12.7611	-308716	-23161.4
523732.835	297.9986572	-3683.227	-0.10586498	1.29E-05	-12.7395	-293102	-23122.1
523733.88	297.98823	-3469.601	-0.105669595	1.40E-05	-12.716	-276102	-23079.5
523734.875	297.9982148	-3273.2985	-0.105474764	1.32E-05	-12.6925	-260481	-23036.9
523735.82	297.9981079	-3093.936	-0.105243332	1.35E-05	-12.6647	-246208	-22986.4
523736.82	297.9979858	-2914.0955	-0.105006715	1.42E-05	-12.6362	-231896	-22934.7
523737.835	297.9976959	-2717.5055	-0.10474094	1.64E-05	-12.6042	-216252	-22876.6
523738.825	297.9971466	-2520.3405	-0.104434769	1.56E-05	-12.5674	-200562	-22809.8
523739.835	297.9968109	-2322.2185	-0.10409785	1.80E-05	-12.5268	-184796	-22736.2
523740.86	297.9968109	-2124.48	-0.103711864	1.78E-05	-12.4804	-169061	-22651.9
523741.85	297.9971008	-1943.6815	-0.103273628	2.27E-05	-12.4276	-154673	-22556.2
523742.85	297.9967804	-1739.052	-0.10276295	2.61E-05	-12.3662	-138389	-22444.6
523743.87	297.9969177	-1522.266	-0.102146162	3.16E-05	-12.292	-121138	-22309.9
523744.88	297.997406	-1340.031	-0.101408465	3.82E-05	-12.2032	-106636	-22148.8
523745.86	297.9970856	-1157.5095	-0.100478556	4.70E-05	-12.0913	-92111.7	-21945.7
523746.85	297.9966431	-939.2865	-0.099237173	6.49E-05	-11.9419	-74746	-21674.5
523747.885	297.9961853	-737.814	-0.097512814	9.47E-05	-11.7344	-58713.4	-21297.9
523748.87	297.9966431	-553.667	-0.094798974	0.000159939	-11.4078	-44059.4	-20705.2
523749.835	297.9968262	-368.562	-0.089584982	0.00035115	-10.7804	-29329.2	-19566.4
523750.835	297.9960175	-182.977	-0.072288698	0.001639299	-8.699	-14560.8	-15788.7
523751.83	297.9958191	18.976	0.022268367	0.006112929	2.679707	1510.062	4863.669
523752.835	297.9951477	220.161	0.082032812	0.000787243	9.871578	17519.86	17916.91
523753.85	297.99469	420.5805	0.091885227	0.000252147	11.05719	33468.73	20068.8
523754.845	297.9948578	620.1395	0.095843857	0.000129715	11.53356	49349.13	20933.41
523755.835	297.9948425	800.363	0.098107552	8.16E-05	11.80596	63690.86	21427.82
523756.85	297.9945831	995.52	0.099614757	6.03E-05	11.98734	79220.96	21757.01
523757.845	297.9943695	1210.68	0.100696549	4.45E-05	12.11751	96342.85	21993.29
523758.845	297.9943238	1400.857	0.101550685	3.58E-05	12.2203	111476.7	22179.84
523759.86	297.9940796	1573.5205	0.102221984	2.71E-05	12.30108	125216.8	22326.46
523760.835	297.9938812	1744.6525	0.10278202	2.27E-05	12.36847	138835	22448.78
523761.81	297.9937592	1930.428	0.103262063	1.98E-05	12.42624	153618.6	22553.63
523762.81	297.9937287	2114.194	0.103676088	1.98E-05	12.47606	168242.2	22644.06
523763.825	297.992981	2295.662	0.104027971	1.68E-05	12.51841	182683	22720.91
523764.84	297.9929199	2476.9395	0.104351181	1.71E-05	12.5573	197108.6	22791.5
523765.84	297.9932404	2640.605	0.104622715	1.49E-05	12.58998	210132.7	22850.81
523766.85	297.9929657	2817.8615	0.104875973	1.29E-05	12.62045	224238.3	22906.12
523767.845	297.9933014	2995.0225	0.105107283	1.57E-05	12.64829	238336.3	22956.64
523768.83	297.993927	3158.4	0.105326717	1.26E-05	12.6747	251337.5	23004.57
523769.82	297.9941864	3339.294	0.105520357	1.26E-05	12.698	265732.6	23046.87
523770.82	297.9933014	3526.698	0.105690866	6.52E-06	12.71852	280645.7	23084.11
523771.82	297.9927979	3710.559	0.10587382	1.23E-05	12.74053	295276.9	23124.07
523772.805	297.9927521	3894.8005	0.106035414	5.98E-06	12.75998	309938.4	23159.36
523773.815	297.9926606	4079.617	0.106183727	1.11E-05	12.77783	324645.6	23191.75
523774.835	297.9924317	4265.3915	0.106317073	1.05E-05	12.79387	339429.1	23220.88
523775.82	297.9923096	4434.512	0.106454958	8.78E-06	12.81046	352887.3	23250.99
523776.805	297.9928436	4619.9985	0.106585785	5.99E-06	12.82621	367647.8	23279.57
523777.82	297.9929962	4806.634	0.106696259	8.55E-06	12.8395	382499.8	23303.7
523778.805	297.9933014	4977.287	0.106818146	1.05E-05	12.85417	396079.9	23330.32
523779.795	297.9935456	5164.0185	0.106912091	9.12E-06	12.86547	410939.5	23350.84
523780.795	297.9934845	5350.558	0.107007923	9.72E-06	12.87701	425783.9	23371.77
523781.795	297.9933167	5521.115	0.107114466	9.38E-06	12.88983	439356.4	23395.04

523782.81	297.9935456	5708.7065	0.107182484	5.24E-06	12.89801	454284.4	23409.89
523783.82	297.9932862	5901.7535	0.107282363	1.00E-05	12.91003	469646.6	23431.71
523784.83	297.9924164	6089.345	0.107361011	1.18E-05	12.9195	484574.7	23448.89
523785.805	297.9927521	6277.606	0.107442281	8.84E-06	12.92928	499556	23466.64
523786.795	297.9927521	6448.831	0.107527073	6.41E-06	12.93948	513181.7	23485.15
523787.81	297.9922486	6637.093	0.107589887	5.63E-06	12.94704	528163.1	23498.87
523788.795	297.9929505	6825.4515	0.107654031	6.41E-06	12.95476	543152.2	23512.88
523789.81	297.9930573	7012.564	0.107726918	1.10E-05	12.96353	558042.1	23528.8
523790.825	297.9920502	7201.3985	0.107777666	1.28E-05	12.96963	573069.1	23539.89
523791.825	297.9923706	7390.521	0.107853164	7.69E-06	12.97872	588119	23556.38
523792.835	297.9926605	7578.783	0.107905663	7.04E-06	12.98504	603100.4	23567.84
523793.855	297.9925842	7750.7745	0.107955295	4.75E-06	12.99101	616787	23578.68
523794.845	297.9928284	7922.861	0.108012175	1.01E-05	12.99785	630481.2	23591.11
523795.805	297.9923706	8111.312	0.108068024	1.03E-05	13.00458	645477.7	23603.3
523796.805	297.9922333	8305.602	0.108118008	9.04E-06	13.01059	660938.8	23614.22
523797.82	297.9924775	8494.8195	0.10817566	1.24E-05	13.01753	675996.3	23626.81
523798.82	297.9923096	8700.404	0.108222548	9.41E-06	13.02317	692356.2	23637.05
523799.81	297.9923401	8872.2995	0.108269211	6.17E-06	13.02879	706035.2	23647.25
523800.795	297.9932099	9028.402	0.108316198	4.93E-06	13.03444	718457.4	23657.51
523801.79	297.9940033	9218.194	0.108358297	4.16E-06	13.03951	733560.6	23666.7
523802.845	297.9943085	9423.778	0.108400872	1.16E-05	13.04463	749920.4	23676
523803.935	297.9944611	9630.319	0.108434709	5.27E-06	13.0487	766356.4	23683.39
523804.975	297.9948578	9820.11	0.108475798	5.83E-06	13.05365	781459.5	23692.37
523806.015	297.9947358	10014.1135	0.10851772	6.94E-06	13.05869	796897.8	23701.52
523807.145	297.9942017	10236.8305	0.108546323	7.55E-06	13.06213	814621.1	23707.77
523809.24	297.994751	10616.797	0.108620056	7.21E-06	13.07101	844857.9	23723.87
523809.86	297.9943543	10739.497	0.108663054	7.29E-06	13.07618	854622	23733.27
523811.065	297.9944306	10962.788	0.108692666	7.69E-06	13.07974	872391	23739.73
523812.35	297.9947815	11220.1495	0.108769107	8.50E-06	13.08894	892871.1	23756.43
523813.64	297.9946594	11465.6425	0.108792752	8.13E-06	13.09179	912406.8	23761.59
523814.89	297.9947357	11671.2255	0.108821962	6.31E-06	13.0953	928766.6	23767.97
523816	297.9947968	11877.479	0.108845795	5.41E-06	13.09817	945179.7	23773.18
523817.08	297.9949799	12089.763	0.108878189	6.59E-06	13.10207	962072.8	23780.25
523818.155	297.9952393	12279.6505	0.108907066	1.05E-05	13.10554	977183.5	23786.56
523819.195	297.9954987	12469.73	0.108940519	8.15E-06	13.10957	992309.6	23793.87
523820.3	297.9956055	12676.2705	0.108960344	7.20E-06	13.11195	1008746	23798.2
523821.51	297.9957581	12916.404	0.109015377	7.25E-06	13.11858	1027855	23810.22
523822.74	297.9959107	13145.3395	0.109050106	1.19E-05	13.12276	1046073	23817.8
523823.88	297.9955445	13335.035	0.109066053	5.28E-06	13.12468	1061168	23821.29
523825.015	297.9954224	13558.707	0.109090207	6.43E-06	13.12758	1078968	23826.56
523826.085	297.9957886	13765.6305	0.109108802	7.50E-06	13.12982	1095434	23830.62
523827.165	297.995163	13955.9975	0.109148909	8.73E-06	13.13465	1110583	23839.38
523828.415	297.994751	14185.2215	0.109179934	1.18E-05	13.13838	1128824	23846.16
523830.585	297.9953308	14598.974	0.109214464	1.02E-05	13.14253	1161749	23853.7
523831.29	297.9954071	14722.2505	0.109221706	4.07E-06	13.14341	1171559	23855.28
523832.415	297.9956208	14929.364	0.109246605	9.11E-06	13.1464	1188041	23860.72
523833.485	297.9955597	15136.478	0.109274626	9.28E-06	13.14977	1204523	23866.84
523834.475	297.9952698	15326.651	0.109297333	7.87E-06	13.15251	1219656	23871.8
523836.505	297.9954834	15711.975	0.109334942	1.06E-05	13.15703	1250319	23880.01
523837.265	297.9957428	15846.542	0.109377172	9.39E-06	13.16211	1261028	23889.24
523838.605	297.9960022	16087.442	0.109392284	9.83E-06	13.16393	1280198	23892.54
523839.805	297.9957428	16317.7175	0.109406254	1.04E-05	13.16561	1298523	23895.59
523840.895	297.9956818	16524.447	0.109439981	1.02E-05	13.16967	1314974	23902.96
523841.99	297.9954834	16730.605	0.109446786	1.24E-05	13.17049	1331379	23904.44
523842.945	297.995224	16904.413	0.109461967	1.32E-05	13.17232	1345210	23907.76
523843.985	297.9953156	17094.299	0.109490761	7.48E-06	13.17578	1360321	23914.05
523845.125	297.9949799	17323.1395	0.109496883	8.48E-06	13.17652	1378532	23915.38
523846.115	297.9945984	17513.5045	0.109515206	9.38E-06	13.17873	1393680	23919.39
523847.24	297.9945984	17720.331	0.109520917	8.51E-06	13.17941	1410139	23920.63
523848.36	297.9948578	17927.7325	0.109555428	1.29E-05	13.18357	1426644	23928.17
523849.55	297.9949493	18134.752	0.109576796	9.71E-06	13.18614	1443118	23932.84
523850.895	297.9946442	18380.628	0.109594639	1.33E-05	13.18828	1462684	23936.74
523852.09	297.9945984	18604.49	0.109618303	1.07E-05	13.19113	1480498	23941.9
523853.305	297.9948273	18828.9265	0.109653825	4.13E-06	13.19541	1498358	23949.66

523854.515	297.9947052	19059.1085	0.109659799	6.02E-06	13.19613	1516676	23950.97
523855.665	297.9949036	19282.5	0.109671366	8.96E-06	13.19752	1534453	23953.49
523856.775	297.9945069	19489.457	0.109689111	7.88E-06	13.19965	1550922	23957.37
523857.925	297.9938507	19684.0275	0.109713455	6.08E-06	13.20258	1566405	23962.69
523859.05	297.9936676	19839.086	0.109712726	6.83E-06	13.20249	1578744	23962.53
523859.97	297.993393	19902.4325	0.109717116	4.56E-06	13.20302	1583785	23963.49
523860.915	297.9934235	19922.336	0.109719024	1.00E-05	13.20325	1585369	23963.9
523861.86	297.9927826	19932.8595	0.109723844	6.70E-06	13.20383	1586207	23964.96
523870.925	297.9933472	19998.8475	0.109730047	8.78E-06	13.20458	1591458	23966.31
523880.775	297.9913178	19904.715	0.109699465	3.69E-05	13.2009	1583967	23959.63
523881.565	297.9911652	19709.8905	0.109693112	1.03E-05	13.20013	1568463	23958.24
523882.815	297.9907532	19412.734	0.109689776	9.46E-06	13.19973	1544816	23957.51
523883.8	297.990738	19205.338	0.109656614	1.24E-05	13.19574	1528312	23950.27
523885.71	297.9907074	18807.096	0.109633899	4.51E-06	13.19301	1496621	23945.31
523886.51	297.9909058	18633.7665	0.109607779	9.31E-06	13.18987	1482828	23939.61
523887.705	297.9909821	18383.201	0.109590118	7.07E-06	13.18774	1462889	23935.75
523888.75	297.9913025	18161.4455	0.109575514	7.90E-06	13.18598	1445242	23932.56
523890.665	297.9914246	17797.081	0.109568949	5.35E-06	13.18519	1416247	23931.12
523892.22	297.9906311	17508.6165	0.109521574	9.91E-06	13.17949	1393291	23920.78
523892.9	297.9906616	17370.6985	0.109492965	8.27E-06	13.17605	1382316	23914.53
523893.985	297.9902496	17175.6445	0.109475136	3.55E-06	13.1739	1366794	23910.63
523895.905	297.9911041	16814.537	0.109444077	5.98E-06	13.17017	1338058	23903.85
523896.64	297.9913483	16660.3495	0.109429079	1.07E-05	13.16836	1325788	23900.58
523897.86	297.9910889	16415.717	0.109399949	1.01E-05	13.16486	1306321	23894.21
523898.9	297.9908753	16216.26	0.109383538	2.06E-06	13.16288	1290449	23890.63
523899.98	297.9908448	16021.494	0.10937116	1.02E-05	13.16139	1274950	23887.92
523901.04	297.9907685	15827.9705	0.109346687	7.81E-06	13.15845	1259550	23882.58
523902.125	297.9907074	15677.985	0.109328326	9.00E-06	13.15624	1242840	23878.57
523903.385	297.990326	15372.8735	0.109289182	7.37E-06	13.15153	1223334	23870.02
523904.635	297.990326	15138.7695	0.109253186	6.22E-06	13.14719	1204705	23862.16
523905.735	297.9911804	14927.4445	0.109231743	1.05E-05	13.14461	1187888	23857.47
523906.735	297.9914856	14734.1125	0.109199679	4.87E-06	13.14076	1172503	23850.47
523907.765	297.9913331	14541.6435	0.109192163	7.10E-06	13.13985	1157187	23848.83
523908.93	297.9913941	14331.16	0.109158679	1.02E-05	13.13582	1140437	23841.52
523910.11	297.9911652	14114.9315	0.109141264	7.44E-06	13.13373	1123231	23837.71
523911.22	297.9914093	13887.334	0.109095216	1.00E-05	13.12818	1105119	23827.66
523912.51	297.991333	13642.7005	0.10908024	1.14E-05	13.12638	1085652	23824.38
523913.86	297.9910126	13392.514	0.109048261	6.43E-06	13.12253	1065742	23817.4
523915.045	297.9906159	13164.726	0.109017464	1.06E-05	13.11883	1047616	23810.67
523916.13	297.9904938	12954.262	0.108990593	6.69E-06	13.11559	1030867	23804.8
523917.225	297.9913636	12743.605	0.108964835	9.12E-06	13.1125	1014104	23799.18
523918.24	297.9913941	12550.177	0.108949612	7.94E-06	13.11066	998711.4	23795.85
523920.14	297.9907837	12191.4585	0.108880279	8.01E-06	13.10232	970165.4	23780.71
523920.84	297.9907837	12055.3605	0.10885725	8.12E-06	13.09955	959335.1	23775.68
523921.905	297.9910889	11861.8375	0.108822822	1.01E-05	13.09541	943935	23768.16
523922.9	297.9914398	11685.0625	0.108798454	8.52E-06	13.09247	929867.7	23762.84
523924.015	297.9909516	11474.501	0.108770299	1.07E-05	13.08909	913111.8	23756.69
523925.005	297.9915467	11275.2345	0.108720176	9.74E-06	13.08305	897254.7	23745.74
523926.94	297.9918823	10891.823	0.108665938	9.65E-06	13.07653	866743.7	23733.9
523927.675	297.9917755	10766.613	0.108621913	1.13E-05	13.07123	856779.8	23724.28
523928.79	297.9915772	10549.7315	0.108581843	1.13E-05	13.06641	839521	23715.53
523930.795	297.9913025	10173.4245	0.108545199	9.88E-06	13.062	809575.4	23707.53
523932.635	297.9929504	9836.456	0.108472877	1.07E-05	13.05329	782760.3	23691.73
523934.165	297.9917145	9539.4115	0.108391713	1.04E-05	13.04353	759122.2	23674
523934.87	297.9914093	9413.648	0.108351219	8.91E-06	13.03865	749114.3	23665.16
523936	297.9911042	9219.287	0.108308288	9.60E-06	13.03349	733647.5	23655.78
523937.07	297.9915925	9007.777	0.108253683	7.86E-06	13.02692	716816.1	23643.85
523938.215	297.9919892	8773.298	0.10820844	1.02E-05	13.02147	698156.9	23633.97
523939.375	297.992157	8544.3975	0.108115429	6.43E-06	13.01028	679941.5	23613.66
523940.575	297.9920959	8315.41	0.108059799	1.10E-05	13.00359	661719.3	23601.51
523941.735	297.992218	8097.852	0.108009765	7.04E-06	12.99756	644406.6	23590.58
523942.76	297.9921418	7903.149	0.107953643	1.16E-05	12.99081	628912.6	23578.32
523944.58	297.9905701	7547.928	0.107888224	6.59E-06	12.98294	600645	23564.03
523946.11	297.9931946	7261.421	0.10776934	1.26E-05	12.96863	577845.5	23538.07

523946.8	297.9931183	7123.8175	0.107709664	8.70E-06	12.96145	566895.4	23525.03
523947.945	297.9927216	6894.5325	0.107628763	1.22E-05	12.95172	548649.5	23507.37
523949.09	297.9923554	6676.619	0.107583144	6.69E-06	12.94623	531308.5	23497.4
523950.28	297.9923096	6464.304	0.107487987	8.51E-06	12.93478	514413	23476.62
523951.29	297.9927063	6286.424	0.107416822	5.16E-06	12.92621	500257.7	23461.07
523953.415	297.992218	5855.975	0.107247909	8.65E-06	12.90589	466003.7	23424.18
523954.165	297.9919892	5735.331	0.107172861	1.04E-05	12.89685	456403.1	23407.79
523955.32	297.9918671	5505.3575	0.107082213	1.74E-06	12.88595	438102.4	23387.99
523956.235	297.9919739	5327.03	0.106989681	5.74E-06	12.87481	423911.6	23367.78
523958.05	297.9920349	4987.485	0.106773453	4.90E-06	12.84879	396891.4	23320.56
523959.625	297.993042	4664.9385	0.106659648	1.11E-05	12.8351	371224	23295.7
523960.02	297.9928284	4595.8255	0.106542486	1.14E-05	12.821	365724.2	23270.11
523960.895	297.99263	4434.3305	0.106406324	1.12E-05	12.80461	352872.8	23240.37
523962.075	297.9925995	4197.7035	0.106265054	1.01E-05	12.78761	334042.6	23209.52
523963.155	297.9921875	3983.999	0.106133738	1.36E-05	12.77181	317036.6	23180.83
523964.15	297.9920197	3787.388	0.105966415	9.52E-06	12.75167	301390.8	23144.29
523965.23	297.9924469	3573.3665	0.105787926	1.03E-05	12.7302	284359.5	23105.31
523966.415	297.9932099	3359.1615	0.105417862	1.36E-05	12.68566	267313.6	23024.48
523967.64	297.9937897	3138.8225	0.105193907	1.50E-05	12.65871	249779.6	22975.56
523968.71	297.9933472	2923.9965	0.104955539	1.40E-05	12.63003	232684.2	22923.5
523969.735	297.99263	2726.3405	0.104681633	1.64E-05	12.59707	216955.3	22863.68
523970.83	297.9923096	2510.8715	0.104384252	1.66E-05	12.56128	199808.8	22798.73
523971.765	297.9929962	2312.6205	0.104050028	1.79E-05	12.52106	184032.5	22725.73
523972.805	297.9938355	2114.054	0.103675704	2.17E-05	12.47602	168231.1	22643.97
523974	297.9933625	1879.9855	0.103243407	2.15E-05	12.424	149604.5	22549.55
523975.04	297.9931946	1698.1085	0.102735239	2.54E-05	12.36284	135131.2	22438.56
523976.12	297.9928894	1498.0645	0.102147005	3.06E-05	12.29206	119212.2	22310.09
523977.195	297.9923859	1274.178	0.101415466	3.79E-05	12.20403	101395.9	22150.31
523978.225	297.9927521	1073.137	0.100504399	4.72E-05	12.09439	85397.53	21951.32
523979.13	297.9929504	889.179	0.099307287	6.31E-05	11.95034	70758.62	21689.86
523980.03	297.9926453	704.618	0.097657285	9.13E-05	11.75178	56071.72	21329.48
523981.055	297.9918366	501.651	0.095113898	0.000150431	11.44572	39920.12	20773.97
523981.97	297.9921417	316.2725	0.090350223	0.00031466	10.87247	25168.17	19733.53
523982.945	297.9927673	156.955	0.076755474	0.001102853	9.236519	12490.08	16764.28
523983.81	297.9931183	63.559	0.04227069	0.001814093	5.086726	5057.865	9232.407
523984.695	297.9933929	25.4095	0.009608915	0.001143309	1.156307	2022.024	2098.698
523985.75	297.993042	6.948	-0.00825031	0.000460066	-0.99282	552.9043	-1801.96
523994.795	297.9937897	0.034	-0.01630671	1.32E-06	-1.9623	2.705634	-3561.57

300